

universität
uulm

Faculty of
Natural Sciences
Institute of Electrochemistry

First-Principles Studies and Reactive Force Field Development in Magnesium-Ion Battery Research

Dissertation

to obtain the academic degree Doctor rerum naturalium (Dr. rer. nat.)
of the Faculty of Natural Sciences at Ulm University

Submitted by:

Florian Nikolaus Fiesinger
born in Augsburg

2023

Version: 02. July 2023

This work was carried out in the period between September 2019 and December 2022 under the supervision of Prof. Dr. Timo Jacob at the Institute of Electrochemistry at Ulm University.

Dean of the Faculty of Natural Sciences at Ulm University:

Prof. Dr. Thorsten Bernhardt

Reviewer:

Prof. Dr. Timo Jacob (First Reviewer)
Prof. Dr. Axel Groß (Second Reviewer)

Day of oral examination:

09. May 2023

Contents

1 Introduction **1**

2 Literature **5**
2.1 Solid-electrolyte interface (SEI) formation 5
2.2 Solvent decomposition on the magnesium anode 9
2.3 Dendrite formation on metal anodes 11
2.4 Electrolytes in magnesium-ion batteries 12

3 Methods **15**
3.1 Multi-scale approach 15
3.2 Density functional theory (DFT) 15
3.2.1 Elementary Quantum Chemistry 17
3.2.2 Hartree-Fock approximation 18
3.2.3 Hohenberg-Kohn theorems 19
3.2.4 Kohn-Sham approach 20
3.3 The ReaxFF reactive force field method 21
3.3.1 Bond-order and bond energy 23
3.3.2 Lone pair energy and atom overcoordination 25
3.3.3 Valance and torsion angle energy 26
3.3.4 Non-bonded interactions 29
3.3.5 Force field optimization 31

4 Results and Discussion **33**
4.1 First-Principles Studies on the Atomistic Properties of Metallic Magnesium as Anode Material in Magnesium-Ion Batteries 33
4.2 Development of an Mg/O ReaxFF Potential and Passivation of the Magnesium Anode by Oxygen Impurities in Magnesium-Ion Batteries . . . 78
4.3 Suitability of Carbazolyl Hauser and Turbo-Hauser Bases as Magnesium-Based Electrolytes 117
4.4 A Novel and Highly Effcient Indolyl-Based Electrolyte for Mg Batteries . 141

5 Conclusion **167**

Bibliography **171**

List of Abbreviations **181**

List of Figures **185**

Achnowledgement **187**

Publications **189**

Curriculum Vitae **191**

Declaration **193**

1 Introduction

Fighting climate change and limiting global warming to 1.5 °C above pre-industrial levels is the key challenge of the 21st century.[1] However, with 59 $GtCO_2$-eq, global net anthropogenic greenhouse gas (GHG) emissions were at an all-time high in 2019 and continue to rise steadily.[2] Only in the last decade (2010-2019), about 410 $GtCO_2$ or 17 % of the historical cumulative net GHG emissions since 1850 (2400 ± 240 $GtCO_2$) were emitted into the atmosphere.[2]

Notably, the transport sector alone accounted for 8.7 $GtCO_2$-eq which were 23 % of global energy-related CO_2 emissions in 2019.[3] Thereof, 70 % of the transport-related emissions are caused by road traffic.[3] To tackle the issue, electromobility, combined with low-carbon electricity has the potential to drastically reduce CO_2 emissions in the future. Recently, the members of the European Parliament announced the position to only allow new passenger cars and light commercial vehicles with zero emissions in the European Union by 2035 as part of the "Fit for 55 in 2030" package.[4] Through these measures, the European Commission expects 30 million emission-free cars and 80,000 emission-free trucks by 2030.[5] The European country Norway is pursuing even more ambitious goals and already intends to achieve CO_2-neutral transport by 2025.[6]

To date, batteries have been the primary electrochemical storage technology used in electric vehicles (EV).[7] From a global perspective, EVs already contribute nearly 10 % of worldwide car sales, and their share is constantly growing.[8] This is supported by data from the International Energy Agency (IEA), according to which the automotive lithium-ion battery demand more than doubled to 340 GWh in 2021.[8] Moreover, there are no signs of a slowdown in growth in the coming years.[9] It is important to note that batteries account for 30 % to 40 % of value in EVs and can therefore be seen as the key component in modern cars.[8]

In general, batteries consist of four main components: the anode (negative electrode), the cathode (positive electrode), the separator, which prevents contact between the two electrodes to avoid a short circuit, and the electrolyte, allowing the

flow of charged ions between the cathode and the anode.[10,11] The battery structure and its working principle are shown in Figure 1.1. During discharge, positively charged cations and negatively charged electrons are initially formed at the anode. Due to the potential difference between the electrodes, the electrons flow through an outer wire to the cathode, producing electricity. In parallel, the cations migrate via the electron-impermeable electrolyte to the cathode to compensate for the generated charge difference. The opposite process occurs during charging.[10,11] The electrodes in batteries are very reactive and lead to the decomposition of the electrolyte upon contact.[12] As a result, boundary regions called solid-electrolyte interface (SEI) form on the anode and cathode, which act as protective layers against further electrolyte decomposition. However, the SEI can also negatively affect a battery's functionality if they are no longer permeable to the cations, thus preventing their deposition on the anode and cathode, respectively.[13]

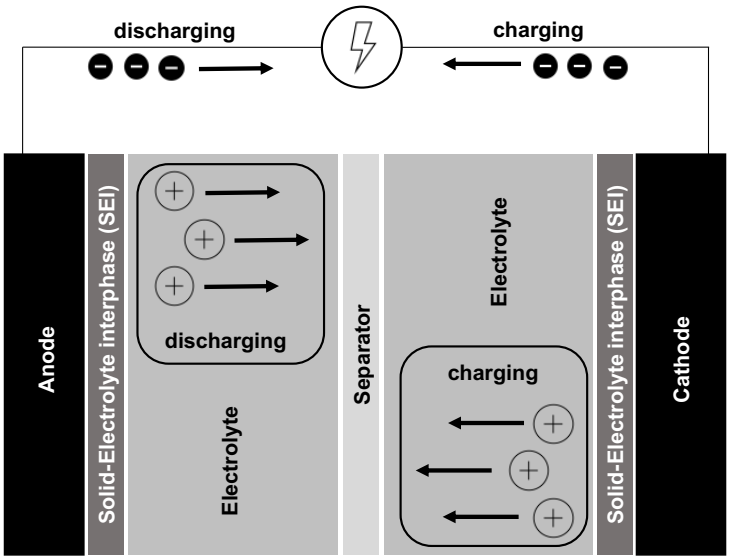

Figure 1.1: Schematic overview and working principle of a rechargeable battery with the main components anode, cathode, separator, and electrolyte. Based on Guo *et al.* and Bella *et al.*[10,11]

Lithium-ion batteries (LIBs) are currently the most effective and well-known battery technology in the automotive sector.[14–18] However, since lithium (Li), like cobalt and graphite, has been classified as critical material by the European Commission, there are major efforts to develop new battery concepts based on chemistry without Li.[19] On the one hand, critical materials are associated with high economic importance and

on the other hand, they are exposed to increased supply risk.[19] Of course, the development of new battery materials not only aims to increase performance and durability further but also to be more cost effective to manufacture and safer to operate.

In this context, magnesium-ion batteries (MIBs) are seen as a promising post-lithium alternative with great potential.[20] When using metallic magnesium (Mg) as anode material, MIBs exhibit high volumetric capacity ($3833\,\mathrm{mAh\,cm^{-1}}$) due to their bivalency, have a low electrochemical potential ($-2.37\,\mathrm{V}$ *vs.* standard hydrogen electrode (SHE)), and are considered save and cost-effective.[21] Furthermore, Mg exhibits a lower tendency of dendrite formation compared to the Li equivalent.[22] Consequently, in chapter ***4.1, First-Principles Studies on the Atomistic Properties of Metallic Magnesium as Anode Material in Magnesium-Ion Batteries***, the metallic properties of Mg were investigated in detail through density functional theory (DFT) calculations.[23] For this purpose, the bulk, surface, and adsorption properties were first calculated, and the thermodynamic equilibrium shape of a Mg nanoparticle was determined using the Wulff construction.[23] In addition, selected self-diffusion processes on Mg(0001) and Mg($10\bar{1}1$) were investigated, and rate constants and activation temperatures were derived to discuss initial surface growth phenomena.[23]

Unfortunately, MIBs are also associated with certain drawbacks. One major challenge is the formation of a passivating boundary layer on top of the Mg anode that is impermeable to Mg cations and thus leads to the breakdown of the battery.[13] The passivating layer may be caused by impurities such as oxygen or water residues in the electrolyte or by contact of the Mg anode with ambient air during processing, storage, or transportation.[24–26] In order to study the degradation processes at the Mg anode in detail, a ReaxFF reactive force field description for Mg and MgO compounds was trained in Section ***4.2, Development of a Mg/O ReaxFF Potential to describe the Passivation Processes in Magnesium-Ion Batteries*** and used to study the oxidation of different Mg surface terminations.[27] Furthermore, the oxidation of a Mg nanoparticle is investigated, as well as its recrystallization into the thermodynamically more stable rock salt structure.[27]

Another major research focus is the search for suitable electrolytes in MIBs.[28–31] Conventional solvents such as ethylene carbonate (EC) cannot be used, since they immediately decompose on the reactive Mg surface.[32] Thereby, an SEI is formed, which, in contrast to Li ions in LIBs, is not permeable to Mg cations and thus inhibits future charging and discharging of the battery.[32] Electrolytes are required to allow reversible Mg deposition with low overpotentials, provide high Coulombic efficiencies and have a wide electrochemical window.[21] In chapters ***4.3, Suitability of***

Carbazolyl Hauser and Turbo-Hauser Bases as Magnesium-Based Electrolytes and ***4.4, A Novel and Highly Efficient Indolyl-Based Electrolyte for Mg Batteries***, two novel electrolytes are proposed that both form Schlenk type equilibria, are halide-free, and are synthesized via an *in-situ* Grignard metalation route.[33,34] To this end, the electrolyte geometry, the solvation energy, and the location of the Schlenk equilibrium were predicted by means of DFT calculations.[33,34]

2 Literature

2.1 Solid-electrolyte interface (SEI) formation

The concept of the SEI was first introduced by Peled in 1979.[35] Peled described the phenomenon that alkali and alkaline earth[36] metals in non-aqueous batteries are immediately covered by a surface layer formed through the reaction between the metal and the electrolyte.[35] According to Peled, the SEI layer consists of insoluble reaction products that form an electronically blocking but ionically conducting interface between electrolyte and anode.[35] A few years later, Peled *et al.* published a concept of what an SEI in LIBs might look like, as shown in Figure 2.1.[37] The authors assumed that the SEI on Li or carbon anodes most likely consists of several layers, with the individual microphases arranged in a mosaic pattern.[37] They also suggested that close to the surface, the phases are primarily composed of inorganic components such as Li_2O or LiF, while close to the solution, partially reduced components such as semicarbonates or polyolefins are more likely to be found.[37]

However, this raises the question of why exactly the SEI occurs between the anode and the electrolyte. Goodenough and Kim explained its chemical origin with a schematic of the relative electron energy in the cathode, the electrolyte, and the anode, which is depicted in Figure 2.2.[38] In the diagram, HOMO is the highest occupied and LUMO the lowest unoccupied molecular orbital, which are separated by the energy barrier E_g, known as the electrochemical window of the electrolyte.[38] Moreover, μ_C and μ_A correspond to the electrochemical potentials of the cathode and the anode, and ϕ_A and ϕ_C are their respective work functions.[38] In Figure 2.2, μ_A lies energetically below the LUMO of the electrolyte.[38] However, in the reverse case depicted as the dashed red box, the energetically higher electrons of the anode would transfer to the electrolyte, ultimately leading to its reduction.[38] The decomposition of the electrolyte causes the formation of a passivation layer, which in return introduces an additional energy barrier for the electrons to overcome.[38] Thus, the SEI prevents further electron transfer from the anode to the electrolyte and hence its decomposition, although the LUMO level is lying still below ϕ_A.[38] The same principle of action applies

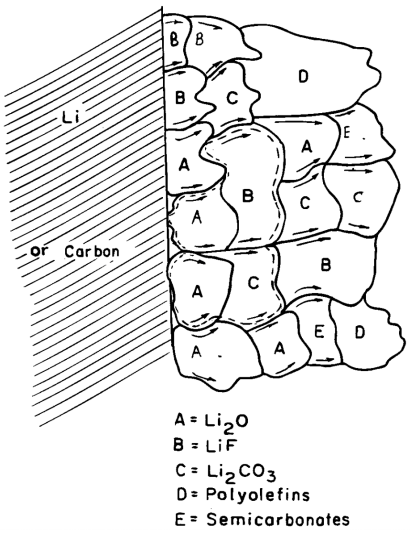

Figure 2.1: Schematic presentation of a polyhetero microphase SEI on lithium or carbon electrode. Taken from Peled *et al.*[37]

to the cathode.[38] μ_C is above the HOMO in figure 2.2, but if μ_C were underneath, the cathode would oxidize the electrolyte. Likewise, the electrolyte would decompose on the cathode side until a SEI prevents further electron transfer.[38] The difference between μ_A and μ_C is equal to the open circuit voltage V_{OC} times the magnitude of the electron charge e:[38]

$$eV_{OC} = \mu_A - \mu_C \leq E_g. \tag{2.1}$$

To avoid SEI formation, eV_{OC} should be smaller than E_g, which means that μ_A and μ_C lie precisely in the electrochemical window of the electrolyte.[38] On the other hand, as explained above, the boundary layers provide kinetic stabilization of the interface between the electrodes and the electrolyte so that a larger eV_{OC} is compensated by the additional barrier of the SEI.[38]

The SEI is formed by the reductive decomposition of electrolyte molecules on the metal surface of the anode and consists of a mixture of organic and inorganic fragments.[12] Unlike Li metal anodes, where the SEI prevents further decomposition of the electrolytes but is still permeable to Li cations, this is not the case with Mg anodes. Here, a passivating, and for Mg cations, impassable layer is formed, whose character and properties are not yet fully understood.[11] A potential explanation for the impermeability of SEI in MIBs in the literature is the larger radius of Mg cations, which

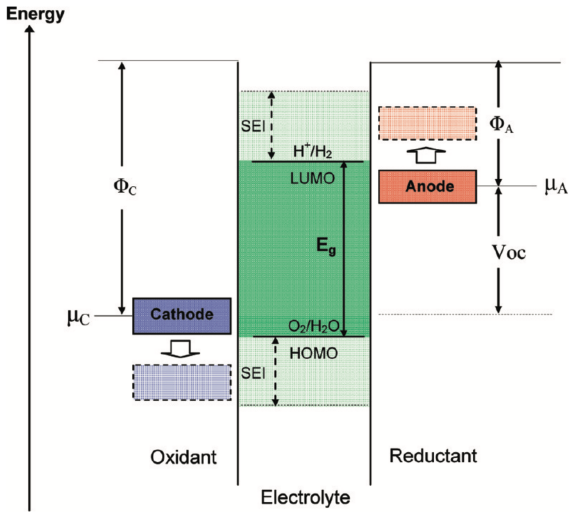

Figure 2.2: Schematic open-circuit energy diagram of an aqueous electrolyte. ϕ_A and ϕ_C are the anode and cathode work functions. E_g is the window of the electrolyte for thermodynamic stability. A $\mu_A >$ LUMO and/or a $\mu_C <$ HOMO requires a kinetic stability by the formation of an SEI layer. Taken from Goodenough and Kim.[38]

is associated with a higher diffusion barrier in organic and inorganic compounds.[32] Therefore, current research focuses on finding suitable electrolytes and anodes that prevent the formation of SEI in MIBs and obtaining theoretical insights into their evolution and growth.

For example, Dou *et al.* proposed that a thin inorganic MgF_2 layer on top of the Mg anode may increase the cycling stability in MIBs and, at the same time, lower the overpotential of Mg deposition.[39] The authors noticed that untreated Mg surfaces are covered with large amounts of strongly bound organic compounds.[39] These organic compounds will crack upon cycling leading to electron leakage and further decomposition of the electrolyte.[39] A thin inorganic layer of MgF_2 reduces electron leakage and simultaneously the formation of large organic SEI layers.[39] Shi *et al.* suggested that the SEI without modification most likely consists of two layers. First, a densely packed inorganic layer, and second, a tightly packed organic layer.[40]

It is generally assumed that the anode reductively decomposes the electrolyte and the reaction products remain adsorbed on the surface.[41] However, the question arises as to how it is nevertheless possible for SEI layer thicknesses of more than 10 nm to form. Theoretically, this should be impossible since the SEI fragments should not conduct

electrons. One possibility is shown by process (a) in Figure 2.3 where the electrolyte is gradually reduced at the surface until finally, with growing SEI layer thickness, insulation increases, and growth terminates.[42] However, Ushirogata *et al.* noticed a low tendency of reduced organic compounds to adhere to the negative anode in DFT calculations. Based on this finding, the authors proposed the near-shore aggregation mechanism, shown as process (b) in Figure 2.3. Just as in process (a), the anode initially decomposes the electrolyte but the electrolyte desorbs back into solution. In the second step, the reduced SEI fragments agglomerate to form clusters that reabsorb back onto the anode once they reach a certain size. In the near-shore aggregation process, the decomposition always takes place directly on the anode surface and still explains the typical SEI layer thicknesses of several dozens of nanometers.[42]

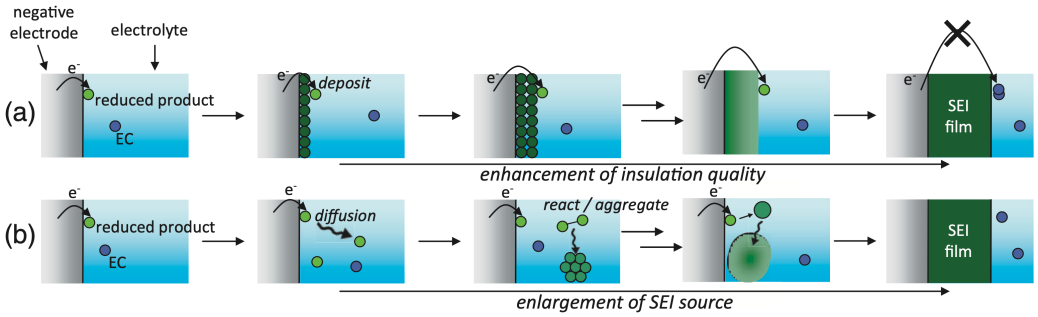

Figure 2.3: Schematic pictures of SEI film formation processes based on (a) surface growth mechanism, and (b) near-shore aggregation mechanism. Taken from Ushirogata *et al.*[42]

Another important aspect is the influence of impurities such as water contamination on the formation of the SEI, although the term passivation is more appropriate in this context.[13] On the one hand, water strongly coordinates to Mg cations, which slows down or complicates the deposition kinetics,[26] and on the other hand, leads to the formation of passivation layers consisting of MgO and $Mg(OH)_2$ compounds.[24,25] According to Connell *et al.*, the addition of $MgCl_2$ to the electrolyte can significantly protect the Mg anode from passivation due to an complex interplay of Cl^- ions with the Mg surface. Moreover, removing the water content in the solvent contributes significantly to preventing a passivation layer.[43]

2.2 Solvent decomposition on the magnesium anode

Unfortunately, polar and aprotic electrolyte solvents such as carbonates, nitriles, lactones, and esters are incompatible with the Mg anode due to their decomposition upon contact.[31] The same is true for many electrolyte anions including ClO_4^-, BF_4^-, PF_6^-, $SO_3CF_3^-$, and AsF_6^-.[31] The only applicable solvents are ethers like 1,2-dimethoxyethane (DME) and tetrahydrofuran (THF), although acetonitrile (ACN) is employed occasionally.[31] Nevertheless, even these solvents are not averse to forming an SEI.[44]

Recently, Lowe and Siegel studied the decomposition pathways of DME on the surfaces Mg(0001), MgO(100), and $MgCl_2$(0001) as shown in Figure 2.4.[44] The authors identified the pristine magnesium surface Mg(0001) as the most reactive, with the two-step decomposition pathway of DME shown in process (a).[44] After overcoming an activation barrier of 0.24 eV, the first C-O bond breaks and segregates a methoxy fragment.[44] Next follows a barrier-free cleavage of the second C-O bond, which leads to the elimination of a second methoxy fragment and the release of an ethylene molecule.[44] Overall, the reaction is strongly exothermic, with two electrons transferred from the surface to the solvent molecule.[44] On MgO(100) and $MgCl_2$(0001), however, solvent decomposition is associated with much higher barriers (2.92 eV *cf.* process (b); 3.52 eV *cf.* process (c) in Figure 2.4) and no electrons are transferred to the solvent.[44] According to Lowe and Siegel, the high activation barriers are not caused by the initial C-O bond breakage but by the subsequent exchange of a hydrogen (H) atom.[44] In summary, the total reaction equations are as follows:[44]

$$\text{Mg(0001)} : C_4H_{10}O_2 \longrightarrow 2\,CH_3O + C_2H_4(g) \tag{2.2}$$

$$\text{MgO(100)} : C_4H_{10}O_2 \longrightarrow CH_3OH + CH_2CHOCH_3 \tag{2.3}$$

$$\text{MgCl}_2\text{(0001)} : C_4H_{10}O_2 \longrightarrow CH_2O + CH_3CH_2OCH_3. \tag{2.4}$$

In contrast, Yu *et al.* showed that 1-methoxy-2-(2-methoxyethoxy)ethane (diglyme) does not decompose readily on pristine Mg(0001) but requires interaction with the surface and a Lewis base.[45] Since the Mg anode is covered with inorganic layers, they suggested a possible decomposition pathway where diglyme first chelates to an undercoordinated Mg sitting in a kink position on a MgO or $Mg(OH)_2$ surface.[45] The deformed diglyme is now subject to backbone stresses that make it susceptible to deprotonation by a Lewis base such as OH^-, ultimately triggering its decomposition.[45] According to DFT calculations performed by Seguin *et al.*, solvents such as DME,

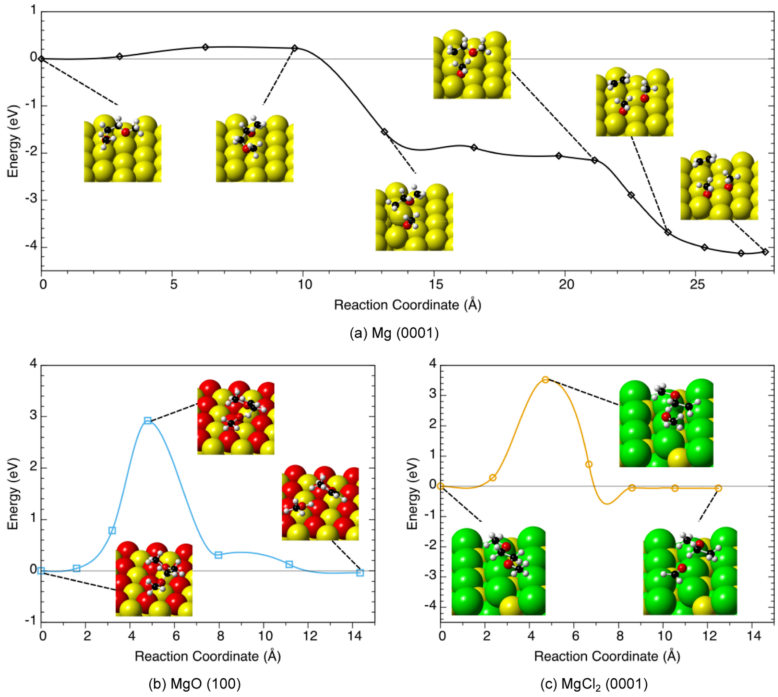

Figure 2.4: Minimum energy pathways for the most favorable DME decomposition reactions on (a) Mg(0001), (b) MgO(100), and (c) $MgCl_2$(0001) obtained using the nudged elastic band method. Energies are with respect to the intact, adsorbed configuration on each surface, corresponding to the point at which the reaction coordinate is equal to zero. Taken from Lowe and Siegel.[44]

ACN, and sulfones exhibit only negative reduction potentials towards metallic Mg and should therefore be stable.[46] However, this changes when the solvents are coordinated in metal complexes.[46] Although the doubly positively charged Mg cation is initially reduced, in the resulting $[Mg(Solv)_6]^{2+}$ complex, the solvent decomposition processes are all exergonic.[46]

Potential strategies to protect the solvent from decomposition include the application of artificial interphases on the Mg anode[47] or using Mg alloy electrodes. Among others, magnesium-bismuth alloys[48,49] and tin electrodes[50] were proposed, which reduces volume capacity but also the tendency of passivation. Other solutions are the use of additives, a weakly coordinating anion design, or the utilization of a three-dimensional magnesiophilic host matrix.[13]

2.3 Dendrite formation on metal anodes

Dendrite formation is known as crystalline growth in a branched, tree-like structure, which usually occurs on metallic anodes.[51] When the branches grow through the separator to the cathode, a short circuit occurs in the battery, leading to cell failure and battery death.[51] In general, dendrite growth occurs mainly in LIBs with metal anodes, which is why Li metal batteries have so far not reached market maturity, and graphite anodes are still predominantly used. In contrast, dendrite growth is much less common in MIBs, which is considered a major advantage.[52] For example, Matsui showed scanning electron images of Li and Mg deposits and demonstrated that Li is more prone to form dendrites at medium current densities and short periods of time.[22] Nevertheless, Davidson *et al.* detected fractal Mg structures (Figure 2.5) in MIBs during deposition of Mg from a 0.5 molar chlorido(methyl)magnesium solution in THF at a constant current density of 0.921 $mA\,cm^{-2}$, which are rather harsh deposition conditions.[53]



Figure 2.5: Digital photograph of fractal Mg structure. Taken from Davidson *et al.*[53]

There are many assumptions why the tendency to form dendrites is lower in MIBs. On the one hand, Jäckle *et al.* has theorized that lower terrace self-diffusion and Ehrlich-Schwoebel barriers on Mg compared to Li surfaces could be one reason for the reduced dendrite growth.[54,55] In contrast, Gaissmaier *et al.* argued that the terrace self-diffusion barrier is not a descriptor of dendritic growth because previously unconsidered exchange processes exist on Na(100), Na(111), and Li(111) with significantly lower activation energies. Gaissmaier *et al.* performed DFT calculations to determine diffusion barriers on Li and Na surfaces within the terrace-step-kink (TSK) model to gain a better understanding of the initial surface growth phenomena.[56,57] In

the TSK model, diffusion processes that may occur during surface growth are investigated and discussed in a structured manner.[58] These include, for example, diffusion processes over a terrace, along an edge, at corners, or across steps.[58] Furthermore, Røe *et al.* showed in DFT calculations that the terrace self-diffusion barrier depends mainly on the coordination environment of the system, specifically the coordination number of the migrating atom, the displacement of the surface atoms, and the reorganization of the electronic structure.[59] The authors concluded that the body-centered cubic (bcc) crystal structure, in which Li is present, is generally more susceptible to dendrite formation than the more densely packed face-centered cubic (fcc) and hexagonal close-packed (hcp) structures.[59]

Another model was presented by Santos and Schmickler, who showed that Li atoms at pyramid peaks have the most negative partial charges.[60] Therefore, the deposition of additional Li atoms could now be amplified at these protrusions.[60] In this way, new tips are constantly formed, which would explain the dendritic form of the structure.[60]

In a recent study, Hagopian *et al.* calculated electro-capillary diagrams of Li, Na, and Mg with a grand-canonical DFT approach.[61] In particular, Hagopian *et al.* demonstrated the presence of a critical overpotential below which one surface becomes more stable than the bulk phase.[61] In this way, the authors identified three independent key properties that contribute to the prevention of dendrites.[61] In the best case, the material should have a high surface tension in combination with a low surface capacitance and a low potential of zero charge (PZC).[61]

2.4 Electrolytes in magnesium-ion batteries

Finding suitable electrolytes that allow reversible plating and stripping is one of the most significant challenges impeding mass-market viability of MIBs.[30] Therefore, it is essential to find the right combination of solvent and salt, where both components must be stable in a wide electrochemical window, show high Coulombic efficiency, and provide superior conductivity.[62] In the following paragraph, various electrolyte solutions for MIBs are presented based on the review by Attias *et al.*[31]

The first electrolytes for MIBs were synthesized in Grignard reactions of organomagnesium and organoaluminum halides in ether solvents.[63,64] For this purpose, Aurbach *et al.* systematically investigated the ratio of Lewis acids and bases in terms of conductivity, anodic stability, and Coulombic efficiency and identified a combination of one equivalent of dibutylmagnesium (Bu_2Mg) and two equivalents of ethylalu-

minum dichloride ($EtAlCl_2$) in THF as the best composition.[65] The so-called dichloro-complex (DCC) showed an optimal Coulombic efficiency of 100 % and a very high ionic conductivity of 1.4 mS cm^{-1}.[31] Moreover, the highly reactive metal-organic components act as scavengers of impurities, preventing the Mg surface's passivation.[31] However, the drawback is low anodic stability of only 2.4 V *vs.* Mg due to β-H elimination reactions.[31] The first Grignard electrolyte without β-H atoms was synthesized by combining phenylmagnesium chloride (PhMgCl) and aluminum trichloride ($AlCl_3$), also known as the all-phenyl complex (APC).[66] APC exhibits a significantly higher electrochemical window of 3.4 V *vs.* Mg while maintaining high Coulombic efficiency and low Mg overpotentials.[31] However, whether the APC electrolyte can be combined with high-capacitance or high-voltage cathodes is still unclear.[31]

Another class of electrolytes originated with Gregory *et al.*, who developed electrolyte solutions based on organoborate compounds.[67] Based on this work, Guo *et al.* demonstrated that the product of triarylborates (BR_3) with Grignard reagents in ethereal solvents results in electrolytes with high Coulombic efficiency (100 %) and anodic stability $>$3.0 V *vs.* Mg.[68] Du *et al.* developed an additional electrolyte based on tris(hexafluoroisopropyl)borate ($[B(HFP)_3]$), magnesium chloride ($MgCl_2$), and Mg powder in DME, which can be combined with a sulfur cathode.[69] The electrolyte showed Coulombic efficiency of only 98 % but ionic conductivity of 5.6 mS cm^{-1}.[31]

The commercially available salt magnesium borohydride ($Mg(BH_4)_2$) is considered highly reductive and therefore acts as scavenger of contaminants similar to Grignard agents.[31] Mohtadi *et al.* were the first to prepare an electrolyte from this salt by dissolving $Mg(BH_4)_2$ in DME and THF.[70] Unfortunately, the electrolyte had very low Coulombic efficiency ($<$40 % for THF, $<$70 % for DME) but was chlorid-free.[31] Chloride anions are regarded to be a double-edged sword. They are needed for reversible electrodeposition but "their presence in solutions may avoid a possible use of transition metal oxide cathode materials and promote corrosion of many conventional current collectors used in batteries, such as aluminum foils".[31]

A promising electrolyte group is based on hexamethyldisilazane (HMDS) and was developed by Zhang *et al.* who reacted Mg-HMDS with $AlCl_3$ in THF.[72,73] The result is a non-reactive electrolyte with high oxidation stability of 3.2 V *vs.* Mg and Coulombic efficiency of 100 %, suitable for application in magnesium sulfur batteries.[31] A variation of the electrolyte was developed by Dongmo *et al.* who replaced the chlorine atoms with bromine atoms to obtain the benefits of the halogens unilaterally but still have a much less corrosive anion.[74]

Electrolytes without metallic compounds based on $MgCl_2$ and $AlCl_3$ are called magnesium aluminum chloride complex (MACC).[75] Active species are $MgCl^+$ and Mg_2Cl^{3+} cations, as well as $AlCl^{4-}$ anions, mostly dissolved in THF.[31] Since no organometallic compounds are present to capture impurities, the anode must first be protected from passivation by galvanostatic cycling in a conditioning process.[31] Afterward, the electrolytes exhibit a Coulombic efficiency of up to 100 % and low overpotentials.[76]

3 Methods

3.1 Multi-scale approach

In general, computational chemistry studies apply one method to study a specific system on a particular time and length scale, while the multi-scale approach attempts to provide a bridge between methods operating on different time and length scales (Figure 3.1).[77] Thus, the electronic properties of a system and its reactivity over time can be studied simultaneously, providing a more comprehensive understanding of the underlying chemistry.

Using the quantum mechanical method density functional theory (DFT), the electronic ground state energy of a system and its electronic properties are determined. Unfortunately, DFT can only handle small chemical systems up to a maximum of a few hundred atoms. To bridge the gap to larger time and length scales, the information learned by DFT is utilized to train a ReaxFF reactive force field.[78,79] Typically, the training process is not straight-line but rather involves many successive training cycles in which the force field is repeatedly trained and tested against DFT reference data. Once the force field is generated, geometry optimizations, nudged elastic band (NEB) calculations[80,81], molecular dynamics (MD), and Monte Carlo (MC) simulations containing up to one million atoms over several nanoseconds are feasible. However, the information about the electronic structure is lost. Both methods, DFT and ReaxFF, are explained in detail in the following subchapters.

3.2 Density functional theory (DFT)

Nowadays, DFT is the most popular method for determining electronic structure related research questions.[82] Its origin lies in the two Hohenberg-Kohn theorems from 1964[83] and the Kohn-Sham formalism from 1965[84], which helped DFT to its breakthrough. Over the years, the method has been continuously improved. Among

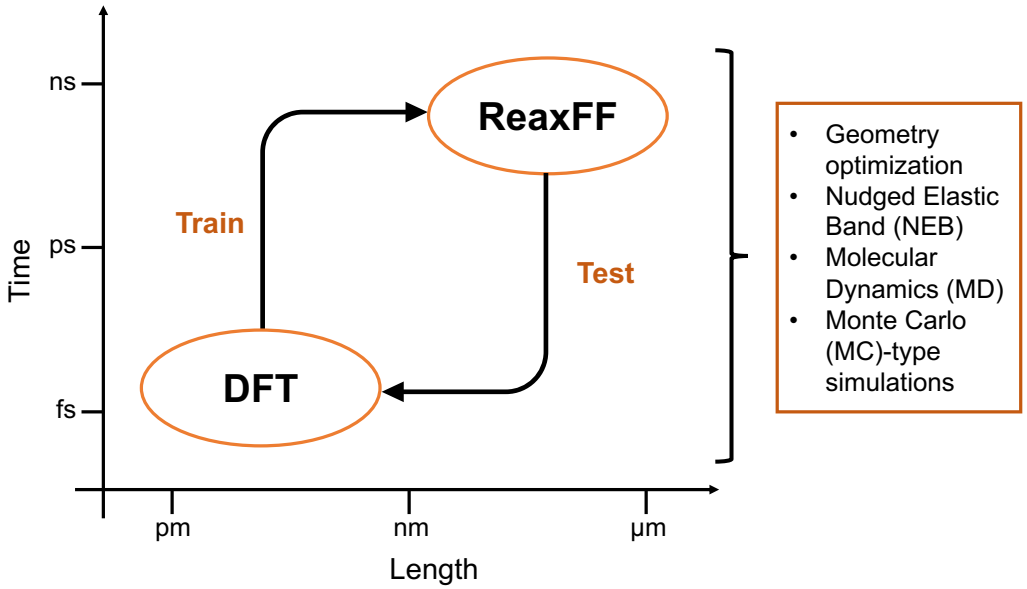

Figure 3.1: Outline of the multi-scale approach. The circular boxes contain the methods (DFT, ReaxFF) operating on different time and length scales. The square box contains tasks that can be performed using either method but in ReaxFF with bigger systems for longer time but at the cost of accuracy. ReaxFF force fields are obtained by successive training and testing cycles against DFT reference data. Based on Mueller *et al.*[77]

the most important milestones was the introduction of the local density approximation (LDA) to describe the exchange and correlation energy in 1980[85,86], which allowed calculations on real materials for the first time.[87] Equally important was the development of the Car-Parrinello method in 1985[88] which allowed for the first time to perform MD simulations using DFT to evaluate interactions. Moreover, in 1996 the generalized gradient approximation (GGA)[89,90] for the exchange and correlation energy was introduced, which reduced the total error of DFT calculations approximately from 1.0 eV to 0.1 eV.[87] Thanks to a large number of commercial (VASP, ADF, *etc.*) and free (Quantum Espresso, GPAW, *etc.*) DFT codes available today, their use has become straightforward, convenient, and widespread.[87] In the following, the basic concepts of DFT are presented based on the textbooks by Koch and Holthausen, Giustino, Lee, and Jensen.[82,87,91,92]

3.2.1 Elementary Quantum Chemistry

All quantum mechanical methods aim at solving the Schrödinger equation, which in the non-relativistic and time-independent case is as follows:

$$\widehat{H}\Psi\left(\vec{x}_1, \vec{x}_2, .., \vec{x}_N, \vec{R}_1, \vec{R}_2, .., \vec{R}_M\right) = E\Psi\left(\vec{x}_1, \vec{x}_2, .., \vec{x}_N, \vec{R}_1, \vec{R}_2, .., \vec{R}_M\right) \tag{3.1}$$

where the system energy E is an eigenvalue of the Hamilton operator $\widehat{H}$ acting on the many-body wave function Ψ for a system consisting of M nuclei with coordinates R and N electrons with coordinates x.[82] The Hamilton operator represents the total energy of the system and considers five contributions composed of kinetic T and potential V energy terms:[82]

$$\widehat{H} = \underbrace{-\frac{1}{2}\sum_{i=1}^{N}\nabla_i^2}_{\widehat{T}_e} \underbrace{-\frac{1}{2}\sum_{A=1}^{M}\frac{1}{M_A}\nabla_A^2}_{\widehat{T}_N} \underbrace{-\sum_{i=1}^{N}\sum_{A=1}^{M}\frac{Z_A}{r_{iA}}}_{\widehat{V}_{Ne}} + \underbrace{\sum_{i=1}^{N}\sum_{j>1}^{N}\frac{1}{r_{ij}}}_{\widehat{V}_{ee}} + \underbrace{\sum_{A=1}^{M}\sum_{B>A}^{M}\frac{Z_A Z_B}{r_{AB}}}_{\widehat{V}_{NN}}. \tag{3.2}$$

$\widehat{T}_e$ and $\widehat{T}_n$ correspond to the kinetic energy of electrons and nuclei. $\widehat{V}_{Ne}$ represents the attractive interactions between electrons and nuclei, and the terms $\widehat{V}_{ee}$ and $\widehat{V}_{NN}$ describe the electron-electron and nucleus-nucleus repulsion, respectively. The indices A and B run from 1 to M, and i and j from 1 to N. M_A is the mass of the nuclei and $Z_{A/B}$ their atomic number. Finally, r is the distance between two electrons, nuclei or between each other, and ∇ represents the Laplacian operator, which produces in Cartesian coordinates the sum of second derivatives of a function:[82]

$$\nabla^2 = \frac{\partial^2}{\partial x^2} + \frac{\partial^2}{\partial y^2} + \frac{\partial^2}{\partial z^2}. \tag{3.3}$$

The Hamiltonian operator in Equation (3.2) is given in atomic units (a.u.), which are used to present equations compactly and straightforwardly.[82] Constant units such as the mass m_e and charge e of an electron, the reduced Planck's constant $\hbar$, or the permittivity of the vacuum $4\pi\epsilon_0$ are simply set to unity and can therefore be omitted from the equation.[82]

Atomic nuclei are many times heavier than electrons – 1836 times in the case of hydrogen – which is why electrons move much faster than nuclei.[91] Therefore, in the famous Born-Oppenheimer approximation, the positions of the nuclei are considered static, which leads to the kinetic energy of the nuclei being zero and to electron-

nucleus interactions corresponding to a constant.[82] This further simplifies Equation (3.2) to the electronic Hamiltonian $\widehat{H}_{\text{elec}}$:[82]

$$\widehat{H}_{\text{elec}} = \underbrace{-\frac{1}{2}\sum_{i=1}^{N}\nabla_i^2}_{\widehat{T}_e} \underbrace{-\sum_{i=1}^{N}\sum_{A=1}^{M}\frac{Z_A}{r_{iA}}}_{\widehat{V}_{Ne}} + \underbrace{\sum_{i=1}^{N}\sum_{j>1}^{N}\frac{1}{r_{ij}}}_{\widehat{V}_{ee}} \tag{3.4}$$

3.2.2 Hartree-Fock approximation

Electrons are fermions with half-integer spin $\left(s = \frac{1}{2}\right)$. Therefore, the wave function must be antisymmetric since an exchange of two electrons must lead to a change of sign of the wave function, also known as the Pauli principle.[92] In the Hartree-Fock scheme, the many-body wave function Ψ_0 is approximated as a single Slater determinant Φ_{SD}.[82] The Slater determinant is an antisymmetrized product of N one-electron wave functions $\chi_i(\vec{x}_i)$.[82]

$$\Psi_0 \approx \Phi_{\text{SD}} = \frac{1}{\sqrt{N!}}\begin{vmatrix} \chi_1(\vec{x}_1) & \chi_2(\vec{x}_1) & \cdots & \chi_N(\vec{x}_1) \\ \chi_1(\vec{x}_2) & \chi_2(\vec{x}_2) & \cdots & \chi_N(\vec{x}_2) \\ \vdots & \vdots & \ddots & \vdots \\ \chi_1(\vec{x}_N) & \chi_2(\vec{x}_N) & \cdots & \chi_N(\vec{x}_N) \end{vmatrix} \tag{3.5}$$

It is important to note that the one-electron wave functions are the product of a spatial orbital $\phi(\vec{r}_i)$ and a spin function $\sigma(s)$, with the spin orbital being either $\alpha(s)$ or $\beta(s)$:[82]

$$\chi_i(\vec{x}_i) = \phi(\vec{r}_i) \cdot \sigma(s) \quad \text{with} \quad \sigma = \alpha, \beta. \tag{3.6}$$

The spin orbitals are orthonormal and so are the one-electron wave functions, with $\langle\alpha|\alpha\rangle = \langle\beta|\beta\rangle = 1$ and $\langle\alpha|\beta\rangle = 0$. Calculating now the expectation value of the electronic Hamilton operator from Equation (3.4) with the single Slater determinant from Equation (3.5), the Hartree-Fock energy expression E_{HF} is obtained:[82]

$$E_{\text{HF}} = \langle\Phi_{\text{SD}}|\widehat{H}_{\text{elec}}|\Phi_{\text{SD}}\rangle = \sum_{i=1}^{N} h_i + \frac{1}{2}\sum_{i=1}^{N}\sum_{j=1}^{N}\Big(\underbrace{J_{ij}}_{\textit{Coulomb}\text{ integral}} - \underbrace{K_{ij}}_{\textit{Exchange}\text{ integral}}\Big) \tag{3.7}$$

where:

$$h_i = \int \chi_i\left(\vec{\mathrm{x}}_i\right)\left\{-\frac{1}{2}\nabla_i^2 - \sum_{A=1}^{M}\frac{Z_A}{r_{iA}}\right\}\chi_i\left(\vec{\mathrm{x}}_i\right) d\vec{\mathrm{x}}_i$$

$$J_{ij} = \int\int \left|\chi_i\left(\vec{x}_i\right)\right|^2 \frac{1}{r_{ij}} \left|\chi_j\left(\vec{x}_j\right)\right|^2 d\vec{x}_i d\vec{x}_j$$

$$K_{ij} = \int\int \chi_i\left(\vec{x}_i\right) \chi_i\left(\vec{x}_j\right) \frac{1}{r_{ij}} \chi_j\left(\vec{x}_i\right) \chi_j\left(\vec{x}_j\right) d\vec{x}_i d\vec{x}_j.$$

The one-electron integral h_i represents the kinetic energy of the electrons and their interactions with the nuclei, while the last two integrals correspond to the *Coulomb* J_{ij} and *exchange* K_{ij} energy. The *Coulomb* integral denotes the repulsion experienced by an electron at position $\vec{x}_i$ due to the average charge distribution of another electron in spin orbital χ_j.[82] On the other hand, the *exchange* integral has no classical interpretation and only arises from the antisymmetry of the Slater determinant due to the Pauli principle. Moreover, the *exchange* term is nonzero only for orbitals with spin-like electrons, due to the orthogonality condition of the spin orbitals. Furthermore, it is important to point out that the double sum in the electron-electron interaction term runs over all electrons with a preceding 1/2 factor. Hence, the *Coulomb* term takes into account an unphysical self-interaction of an electron with itself, which is exactly canceled out by the corresponding *exchange* term.[82]

3.2.3 Hohenberg-Kohn theorems

The Hohenberg-Kohn theorems in 1964 form the cornerstone of modern DFT.[83] As the name indicates, the central variable in DFT is the electron density $\rho(\vec{r})$ instead of the wave function, which is defined as the sum of all probabilities of finding electrons in the non-interacting Kohn-Sham orbitals φ_i:[87]

$$\rho(\vec{r}) = \sum_i \left|\varphi_i(\vec{r}_i)\right|^2 . \tag{3.8}$$

The integration of the electron density over the whole space delivers the system's total number of electrons n:[91]

$$\int \rho(\vec{r}) d\vec{r} = n. \tag{3.9}$$

According to the first Hohenberg-Kohn theorem, there cannot be two different external potentials V_{Ne} for the same ground-state electron density $\rho_0(\vec{r})$.[82] In other words, Hohenberg and Kohn proved that all properties of an electronic system in the ground state are uniquely determined by the electron density $\rho(\vec{r})$ and thus, the ground-state energy must be a functional of the ground-state electron density.[82] The full energy expression can be further subdivided in a system dependent component

for the electron-nuclei interactions $E_{Ne}[\rho_0]$ and a universal valid component – the Hohenberg-Kohn functional $F_{HK}[\rho_0]$ – for the kinetic energy $E_{kin}[\rho_0]$ and the electron-electron repulsion $E_{ee}[\rho_0]$:[82]

$$E_0[\rho_0] = \langle \Psi | \widehat{V}_{Ne} + \widehat{T}_e + \widehat{V}_{ee} | \Psi \rangle = \underbrace{\int \rho_0(\vec{r}) V_{Ne} d\vec{r}}_{E_{Ne}[\rho_0]} + \underbrace{T[\rho_0] + E_{ee}[\rho_0]}_{F_{HK}[\rho_0]} \tag{3.10}$$

The second Hohenberg-Kohn theorem provides the recipe for finding the ground state electron density ρ_0, wherein the general from of the functional is still unknown.[82] A positive trial density $\tilde{\rho}$ which satisfies the condition in Equation (3.9) and which is associated with an external potential represents an upper bond to the true ground state energy E_0.[82] Thus, only if the functional gets supplied with ρ_0, the functional delivers in return the true ground-state energy E_0.[82]

$$E_0[\rho_0] \leq E[\tilde{\rho}] = E_{Ne}[\tilde{\rho}] + T[\tilde{\rho}] + E_{ee}[\tilde{\rho}] \tag{3.11}$$

The concept is also known as variational principle.[91]

3.2.4 Kohn-Sham approach

Kohn and Sham formulated an energy expression for the previously unknown Hohenberg-Kohn functional F_{HK}.[84] Their approach was to decompose the kinetic energy T_e into a non-interacting T_e^{non} and an interacting component T_e^{int}, where calculations of the non-interacting component is inspired by the Hartree-Fock approach. The interacting component due to electron correlation effects has been neglected so far.[91] Moreover, Kohn and Sham subdivided the electron-electron interactions E_{ee} into contributions from the classical Coulomb interaction E_J and non-classical contributions from self-interaction and exchange E_X, as well as electron correlation E_C^{int}.[91]

$$E = E_{Ne} + F_{HK} = E_{Ne} + \underbrace{T_e^{non} + T_e^{int}}_{T_e} + \underbrace{E_J + E_X + E_C^{int}}_{E_{ee}} \tag{3.12}$$

Next, Kohn and Sham created a new energy term that included all the non-classical energy terms they did not yet know how to calculate. They called this term exchange-correlation energy E_{XC}, containing the self-interaction correction and exchange energy E_X due to the antisymmetry of the Slater determinant and the electronic correlation effects E_C from the kinetic energy T_e^{int} and the electron-electron interactions

E_C^{int}:[91]

$$E_{XC} = E_X + \underbrace{T_e^{int} + E_C^{int}}_{E_C} = E_X + E_C \tag{3.13}$$

The complete energy expression of the interacting system is as follows where, except for the unknown exchange-correlation energy, all the remaining terms have an explicit form:[82]

$$\begin{aligned} E[\rho(\vec{r})] =& E_{Ne} + T_e^{non} + E_J + E_{XC} \\ =& -\sum_{i=1}^{N} \int \sum_{A=1}^{M} \frac{Z_A}{r_{iA}} \left|\varphi_i\left(\vec{r}_i\right)\right|^2 d\vec{r}_i - \frac{1}{2}\sum_{i=1}^{N} \langle\varphi_i|\nabla_i^2|\varphi_i\rangle \\ &+ \frac{1}{2}\sum_{i=1}^{N}\sum_{j=1}^{N} \int\int \left|\varphi_i\left(\vec{r}_i\right)\right|^2 \frac{1}{r_{ij}} \left|\varphi_j\left(\vec{r}_j\right)\right|^2 d\vec{r}_i d\vec{r}_j + E_{XC}[\rho(\vec{r})] \end{aligned} \tag{3.14}$$

If the exchange-correlation functional were also known, the Kohn-Sham approach would be exact because there are no other approximations.[82] However, since this is not the case, many functionals have been proposed over the years, classified on Jacob's ladder according to their accuracy, performance, and the number of parameters fitted.[92] Examples include the LDA, the popular GGA functional from Perdew, Burke, and Ernzerhof (PBE), or the semi-empirical hybrid GGA functional Becke, 3-parameter, Lee–Yang–Parr (B3LYP).[92]

3.3 The ReaxFF reactive force field method

ReaxFF is a reactive force field method introduced in 2001 by van Duin *et al.* to perform large-scale MD simulations.[78] The accurate description of bond breaking and formation is achieved with a continuous bond-order function derived directly from the bond distance of a pair of atoms.[79] The total system energy E_{System} is composed of several bond-order dependent and independent energy terms, which are summarized by the following equation:

$$E_{\text{System}} = E_{\text{bond}} + E_{\text{val}} + E_{\text{tors}} + E_{\text{lp}} + E_{\text{over}} + E_{\text{Coulomb}} + E_{\text{vdWaals}} + E_{\text{specific}}. \tag{3.15}$$

The bond energy E_{bond}, the three-body angular energy E_{val} and four-body torsional energy E_{tors}, and the penalty energy terms for broken lone pairs E_{lp} and overcoordinated atoms E_{over} are bond-order dependent. Bond-order independent energy terms

are the electrostatic Coulomb potential E_{Coulomb} and the dispersive van der Waals interactions E_{vdWaals}, which includes the inner wall shielding potential $E_{\text{innerWall}}$. The last energy term E_{specific} in Equation (3.15) summarizes energy contributions that were not relevant to the Mg/O force field trained in this thesis but are part of the ReaxFF framework like atom undercoordination E_{under}, the penalty energy term for atoms sharing two double bonds E_{pen}, the conjugation term for NO_2-groups E_{coa}, a second conjugation terms for aromatic systems E_{conj}, the term to describe hydrogen bonding $E_{\text{H-bond}}$, another correction term for triple bonds between two carbon atoms E_{C2} and in carbon monoxide systems E_{trip}, the term for the long-range dispersion interactions E_{lg}[93], and the correction term for the Fe-dimer $E_{\text{Fe-dim}}$[94]. A schematic overview of the working principle of ReaxFF is summarized in Figure 3.2, which is discussed in detail in the following subsections based on the publication from Chenoweth *et al.* and the ReaxFF user manual.[79,95]

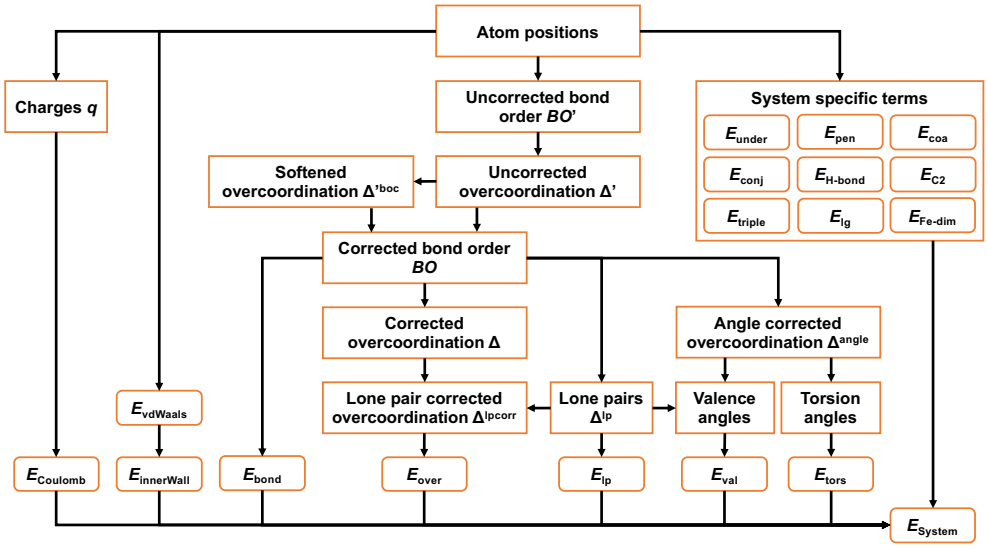

Figure 3.2: Overview of the working principle of ReaxFF. Based on van Duin.[95]

ReaxFF parameter sets are available for various materials classified into combustion, aqueous, and independent branches.[96] Parameter sets within a branch can be thoroughly combined as their general and atomic parameters correspond. In general, parameter sets can consist of over 100 parameters, which are divided into seven different sections in ReaxFF. These include the general section, which contains 39 parameters; the atom section, with 32 parameters per atom; the bonding section, with 16 parameters per bond; and another 6 parameters per bond in the off-diagonal

section. Furthermore, there is the angle section with 7 parameters per atom triplet and the torsion section with 7 parameters per atom quadruple. Finally, the last section is for hydrogen bonding with 4 parameters per atom triplet.[95] As a guideline, general and atomic parameters should only be changed when no other option is left, as this ensures that force field parameters can be easily interchanged.

3.3.1 Bond-order and bond energy

A key assumption of ReaxFF is that the uncorrected bond-order BO'_{ij} is directly related to the inter-atomic distance r_{ij} between a pair of atoms i and j.[78,79,95] The uncorrected bond-order function BO'_{ij} consists of three components with shares for the σ- (BO'^{σ}_{ij}), π- (BO'^{π}_{ij}), and $\pi\pi$-bond ($BO'^{\pi\pi}_{ij}$) contributions and is defined as:

$$BO'_{ij} = \underbrace{\exp\left[p_{\mathrm{bo1}}\left(\frac{r_{ij}}{r_0^{\sigma}}\right)^{p_{\mathrm{bo2}}}\right]}_{BO'^{\sigma}_{ij}} + \underbrace{\exp\left[p_{\mathrm{bo3}}\left(\frac{r_{ij}}{r_0^{\pi}}\right)^{p_{\mathrm{bo4}}}\right]}_{BO'^{\pi}_{ij}} + \underbrace{\exp\left[p_{\mathrm{bo5}}\left(\frac{r_{ij}}{r_0^{\pi\pi}}\right)^{p_{\mathrm{bo6}}}\right]}_{BO'^{\pi\pi}_{ij}} \tag{3.16}$$

where r_0 are the equilibrium bond distances and p_{bo1} to p_{bo6} are empirical parameters from the bonding section. The function is continuous throughout and thus offers constant differentiability of the energy landscape, which is necessary to calculate the forces acting on the atoms.[96] The forces are needed to perform geometry optimizations or to calculate the acceleration of atoms in MD simulations.

For each atom i, an uncorrected overcoordination Δ'_i can be calculated via the sum of its bond-orders with respect to its bonding electrons Val_i:[79,95]

$$\Delta'_i = -Val_i + \sum_{j=1}^{\mathrm{nbrs}(i)} BO'_{ij}. \tag{3.17}$$

The uncorrected overcoordination guides how much the bond-order has to be corrected. In order to allow lone electron pairs such as in oxygen to break up and participate in bonds or generally to foster higher coordination environments, the correction for some elements is softened by introducing a second overcoordination definition Δ'^{boc}_i:[79,95]

$$\Delta'^{\mathrm{boc}}_i = -Val^{\mathrm{boc}}_i + \sum_{j=1}^{\mathrm{nbrs}(i)} BO'_{ij}. \tag{3.18}$$

The overcoordination definitions vary due to different values for the bonding electrons

Val_i and the adjusted bonding electrons Val_i^{boc}. While Val_i = 2 for magnesium and oxygen, the adjusted number of bonding electrons equals $Val_{\mathrm{Mg}}^{\mathrm{boc}}$ = 6 for magnesium and $Val_{\mathrm{O}}^{\mathrm{boc}}$ = 4 for oxygen.[27] Thereupon, the corrected bond-order BO_{ij} is calculated by multiplying the several contributions of the uncorrected bond-order BO'_{ij} with the correction functions f_1 to f_5 as shown in detail in the Equations (3.23) to (3.27):[79,95]

$$BO_{ij} = BO_{ij}^{\sigma} + BO_{ij}^{\pi} + BO_{ij}^{\pi\pi} \tag{3.19}$$

$$BO_{ij}^{\sigma} = BO_{ij}^{'\sigma} \cdot f_1(\Delta_i^{'}, \Delta_j^{'}) \cdot f_4(\Delta_i^{'}, BO_{ij}^{'}) \cdot f_5(\Delta_j^{'}, BO_{ij}^{'}) \tag{3.20}$$

$$BO_{ij}^{\pi} = BO_{ij}^{'\pi} \cdot f_1(\Delta_i^{'}, \Delta_j^{'})^2 \cdot f_4(\Delta_i^{'}, BO_{ij}^{'}) \cdot f_5(\Delta_j^{'}, BO_{ij}^{'}) \tag{3.21}$$

$$BO_{ij}^{\pi\pi} = BO_{ij}^{'\pi\pi} \cdot f_1(\Delta_i^{'}, \Delta_j^{'})^2 \cdot f_4(\Delta_i^{'}, BO_{ij}^{'}) \cdot f_5(\Delta_j^{'}, BO_{ij}^{'}) \tag{3.22}$$

$$f_1(\Delta_i^{'}, \Delta_j^{'}) = \frac{1}{2} \cdot \left(\frac{Val_i + f_2(\Delta_i^{'}, \Delta_j^{'})}{Val_i + f_2(\Delta_i^{'}, \Delta_j^{'}) + f_3(\Delta_i^{'}, \Delta_j^{'})} + \frac{Val_j + f_2(\Delta_i^{'}, \Delta_j^{'})}{Val_j + f_2(\Delta_i^{\prime}, \Delta_j^{\prime}) + f_3(\Delta_i^{'}, \Delta_j^{'})} \right) \tag{3.23}$$

$$f_2(\Delta_i^{'}, \Delta_j^{'}) = \exp\left(-p_{\mathrm{boc1}} \cdot \Delta_i^{\prime}\right) + \exp\left(-p_{\mathrm{boc1}} \cdot \Delta_j^{\prime}\right) \tag{3.24}$$

$$f_3(\Delta_i^{'}, \Delta_j^{'}) = -\frac{1}{p_{\mathrm{boc2}}} \cdot \ln\left\{ \frac{1}{2} \cdot \left[\exp\left(-p_{\mathrm{boc2}} \cdot \Delta_i^{\prime}\right) + \exp\left(-p_{\mathrm{boc2}} \cdot \Delta_j^{\prime}\right) \right] \right\} \tag{3.25}$$

$$f_4(\Delta_i^{'}, BO_{ij}^{'}) = \frac{1}{1 + \exp\left(-p_{\mathrm{boc3}} \cdot (p_{\mathrm{boc4}} \cdot BO_{ij}^{\prime} \cdot BO_{ij}^{\prime} - \Delta_i^{\prime\mathrm{boc}}) + p_{\mathrm{boc5}}\right)} \tag{3.26}$$

$$f_5(\Delta_j^{'}, BO_{ij}^{'}) = \frac{1}{1 + \exp\left(-p_{\mathrm{boc3}} \cdot (p_{\mathrm{boc4}} \cdot BO_{ij}^{\prime} \cdot BO_{ij}^{\prime} - \Delta_j^{\prime\mathrm{boc}}) + p_{\mathrm{boc5}}\right)}. \tag{3.27}$$

Note that the softened overcoordination definition from Equation (3.18) enters the correction Equations (3.26) and (3.27), while the uncorrected overcoordination from Equation (3.17) is used in Equations (3.23) to (3.25). p_{boc1} to p_{boc6} are empirical parameters from the general and the atom section. With the corrected bond-order BO_{ij}, a corrected overcoordination Δ_i can be calculated in accordance with the previous procedure:[79,95]

$$\Delta_i = -Val_i + \sum_{j=1}^{\mathrm{nbrs}(i)} BO_{ij}. \tag{3.28}$$

Finally, the corrected bond-order BO_{ij} is used to calculate the bond energy E_{bond}:

$$E_{\mathrm{bond}} = -D_{\mathrm{e}}^{\sigma} \cdot BO_{ij}^{\sigma} \cdot \exp\left[p_{\mathrm{be1}} \left(1 - \left(BO_{ij}^{\sigma} \right)^{p_{\mathrm{be2}}} \right) \right] - D_{\mathrm{e}}^{\pi} \cdot BO_{ij}^{\pi} - D_{\mathrm{e}}^{\pi\pi} \cdot BO_{ij}^{\pi\pi} \tag{3.29}$$

where D_{e} are dissociation energy contributions from the σ-, π-, and $\pi\pi$-bond fractions, and p_{be1} and p_{be2} are bond energy parameters.[79,95]

3.3.2 Lone pair energy and atom overcoordination

If the bond-order exceeds a certain level and lone pairs, for example in case of oxygen atoms, participate in bonding, a penalty energy must be expended. The lone pair energy E_{lp} is calculated by first determining the difference Δ_i^{e} between the total number of outer shell electrons Val_i^{e} and the corrected sum of bond-orders BO_{ij} around an atom i:[79,95]

$$\Delta_i^{\mathrm{e}} = -Val_i^{\mathrm{e}} + \sum_{j=1}^{\mathrm{nbrs}(i)} BO_{ij}. \tag{3.30}$$

Now, the actual $n_{\mathrm{lp},i}$ and the optimal amount of lone pairs $n_{\mathrm{lp,opt}}$ at atom i are determined with Equations (3.31) and (3.32):

$$n_{\mathrm{lp},i} = -\mathrm{int}\left(\frac{\Delta_i^{\mathrm{e}}}{2}\right) + \exp\left[-p_{\mathrm{lp1}} \cdot \left(2 + \Delta_i^{\mathrm{e}} - 2 \cdot \mathrm{int}\left\{\frac{\Delta_i^{\mathrm{e}}}{2}\right\}\right)^2\right] \tag{3.31}$$

$$n_{\mathrm{lp,opt}} = \frac{1}{2} \cdot (Val_i^{\mathrm{e}} - Val_i) \tag{3.32}$$

where p_{lp1} is a general parameter, the int-function truncates the decimal places, and Val_i^{e} and Val_i are the outer shell and the bonding electrons.[79,95] For heavier atoms with a mass greater than 21 u, as is the case with magnesium, $n_{lp,i}$ is set equal to $n_{lp,opt}$. Next, the deviation Δ_i^{lp} of the actual from the optimal number of lone pairs is calculated:

$$\Delta_i^{\mathrm{lp}} = n_{\mathrm{lp,opt}} - n_{\mathrm{lp},i} \tag{3.33}$$

which in the case of magnesium is always zero. In the example of oxygen with its six valence electrons ($Val_{\mathrm{O}}^{\mathrm{e}} = 6$), two of these electrons are typically involved in a bond ($Val_{\mathrm{O}} = 2$). Therefore, four electrons are not involved and are part of two lone pairs ($n_{\mathrm{lp,opt,O}} = 2$). With a bond-order greater than two, the electrons of the lone pairs would also be involved in bonding, which would first require their gradual breakup.[79,95] The amount of energy needed to do so is expressed by the lone pair energy E_{lp}, which is calculated using Equation (3.34):

$$E_{\mathrm{lp}} = \frac{p_{\mathrm{lp2}} \cdot \Delta_i^{\mathrm{lp}}}{1 + \exp\left(-75 \cdot \Delta_i^{\mathrm{lp}}\right)} \tag{3.34}$$

where p_{lp2} is an atom parameter.[79,95]

ReaxFF considers overcoordination also in the general case. For this purpose, the

corrected overcoordination Δ_i from Equation (3.28) is first adjusted for broken lone pairs Δ_i^{lp} to avoid double-counting:[79,95]

$$\Delta_i^{\mathrm{lpcorr}} = \Delta_i - \frac{\Delta_i^{\mathrm{lp}}}{1 + p_{\mathrm{ovun3}} \cdot \exp\left(p_{\mathrm{ovun4}} \cdot \left\{\sum_{j=1}^{\mathrm{nbrs}(i)} \left(\Delta_j - \Delta_j^{\mathrm{lp}}\right) \cdot \left(BO_{ij}^{\pi} + BO_{ij}^{\pi\pi}\right)\right\}\right)}. \tag{3.35}$$

Since there are no π- or $\pi\pi$-bonds in the Mg/O system, the second rather lengthy term in the denominator goes to zero and the equation simplifies to $\Delta_i^{\mathrm{lpcorr}} = \Delta_i - \Delta_i^{\mathrm{lp}}$.[27] Now, with the overcoordination adjusted for the lone pairs $\Delta_i^{\mathrm{lpcorr}}$, the penalty energy for the overcoordination E_{over} can be calculated:[79,95]

$$E_{\mathrm{over}} = \frac{\sum_{j=1}^{\mathrm{nbond}} p_{\mathrm{ovun1}} \cdot D_{\mathrm{e}}^{\sigma} \cdot BO_{ij}}{\Delta_i^{\mathrm{lpcorr}} + Val_i} \cdot \Delta_i^{\mathrm{lpcorr}} \cdot \left[\frac{1}{1 + \exp\left(p_{\mathrm{ovun2}} \cdot \Delta_i^{\mathrm{lpcorr}}\right)}\right] \tag{3.36}$$

The last term ensures that in case of negative overcoordination ($\Delta_i^{\mathrm{lpcorr}} < 0$) E_{over} quickly goes to zero.[78] p_{ovun1} is a bonding parameter that should preferably be fitted, while p_{ovun2} to p_{ovun4} belong to the general and atomic parameter section.[95]

3.3.3 Valance and torsion angle energy

The valence angle energy E_{val} describes the energy associated with deviations from an equilibrium angle Θ_0 (BO) spanned between three atoms i, j, and k. A particular feature of ReaxFF is that the equilibrium angle adapts to the geometry conditions around the central atom j, such as the number of π-bonds, the degree of over- and undercoordination, or the number of lone pairs $n_{\mathrm{lp},j}$.[79,95] Thereby, a new definition for the overcoordination $\Delta_j^{\mathrm{angle}}$ is introduced in Equation (3.37) for angle and torsion terms, which is controlled by the valence parameter Val_j^{angle} in the atom section. For non-metals such as oxygen, Val_j^{angle} is normally equal to Val_i^{boc} (both 4), but may be individually tailored. For magnesium Val_j^{angle} equals 3, despite its two valence electrons.[27]

$$\Delta_j^{\mathrm{angle}} = -Val_j^{\mathrm{angle}} + \sum_{n=1}^{\mathrm{nbrs}(j)} BO_{jn}. \tag{3.37}$$

Next, the sum of π-bond-orders SBO are determined in Equation (3.38) to identify the degree to which the equilibrium angle must be modified.[79,95] In the second part of Equation (3.38), the influence of the overcoordination previously calculated

in Equation (3.37) and the number of lone pairs determined in Equation (3.31) are considered.[79,95]

$$\begin{aligned} SBO = & \sum_{n=1}^{\mathrm{nbrs}(j)} \left(BO_{jn}^{\pi} + BO_{jn}^{\pi\pi} \right) \\ & + \left[1 - \prod_{n=1}^{\mathrm{nbrs}(j)} \exp\left(-BO_{jn}^{8} \right) \right] \cdot \left(-\Delta_{j}^{\mathrm{angle}} - p_{\mathrm{val8}} \cdot n_{\mathrm{lp},j} \right). \end{aligned} \tag{3.38}$$

Moreover, ReaxFF ensures with an redefinition of the sum of π-bond-orders $SBO2$ that no singularities occur at the extrema at $SBO = 0$ and $SBO = 2$.[78]

$$SBO2 = \begin{cases} 0, & \text{if } SBO \leqslant 0 \\ SBO^{p_{\mathrm{val9}}}, & \text{if } 0 < SBO < 1 \\ 2 - (2 - SBO)^{p_{\mathrm{val9}}}, & \text{if } 1 < SBO < 2 \\ 2, & \text{if } SBO > 2 \end{cases} \tag{3.39}$$

Thereupon, the equilibrium angle $\Theta_0\,(BO)$ is determined based on the geometry:

$$\Theta_0\,(BO) = \pi - \Theta_{0,0} \cdot \{1 - \exp\left[-p_{val10} \cdot (2 - SBO2)\right]\} \tag{3.40}$$

where $\Theta_{0,0}$ is the deviation of the equilibrium angle from 180° in a system without π-bonds and zero overcoordination.[79,95] As an example, equation (3.40) ensures that $\Theta_0\,(BO)$ in a sp^3 hybridized system corresponds to 109.5°, while in an sp^2- or sp-hybridized system the angle continuously transitions to the higher values of 120° and 180°, respectively.[78] In the Mg/O system, there are no π-bonds, making the first term in Equation (3.38) always equal to zero.[27] Nevertheless, even in such a system, the equilibrium angle could be influenced by the overcoordination definition in Equation (3.37) via the atom parameter Val_j^{angle}. The valence angle energy E_{val} is now calculated as follows:

$$E_{\mathrm{val}} = f_7(BO_{ij}) \cdot f_7(BO_{jk}) \cdot f_8(\Delta_j) \cdot \left\{ p_{\mathrm{val1}} - p_{\mathrm{val1}} \exp\left[-p_{\mathrm{val2}} \left(\Theta_0\,(BO) - \Theta_{ijk} \right)^2 \right] \right\} \tag{3.41}$$

where Θ_{ijk} is the present angle between the atom triple i, j, and k.[79,95] The auxiliary terms f_7 and f_8 lead to a vanishing of the angular term once the bond-order approaches zero or to its increase in the case of undercoordination:[78]

$$f_7(BO_{ij}) = 1 - \exp\left(-p_{\mathrm{val3}} \cdot BO_{ij}^{p_{\mathrm{val4}}} \right) \tag{3.42}$$

$$f_8(\Delta_j) = p_{\text{val5}} - (p_{\text{val5}} - 1) \cdot \frac{2 + \exp\left(p_{\text{val6}} \cdot \Delta_j^{\text{angle}}\right)}{1 + \exp\left(p_{\text{val6}} \cdot \Delta_j^{\text{angle}}\right) + \exp\left(-p_{\text{val7}} \cdot \Delta_j^{\text{angle}}\right)}. \quad (3.43)$$

The angle parameters p_{val1} and p_{val2} adjust the magnitude and shape of the angular term, while the angle parameters p_{val4} and p_{val7} control the influence of the bond-order and atom undercoordination.[79,95] The remaining parameters between p_{val1} and p_{val10} belong to the general and atom section, which should not be modified.

The torsion angle ω_{ijkl} is the angle between two intersecting planes, each passing through three atoms i, j, k and j, k, l, where two of the atoms (j and k) coincide.[79,95] The torsion energy E_{tors} is mainly relevant in organic molecules in sp^3 hybridized systems, but can also be helpful in correctly describing high-energy compounds such as peroxide structures and is calculated as follows:

$$\begin{aligned} E_{\text{tors}} =& f_{10}(BO_{ij}, BO_{jk}, BO_{kl}) \cdot \sin\Theta_{ijk} \cdot \sin\Theta_{jkl} \cdot \left[\frac{1}{2} V_1 \cdot (1 + \cos\omega_{ijkl}) \right. \\ &+ \frac{1}{2} V_2 \cdot \exp\left\{p_{\text{tor1}} \cdot \left[1 - \left(BO_{jk}^{\pi} - 1 + f_{11}(\Delta_j, \Delta_k)\right)\right]^2\right\} \cdot \left(1 - \cos 2\omega_{ijkl}\right) \\ &\left. + \frac{1}{2} V_3 \cdot \left(1 + \cos 3\omega_{ijkl}\right) \right] \end{aligned} \quad (3.44)$$

where ω_{ijkl} is the present torsion angle, Θ_{ijk} and Θ_{jkl} are valence angles, and V_1, V_2, V_3, and p_{tor1} are torsion parameters that have to be fitted.[79,95] The V_2 term reaches its maximum at a double bond between the atoms j and k but rapidly diminishes at smaller bond-orders, whereas the sinusoidal functions over the valence angles ensure that the torsion energy disappears when one of the valence angles approaches 180 °.[78] Furthermore, the auxiliary term f_{10} causes the torsion energy to approach zero when the bonds in the torsion angle dissociate and f_{11} weakens the influence of the bond order in the V_2 term for overcoordinated atoms that share a too-short bond[78]:

$$\begin{aligned} f_{10}(BO_{ij}, BO_{jk}, BO_{kl}) = &\left[1 - \exp\left(-p_{\text{tor2}} \cdot BO_{ij}\right)\right] \cdot \left[1 - \exp\left(-p_{\text{tor2}} \cdot BO_{jk}\right)\right] \\ &\cdot \left[1 - \exp\left(-p_{\text{tor2}} \cdot BO_{kl}\right)\right] \end{aligned} \quad (3.45)$$

$$f_{11}(\Delta_j, \Delta_k) = \frac{2 + \exp\left[-p_{tor3} \cdot \left(\Delta_j^{\text{angle}} + \Delta_k^{\text{angle}}\right)\right]}{1 + \exp\left[-p_{\text{tor3}} \cdot \left(\Delta_j^{\text{angle}} + \Delta_k^{\text{angle}}\right)\right] + \exp\left[p_{\text{tor4}} \cdot \left(\Delta_j^{\text{angle}} + \Delta_k^{\text{angle}}\right)\right]}. \quad (3.46)$$

The parameters p_{tor2} to p_{tor4} are from the general section and should not be changed. $\Delta_{j,k}^{angle}$ corresponds to the angle corrected overcoodination from Equation (3.37) and is controlled by the atom parameter $Val_{j,k}^{angle}$.

3.3.4 Non-bonded interactions

The non-bonded interactions are composed of the van der Waals and Coulomb forces and are usually calculated between all atoms in ReaxFF to avoid energy jumps during bond breaking.[78] However, to simultaneously keep the computational effort low, a cutoff radius R_{cut} was integrated into ReaxFF, within which only the non-bonded interactions are calculated.[79,95] At the same time, to avoid energy discontinuities when charged particles leave or enter R_{cut}, ReaxFF uses a distance-dependent 7th order polynomial Taper term $Tap(r_{ij})$ whose first, second, and third derivatives are continuous and go to zero at R_{cut}:

$$\begin{aligned} Tap(r_{ij}) = & Tap_7 \cdot r_{ij}^7 + Tap_6 \cdot r_{ij}^6 + Tap_5 \cdot r_{ij}^5 + Tap_4 \cdot r_{ij}^4 + Tap_3 \cdot r_{ij}^3 + Tap_2 \cdot r_{ij}^2 \\ & + Tap_1 \cdot r_{ij} + Tap_0 \end{aligned} \tag{3.47}$$

where r_{ij} is the distance between two atoms i and j. The terms Tap_0 to Tap_7 from Equation (3.47) are defined as follows:[79,95]

$$\begin{aligned} Tap_7 &= 20/R_{cut}^7 \\ Tap_6 &= -70/R_{cut}^6 \\ Tap_5 &= 84/R_{cut}^5 \\ Tap_4 &= -35/R_{cut}^4 \\ Tap_3 &= 0 \\ Tap_2 &= 0 \\ Tap_1 &= 0 \\ Tap_0 &= 1. \end{aligned} \tag{3.48}$$

The van der Waals energy $E_{vdWaals}$ is then described with a distance-corrected Morse potential:

$$E_{vdWaals} = Tap(r_{ij}) \cdot D_{ij} \cdot \left\{ \exp\left[\alpha_{ij} \cdot \left(1 - \frac{f_{13}(r_{ij})}{r_{vdW}}\right)\right] - 2 \cdot \exp\left[\frac{1}{2} \cdot \alpha_{ij} \cdot \left(1 - \frac{f_{13}(r_{ij})}{r_{vdW}}\right)\right] \right\} \tag{3.49}$$

where D_{ij}, α_{ij}, and r_{vdW} are off-diagonal parameters that must be fitted.[79,95] The shielding term f_{13} avoids excessively high repulsions between bonded atoms and atoms that share a common valence angle:

$$f_{13}(r_{ij}) = \left[r_{ij}^{p_{\text{vdW1}}} + \left(\frac{1}{\gamma_w} \right)^{p_{\text{vdW1}}} \right]^{\frac{1}{p_{\text{vdW1}}}} . \tag{3.50}$$

The parameters p_{vdW1} and γ_w belong to the general and atomic parameters, respectively. The counterpart to shielding is the inner wall term, which can be used to compensate for too strong Coulomb interactions. For example, in grand-canonical Monte Carlo (GCMC) simulations, if an atom is inserted too close to the next atom, the attractive Coulomb forces can significantly outweigh the van der Waals repulsions, resulting in a drop in the potential energy curve.[27] This phenomenon is often referred to as the polarization catastrophe. The inner wall potential $E_{\text{innerWall}}$ offers one way to delay the polarization catastrophe, which is added on top of the van der Waals energy:

$$E_{\text{innerWall}} = p_{\text{c2}} \cdot \exp\left(p_{\text{c3}} \cdot \left(1 - \frac{r_{ij}}{p_{\text{c1}}} \right) \right) . \tag{3.51}$$

p_{c1}, p_{c2}, and p_{c3} are empirical parameters from the atom section.[97,98] For atomic pairs consisting of different elements, the parameters from Equation (3.51) correspond to the square root of the product of the corresponding atom parameters. Unfortunately, the inner wall potential is only included in the implementation from the Amsterdam Modeling Suite (AMS) but not in the standalone ReaxFF version.[97,98] Thus, the following points must be considered when using the inner wall potential. First, atomic parameters must be changed, which should generally be avoided. Second, training is not possible via the optimization routine in standalone ReaxFF, but only directly in the AMS version or by hand. And third, the missing implementation may lead to varying results between the standalone ReaxFF and the AMS version.

To obtain the Coulomb energy E_{Coulomb}, all atomic charges q_i are first determined using the polarizable charge approach electron equilibration method (EEM) from Mortier *et al.*[99] The charges are mainly influenced by the element's electronic negativity χ_i and atomic hardness η_i. In general, the atomic hardness should be above 7 to prevent the polarization catastrophe, but a lower value had to be chosen in the case of magnesium.[27] Otherwise, the bulk properties and charges were not described correctly.[27] An extension to EEM is the atom-condensed Kohn-Sham DFT approximated to second order (ACKS2) method, which adds an additional term due to the Kohn-Sham kinetic energy.[100] Besides, the introduction of reference charges pre-

vents residual charges from being assigned to dissociated molecules, which is a major drawback of the EEM method. However, ACKS2 is computationally expensive, especially for larger systems, and has not yet been implemented in the ReaxFF standalone version used for the training of the magnesium-oxygen interactions performed in this work. After the charges have been computed, the Coulomb energy E_{Coulomb} is calculated via the following equation:

$$E_{\text{Coulomb}} = \frac{1}{2} \sum_{i \neq j}^{natoms} Tap(r_{ij}) \cdot C \cdot \frac{q_i \cdot q_j}{\left[r_{ij}^3 + \left(\gamma_i \gamma_j \right)^{-3/2} \right]^{1/3}} \tag{3.52}$$

where $Tap(r_{ij})$ is the Taper correction from Equation (3.47), C is the Coulomb constant $\frac{1}{4\pi\epsilon_0}$ and γ are shot-range atomic damping parameters to adjust for orbital overlap at small atom distances.[79,95]

3.3.5 Force field optimization

During force field optimization, the goal is to reproduce a training set obtained from literature or quantum mechanical (QC) calculations. For this purpose, ReaxFF calculates an error function, which sums up the deviation between ReaxFF $x_{i,\text{ReaxFF}}$ and literature/QC $x_{i,\text{QC/Lit}}$ training data:

$$\text{Error}^{\text{ReaxFF}} = \sum_{i=1}^{n} \left(\frac{x_{i,\text{ReaxFF}} - x_{i,\text{QC/Lit}}}{\sigma} \right)^2 \tag{3.53}$$

where σ is a weighting factor and n the amount of training set entries.[101] In the standalone ReaxFF version, the successive one-parameter parabolic interpolation (SOPPI) optimizer is used to minimize the error function, characterized by its robustness and ease of use.[95] The parameters are sequentially processed, by fitting a parabola through the current parameter value and a lower and upper boundary. Now, the optimal and new force field parameter is obtained by extrapolation. The magnesium–oxygen interactions were trained by the mentioned procedure in this thesis.[27] Recently, many sophisticated optimization algorithms have been proposed that sample the entire force field parameter landscape and thus avoid getting trapped in local minima.[96] These approaches are mostly based on MC[102] as well as generic[103–105] or evolutionary[106,107] algorithms.

4 Results and Discussion

4.1 First-Principles Studies on the Atomistic Properties of Metallic Magnesium as Anode Material in Magnesium-Ion Batteries

The following article is reprinted without changes from Florian Fiesinger, Daniel Gaissmaier, Matthias van den Borg, Timo Jacob: First-Principles Studies on the Atomistic Properties of Metallic Magnesium as Anode Material in Magnesium-Ion Batteries, *ChemSusChem* **2022**, *15*, e202200414, published by Wiley-VCH GmbH as an open access article (`https://doi.org/10.1002/cssc.202200414`) under the terms of the Creative Commons Attribution License CC BY-NC-ND 4.0 (`https://creativecommons.org/licenses/by-nc-nd/4.0/`), which permits sharing, copying, and redistributing of the material in any medium or format.[23] ©2022 The authors.

Author Contributions: Florian Fiesinger performed all the calculations and analyzed together with Daniel Gaissmaier, Matthias van den Borg, and Timo Jacob. The initial manuscript draft was written by Florian Fiesinger and all authors commented on the manuscript. Timo Jacob supervised the research.

ChemSusChem

Research Article
doi.org/10.1002/cssc.202200414

Chemistry Europe
European Chemical Societies Publishing

www.chemsuschem.org

Check for updates

18648564, 2022, 14, Downloaded from https://chemistry-europe.onlinelibrary.wiley.com/doi/10.1002/cssc.202200414 by KIZ der Universität Ulm, Wiley Online Library on [21/10/2022]. See the Terms and Conditions (https://onlinelibrary.wiley.com/terms-and-conditions) on Wiley Online Library for rules of use; OA articles are governed by the applicable Creative Commons License

First-Principles Studies on the Atomistic Properties of Metallic Magnesium as Anode Material in Magnesium-Ion Batteries

Florian Fiesinger,[a] Daniel Gaissmaier,[a, b, c] Matthias van den Borg,[a] and Timo Jacob*[a, b, c]

Rechargeable magnesium-ion batteries (MIBs) are a promising alternative to commercial lithium-ion batteries (LIBs). They are safer to handle, environmentally more friendly, and provide a five-time higher volumetric capacity (3832 mAh cm^{-3}) than commercialized LIBs. However, the formation of a passivation layer on metallic Mg electrodes is still a major challenge towards their commercialization. Using density functional theory (DFT), the atomistic properties of metallic magnesium, mainly well-selected self-diffusion processes on perfect and imperfect Mg surfaces were investigated to better understand the initial surface growth phenomena. Subsequently, rate constants and activation temperatures of crucial diffusion processes on Mg(0001) and Mg(10$\bar{1}$1) were determined, providing preliminary insights into the surface kinetics of metallic Mg electrodes. The obtained DFT results provide a data set for parametrizing a force field for metallic Mg or performing kinetic Monte-Carlo simulations.

Introduction

Rechargeable batteries are of outstanding importance in achieving global climate goals as they play a key role in electronic applications, in the mobility sector for the electrification of cars, or stationary grid energy storage systems for surplus wind and solar power. The most prominent representatives are Lithium-ion batteries (LIBs),[1–5] which are facing controversy due to the use of critical raw materials such as lithium, cobalt, nickel, or graphite.[6] Metallic lithium anodes have a high theoretical capacity (3861 mAh g^{-1}), the lowest negative electrochemical potential (−3.04 V vs. standard hydrogen electrode (SHE)), and a low density (0.59 g cm^{-3}), however, are prone to form dendrites.[7] Dendrites are needle-shaped structures leading to short circuits, thermal runaways, and even battery failures, although promising approaches such as the electrostatic shielding of the lithium surface through additives have been proposed to tackle this problem.[8] Due to these safety concerns, graphite with intercalated lithium ions is still used as anode material in commercial LIBs, reducing its theoretical capacity by roughly one order of magnitude to 372 mAh g^{-1} in present day commercial LIBs.[9]

Therefore, rechargeable multivalent magnesium-ion batteries (MIBs) have emerged as a promising alternative, mainly due to the bivalency of the magnesium atom, which allows it to carry twice the charge resulting in a higher volumetric capacity (3833 mAh cm^{-3} vs. 777 mAh cm^{-3} of graphite anodes in commercial LIBs).[10] Additionally, magnesium has a low electrochemical potential (−2.37 V vs. SHE), is highly abundant, of low cost, and is environmentally friendly. These benefits are reflected in the exponentially increasing number of publications that have recently been dedicated to the topic of MIBs, as shown in Figure 1 from the publication by Li et al.[11] On the other hand, a great deal of effort is required to find suitable

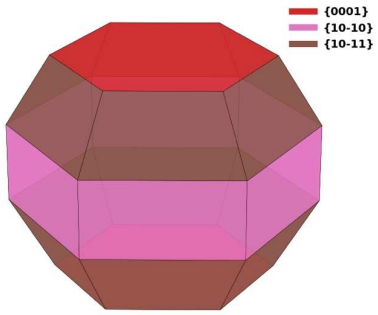

Figure 1. Thermodynamic equilibrium shape of a magnesium crystal as determined by the calculated Wulff construction. All surface energies (PBE) from Table S5 were included in the evaluation of the Wulff shape.

[a] F. Fiesinger, D. Gaissmaier, M. van den Borg, Prof. T. Jacob
Institute of Electrochemistry
Ulm University
Albert-Einstein-Allee 47, 89081 Ulm (Germany)
E-mail: timo.jacob@uni-ulm.de
[b] D. Gaissmaier, Prof. T. Jacob
Helmholtz Institute Ulm (HIU) Electrochemical Energy Storage
Helmholtzstr. 11, 89081 Ulm (Germany)
[c] D. Gaissmaier, Prof. T. Jacob
Karlsruhe Institute of Technology (KIT)
P.O. Box 3640, 76021 Karlsruhe, (Germany)

Supporting information for this article is available on the WWW under https://doi.org/10.1002/cssc.202200414

© 2022 The Authors. ChemSusChem published by Wiley-VCH GmbH. This is an open access article under the terms of the Creative Commons Attribution Non-Commercial NoDerivs License, which permits use and distribution in any medium, provided the original work is properly cited, the use is non-commercial and no modifications or adaptations are made.

© 2022 The Authors. ChemSusChem published by Wiley-VCH GmbH

ChemSusChem
Research Article
doi.org/10.1002/cssc.202200414
Chemistry Europe
European Chemical Societies Publishing

18648564, 2022, 14, Downloaded from https://chemistry-europe.onlinelibrary.wiley.com/doi/10.1002/cssc.202200414 by KIZ der Universität Ulm, Wiley Online Library on [21/10/2022]. See the Terms and Conditions (https://onlinelibrary.wiley.com/terms-and-conditions) on Wiley Online Library for rules of use; OA articles are governed by the applicable Creative Commons License

electrolytes that allow reversible magnesium deposition while at the same time providing a broad electrochemical window.[9,12] Conventional carbonate electrolytes cannot be used for rechargeable MIBs because the solid-electrolyte interface (SEI) formed by decomposition products of the electrolyte is not permeable to magnesium cations, in contrast to lithium cations.[10,13] Proposed solutions are electrolytes based on Grignard reagents, $Mg(TFSI)_2$ salts or ionic liquids, as well as the use of polymeric interlayers as artificial SEI.[13,14] Nevertheless, the structure and growth mechanism of SEI formation remains poorly understood due to its high complexity, highlighting the need for adequate theoretical modeling on different time and length scales.[15]

The second controversial issue is whether dendrite formation is possible on metallic magnesium anodes. On the one hand, the tendency of occurrence is significantly lower than for the lithium equivalent,[16] yet dendrites have been demonstrated under harsh deposition conditions, as shown by the Banerjee group.[17] As a result, there have been requests to conduct experiments to determine critical current densities[18] and to define precise voltage windows[19] for dendrite-free regions. In a recently published study, the critical overpotential of dendrite formation on lithium, sodium, and magnesium was calculated using a grand-canonical density functional theory (DFT) approach, indicating a combination of high surface tension, low surface capacitance, and low potential of zero charge (PZC) as indicators for mitigated dendrite growth.[20] Another explanation for enhanced dendrite growth on lithium compared to magnesium surfaces includes the accumulation of negative excess charges at the peaks of protrusions of the lithium electrodes inducing a strong electric field that attracts further lithium cations.[21] In addition, lower step-down and terrace self-diffusion barriers of magnesium compared to lithium are considered responsible for the reduced dendrite growth.[22,23]

In this work, periodic DFT calculations have been performed to determine the atomistic properties of magnesium and to explain the initial stages of surface growth. This technique has previously been applied for lithium[24] and sodium[25] in our group. For this purpose, the bulk, surface, and adsorption properties of magnesium were first calculated. Based on the obtained surface energies, the corresponding equilibrium shape of a magnesium crystal was determined within the framework of the Wulff construction.[26] Subsequently, a wide variety of two- and three-dimensional diffusion processes on perfect and imperfect Mg(0001) and Mg(10$\bar{1}$1) surfaces were investigated and analyzed concerning surface growth phenomena. Finally, the obtained DFT results provide a data set for parametrizing a force field for metallic Mg or performing kinetic Monte-Carlo studies.[27,28]

Results and Discussion

Surface properties and Wulff construction of a magnesium crystal

The surface energy [Eq. (1)] is regarded as a measure for the stability of a surface and determines the equilibrium shape of a crystal.[29] In agreement with literature,[30–32] Mg(0001) is the most stable crystal surface, followed by Mg(10$\bar{1}$0)A and Mg-(10$\bar{1}$1), which differ in our calculations by less than 1 meV Å^{-2} (Table 1). Mg(0001) lies in the basal plane of the hcp unit cell, which is characterized by a particularly high packing density, resulting in thermodynamic stabilization.[33] At this point, we refer to the work of Tang et al., who established a model to predict the relative stability of magnesium surfaces based on the number of broken basal and non-basal bonds.[34] They also showed that Friedel oscillations are especially present on low-index Mg surfaces, influencing surface relaxation. On the other hand, on high index surfaces, relaxation is driven by charge depletion and charge smoothing effects. In an embedded atom method (EAM) potential study, Mg (10$\bar{1}$1) was considered to be the second most stable surface, which is not the case according to our DFT calculations.[35] Caution is required for Mg(10$\bar{1}$0) since there are two possible surface terminations Mg(10$\bar{1}$0)A and Mg (10$\bar{1}$0)B, which are shown in Figure S2. Mg(10$\bar{1}$0)B differs from Mg(10$\bar{1}$0)A by one missing row and is characterized by parallel atomic lines making deep channels. Mg(10$\bar{1}$0)A also has channels, but not as distinct as in Mg(10$\bar{1}$0)B. Surface energies calculated with the BEEF-vdW functional are generally lower but have the same stability sequence. All PBE results are within the error range of the BEEF-vdW functional. Further surface energies (that also entered the following Wulff construction) and a literature data summary are provided in Table S5. In addition, we refer to the adsorption properties chapter in the Supporting Information for a detailed adsorption energy study of Mg on Mg(0001), Mg(10$\bar{1}$0)A, Mg(10$\bar{1}$0)B and Mg(10$\bar{1}$1).

Interestingly, and as already shown in literature,[30,31] the Wulff construction (Figure 1) reveals for both functionals (PBE, BEEF-vdW) a reverse order of the area fractions versus surface energies. Our calculations confirm that Mg(10$\bar{1}$1) has the largest area share with 48.6% (Table 2), although it is only the third most stable surface, followed by Mg(10$\bar{1}$0)A (27.9%) and Mg(0001) (23.7%) as shown in Table 2. Other publications also

Table 1. Surface energies γ for selected magnesium surfaces calculated with Equation (1) and from literature. For the BEEF-vdW functional, the calculated standard deviations of the surface energies are given in parenthesis.

Surface	γ [meV Å^{-2}] this work PBE	BEEF-vdW	other work experiment[38]
Mg(0001)	33.9	38.7 (9)	51.0
Mg(10$\bar{1}$0)A	40.3	44.9 (9)	
Mg(10$\bar{1}$1)	40.9	45.8 (8)	
Mg(10$\bar{1}$0)B	55.5	59.4 (11)	

© 2022 The Authors. ChemSusChem published by Wiley-VCH GmbH

ChemSusChem
Research Article
doi.org/10.1002/cssc.202200414
Chemistry Europe
European Chemical Societies Publishing

18648564, 2022, 14, Downloaded from https://chemistry-europe.onlinelibrary.wiley.com/doi/10.1002/cssc.202200414 by KIT der Universitat Ulm, Wiley Online Library on [21/10/2022]. See the Terms and Conditions (https://onlinelibrary.wiley.com/terms-and-conditions) on Wiley Online Library for rules of use; OA articles are governed by the applicable Creative Commons License

Table 2. Calculated (PBE and BEEF-vdW) and literature area fractions of the magnesium surface Mg(0001), Mg(10$\bar{1}$0)A, and Mg(10$\bar{1}$1) from the calculated Wulff construction shown in Figure 1.

Functional	Area fraction [%] Mg(0001)	Mg(10$\bar{1}$0)A	Mg(10$\bar{1}$1)	Ref.
PBE	23.7	27.9	48.6	this work
BEEF-vdW	22.4	25.8	50.5	this work
PBE	22.5	27.2	49.5	[30]
PBE	25.0	33.0	42.0	[31]

assign Mg(11$\bar{2}$0) area fractions in the Wulff construction, which was not observed in our case.[35,36] It is important to mention that even over a wide potential range, the shape of the magnesium crystal behaves almost constant, which suggests that in the working potential range of magnesium batteries, our calculated surface area fractions are still valid.[37] The calculated area fractions emphasize the need to study the diffusion properties of all three surfaces collectively, rather than looking at one surface termination individually.

Terrace self-diffusion on Mg(0001), Mg(10$\bar{1}$0)A, and Mg(10$\bar{1}$1)

To understand the mobility of Mg atoms on defect-free surfaces, we examined the terrace self-diffusion barriers on the three thermodynamic most stable surfaces Mg(0001), Mg(10$\bar{1}$0)A, and Mg(10$\bar{1}$1). A schematic illustration of the initial (atoms marked in green) and final (atoms marked in red) positions is shown in Figure 2. The respective barriers were calculated with Equation (2) and are summarized in Table 3. Additionally, estimated prefactors and room-temperature reaction rates, calculated with Equation (5), are provided for the PBE and the BEEF-vdW functionals in the Supporting Information, as well as the energy profiles of the respective processes (Table S7, Table S8, Figure S4).

Diffusion of a single Mg adatom on Mg(0001) occurs almost barrier-free from the thermodynamic most stable fcc to the slightly increased hcp position in a hopping mechanism [$fcc_0 \rightarrow hcp_1$, $E_a = 0.02$ eV]. Roe et al. justified the low terrace self-diffusion barrier on Mg(0001) with the small coordination number of 3 of the migrating atom, an intrinsic property of the hexagonally close-packed {0001}-facet.[39] A possible exchange process for Mg(0001) seems highly unfavorable [$fcc_0 \rightarrow hcp_2$ (Ex.), $E_a = 0.74$ eV], which is also true for all investigated Mg surfaces in contrast to the alkali metal Na(100) in which the exchange process is dominating.[25] The morphology of Mg-(10$\bar{1}$0)A is characterized, as mentioned earlier, by channels running parallel to each other. Diffusion within a channel has a minor barrier [$ob_0 \leftrightarrow ob_1$, $E_a = 0.02$ eV], while transitions across channels have approximately 20-fold higher barriers for hopping and exchange processes [$ob_0 \leftrightarrow ob_2$, $E_a = 0.42$ eV; $ob_0 \leftrightarrow ob_2$ (Ex.), $E_a = 0.46$ eV]. In the case of Mg(10$\bar{1}$1), diffusion between adjacent and opposite hollow positions was studied. Adjacent diffusion [$h_0 \leftrightarrow h_1$, $E_a = 0.30$ eV] is more likely than diffusion between opposing sites [$h_0 \leftrightarrow h_2$, $E_a = 0.42$ eV]. The PBE and BEEF-vdW calculations are consistent and in agreement with literature.[23,30,36,39] Recently, Jäckle et al. suggested that the low terrace self-diffusion barrier of magnesium on Mg(0001) may indicate the lack of dendrite growth.[23] This statement should be evaluated considering that the barriers on Mg(10$\bar{1}$1), the surface with the largest area fraction of the Wulff particle, are several times higher than for Mg(0001), which is also valid on Mg(10$\bar{1}$0)A for diffusion across a channel.

Dimer interaction energies on Mg(0001), Mg(10$\bar{1}$0)A, and Mg(10$\bar{1}$1)

The formation of polyatomic clusters represents the first stage of island formation. Here the question arises if attractive or repulsive interactions between adatoms are at play, resulting in a uniform distribution of the adsorbates or the formation of dimer, trimer, or cluster structures. Thus, we calculated the interaction energies E_{int} with Equation (3) for merged and more distant dimer configurations, as shown in Figure 3. Our calculations reveal high negative interaction energies between two merged Mg adsorbates (second atom placed at position 1 or 6 for Mg(0001), 1 for Mg(10$\bar{1}$0), and 1 or 4 for Mg(10$\bar{1}$1)) and an interaction energy sequence given by $E_{int,Mg(0001)} > E_{int,Mg(10\bar{1}1)} > E_{int,Mg(10\bar{1}0)A}$, as shown in detail in Tables 4, 5, and 6. The differences in interaction energies may be related directly to the number of nearest surface atoms of the adsorbates following the opposite order ($3_{Mg(0001)} < 4_{Mg(10\bar{1}1)} < 5_{Mg(10\bar{1}0)A}$). The two possible merged dimer conformations on Mg(0001) are shown in Figure 4. Notice the final configuration in Figure 4a, which results from placing the second atom at position 1. Interestingly, both atoms are no longer in their initial fcc- but

Table 3. Activation energies E_a for forward and backward terrace self-diffusion processes calculated with Equation (2) (PBE and BEEF-vdW) and from literature. For the BEEF-vdW functional the calculated standard deviations of the activation energies are given in parentheses.

Terrace	Pathway	E_a^{for} [eV] this work PBE	BEEF-vdW	other work PBE	E_a^{rev} [eV] this work PBE	BEEF-vdW	other work PBE
Mg(0001)	$fcc_0 \leftrightarrow hcp_1$	0.02	0.02 (0.02)	0.02[23,30,39], 0.03[36]	0.01	0.01 (0.01)	0.02[23,30,39], 0.03[36]
	$fcc_0 \leftrightarrow hcp_2$ (Ex.)	0.74	0.79 (0.23)	0.79[30]	0.72	0.77 (0.23)	0.79[30]
Mg(10$\bar{1}$0)A	$ob_0 \leftrightarrow ob_1$	0.02	0.02 (0.04)	0.02[30]	0.02	0.02 (0.04)	0.02[30]
	$ob_0 \leftrightarrow ob_2$	0.42	0.35 (0.15)	0.45[30]	0.42	0.35 (0.15)	0.45[30]
	$ob_0 \leftrightarrow ob_2$ (Ex.)	0.46	0.47 (0.14)	0.56[30]	0.46	0.47 (0.14)	0.56[30]
Mg(10$\bar{1}$1)	$h_0 \leftrightarrow h_1$	0.30	0.27 (0.06)	0.29[30]	0.30	0.27 (0.06)	0.29[30]
	$h_0 \leftrightarrow h_1$ (Ex.)	0.59	0.62 (0.16)	0.57[30]	0.59	0.62 (0.16)	0.57[30]
	$h_0 \leftrightarrow h_2$	0.42	0.38 (0.08)	0.41[30]	0.42	0.38 (0.08)	0.41[30]

© 2022 The Authors. ChemSusChem published by Wiley-VCH GmbH

ChemSusChem
Research Article
doi.org/10.1002/cssc.202200414
Chemistry Europe
European Chemical Societies Publishing

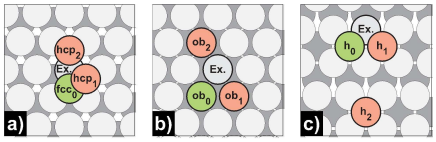

Figure 2. Schematic representation of terrace self-diffusion processes on a) Mg(0001), b) Mg(10$\bar{1}$0)A, and c) Mg(10$\bar{1}$1). Green-colored atoms mark the initial, while red-colored atoms mark the final positions.

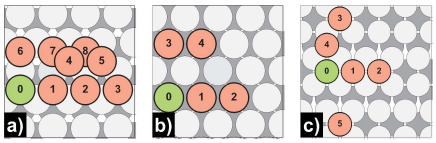

Figure 3. Schematic illustration of dimer configuration sites for the interaction energies E_{int} given in Table 4, Table 5, and Table 6 for a) Mg(0001), b) Mg(10$\bar{1}$0)A, and c) Mg(10$\bar{1}$1). The first atom is always located at the green position 0, while the second adatom is initially placed on the red positions.

Table 4. Calculated (PBE/BEEF-vdW) and theoretical reference dimer interaction energies E_{int} of two Mg adatoms adsorbed on (6×6) Mg(0001). E_{int} was calculated with Equation (3) and the adatoms were initially placed at positions 0 & *x*. For the BEEF-vdW functional, the calculated standard deviation of the dimer interaction energy E_{int} is given in parenthesis.

Position	E_{int} [eV] for Mg(0001) this work PBE	BEEF-vdW	other work PBE	Ref.
0 & 1	−0.51	−0.40 (0.13)	−0.50	[22,30]
0 & 2	−0.05	−0.02 (0.12)	–	–
0 & 3	−0.04	0.00 (0.09)	–	–
0 & 4[a]	−0.54	−0.43 (0.11)	−0.05	[30]
0 & 5	−0.03	0.01 (0.13)	–	–
0 & 6	−0.54	−0.43 (0.11)	−0.50	[22]
0 & 7[a]	−0.54	−0.43 (0.11)	–	–
0 & 8	−0.04	−0.01 (0.08)	–	–

[a] Not stable; transition into fcc-hcp configuration (Figure 4b); second atom moves to position 6.

Table 5. Calculated (PBE/BEEF-vdW) and theoretical reference dimer interaction energies E_{int} of two Mg adatoms on (6×3) Mg(10$\bar{1}$0)A. E_{int} was calculated with Equation (3) and the adatoms were initially placed at positions 0 & *x*. For the BEEF-vdW functional, the calculated standard deviation of the dimer interaction energy E_{int} is given in parenthesis.

Position	E_{int} [eV] for Mg(10$\bar{1}$0)A this work PBE	BEEF-vdW	other work PBE	Ref.
0 & 1	−0.28	−0.25 (0.06)	−0.25	[30]
0 & 2	−0.01	−0.02 (0.01)	–	–
0 & 3	0.02	0.02 (0.02)	–	–
0 & 4	0.01	0.01 (0.01)	–	–

moved to bridge-like positions after relaxation. Moreover, the dimer relaxes to the same final configuration when both atoms are initially placed in the neighboring hcp positions with an interaction energy of 0.51 eV. In the thermodynamically more stable merged dimer conformation (E_{int} = 0.54 eV), one atom is located in an fcc or hcp position above a surface atom, as shown in Figure 4b. One should note that on Mg(0001), the more distant dimer configurations (second atom at position 2, 3, 5, or 8) also exhibit negative interaction energies for the PBE functional ($E_{int} < -0.03$ eV), which are on the order of the terrace self-diffusion barrier. If the second Mg adsorbate is initially placed in positions 4 and 7, in the relaxed geometry, the atom moves to position 6 (same geometry as in Figure 4b). Two conformations with noticeable interaction energies are also present on Mg(10$\bar{1}$1). In the thermodynamically more stable conformation, both adsorbates are in adjacent hollow positions (0 & 3) and have an interaction energy of −0.31 eV. In the thermodynamic less stable conformation, one atom sits in a hollow- and the other in an fcc-like position (0 & 1). Since the atom sitting in fcc position coordinates to only three surface atoms, the interaction to the second adsorbate is slightly higher (−0.35 eV). For the BEEF-vdW functional, the differences in interaction energies are less pronounced for the two dimer conformations on Mg(10$\bar{1}$1) and drop at greater atom distances for all investigated surfaces to negligible values ($|E_{int}| \leq$ 0.02 eV). Nevertheless, the PBE interaction energy sequence is consistent with the BEEF-vdW calculations and literature but differs in representing the long-range attraction.[23,30]

Table 6. Calculated (PBE/BEEF-vdW) and theoretical reference dimer interaction energies E_{int} of two Mg adatoms adsorbed on (6×3) Mg(10$\bar{1}$1). E_{int} was calculated with Equation (3) and the adatoms were initially placed at positions 0 & *x*. For the BEEF-vdW functional, the calculated standard deviation of the dimer interaction energy E_{int} is given in parenthesis.

Position	E_{int} [eV] for Mg(10$\bar{1}$1) this work PBE	BEEF-vdW	other work PBE	Ref.
0 & 1	−0.31	−0.28 (0.05)	−0.31	[30]
0 & 2	0.01	0.01 (0.02)	–	–
0 & 3	−0.01	0.00 (0.02)	–	–
0 & 4[a]	−0.35	−0.29 (0.07)	–	–
0 & 5	−0.01	−0.01 (0.02)	–	–

[a] Since the adsorption site of atom 4 is not stable outside of the dimer configuration, the adsorption energy for this atom was assumed to be equivalent to an fcc position on Mg(0001) to calculate the interaction energies.

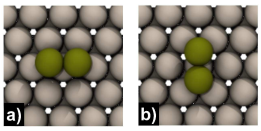

Figure 4. a) One of two possible merged dimer structures on Mg(0001) where both adsorbates are located at bridge-like positions. b) The second thermodynamically more stable merged dimer structure with one adsorbate at an fcc and a hcp position.

© 2022 The Authors. ChemSusChem published by Wiley-VCH GmbH

18645641, 2022, 14, Downloaded from https://chemistry-europe.onlinelibrary.wiley.com/doi/10.1002/cssc.202200414 by KIZ der Universität Ulm, Wiley Online Library on [21/10/2022]. See the Terms and Conditions (https://onlinelibrary.wiley.com/terms-and-conditions) on Wiley Online Library for rules of use; OA articles are governed by the applicable Creative Commons License

ChemSusChem
Research Article
doi.org/10.1002/cssc.202200414
Chemistry Europe
European Chemical Societies Publishing

18648564, 2022, 14, Downloaded from https://chemistry-europe.onlinelibrary.wiley.com/doi/10.1002/cssc.202200414 by KIT der Universitat Ulm, Wiley Online Library on [21/10/2022]. See the Terms and Conditions (https://onlinelibrary.wiley.com/terms-and-conditions) on Wiley Online Library for rules of use; OA articles are governed by the applicable Creative Commons License

Dimer and trimer self-diffusion on Mg(0001) and Mg(10$\bar{1}$1)

As the interaction energy studies have already indicated, the dimer and trimer diffusion barriers (Figure 5, Figure 6, Table 7) reveal that when two adsorbates meet on Mg(0001), they immediately agglomerate [$D_{0/2}\rightarrow D_{1/3}$, $E_a^{for} < 0.005$ eV]. We could only detect a minor barrier below a certain distance, which we may explain, on the one hand, because of the low terrace self-diffusion barrier on Mg(0001) ($E_a = 0.01/0.02$ eV) and, on the other hand, the still evident dimer interaction energy at larger distances (e.g., −0.05 eV for adatoms at positions 0 & 2, which is the initial structure for the dimer merge II process). On the contrary, the activation energies for its separation are multiple times higher [$D_{1/3}\rightarrow D_{0/2}$, $E_a^{rev} = 0.49/0.46$ eV], indicating that one dimer can already be considered a center for further island growth. Also noteworthy is that from the time of dimer formation, the propagation as a dimer on Mg(0001) is higher [$CD_0\leftrightarrow CD_1$, $E_a = 0.07$ eV] than that of the monomer still, the dimer is highly mobile. The transition between the observed dimer configurations occurs almost barrierless [$CD_0\leftrightarrow CD_2$, $E_a = 0.01$ eV].

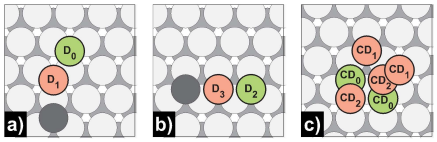

Figure 5. Schematic representation of dimer self-diffusion processes on Mg(0001): a) dimer merge I; b) dimer merge II; c) dimer concerted. Green-colored atoms mark the initial, while red-colored atoms mark the final positions.

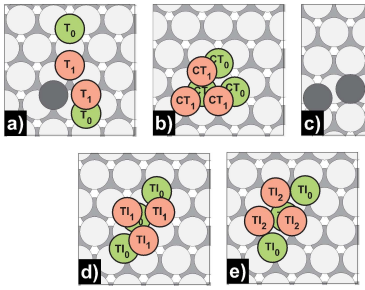

Figure 6. Schematic representation of trimer self-diffusion processes on Mg(0001): a) trimer merge; b) trimer concerted; c) trimer linear; d) trimer interchange I; e) trimer interchange II. Green-colored atoms mark the initial, while red-colored atoms mark the final positions.

Table 7. Activation energies E_a for forward and backward dimer and trimer self-diffusion processes on Mg(0001) calculated with Equation (2) (PBE). The forward activation barriers for the dimer and trimer merge processes did not equal exactly 0.00 eV but were below 0.005 eV while rounding to the second decimal place.

Diffusin on Mg(0001)	Path	Pathway	E_a^{for} [eV]	E_a^{rev} [eV]
dimer	merge	$D_0\leftrightarrow D_1$	0.00	0.49
		$D_2\leftrightarrow D_3$	0.00	0.46
	concerted	$CD_0\leftrightarrow CD_1$	0.07	0.07
		$CD_0\leftrightarrow CD_2$	0.01	0.01
trimer	merge	$T_0\leftrightarrow T_1$	0.00	0.64
	concerted	$CT_0\leftrightarrow CT_1$	0.02	0.12
	linear	$TL_0\leftrightarrow TL_2$	0.01	0.47
		$TL_1\leftrightarrow TL_2$	0.02	0.46
	interchange	$TI_0\leftrightarrow TI_1$	0.06	0.17
		$TI_0\leftrightarrow TI_2$	0.07	0.20

On Mg(10$\bar{1}$1) (Figure 7 and Table 8), however, there are clearly distinguishable barriers for forward and reverse processes. In the case of two atoms approaching each other within a channel, the forward barrier is about half as large as the reverse barrier [$d_0\leftrightarrow d_1$, $E_a^{for} = 0.25$ eV, $E_a^{rev} = 0.58$ eV]. If dimer formation proceeds across the channel along the [10$\bar{1}$2]-direction, diffusion takes place in a two-step process, but with lower forward barriers in each case [$d_2\rightarrow d_3$, $E_a^{for} = 0.19$ eV; $d_3\rightarrow d_1$, $E_a^{for} = 0.15$ eV], making this process very likely to occur. The process across the channel opposite to the [10$\bar{1}$2]-direction exhibits both the highest forward and reverse barrier for all investigated dimer formation processes [$d_4\leftrightarrow d_1$, $E_a^{for} = 0.37$ eV, $E_a^{rev} = 0.67$ eV]. Concerted movement of a dimer on Mg(10$\bar{1}$1) is again significantly increased compared to Mg(0001) [$cd_0\leftrightarrow cd_1$, $E_a = 0.54$ eV], as already observed with terrace self-diffusion.

If a third atom is approaching, a linear or a triangular trimer is formed, depending on the side of the attack. For Mg(0001), no or only extremely low barriers could be determined [$T_0\rightarrow T_1$, $E_a^{for} = 0.00$ eV; $TL_{0/1}\rightarrow TL_2$, $E_a^{for} = 0.01/0.02$ eV], as was already the case for the dimer formation. In turn, the linear form can

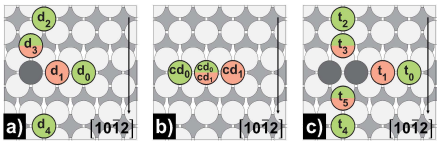

Figure 7. Schematic representation of dimer and trimer self-diffusion processes on Mg(10$\bar{1}$1): a) dimer merge; b) dimer concerted; c) trimer merge. Green-colored atoms mark the initial, while red-colored atoms mark the final positions.

Table 8. Activation energies E_a for forward and backward dimer and trimer self-diffusion processes on Mg(10$\bar{1}$1) calculated with Equation (2) (PBE).

Diffusion on Mg(10$\bar{1}$1)	Path	Pathway	E_a^{for} [eV]	E_a^{rev} [eV]
dimer	merge	$d_0\leftrightarrow d_1$	0.25	0.58
		$d_2\leftrightarrow d_3$	0.19	0.13
		$d_3\leftrightarrow d_1$	0.15	0.51
		$d_4\leftrightarrow d_1$	0.37	0.67
	concerted	$cd_0\leftrightarrow cd_1$	0.54	0.54
trimer	merge	$t_0\leftrightarrow t_1$	0.26	0.58
		$t_2\leftrightarrow t_3$	0.19	0.20
		$t_3\leftrightarrow t_1$	0.27	0.54
		$t_4\leftrightarrow t_5$	0.31	0.57
		$t_5\leftrightarrow t_1$	0.24	0.28

© 2022 The Authors. ChemSusChem published by Wiley-VCH GmbH

ChemSusChem
Research Article
doi.org/10.1002/cssc.202200414
Chemistry Europe
European Chemical Societies Publishing

18645641, 2022, 14, Downloaded from https://chemistry-europe.onlinelibrary.wiley.com/doi/10.1002/cssc.202200414 by KIZ der Universität Ulm, Wiley Online Library on [21/10/2022]. See the Terms and Conditions (https://onlinelibrary.wiley.com/terms-and-conditions) on Wiley Online Library for rules of use; OA articles are governed by the applicable Creative Commons License

transform itself into the thermodynamically more stable triangular trimer form. However, from a kinetic point of view, the barrier of the interchange to a hcp trimer is slightly lower [$TI_0 \rightarrow TI_1$, $E_a = 0.06$ eV] than that of the fcc counterpart [$TI_0 \rightarrow TI_2$, $E_a = 0.07$ eV]. Nevertheless, at a later stage, the hcp trimer should clearly switch to the thermodynamically preferred fcc position with a minor barrier [$CD_0 \leftrightarrow CD_1$, $E_a^{for} = 0.02$ eV, $E_a^{rev} = 0.12$ eV].

On the other hand, this contrasts with the hcp packaging series of metallic Mg that should follow the ABABAB-stacking sequence. Two questions arise, first, why are fcc sites favored over hcp sites for smaller islands, and second, at what critical island size does the original packing order become thermodynamically more stable again. Therefore, for islands up to a size of 7 atoms and full monolayers (MLs) (36 atoms) on (6×6) Mg(0001), the adsorption energies per atom were calculated as shown in Figure S5. Additionally, the exact adsorption energies per atom for the islands and for full hcp and fcc MLs, as well as the stacking fault energies, may be found in Table S9. It turns out that starting from a heptamer adsorption is slightly favored on hcp sites, while tetramers, pentamers, and hexamers are indifferent. This finding is consistent with the results of Ortigoza et al. The group confirmed stacking fault up to the trimer but also used only half of the unit cell size ((3×3) vs. (6×6)). They blame Friedel oscillations for inducing an increased charge density at the fcc pocket, which noticeably stabilizes the bond of the adsorbate to its nearest neighbors. At the same time, however, the increased charge density at adjacent fcc positions vanishes, which explains the renewed preference of the hcp position for larger adislands.[40]

On the second studied surface Mg(10$\bar{1}$1), the barriers for trimer formation are generally higher than on Mg(0001). In addition, the linear trimer form is thermodynamically more stable with respect to the triangular trimer form. If an atom encounters a dimer within a channel, the barriers are roughly equivalent to those of the dimer formation [$t_0 \leftrightarrow t_1$, $E_a^{for} = 0.26$ eV, $E_a^{rev} = 0.58$ eV]. Diffusion across the channel proceeds in a two-step process along [$t_2 \rightarrow t_3$, $E_a^{for} = 0.19$ eV; $t_3 \rightarrow t_1$, $E_a^{for} = 0.27$ eV] and opposite to the [10$\bar{1}$2]-direction [$t_4 \rightarrow t_5$, $E_a^{for} = 0.31$ eV; $t_5 \rightarrow t_1$, $E_a^{for} = 0.24$ eV] with the triangle trimer form as intermediate. The barriers are very similar for all investigated processes, making it difficult to draw accurate predictions about the preferred pathway of trimer formation. However, surface growth should most likely proceed in a line along the hollow sites perpendicular to the [10$\bar{1}$2]-direction. The use of kinetic Monte-Carlo simulations could provide further insights.[41]

Step, kink, and corner self-diffusion on Mg(0001) and Mg(10$\bar{1}$1)

After the formation of initial polyatomic clusters, we would like to discuss further surface growth, especially island formation, by studying additional processes of the terrace–step-kink (TSK) model (step-edge, step-vacancy, kink, inner-corner, and outer-corner).[42] The TSK model describes the diffusion processes taking place during surface growth and discusses several growth mechanisms.[43] As described previously, islands on Mg(0001) are more stable on hcp sites starting from a heptamer. Thus, only processes at hcp steps, kinks, and corners were investigated, which consist of more than 7 atoms. The activation energies of the processes studied may be found in Table 9 for Mg(0001) and Table 10 for Mg(10$\bar{1}$1) with schematic representations shown in Figure 8, Figure 9, and Figure 10.

Table 9. Activation energies E_a for forward and backward step-edge, step-vacancy, kink and corner self-diffusion processes on Mg(0001) calculated with Equation (2) (PBE).

Diffusion on Mg(0001)	Path	Pathway	E_a^{for} [eV]	E_a^{rev} [eV]
step-edge	[11$\bar{2}$0]-step	$S_0 \leftrightarrow S_1$	0.03	0.70
		$S_1 \leftrightarrow S_2$	0.22	0.22
	[$\bar{1}\bar{1}$20]-step	$S_3 \leftrightarrow S_4$	0.02	0.63
		$S_4 \leftrightarrow S_5$	0.15	0.15
step-vacancy	[11$\bar{2}$0]-step	$SV_0 \leftrightarrow SV_1$	0.03	1.15
	[$\bar{1}\bar{1}$20]-step	$SV_2 \leftrightarrow SV_3$	0.02	1.23
kink	[11$\bar{2}$0]-step	$K_0 \leftrightarrow K_1$	0.45	0.17
		$K_0 \leftrightarrow K_2$	0.91	0.02
		$K_0 \leftrightarrow K_3$	0.51	0.29
	[$\bar{1}\bar{1}$20]-step	$K_4 \leftrightarrow K_5$	0.46	0.12
		$K_4 \leftrightarrow K_6$	0.92	0.01
		$K_4 \leftrightarrow K_7$	0.56	0.22
inner-corner	60 corner: [11$\bar{2}$0]-step	$IC_0 \leftrightarrow IC_1$	0.63	0.10
	60 corner: [$\bar{1}\bar{1}$20]-step	$IC_2 \leftrightarrow IC_3$	0.62	0.08
	120 corner	$IC_4 \leftrightarrow IC_5$	0.43	0.18
		$IC_4 \leftrightarrow IC_6$	0.43	0.10
outer-corner	240 corner	$OC_0 \leftrightarrow OC_1$	0.29	0.22
		$OC_0 \leftrightarrow OC_1$ (Ex.)	0.41	0.33
	300 corner: [11$\bar{2}$0]-step	$OC_2 \leftrightarrow OC_3$ $OC_5 \leftrightarrow OC_4$	0.24	0.00
		$OC_3 \leftrightarrow OC_4$	0.03	0.03
		$OC_2 \leftrightarrow OC_5$ (Ex.)	0.32	0.32
	300 corner: [$\bar{1}\bar{1}$20]-step	$OC_6 \leftrightarrow OC_7$ $OC_8 \leftrightarrow OC_7$	0.20	0.03
		$OC_6 \leftrightarrow OC_8$ (Ex.)	0.16	0.16

© 2022 The Authors. ChemSusChem published by Wiley-VCH GmbH

ChemSusChem
Research Article
doi.org/10.1002/cssc.202200414
Chemistry Europe
European Chemical Societies Publishing

Table 10. Activation energies E_a for forward and backward step-edge self-diffusion processes on Mg(10$\bar{1}$1) calculated with Equation (2) (PBE).

Diffusion on Mg(10$\bar{1}$1)	Path	Pathway	E_a^{for} [eV]	E_a^{rev} [eV]
step-edge	[1$\bar{2}$10]A-step	$s_0 \leftrightarrow s_1$	0.35	0.59
		$s_1 \leftrightarrow s_2$	0.13	0.13
	[$\bar{1}$2$\bar{1}$0]B-step	$s_3 \leftrightarrow s_4$	0.44	0.73
		$s_4 \leftrightarrow s_5$	0.16	0.16
	[1$\bar{2}$10]A-step	$s_6 \leftrightarrow s_7$	0.14	0.18
		$s_7 \leftrightarrow s_8$	0.01	0.01
	[1$\bar{2}$10]B-step	$s_9 \leftrightarrow s_{10}$	0.36	0.95
		$s_{10} \leftrightarrow s_{11}$	0.40	0.40
	[10$\bar{1}$2]-step	$s_{12} \leftrightarrow s_{13}$	0.18	0.71
		$s_{13} \leftrightarrow s_{14}$	0.45	0.45

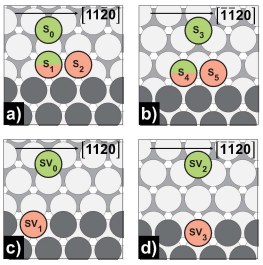

Figure 8. Schematic representation of step-edge and step-vacancy self-diffusion processes on Mg(0001): a) step-edge [11$\bar{2}$0]-step; b) step-edge [$\bar{1}\bar{1}$20]-step; c) step-vacancy [11$\bar{2}$0]-step; d) step-vacancy [$\bar{1}\bar{1}$20]-step. Green-colored atoms mark the initial, while red-colored atoms mark the final positions.

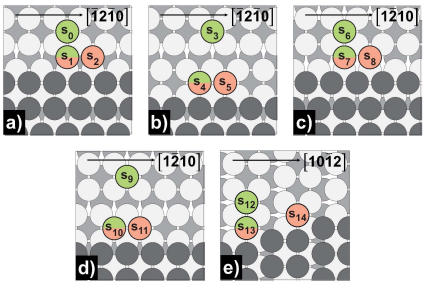

Figure 9. Schematic representation of step-edge self-diffusion processes on Mg(1011): a) step-edge [$\bar{1}$2$\bar{1}$0]A-step; b) step-edge [$\bar{1}$2$\bar{1}$0]B-step; c) step-edge [1$\bar{2}$10]A-step; d) step-edge [1$\bar{2}$10]B-step; e) step-edge [10$\bar{1}$2]-step. Green-colored atoms mark the initial, while red-colored atoms mark the final positions.

Initially, we want to discuss the process of a free atom approaching the step-edge on Mg(0001). As we have already seen with similar dimer and trimer processes, the forward barrier is negligibly small, but the detachment barrier is many times higher [$S_{0/3} \leftrightarrow S_{1/4}$, $E_a^{for} = 0.03/0.02$ eV, $E_a^{rev} = 0.70/0.63$ eV].

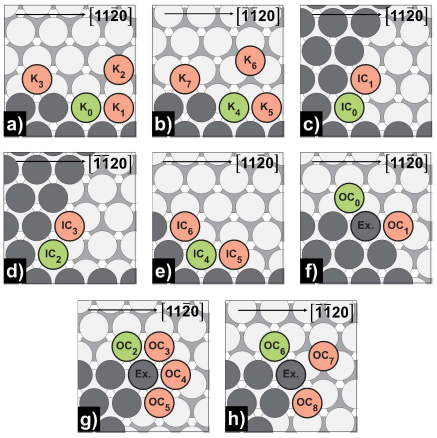

Figure 10. Schematic representation of kink, inner- and outer-corner self-diffusion processes on Mg(0001): a) kink [11$\bar{2}$0]-step; b) kink [$\bar{1}\bar{1}$20]-step; c) 60 inner-corner [11$\bar{2}$0]-step; d) 60 inner-corner [$\bar{1}\bar{1}$20]-step; e) 120 inner-corner; f) 240 outer-corner; g) 300 outer-corner [11$\bar{2}$0]-step; h) 300 outer-corner [$\bar{1}\bar{1}$20]-step. Green-colored atoms mark the initial, while red-colored atoms mark the final positions.

This observation becomes even more evident with a defect in the edge. Edge-vacancy formation has the highest barrier of all diffusion processes studied [$SV_{1/3} \rightarrow SV_{0/2}$, $E_a^{rev} = 1.15/1.23$ eV], indicating an extremely low probability of occurrence. It must be added that all fcc and hcp adsorption sites between the initial and the final state of the processes of approaching atoms are unstable and terminate in the initial state during relaxation. Once again, this underlines the high interaction energy on Mg(0001).

On Mg(10$\bar{1}$1), it is noticeable that an approaching atom hast to overcome higher forward barriers of at least 0.14 up to 0.44 eV, depending on the direction of the step. However, this behavior is expected since the barriers for terrace self-diffusion on Mg(10$\bar{1}$1) are already at least 0.30 eV. The ratio between forward and reverse barriers is between 1–4 times, significantly lower than for Mg(0001) (25–40 times).

Step-edge diffusion on Mg(0001) along the [$\bar{1}\bar{1}$20] direction [$S_4 \leftrightarrow S_5$, $E_a = 0.15$ eV] is more probable compared to the [11$\bar{2}$0] direction [$S_4 \leftrightarrow S_5$, $E_a = 0.22$ eV]. We explain the difference in energy by considering the structure of the respective transition state (TS). In the TS of the [$\bar{1}\bar{1}$20]-directed step, the nearest neighbor atom in the edge row pulls slightly back, leaving a pocket for the diffusing atom to settle in a stabilized fcc-like position (Figure S10). The step-edge diffusion barriers are in agreement with results from Jäckle et al., assuming the growth of triangular islands with only $<\bar{1}\bar{1}20>$-directed steps due to the preferred diffusion along the [$\bar{1}\bar{1}$20] direction.[23] Furthermore, the formation of fractal islands can almost be excluded since the step-edge barriers are easily overcome at room

© 2022 The Authors. ChemSusChem published by Wiley-VCH GmbH

18645641, 2022, 14, Downloaded from https://chemistry-europe.onlinelibrary.wiley.com/doi/10.1002/cssc.202200414 by KIT der Universitat Ulm, Wiley Online Library on [21/10/2022]. See the Terms and Conditions (https://onlinelibrary.wiley.com/terms-and-conditions) on Wiley Online Library for rules of use; OA articles are governed by the applicable Creative Commons License

ChemSusChem
Research Article
doi.org/10.1002/cssc.202200414
Chemistry Europe
European Chemical Societies Publishing

18648564, 2022, 14, Downloaded from https://chemistry-europe.onlinelibrary.wiley.com/doi/10.1002/cssc.202200414 by KIT der Universitat Ulm, Wiley Online Library on [21/10/2022]. See the Terms and Conditions (https://onlinelibrary.wiley.com/terms-and-conditions) on Wiley Online Library for rules of use; OA articles are governed by the applicable Creative Commons License

temperature (see section Activation temperature of diffusion processes on Mg(0001) and Mg(10$\bar{1}$1)). Fractal islands are formed when an adatom arrives at an edge, but relaxation to a more favorable position is hindered.[43]

Looking at the diffusion along the steps on Mg(10$\bar{1}$1), it is noticeable that depending on the directions, the barriers are very heterogeneous. On the one hand, there is barrierless diffusion along the [1$\bar{2}$10]A-directed step [$s_7 \leftrightarrow s_8$, $E_a = 0.01$ eV], while diffusion along the [$\bar{1}$2$\bar{1}$0]A- and [$\bar{1}$2$\bar{1}$0]B-directed steps [$s_{1/4} \leftrightarrow s_{2/5}$, $E_a = 0.13/0.16$ eV] is of the same order of magnitude as for Mg(0001) along [$\bar{1}\bar{1}$20], and finally, diffusion along [1$\bar{2}$10]B and [10$\bar{1}$2] [$s_{10/11} \leftrightarrow s_{13/14}$, $E_a = 0.40/0.45$ eV] is about 3 times higher compared to diffusion along the [$\bar{1}$2$\bar{1}$0]A-directed step. The reason might be due to different coordination of the diffusing atom in the initial/final sites (hollow *vs.* fcc-like sites).

Looking at the 240 -outer-corner process [$OC_0 \leftrightarrow OC_1$, $E_a^{for} = 0.29$ eV, $E_a^{rev} = 0.22$ eV], we notice a thermodynamically favored OC_0 site, strengthening the hypothesis of growth of triangular islands with only $<\bar{1}\bar{1}20>$- steps on Mg(0001).[23] Alternatively, hexagonal islands with alternating $<11\bar{2}0>$- and $<\bar{1}\bar{1}20>$-steps would be possible at higher temperatures due to vibrational and configurational entropy effects, as assumed for fcc Al(111).[44] The competing exchange process at the 240 -outer-corner has a higher activation energy and seems unfavorable [$OC_0 \leftrightarrow OC_1$ (Ex.), $E_a^{for} = 0.41$ eV, $E_a^{rev} = 0.33$ eV]. Equally of interest is the diffusion behavior at the [11$\bar{2}$0]-directed 300 -corner consisting of three successive hopping steps. First, the adatom jumps from the edge to the tip of the corner [$OC_{2/4} \leftrightarrow OC_{3/5}$, $E_a^{for} = 0.24$ eV], switches sides in a symmetrical process [$OC_3 \leftrightarrow OC_4$, $E_a = 0.03$ eV] and finally moves barrierless to its final position [$OC_{2/4} \leftrightarrow OC_{3/5}$, $E_a^{rev} = 0.00$ eV]. In contrast, at the [$\bar{1}\bar{1}$20]-directed corner, the exchange process is kinetically preferred with the atom at the tip as exchange partner [$OC_6 \leftrightarrow OC_8$ (Ex.), $E_a = 0.16$ eV]. When looking at the inner corner processes, it becomes clear that in both 60 - and 120 -processes, maximization of the binding partners is associated with lower barriers. In the 120 -processes, the number of binding partners increases from 2 to 3 [$IC_4 \leftrightarrow IC_{5/6}$, $E_a^{for} = 0.43$ eV, $E_a^{rev} = 0.18/0.10$ eV], and in the 60 -processes from 2 to 4 [$IC_{0/2} \leftrightarrow IC_{1/3}$, $E_a^{for} = 0.63/0.62$ eV, $E_a^{rev} = 0.10/0.18$ eV], which is associated with forward/reverse barrier ratios of 2–4 and 6–8, respectively. For completion, the processes at the kink sites were studied. The barriers along the steps are similar to the respective 120 -corner processes [$K_{0/4} \leftrightarrow K_{1/5}$, $E_a^{for} = 0.45/0.46$ eV, $E_a^{rev} = 0.17/0.12$ eV]. The barriers to leaving the kink position in the direction of the terrace also match the pattern [$K_{0/4} \leftrightarrow K_{2/6}$, $E_a^{for} = 0.91/0.92$ eV, $E_a^{rev} = 0.02/0.01$ eV]. The barrier height is exactly between the step-edge and edge-vacancy activation energy, accompanied by breaking 2 and 4 bonds, respectively. In addition, the process of forming kink sites is favored over the formation of corners [$K_{0/4} \leftrightarrow K_{3/7}$, $E_a^{for} = 0.51/0.56$ eV, $E_a^{rev} = 0.29/0.22$ eV] indicating compact rather than fractal islands.

Ehrlich-Schwoebel barrier and upper step self-diffusion on Mg(0001) and Mg(10$\bar{1}$1)

So far, we have only considered 2-dimensional processes. However, to get a complete picture of surface growth, 3-dimensional processes such as upper-step diffusion followed by its descent are particularly important. The activation energies of the respective processes (step-down, step-down (dimer), upper-step) as well as the calculated Ehrlich-Schwoebel barriers for Mg(0001) and Mg(10$\bar{1}$1) are summarized in Table 11 and Table 12. The schematic illustrations of the processes are given in Figure 11 and Figure 12.

Exactly as we have already seen for the terrace self-diffusion on Mg(0001), the upper-step diffusion onwards the step-edge occurs almost barrierless for both facets. Nevertheless, there are small differences from a kinetic and thermodynamic perspective. For example, on [$\bar{1}\bar{1}$20]- [$US_{4/5} \leftrightarrow US_{5/6}$, $E_a^{for} = 0.00$ eV, $E_a^{rev} = 0.03/0.02$ eV] as opposed to [11$\bar{2}$0]-steps [$US_0 \leftrightarrow US_1$, $E_a^{for} = 0.02$ eV, $E_a^{rev} = 0.01$ eV; $US_1 \leftrightarrow US_2$, $E_a^{for} = 0.01$ eV, $E_a^{rev} = 0.03$ eV], both forward barriers of the two step-process are lower than the reverse barriers. Moreover, from a thermodynamic point of view, the energy difference between the US_2 and US_0 sites is much smaller (7 meV) than between US_6 and US_4 sites (40 meV), indicating that diffusion occurs preferentially toward the [$\bar{1}\bar{1}$20]-directed step-edges, followed by the subsequent descent. Likewise, upper-step diffusion could only be studied along the

Table 11. Activation energies E_a for forward and backward step-down, step-down (dimer) and upper-step self-diffusion processes on Mg(0001) were calculated with Equation (2) (PBE). In addition, the Ehrlich-Schwoebel barriers E_{ES} were calculated for the step-down diffusion processes using Equation (4). The forward activation barriers for the upper-step processes at the [$\bar{1}\bar{1}$20]-step did not equal exactly 0.00 eV but were below 0.005 eV while rounding to the second decimal place.

Diffusion on Mg(0001)	Path	Pathway	E_a^{for} [eV]	E_a^{rev} [eV]	E_{ES} [eV]
step-down	[11$\bar{2}$0]-step	$E_0 \leftrightarrow E_1$	0.09	0.75	0.07
		$E_0 \leftrightarrow E_1$ (Ex.)	0.01	0.67	−0.02
	[$\bar{1}\bar{1}$20]-step	$E_2 \leftrightarrow E_3$	0.16	0.70	0.14
		$E_2 \leftrightarrow E_3$ (Ex.)	0.02	0.56	−0.01
step-down (dimer)	[11$\bar{2}$0]-step	$ED_0 \leftrightarrow ED_1$	0.58	0.74	
		$ED_0 \leftrightarrow ED_1$ (Ex.)	0.21	0.38	
	[$\bar{1}\bar{1}$20]-step	$ED_2 \leftrightarrow ED_3$	0.67	0.68	
		$ED_2 \leftrightarrow ED_3$ (Ex.)	0.11	0.15	
upper-step	[11$\bar{2}$0]-step	$US_0 \leftrightarrow US_1$	0.02	0.01	
		$US_1 \leftrightarrow US_2$	0.01	0.03	
		$US_2 \leftrightarrow US_3$	0.02	0.02	
	[$\bar{1}\bar{1}$20]-step	$US_4 \leftrightarrow US_5$	0.00	0.03	
		$US_5 \leftrightarrow US_6$	0.00	0.02	

© 2022 The Authors. ChemSusChem published by Wiley-VCH GmbH

ChemSusChem
Research Article
doi.org/10.1002/cssc.202200414
Chemistry Europe
European Chemical Societies Publishing

18645641, 2022, 14, Downloaded from https://chemistry-europe.onlinelibrary.wiley.com/doi/10.1002/cssc.202200414 by KIT der Universitat Ulm, Wiley Online Library on [21/10/2022]. See the Terms and Conditions (https://onlinelibrary.wiley.com/terms-and-conditions) on Wiley Online Library for rules of use; OA articles are governed by the applicable Creative Commons License

Table 12. Activation energies E_a for forward and backward step-down self-diffusion processes on Mg(10$\bar{1}$1) were calculated using Equation (2) (PBE) and the Ehrlich–Schwoebel barriers E_{ES} were calculated using Equation (4).

Diffusion on Mg(10$\bar{1}$1)	Path	Pathway	E_a^{for} [eV]	E_a^{rev} [eV]	E_{ES} [eV]
step-down	[$\bar{1}$2$\bar{1}$0]A-step	$e_0 \leftrightarrow e_1$	0.44	0.67	0.14
		$e_0 \leftrightarrow e_2$ (Ex.)	0.11	0.34	−0.19
	[$\bar{1}$2$\bar{1}$0]B-step	$e_3 \leftrightarrow e_4$	0.43	0.75	0.13
		$e_3 \leftrightarrow e_4$ (Ex.)	0.26	0.58	−0.04
	[1$\bar{2}$10]A-step	$e_5 \leftrightarrow e_6$	0.29	0.04	–
		$e_6 \leftrightarrow e_7$	0.12	0.42	−0.18
		$e_5 \leftrightarrow e_7$ (Ex.)	0.47	0.53	0.17
	[1$\bar{2}$10]B-step	$e_8 \leftrightarrow e_9$	0.44	0.96	0.14
		$e_8 \leftrightarrow e_{10}$ (Ex.)	0.07	0.59	−0.23
	[10$\bar{1}$2]-step	$e_{11} \leftrightarrow e_{12}$	0.38	0.89	0.08
		$e_{11} \leftrightarrow e_{12}$ (Ex.)	0.20	0.71	−0.10

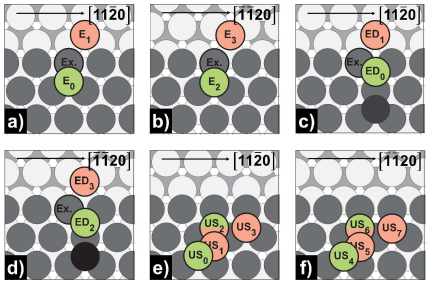

Figure 11. Schematic representation of step-down, step-down (dimer) and upper-step self-diffusion processes on Mg(0001): a) step-down [11$\bar{2}$0]-step; b) step-down [$\bar{1}\bar{1}$20]-step; c) step-down (dimer) [11$\bar{2}$0]-step; d) step-down (dimer) [$\bar{1}\bar{1}$20]-step; e) upper-step [11$\bar{2}$0]-step; f) upper-step (dimer) [$\bar{1}\bar{1}$20]-step. Green-colored atoms mark the initial, while red-colored atoms mark the final positions.

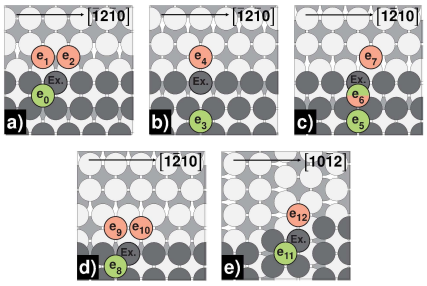

Figure 12. Schematic representation of step-down self-diffusion processes on Mg(10$\bar{1}$1): a) step-down [$\bar{1}$2$\bar{1}$0]A-step; b) step-down [$\bar{1}$2$\bar{1}$0]B-step; c) step-down [1$\bar{2}$10]A-step; d) step-down [1$\bar{2}$10]B-step; e) step-down [10$\bar{1}$2]-step. Green-colored atoms mark the initial, while red-colored atoms mark the final positions.

step-edge at [11$\bar{2}$0]-steps [$US_2 \leftrightarrow US_3$, $E_a = 0.02$ eV], while at [$\bar{1}\bar{1}$20]-steps [$US_6 \leftrightarrow US_7$] the diffusing atom immediately descends to the lower level (drops down to E_2 site). In general, the descent takes place via the exchange process [$E_{0/2} \leftrightarrow E_{1/3}$ (Ex.), $E_a^{for} = 0.01/0.02$ eV, $E_a^{rev} = 0.69/0.56$ eV]. In both cases, this has a significantly reduced barrier compared to the corresponding hopping processes [$E_{0/2} \leftrightarrow E_{1/3}$, $E_a^{for} = 0.09/0.16$ eV, $E_a^{rev} = 0.75/0.70$ eV]. In addition, the exchange processes show negative Ehrlich-Schwoebel barriers indicating a uniform and smooth growth due to a high rate of interlayer mass transport.[43] Likewise, the descent is clearly preferred to the ascent following the observed increase in coordination partners. All step-down barriers are in agreement with the literature.[23,36]

Going one step further, we wanted to investigate the influence of a second adatom on the step-down barriers. It becomes immediately apparent that the barriers to descent for hopping [$ED_{0/2} \leftrightarrow ED_{1/3}$, $E_a^{for} = 0.58/0.67$ eV, $E_a^{rev} = 0.74/0.68$ eV] as well as exchange processes [$ED_{0/2} \leftrightarrow ED_{1/3}$ (Ex.), $E_a^{for} = 0.21/0.11$ eV, $E_a^{rev} = 0.38/0.15$ eV] increase significantly. It can be assumed that the larger the cluster, the stronger the effect. For smooth surface growth, the adatom must reach the step-edge faster than it reaches another adatom. Thus, the higher the deposition rate, the more likely new islands aggregate on top of existing islands before the bottom layer is fully complete.[43] A further interesting case is the exchange process at the [$\bar{1}\bar{1}$20]-step. In this process, the barriers for ascent and descent are very close together. However, it is important to note that the second atom follows the diffusing atom into the fcc position above the exchange atom during descent. This arrangement maintains the dimer conformation until beyond the TS (Figure S11) and lowers the activation energy of the process to half of the corresponding exchange process at the [11$\bar{2}$0]-step.

On Mg(10$\bar{1}$1), in almost all cases (except [1$\bar{2}$10]A-step), the exchange process has the lowest barrier on the descent. The smallest step-down barrier is found at the [1$\bar{2}$10]B-step [$e_8 \leftrightarrow e_9$ (Ex.), $E_a^{for} = 0.07$ eV], whereas the lowest ascent barrier is found at the [$\bar{1}$2$\bar{1}$0]A-step [$e_0 \leftrightarrow e_2$ (Ex.), $E_a^{rev} = 0.34$ eV]. The most frequent descent route is likely to be along the [10$\bar{1}$2]-step [$e_{11} \leftrightarrow e_{12}$ (Ex.), $E_a^{for} = 0.20$ eV]. Here an adatom can diffuse within a channel to the edge, and subsequently descend via the exchange process.

© 2022 The Authors. ChemSusChem published by Wiley-VCH GmbH

ChemSusChem
Research Article
doi.org/10.1002/cssc.202200414
Chemistry Europe
European Chemical Societies Publishing

18645641, 2022, 14, Downloaded from https://chemistry-europe.onlinelibrary.wiley.com/doi/10.1002/cssc.202200414 by KIT der Universitat Ulm, Wiley Online Library on [21/10/2022]. See the Terms and Conditions (https://onlinelibrary.wiley.com/terms-and-conditions) on Wiley Online Library for rules of use; OA articles are governed by the applicable Creative Commons License

Activation temperature of diffusion processes on Mg(0001) and Mg(10$\bar{1}$1)

In addition to the diffusion barriers, we calculated the pre-exponential factors of the Arrhenius equations via the Einstein approximation using Equation (5) to determine the activation temperatures of the processes studied on Mg(0001) and Mg(10$\bar{1}$1) using Equation (6). The obtained activation temperatures at which the respective diffusion processes start to contribute to surface growth are shown in Figures 13 and 14.

On Mg(0001), processes such as terrace self-diffusion, the formation of dimers and trimers, and the step-down process do not have significant barriers and are already activated at temperatures below 25 K. It must be noted that dimer and trimer formation is highly favored compared to the respective separation processes due to a very high interaction energy. At this point, we would like to address the hypothesis that lower terrace self-diffusion and step-down barriers on Mg(0001) vs. Li(100) are responsible for reduced dendrite formation.[23] We were able to confirm lower barriers for Mg(0001). However, the corresponding processes for metallic lithium become activated at 16 and 43 K, respectively.[24] At room temperature, these processes should run almost equally and have no significant influence on dendrite formation. We believe that to adequately explain dendrite growth, a holistic and more exhaustive model needs to be developed that considers the influence of the SEI interface, the stability of different surface terminations, the diffusion barriers on the respective surfaces, the applied potential, the deposition conditions, and the electrolyte used. It remains an open question to what extent this is already possible with the current theoretical tools. However, the data presented in this work could serve as a reference for future studies where these additional effects are successively accounted for.

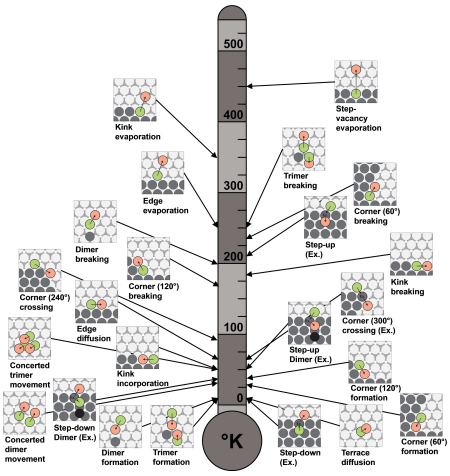

Figure 13. Activation temperatures of diffusion processes to impact surface growth on Mg(0001).

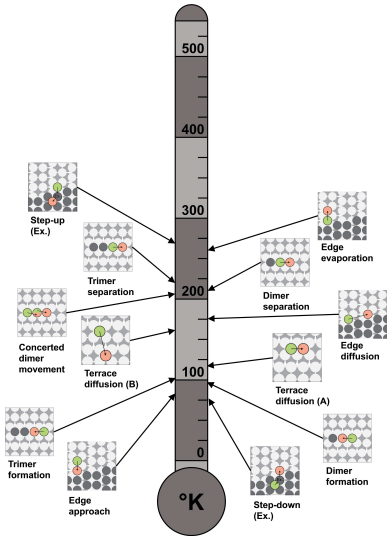

Figure 14. Activation temperatures of diffusion processes to impact surface growth on Mg(10$\bar{1}$1).

At a temperature below 100 K on Mg(0001), a variety of further diffusion processes become active such as dimer and trimer propagation, diffusion along an edge, the formation of 60° and 120° corners, switching sides at 240° and 300° corners and kink incorporation. Especially the activated corner-crossing barriers contribute to the growth of compact rather than fractal islands.[43] Interestingly, both the dimer step-down and step-up processes become possible in this temperature range, contrary to uniform and smooth surface growth.

On Mg(10$\bar{1}$1), we found that the activation temperatures for diffusion processes are generally higher. Below 100 K, it is only possible for an adatom to step-down, form a dimer, or diffuse towards an edge. Terrace diffusion within and across a channel and diffusion along an edge on Mg(10$\bar{1}$1) becomes possible at elevated temperatures above 100 K.

In the same temperature range, processes in which the coordination number of the diffusing atom is reduced become available on Mg(0001), such as in the 120° corner and kink breaking processes. Above 200 K, the dimer and trimer separation processes, edge evaporation, and 60° corner separation are also enabled, as well as the step-up process. Despite that, the statement still applies that bond breakages are extremely unlikely for magnesium and that the increase of the coordination number always proceeds preferentially. For exam-

© 2022 The Authors. ChemSusChem published by Wiley-VCH GmbH

ChemSusChem
Research Article
doi.org/10.1002/cssc.202200414
Chemistry Europe
European Chemical Societies Publishing

18648564, 2022, 14, Downloaded from https://chemistry-europe.onlinelibrary.wiley.com/doi/10.1002/cssc.202200414 by KIZ der Universitat Ulm, Wiley Online Library on [21/10/2022]. See the Terms and Conditions (https://onlinelibrary.wiley.com/terms-and-conditions) on Wiley Online Library for rules of use; OA articles are governed by the applicable Creative Commons License

ple, kink evaporation and the formation of a step-vacancy are not possible at room temperature for Mg(0001). Nevertheless, activated evaporation and separation processes are necessary for island ripening (redistribution of mass).[43] We assume many small islands form in the low-temperature range, and new adsorbates join existing ones. At higher temperatures, island ripening should begin, and smaller islands dissolve at the expense of larger islands.

On Mg(10$\bar{1}$1), all processes studied can occur at ambient conditions. In the temperature range between 200 and 300 K, dimer and trimer separation, edge evaporation, and the exchange step-up process are activated. In addition, concerted dimer propagation proceeds at about 200 K.

At this point, we would like to refer to the Supporting Information, which summarizes all calculated data. Table S7 and Table S8 show the pre-exponential factors, activation energies, room-temperature rate constants, and activation temperatures for the terrace self-diffusion processes for the PBE and BEEF-vdW functionals, respectively. Corresponding schematic representations and energy profiles are provided in Figure S4. In addition, overviews of all investigated diffusion processes on Mg(0001) are available in Figure S6 and on Mg(10$\bar{1}$1) in Figure S8. The corresponding pre-exponential factors, activation energies, room temperature rate constants, activation temperatures, and energy profiles may be found in Table S10, Figure S7, Table S11, and Figure S9.

Conclusion

This work aimed to determine and summarize the atomistic properties of magnesium and discuss the initial stages of surface growth in a possible magnesium-ion battery. Therefore, well-selected self-diffusion processes on perfect and imperfect Mg surfaces were investigated to better understand the initial surface growth phenomena at the level of density functional theory. We are aware that in a real battery environment, the operation conditions, the potential, the electrolyte, charge- and discharge products, and especially the SEI environment might have a tremendous impact on the atomistic properties of magnesium. For this reason, we do not want to make any statements about possible dendrite growth based on our results, as we believe this is not possible with pure DFT. Nevertheless, we still believe that our studies already provide informative insights into the actual processes taking place.

First, the present calculations confirm the preference of magnesium to crystallize in a hcp crystalline structure at ambient conditions, with surface terminations Mg(0001), Mg-(10$\bar{1}$0)A, and Mg(10$\bar{1}$1) being, in this order, most stable. Interestingly, the surface proportions in a nanocrystal are quite different. According to the Wulff construction, Mg(10$\bar{1}$1) has the largest share of the surface with a surface fraction of about 50%, while the remaining area is distributed evenly between Mg(0001) and Mg(10$\bar{1}$0)A, as shown in Figure 1. The Wulff construction clearly illustrates that diffusion properties must be discussed for all three surfaces collectively and cannot be limited to the thermodynamically most stable surface Mg(0001), as done in previous studies.

Terrace self-diffusion of single atoms runs almost barrier-free on Mg(0001) but with higher activation energies on Mg(10$\bar{1}$1). When adsorbates collide on the surfaces, initial dimer, trimer, and cluster structures are formed, which is highly favored due to high attractive interactions between the adsorbates. The small cluster structures can be seen as seeds for further island growth, which shape on Mg(0001) could be either triangular with only $<\bar{1}\bar{1}20>$- steps as proposed by Jäckle et al.[23] or hexagonal with alternating $<11\bar{2}0>$- and $<\bar{1}\bar{1}20>$-steps at elevated temperatures.[44] However, the island pattern should be compact rather than fractal due to low step-edge and corner crossing barriers.[43] On Mg(10$\bar{1}$1), the diffusion barriers are in general higher compared to Mg(0001), but the ratios for bond formation and breakage are closer together. All processes studied on Mg(10$\bar{1}$1) can occur at ambient conditions, while on Mg(0001) kink evaporation and the formation of a step-vacancy are not activated at room temperature. Surface growth on Mg(10$\bar{1}$1) could proceed in a line along the *hollow* sites perpendicular to the [10$\bar{1}$2]-direction.

The three-dimensional diffusion studies reveal negative Ehrlich-Schwoebel barriers for all investigated exchange descend processes on Mg(0001) and Mg(10$\bar{1}$1) (except [1$\bar{2}$10]A-step), indicating a uniform and smooth surface growth due to a high rate of interlayer mass transport at low deposition rates.[43] However, a second adatom significantly increases the descent barriers for hopping and exchange processes, fostering the aggregation of new islands on top of existing islands if the adatom meets another adatom faster than it reaches the step-edge.

All generated data will be used in a future work as a training set for parameterizing the reactive force field ReaxFF. ReaxFF allows a more realistic investigation of the battery system by including the electrolyte, and at the same time, lowers the computational cost but with similar accuracy.[27,28,45] Furthermore, the calculated rate constants may be used in kinetic Monte-Carlo simulations to investigate and visualize the kinetic effects of surface growth.[41]

Theoretical Section

Periodic DFT calculations were performed with the plane-wave based Vienna ab initio simulation package (VASP).[46,47] The core electrons were described using the projector augmented wave (PAW)[48] method of Blöchl as implemented in VASP.[49] Exchange correlation effects were described within the generalized gradient approximation (GGA) of Perdew, Burke, and Enzerhof (PBE).[50] Additionally, the Bayesian error estimation functional with van der Waals correlation (BEEF-vdW) was applied to determine the standard deviation of the investigated quantities.[51] A plane-wave cutoff energy of 400 eV was employed after detailed convergence studies (Figure S1 in the Supporting Information), where Mg 2 s electrons were described as valence electrons. Following the scheme of Monkhorst and Pack, a *k*-point mesh density of at least 0.14 $Å^{-1}$ was applied for all total energy calculations.[52] Thermal smearing of one-electron states was allowed using the Gaussian smearing method ($\sigma = 0.1$ eV) to determine the partial occupancies of each orbital and acquire faster convergence with respect to the

© 2022 The Authors. ChemSusChem published by Wiley-VCH GmbH

ChemSusChem
Research Article
doi.org/10.1002/cssc.202200414
Chemistry Europe
European Chemical Societies Publishing

number of *k*-points. The electronic self-consistent field (SCF) was considered converged when the total energy difference was less than 10^{-5} eV, and the norms of all the forces were smaller than 10^{-3} eV·Å^{-1}. Surface energies were calculated on symmetrical (1 × 1) cells with a minimum slab thickness of 30 Å and a minimum vacuum region of 20 Å (Table S1). A single atom in the middle of the slab was fixed to avoid net translations.[24] Adsorption energies, dimer interaction, diffusion barriers, and frequencies were generally calculated on converged slabs with 6 surface layers, where the two uttermost layers were fixed to emulate bulk properties. If it became necessary, vicinal slabs were used. The exact surface characteristics are summarized in Table S2. According to a detailed bulk study, the lattice constants used for hcp magnesium were $a_0 = 3.18$ Å and $c_0 = 5.21$ Å for all employed structures (Table S3). A detailed comparison of the bulk properties with literature is also provided in the bulk properties chapter in the Supporting Information. The minimum energy path (MEP) was determined with the climbing image nudged elastic band (CI-NEB) method as implemented in the transition state tools for VASP (VTST) with generally 7 images between the initial states separated by a spring constant of 5.0 eV Å^{-2}.[53,54] As an initial guess for the MEP the image-dependent pair potential (IDPP) was applied.[55,56] To confirm the transition state and to determine rate constants, we calculated vibrational frequencies with the dynamical matrix method from the VTST package. For this purpose, the electronic and ionic convergence criteria were increased to 10^{-8} eV and 10^{-8} eV Å^{-1}, respectively, and the diffusing as well as the nearest neighbor atoms along the diffusion pathway were symmetrically displaced by 0.007 Å in each spatial direction.

The surface energy γ is defined as the surface excess free energy per unit area and was calculated by subtracting a multiple of the bulk energy $N{\cdot}E_{bulk}$ from the energy of the slab E_{slab}, divided by the area of the surface A times two (because of the symmetric slab configuration):

$$\gamma = \frac{1}{2A}\left(E_{slab} - N \cdot E_{bulk}\right) \tag{1}$$

All surface energies were employed to carry out the Wulff construction.[26] The area fractions of the facets were calculated using the Python package WulffPack for a nanocrystal with 5000 atoms.[57]

The activation energies $E_a^{for/rev}$ for forward and backward diffusion processes correspond to the energy differences between the energy of the transition state E_{TS} and the energy of the initial and final structure $E_{IS/FS}$, respectively:

$$E_a^{for/rev} = E_{TS} - E_{IS/FS} \tag{2}$$

The interaction energy E_{int} for the dimer configurations was calculated by subtracting two times the adsorption energy of a monomer $E_{ad}^{monomer}$ from the adsorption energy of a dimer E_{ad}^{dimer}:

$$E_{int} = E_{ad}^{dimer} - 2 \cdot E_{ad}^{monomer} \tag{3}$$

We refer here to the chapter on adsorption energies in the Supporting Information, where the adsorption energies calculated with Equation (S3) for the surfaces Mg(0001), Mg(10$\bar{1}$0), and Mg(10$\bar{1}$1) are listed in Table S6.

Furthermore, we determined the Ehrlich-Schwoebel barrier E_{ES} for all step-down diffusion processes.[58–60] E_{ES} corresponds to the energy barrier that a descending atom must overcome in addition to the terrace self-diffusion barrier and was calculated by subtracting the terrace self-diffusion barrier $E_a^{for(terrace)}$ from the activation barrier of the step-down process $E_a^{for(stepdown)}$:

$$E_{ES} = E_a^{for\ (step-down)} - E_a^{for\ (terrace)} \tag{4}$$

The reaction rate $k_{@RT}$ at room temperature ($T = 293.15$ K) was calculated for each diffusion process by means of transition state theory as given by the Arrhenius equation:

$$k_{@RT} = \nu \cdot \exp\left(-\frac{E_a}{k_B T}\right) \tag{5}$$

where the pre-exponential factor ν was determined based on the Einstein approximation[61] with the vibrational frequencies of the diffusing adatom and the nearest surface atoms along the migration pathway for the initial and the transition state. E_a equals the activation energy and k_B is the Boltzmann constant.

The activation temperature T_a above which a process runs at the rate Γ was calculated with the equation used by Bogicevic et al.[62] Above T_a, a process is considered to be 'activated' following the formula:

$$T_a = \frac{E_a/k_B}{\ln(\nu/\Gamma)} \tag{6}$$

Since the rate Γ depends on the experimental growth rate, $\Gamma = 1\ s^{-1}$ was set, which is valid for a deposition rate of about 0.001–0.1 ML s^{-1}. As indicated, E_a corresponds to the activation energy, k_B to the Boltzmann constant, and ν to the pre-exponential factor. For some processes ($D_0 \leftrightarrow D_1$, $D_2 \leftrightarrow D_3$, $T_0 \leftrightarrow T_1$, $E_2 \leftrightarrow E_3$ (Ex.)) with very small activation barriers (< 0.02 eV), the pre-exponential factor could not be determined due to imaginary frequencies in the TS. In these cases, a value of $\nu = 5.0{\cdot}10^{12}\ s^{-1}$ was assumed, which corresponds to the average value of the pre-exponential factor, usually in the range between 10^{12}–$10^{13}\ s^{-1}$.

Acknowledgements

This work contributes to the research performed at CELEST (Center for Electrochemical Energy Storage Ulm-Karlsruhe) and was partly funded by the German Research Foundation (DFG) under Project-ID 390874152 (POLiS Cluster of Excellence). Further support through the DFG-research unit FOR-5065 (ELSICS) under Project-ID 428906592 is gratefully acknowledged. The authors acknowledge support by the state of Baden-Württemberg through bwHPC and the German Research Foundation (DFG) through grant no INST 40/575-1 FUGG (JUSTUS 2 cluster). Open Access funding enabled and organized by Projekt DEAL.

Conflict of Interest

The authors declare no conflict of interest.

Data Availability Statement

The data that support the findings of this study are openly available in zenodo at https://doi.org/10.5281/zenodo.6416097.

© 2022 The Authors. ChemSusChem published by Wiley-VCH GmbH

18648564, 2022, 14, Downloaded from https://chemistry-europe.onlinelibrary.wiley.com/doi/10.1002/cssc.202200414 by KIT der Universitat Ulm, Wiley Online Library on [21/10/2022]. See the Terms and Conditions (https://onlinelibrary.wiley.com/terms-and-conditions) on Wiley Online Library for rules of use; OA articles are governed by the applicable Creative Commons License

ChemSusChem
Research Article
doi.org/10.1002/cssc.202200414
Chemistry Europe
European Chemical Societies Publishing

18645641, 2022, 14, Downloaded from https://chemistry-europe.onlinelibrary.wiley.com/doi/10.1002/cssc.202200414 by KIT der Universitat Ulm, Wiley Online Library on [21/10/2022]. See the Terms and Conditions (https://onlinelibrary.wiley.com/terms-and-conditions) on Wiley Online Library for rules of use; OA articles are governed by the applicable Creative Commons License

Keywords: anodes · batteries · density functional theory · magnesium · surface growth •

[1] J. B. Goodenough, K.-S. Park, *J. Am. Chem. Soc.* **2013**, *135*, 1167–1176.
[2] J. B. Goodenough, *Nat. Electron.* **2018**, *1*, 204.
[3] M. Armand, J.-M. Tarascon, *Nature* **2008**, *451*, 652–657.
[4] A. Manthiram, *Nat. Commun.* **2020**, *11*, 1550.
[5] A. Manthiram, *ACS Cent. Sci.* **2017**, *3*, 1063–1069.
[6] M. Fichtner, *Magnesium Batteries: Research and Applications*, Royal Society of Chemistry, Cambridge, **2019**, pp. 1–16.
[7] J. Muldoon, C. B. Bucur, T. Gregory, *Chem. Rev.* **2014**, *114*, 11683–11720.
[8] F. Ding, W. Xu, G. L. Graff, J. Zhang, M. L. Sushko, X. Chen, Y. Shao, M. H. Engelhard, Z. Nie, J. Xiao, X. Liu, P. V. Sushko, J. Liu, J. G. Zhang, *J. Am. Chem. Soc.* **2013**, *135*, 4450–4456.
[9] H. D. Yoo, I. Shterenberg, Y. Gofer, G. Gershinsky, N. Pour, D. Aurbach, *Energy Environ. Sci.* **2013**, *6*, 2265.
[10] J. Song, E. Sahadeo, M. Noked, S. B. Lee, *J. Phys. Chem. Lett.* **2016**, *7*, 1736–1749.
[11] D. Li, Y. Yuan, J. Liu, M. Fichtner, F. Pan, *J. Magnesium Alloys* **2020**, *8*, 963–979.
[12] I. Shterenberg, M. Salama, Y. Gofer, E. Levi, D. Aurbach, *MRS Bull.* **2014**, *39*, 453–460.
[13] Z. Liang, C. Ban, *Angew. Chem. Int. Ed.* **2021**, *60*, 11036–11047.
[14] S.-B. Son, T. Gao, S. P. Harvey, K. X. Steirer, A. Stokes, A. Norman, C. Wang, A. Cresce, K. Xu, C. Ban, *Nat. Chem.* **2018**, *10*, 532–539.
[15] A. Wang, S. Kadam, H. Li, S. Shi, Y. Qi, *npj Comput. Mater.* **2018**, *4*, 15.
[16] M. Matsui, *J. Power Sources* **2011**, *196*, 7048–7055.
[17] R. Davidson, A. Verma, D. Santos, F. Hao, C. Fincher, S. Xiang, J. Van Buskirk, K. Xie, M. Pharr, P. P. Mukherjee, S. Banerjee, *ACS Energy Lett.* **2019**, *4*, 375–376.
[18] P. Bonnick, J. Muldoon, *Adv. Funct. Mater.* **2020**, *30*, 1–15.
[19] C. M. MacLaughlin, *ACS Energy Lett.* **2019**, *4*, 572–575.
[20] A. Hagopian, M.-L. Doublet, J.-S. Filhol, *Energy Environ. Sci.* **2020**, *13*, 5186–5197.
[21] E. Santos, W. Schmickler, *Angew. Chem. Int. Ed.* **2021**, *60*, 5876–5881; *Angew. Chem.* **2021**, *133*, 5940–5945.
[22] M. Jäckle, A. Groß, *J. Chem. Phys.* **2014**, *141*, 174710.
[23] M. Jäckle, K. Helmbrecht, M. Smits, D. Stottmeister, A. Groß, *Energy Environ. Sci.* **2018**, *11*, 3400–3407.
[24] D. Gaissmaier, D. Fantauzzi, T. Jacob, *J. Chem. Phys.* **2019**, *150*, 041723.
[25] D. Gaissmaier, M. Borg, D. Fantauzzi, T. Jacob, *ChemSusChem* **2020**, *13*, 771–783.
[26] G. Wulff, *Z. Kristallogr.* **1901**, *34*, 449–530.
[27] A. C. T. van Duin, S. Dasgupta, F. Lorant, W. A. Goddard, *J. Phys. Chem. A* **2001**, *105*, 9396–9409.
[28] K. Chenoweth, A. C. T. van Duin, W. A. Goddard, *J. Phys. Chem. A* **2008**, *112*, 1040–1053.
[29] L. Vitos, A. V. Ruban, H. L. Skriver, J. Kollár, *Surf. Sci.* **1998**, *411*, 186–202.
[30] A. Kopač Lautar, D. Kopač, T. Rejec, T. Bančič, R. Dominko, *Phys. Chem. Chem. Phys.* **2019**, *21*, 2434–2442.
[31] R. Tran, Z. Xu, B. Radhakrishnan, D. Winston, W. Sun, K. A. Persson, S. P. Ong, *Sci. Data* **2016**, *3*, 160080.
[32] D. P. Ji, Q. Zhu, S. Q. Wang, *Surf. Sci.* **2016**, *651*, 137–146.
[33] C. Kittel, *Introduction to Solid State Physics*, 8th ed., Wiley, New York, **2004**.
[34] J.-J. Tang, X.-B. Yang, L. OuYang, M. Zhu, Y.-J. Zhao, *J. Phys. D* **2014**, *47*, 115305.
[35] C. G. Johansen, H. Huang, T. M. Lu, *Comput. Mater. Sci.* **2009**, *47*, 121–127.
[36] H. Chu, H. Huang, J. Wang, *Sci. Rep.* **2017**, *7*, 5167.
[37] A. Hagopian, D. Kopač, J.-S. Filhol, A. Kopač Lautar, *Electrochim. Acta* **2020**, *353*, 136493.
[38] B. J. Keene, *Int. Mater. Rev.* **1993**, *38*, 157–192.
[39] I. T. Røe, S. M. Selbach, S. K. Schnell, *J. Phys. Chem. Lett.* **2020**, 2891–2895.
[40] M. Alcántara Ortigoza, M. Aminpour, T. S. Rahman, *Phys. Rev. B* **2015**, *91*, 115401.
[41] M. Andersen, C. Panosetti, K. Reuter, *Front. Chem.* **2019**, *7*, 1–24.
[42] W. K. Burton, N. Cabrera, F. C. Frank, *Phil. Trans. R. Soc. A* **1951**, *243*, 299–358.
[43] Z. Zhang, M. G. Lagally, *Science* **1997**, *276*, 377–383.
[44] R. Stumpf, M. Scheffler, *Phys. Rev. B* **1996**, *53*, 4958–4973.
[45] T. P. Senftle, S. Hong, M. M. Islam, S. B. Kylasa, Y. Zheng, Y. K. Shin, C. Junkermeier, R. Engel-Herbert, M. J. Janik, H. M. Aktulga, T. Verstraelen, A. Grama, A. C. T. Van Duin, *npj Comput. Mater.* **2016**, *2*, 15011.
[46] G. Kresse, J. Furthmüller, *Phys. Rev. B* **1996**, *54*, 11169–11186.
[47] G. Kresse, J. Furthmüller, *Comput. Mater. Sci.* **1996**, *6*, 15–50.
[48] P. E. Blöchl, *Phys. Rev. B* **1994**, *50*, 17953–17979.
[49] D. Joubert, *Phys. Rev. B* **1999**, 59, 1758–1775.
[50] J. P. Perdew, K. Burke, M. Ernzerhof, *Phys. Rev. Lett.* **1996**, *77*, 3865–3868.
[51] J. Wellendorff, K. T. Lundgaard, A. Møgelhøj, V. Petzold, D. D. Landis, J. K. Nørskov, T. Bligaard, K. W. Jacobsen, *Phys. Rev. B* **2012**, *85*, 235149.
[52] H. J. Monkhorst, J. D. Pack, *Phys. Rev. B* **1976**, *13*, 5188–5192.
[53] G. Henkelman, H. Jónsson, *J. Chem. Phys.* **2000**, *113*, 9978–9985.
[54] G. Henkelman, B. P. Uberuaga, H. Jónsson, *J. Chem. Phys.* **2000**, *113*, 9901–9904.
[55] S. Smidstrup, A. Pedersen, K. Stokbro, H. Jónsson, *J. Chem. Phys.* **2014**, *140*, 214106.
[56] A. Hjorth Larsen et al., *J. Phys. Condens. Matter* **2017**, *29*, 273002.
[57] J. Rahm, P. Erhart, *J. Open Source Softw.* **2020**, *5*, 1944.
[58] G. Ehrlich, F. G. Hudda, *J. Chem. Phys.* **1966**, *44*, 1039–1049.
[59] R. L. Schwoebel, E. J. Shipsey, *J. Appl. Phys.* **1966**, *37*, 3682–3686.
[60] S. J. Liu, H. Huang, C. H. Woo, *Appl. Phys. Lett.* **2002**, *80*, 3295–3297.
[61] J. D. Head, *Int. J. Quantum Chem.* **1997**, *65*, 827–838.
[62] A. Bogicevic, J. Strömquist, B. I. Lundqvist, *Phys. Rev. Lett.* **1998**, *81*, 637–640.

Manuscript received: February 25, 2022
Revised manuscript received: March 29, 2022
Accepted manuscript online: March 30, 2022
Version of record online: May 18, 2022

© 2022 The Authors. ChemSusChem published by Wiley-VCH GmbH

ChemSusChem

Supporting Information

First-Principles Studies on the Atomistic Properties of Metallic Magnesium as Anode Material in Magnesium-Ion Batteries

Florian Fiesinger, Daniel Gaissmaier, Matthias van den Borg, and Timo Jacob*© 2022 The Authors. ChemSusChem published by Wiley-VCH GmbH. This is an open access article under the terms of the Creative Commons Attribution Non-Commercial NoDerivs License, which permits use and distribution in any medium, provided the original work is properly cited, the use is non-commercial and no modifications or adaptations are made.

Table of Contents

Theoretical section *2*

Bulk properties *3*

Surface properties *5*

Adsorption properties *6*

Diffusion properties *9*

References *30*

S1

Theoretical section

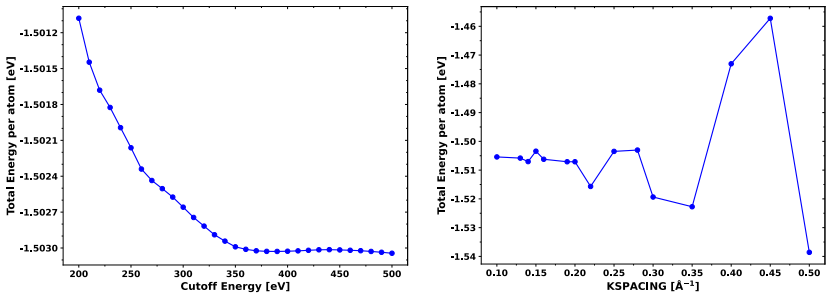

Figure S1. Convergence studies of the cutoff energy (≙ ENCUT Tag) and grid density of the k-points (≙ KSPACING Tag).

Table S1. Number of layers used for the calculation of surface energies.

Surface	Layers	Surface	Layers
Mg(0001)	7	Mg(11$\bar{2}$2)	24
Mg(10$\bar{1}$0)A/ Mg(10$\bar{1}$0)B	12	Mg(11$\bar{2}$0)	20
Mg(10$\bar{1}$1)	14	Mg(21$\bar{3}$1)	32
Mg(10$\bar{1}$2)A/ Mg(10$\bar{1}$2)B	18	Mg(22$\bar{4}$1)	40
Mg(21$\bar{3}$0)A/ Mg(21$\bar{3}$0)B	30	Mg(11$\bar{2}$1)	22
Mg(21$\bar{3}$2)	32	Mg(20$\bar{2}$1)	24

Table S2. Surface directions, number of layers and supercell used for the calculation of adsorption, dimer interaction, diffusion, and frequency properties. One layer consists of 2 Mg atoms for Mg(0001). The asterisk * indicates the use of vicinal slabs.

Surface	Property/Process	Direction	Layers	Supercell
Mg(0001)	Adsorption, Dimer interaction	[0001]	3	6×6
	Terrace, Dimer, Trimer			
	Kink, Inner-corner, Outer-corner ([$\bar{1}\bar{1}$20]-step)	[10$\bar{1}$6]*	20	6×1
	Kink, Inner-corner, Outer-corner ([11$\bar{2}$0]-step)	[10$\bar{1}\bar{6}$]*	20	6×1
	Step-edge, Step-vacancy, Step-down, Step-down (dimer), Upper-step ([$\bar{1}\bar{1}$20]-step)	[10$\bar{1}$8]*	26	4×1
	Step-edge, Step-vacancy, Step-down, Step-down (dimer), Upper-step ([11$\bar{2}$0]-step)	[10$\bar{1}\bar{8}$]*	26	4×1
Mg(10$\bar{1}$0)	Adsorption, Dimer interaction	[10$\bar{1}$0]	6	6×3
	Terrace			
Mg(10$\bar{1}$1)	Adsorption, Dimer interaction	[10$\bar{1}$1]	6	6×3
	Terrace, Dimer, Trimer			
	Step-edge, Step-down ([$\bar{1}$2$\bar{1}$0]A/B-step)	[30$\bar{3}$2]*	18	5×1
	Step-edge, Step-down ([1$\bar{2}$10]A/B-step)	[30$\bar{3}$4]*	21	5×1
	Step-edge, Step-down ([10$\bar{1}$2]-step)	[51$\bar{6}$5]*	34	3×1

Bulk properties

The bulk properties of magnesium, including lattice constants, binding energies, and bulk moduli, were calculated for the following crystal structures with the PBE and the BEEF-vdW functional: hexagonal-closed-packed (*hcp*), double-hexagonal-closed-packed (*dhcp*), body-centered-cubic (*bcc*), face-centered-cubic (*fcc*), simple cubic (*sc*), β-tungsten (*a15*) and diamond (*dia*). The calculated values for both functionals for all crystal structures and a comparison with experimentally obtained data are shown in Table S3. Magnesium crystallizes in accordance with experimental studies in a *hcp* structure under ambient conditions. The calculated cohesive energy of 1.50 eV·atom^{-1} (Equation (S1)) from the PBE functional is in almost perfect agreement with the experimental value (Table S3) and with other theoretical studies (Table S4). The BEEF-vdW functional slightly underestimates the cohesive energy, but it is within its estimated error. Moriarty *et al.* first predicted a phase transformation from the *hcp* to the *bcc* structure at around 50 GPa from generalized pseudopotential theory[1–3], which Olijnyk and Holzapfel later confirmed by X-ray diffraction (XRD).[4] This is contradicted by the study of Erandonea *et al.*, who assumed the *dhcp* instead of the *bcc* structure at high pressures and temperatures.[5] Moriarty *et al.* also predicted a second phase transformation from the *bcc* to the *fcc* structure at even higher pressures[2], which could not be observed experimentally.[6]

Table S3. Calculated and experimentally observed physical constants for different bulk phases of magnesium. The lattice constants a_0 and c_0 are given in Å, bulk moduli B_0 in GPa, and the cohesive energy E_{coh} (Equation (S1)) in eV·atom^{-1}. For the BEEF-vdW functional, the calculated standard deviation of the cohesive energy is given in parenthesis. The experimental results were taken from Kittel *et al.*[7] The influence of the zero-point vibrational energy E_{ZPVE} on the experimental values is given in parentheses. The values were adapted from Alchagirov *et al.* for a_0, c_0, and B_0 and calculated with Equation (S2) for E_{coh}.[8]

Bulk properties		This work		Other works
		PBE	BEEF-vdW	Experiment
hcp	a_0	3.18	3.19	3.21 (0.00)
	c_0	5.21	5.21	5.21 (0.00)
	B_0	36.5	37.1	35.4 (-0.04)
	E_{coh}	1.50	1.33 (0.27)	1.51 (0.04)
dhcp	a_0	3.19	3.18	
	c_0	10.43	10.43	
	B_0	36.1	36.7	
	E_{coh}	1.49	1.33	
bcc	a_0	3.57	3.58	
	B_0	35.3	35.4	
	E_{coh}	1.48	1.30 (0.28)	
fcc	a_0	4.52	4.52	
	B_0	35.9	36.66	
	E_{coh}	1.49	1.32 (0.27)	
sc	a_0	3.02	3.02	
	B_0	23.2	23.2	
	E_{coh}	1.12	0.94 (0.22)	
a15	a_0	5.72	5.72	
	B_0	34.7	35.1	

	E_{coh}	1.46	1.28 (0.27)	
dia	a_0	6.85	6.97	
	B_0	10.9	9.1	
	E_{coh}	0.73	0.56 (0.11)	

Table S4. Calculated (PBE/BEEF-vdW) and literature physical constants of the *hcp* bulk phase of magnesium. The lattice constants a_0 and c_0 are given in Å, bulk moduli B_0 in GPa and the cohesive energy E_{coh} in eV·atom^{-1}.

Bulk properties		a_0	c_0	B_0	E_{coh}	Code
This work	**PBE**	3.18	5.21	36.5	1.50	VASP
	BEEF-vdW	3.19	5.21	37.1	1.33	VASP
Other works	**PBE**[9]	3.19	5.18	-	1.51	VASP
	PBE[10]	3.19	5.18	-	1.50	VASP
	PBE[11]	3.22	5.12	-	1.50	VASP
	PW91[12]	3.21	5.16	35.5	1.45	Quantum Espresso
	PBE[12]	3.20	5.20	-	1.50	VASP
	PW91[13]	3.18	5.14	35.5	1.50	fhi96md
	PBE[14]	3.19	5.18	-	-	VASP
	LDA[14]	3.12	5.08	-	-	VASP
	PBE[15]	3.19	5.22	-	-	VASP
	PW91[15]	3.19	5.20	-	-	VASP
	PBE[16]	3.19	5.18	-	-	VASP
	Experiment[7]	3.21	5.21	35.6	1.51	

The cohesive energy E_{coh} is defined as the energy gain an isolated atom receives when it is embedded in a certain crystal structure. It was calculated by subtracting the energies of the isolated atoms E_{atom} from the energy of the bulk crystal structure E_{bulk}, divided by the total number of atoms N in the bulk structure:

$$E_{\mathrm{coh}} = -\frac{1}{N}(E_{\mathrm{bulk}} - N \cdot E_{\mathrm{atom}}) \quad \text{(S1)}$$

Bulk moduli were calculated based on the jellium equation of state.[17] In order to be able to compare the theoretical cohesive energy with the experimental reference, the zero-point vibrational energy E_{ZPVE} was estimated as follows:[8]

$$E_{\mathrm{ZPVE}} = \frac{9}{8} k_{\mathrm{B}} \theta_{\mathrm{D}} \quad \text{(S2)}$$

k_{B} corresponds to the Boltzmann constant and θ_{D} to the Debye temperature, which is 400 K for magnesium.[8]

Surface properties

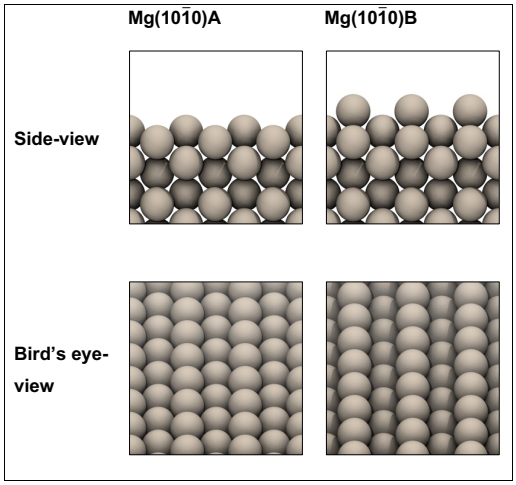

Figure S2. Representation of the surface terminations A and B of surface Mg(10$\bar{1}$0). The respective structures are shown in a side- and a bird's eye-view.

Table S5. Calculated (PBE/BEEF-vdW) and literature surface energies γ for low- and high-index surfaces of magnesium. The surface energy γ is given in meV·Å^{-2}. For the BEEF-vdW functional the calculated standard deviation of the surface energy is given in parenthesis.

γ	This work		Other works			
	PBE	BEEF-vdW	PBE	PBEsol	EAM	Experiment
Mg(0001)	33.9	38.7 (9)	34.6[9], 32.5[10], 32.5[11], 33.0[14], 31.8[18]	39.0[15], 35.0[16]	31.0[19]	51.0[20]
Mg(10$\bar{1}$0)A	40.2	44.9 (9)	39.9[9], 40.1[14], 37.4[18]		32.0[19]	
Mg(10$\bar{1}$1)	40.9	45.8 (8)	40.9[9], 46.4[14], 39.3[18]	45.9[15], 51.2[16]	31.1[19]	
Mg(10$\bar{1}$2)A	44.9	49.6 (10)	38.4[14], 43.7[18]			
Mg(21$\bar{3}$0)A	45.9	50.6 (10)	46.6[14], 43.7[18]			
Mg(10$\bar{1}$2)B	46.1	50.9 (10)				
Mg(21$\bar{3}$2)	46.7	51.3 (10)	46.2[18]			
Mg(11$\bar{2}$2)	46.8	51.3 (10)	48.4[14], 46.2[18]			
Mg(11$\bar{2}$0)	47.1	51.7 (10)	45.7[9], 44.9[18]	51.4[15], 34.3[16]		
Mg(21$\bar{3}$1)	47.1	51.7 (10)	45.6[18]			
Mg(22$\bar{4}$1)	47.9	52.5 (10)	46.8[18]			
Mg(11$\bar{2}$1)	48.7	53.0 (10)	48.1[9], 47.7[14], 47.4[18]			
Mg(20$\bar{2}$1)	48.8	53.4 (10)	48.1[18]			
Mg(21$\bar{3}$0)B	52.0	56.3 (11)		56.1[15]		
Mg(10$\bar{1}$0)B	55.5	59.4 (11)	53.7[11]	60.6[15], 38.5[16]		

Adsorption properties

The adsorption energy provides information about which positions are preferentially populated. Consequently, adsorption of Mg was studied on the surfaces present according to the Wulff shape (Mg(0001), Mg(10$\bar{1}$0)A, Mg(10$\bar{1}$1)) as well as, for the sake of completeness, on Mg(10$\bar{1}$0)B. The respective adsorption energies (PBE/BEEF-vdW) and available literature data (PBE) are summarized in Table S6. In addition, a schematic representation of all adsorption sites studied is provided in Figure S3.

The highest energy gain results from adsorption on the *bridge-bottom* position on Mg(10$\bar{1}$0)B (-1.64 eV), which is also the only stable adsorption site on this surface. The high adsorption energy seems logical since Mg(10$\bar{1}$0)B, the surface termination with the highest surface energy, aims for its stabilization by a transformation into the much more stable counterpart Mg(10$\bar{1}$0)A. In fact, this becomes even more evident when comparing the structural environments of the adsorption sites in Figure S3. Mg(10$\bar{1}$0)B is characterized by deep channels running parallel. Adsorption at the *bridge-bottom* position coordinates the adsorbate to six adjacent neighbors, more than in any other site, regardless of the surface. The second highest adsorption energy was found for Mg(10$\bar{1}$0)A at the *ontop-bottom* site (-1.00 eV), significantly lower than on Mg(10$\bar{1}$0)B. Mg(10$\bar{1}$0)A also exhibits channels, although they are not as deep as in Mg(10$\bar{1}$0)B, and the number of coordination partners of an adsorbate is reduced to five. Following closely behind with a 0.03 eV lower adsorption energy (-0.97 eV) is the *hollow* site on Mg(10$\bar{1}$1), where the adsorbate has a coordination number of four. These two sites have the highest adsorption energies for the surfaces present in the Wulff shape, indicating primary adsorption to occur on Mg(10$\bar{1}$0)A and Mg(10$\bar{1}$1).

There are two stable adsorption sites in the case of the most stable surface Mg(0001). Preferred adsorption occurs at the *fcc* site (-0.58 eV), which is energetically slightly favored compared to the *hcp* site (-0.56 eV). Thus, both adsorption energies are approximately 40% lower than the corresponding adsorption energies on Mg(10$\bar{1}$0)A and Mg(10$\bar{1}$1). Clarification may be found again by considering the morphology. Mg(0001) has a flat surface with a high packaging density. The coordination of the adsorbate occurs only to three surface atoms. Moreover, the energetically similar but unstable *bridge* site already allows the prediction of a low terrace self-diffusion barrier. At this point, we refer to the work of Lautar *et al.* in which potential energy surfaces (PES) were calculated, clearly showing the varying energy landscapes for Mg(0001), Mg(10$\bar{1}$0)A, and Mg(10$\bar{1}$1).[9] We also want to reference two EAM potentials for magnesium by Liu et *al*.[21] and Sun et *al*.[22] However, in the potential of Liu et *al*., only the *bridge* position on Mg(0001) is stable, which is not the case according to our DFT calculations.[19] We also want to point to the section Dimer and trimer self-diffusion on Mg(0001) and Mg(10$\bar{1}$1), which further clarifies why *fcc* sites are energetically favored over hcp sites, although this contradicts the nature of the *hcp* lattice, which should follow the ABABAB-stacking sequence.

All calculated adsorption energies are consistent with previously published theoretical results (on PBE level).[9,10,12,23] The error range for the BEEF-vdW functional varies between 0.10 and 0.31 eV, indicating a strong dependence on the chosen functional. However, all PBE results are within the BEEF-vdW standard deviation, and the energy ratios are equal for both functionals.

Table S6. The adsorption energies E_{ad} of an adsorbed Mg atom on Mg(0001), Mg(10$\bar{1}$0) and Mg(10$\bar{1}$1) calculated with Equation (S3) (PBE and BEEF-vdW) and literature data. All values are given in eV·atom^{-1}. For the BEEF-vdW functional, the calculated standard deviation of the adsorption energy E_{ad} is given in parenthesis. A schematic representation of all adsorption sites studied is given in Figure S3.

E_{ad}	Adsorption site	This work		Other works
		PBE	BEEF-vdW	PBE
Mg(0001)	fcc	-0.58	-0.48 (0.15)	-0.58[9], -0.59[10]
	hcp	-0.56	-0.47 (0.14)	-0.56[9], -0.57[10]
	bridge[a]	-0.56	-0.46 (0.14)	-0.57[10]
	ontop[a]	-0.45	-0.38 (0.12)	-0.44[10]
Mg(10$\bar{1}$0)A	ontop-bottom	-1.00	-0.86 (0.23)	-1.03[9]
	bridge-bottom[a]	-0.97	-0.84 (0.21)	
	ontop-up[a]	-0.46	-0.42 (0.10)	
	bridge-up[a]	-0.58	-0.51 (0.12)	
Mg(10$\bar{1}$0)B	ontop-bottom[a]	-1.23	-1.04 (0.25)	
	bridge-bottom	-1.64	-1.45 (0.31)	
	ontop-up[a]	-0.42	-0.38 (0.10)	
	bridge-up[a]	-0.52	-0.50 (0.12)	
Mg(10$\bar{1}$1)	hollow	-0.97	-0.83 (0.19)	-0.97[9]

[a] unstable configuration; fixed with constraints.

Adsorption energies E_{ad} were obtained by subtracting the energy of the pure surface E_{slab} plus the energy of an isolated magnesium atom $E_{\mathrm{Mg-atom}}$ from the energy of the relaxed system E_{tot} containing the slab with the adsorbed atom:

$$E_{\mathrm{ad}} = E_{\mathrm{tot}} - (E_{\mathrm{slab}} + E_{\mathrm{Mg-atom}}) \quad \text{(S3)}$$

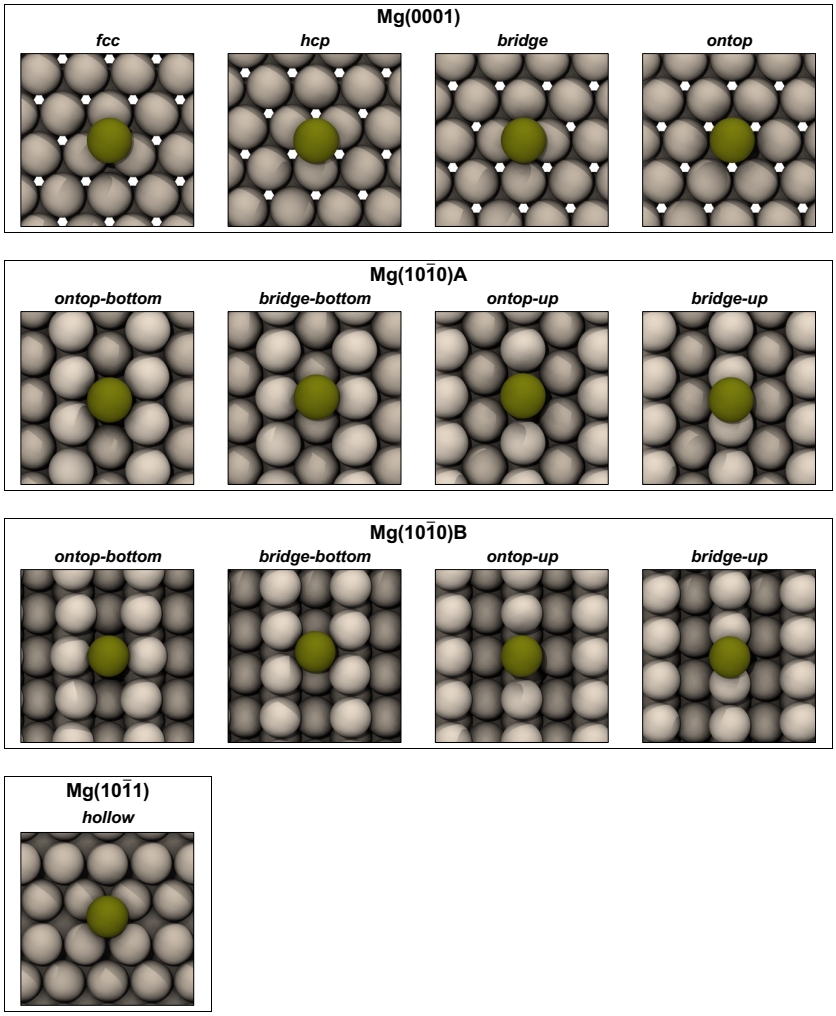

Figure S3. Schematic representation of the adsorption sites on Mg(0001), on the two surface terminations A and B of Mg(10$\bar{1}$0) and on Mg(10$\bar{1}$1).

Diffusion properties

Table S7. Pre-exponential factors ν, activation energies E_a, rate constants $k_{@RT}$, and activation temperatures T_a for forward and backward terrace self-diffusion processes from PBE calculations. The values are given in 10^{12} Hertz, eV, Hz, and K, respectively.

Terrace	Pathway	ν^{for}	E_a^{for}	$k_{@RT}^{for}$	T_a^{for}	ν^{rev}	E_a^{rev}	$k_{@RT}^{rev}$	T_a^{rev}
Mg(0001)	$fcc_0 \leftrightarrow hcp_1$	0.6	0.02	2.7E+11	9	1.3	0.01	1.0E+12	2
	$fcc_0 \leftrightarrow hcp_2$ (Ex.)	3.0	0.74	6.0E-01	298	4.1	0.72	1.6E+00	289
Mg(10$\bar{1}$0)	$ob_0 \leftrightarrow ob_1$	1.2	0.02	4.6E+11	10	1.2	0.02	4.6E+11	10
	$ob_0 \leftrightarrow ob_2$	1.2	0.42	6.8E+04	176	1.2	0.42	6.8E+04	176
	$ob_0 \leftrightarrow ob_2$ (Ex.)	0.7	0.46	7.3E+03	198	0.7	0.46	7.3E+03	198
Mg(10$\bar{1}$1)	$h_0 \leftrightarrow h_1$	7.2	0.30	5.2E+07	117	7.2	0.30	5.2E+07	117
	$h_0 \leftrightarrow h_1$ (Ex.)	4.7	0.59	3.0E+02	236	4.7	0.59	3.0E+02	236
	$h_0 \leftrightarrow h_2$	4.5	0.42	2.5E+05	168	7.8	0.42	4.3E+05	165

Table S8. Pre-exponential factors ν, activation energies E_a, rate constants $k_{@RT}$, and activation temperatures T_a for forward and backward terrace self-diffusion processes from BEEF-vdW calculations. The values are given in 10^{12} Hertz, eV, Hz, and K, respectively.

Terrace	Pathway	ν^{for}	E_a^{for}	$k_{@RT}^{for}$	T_a^{for}	ν^{rev}	E_a^{rev}	$k_{@RT}^{rev}$	T_a^{rev}
Mg(0001)	$fcc_0 \leftrightarrow hcp_1$	3.5	0.02 (0.02)	1.5E+12	8	3.4	0.01 (0.01)	2.6E+12	4
	$fcc_0 \leftrightarrow hcp_2$ (Ex.)	5.8	0.79 (0.23)	1.7E-01	312	9.6	0.77 (0.23)	5.3E-01	299
Mg(10$\bar{1}$0)	$ob_0 \leftrightarrow ob_1$	8.1	0.02 (0.04)	3.8E+12	8	8.1	0.02 (0.04)	3.8E+12	8
	$ob_0 \leftrightarrow ob_2$	6.2	0.35 (0.15)	6.7E+06	138	6.2	0.35 (0.15)	6.7E+06	138
	$ob_0 \leftrightarrow ob_2$ (Ex.)	4.8	0.47 (0.14)	3.7E+04	187	4.8	0.47 (0.14)	3.7E+04	187
Mg(10$\bar{1}$1)	$h_0 \leftrightarrow h_1$	5.8	0.27 (0.06)	1.2E+08	107	5.8	0.27 (0.06)	1.2E+08	107
	$h_0 \leftrightarrow h_1$ (Ex.)	1.7	0.62 (0.16)	3.4E+01	255	1.7	0.62 (0.16)	3.4E+01	255
	$h_0 \leftrightarrow h_2$	5.4	0.38 (0.08)	1.8E+06	150	4.7	0.38 (0.08)	1.6E+06	151

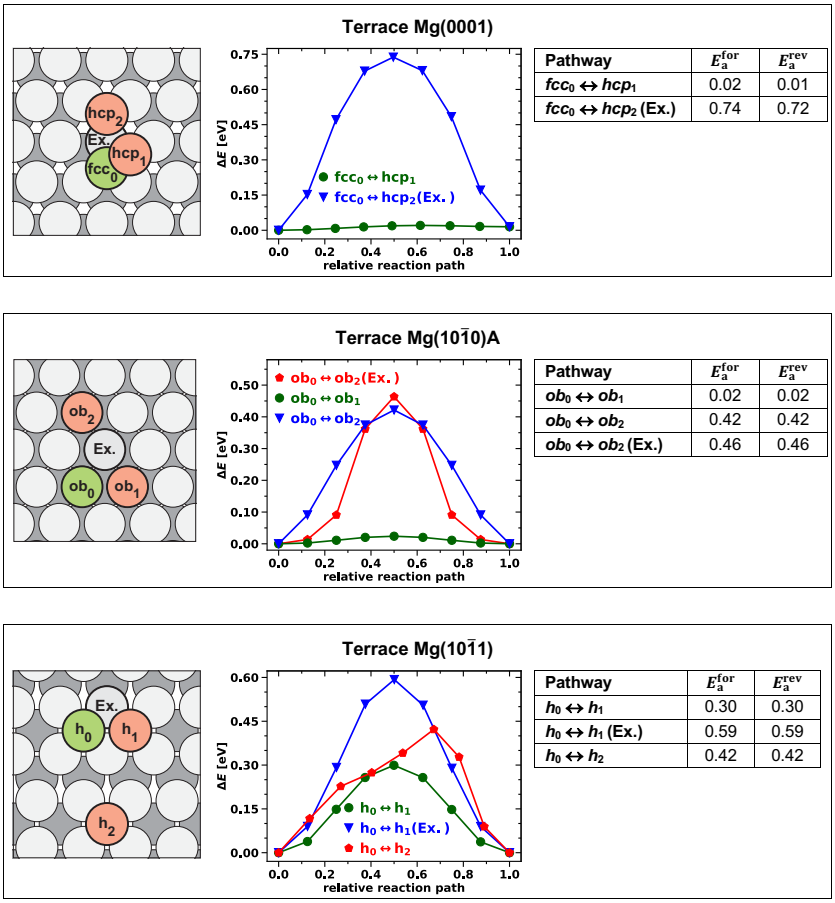

Pathway	E_a^{for}	E_a^{rev}
$fcc_0 \leftrightarrow hcp_1$	0.02	0.01
$fcc_0 \leftrightarrow hcp_2$ (Ex.)	0.74	0.72

Pathway	E_a^{for}	E_a^{rev}
$ob_0 \leftrightarrow ob_1$	0.02	0.02
$ob_0 \leftrightarrow ob_2$	0.42	0.42
$ob_0 \leftrightarrow ob_2$ (Ex.)	0.46	0.46

Pathway	E_a^{for}	E_a^{rev}
$h_0 \leftrightarrow h_1$	0.30	0.30
$h_0 \leftrightarrow h_1$ (Ex.)	0.59	0.59
$h_0 \leftrightarrow h_2$	0.42	0.42

Figure S4. Schematic representation, energy profile and PBE activation energies E_a of terrace self-diffusion processes on Mg(0001), Mg(10$\bar{1}$0), and Mg(10$\bar{1}$1). Green-colored atoms mark the initial, while red-colored atoms mark the final positions. The values are given in eV.

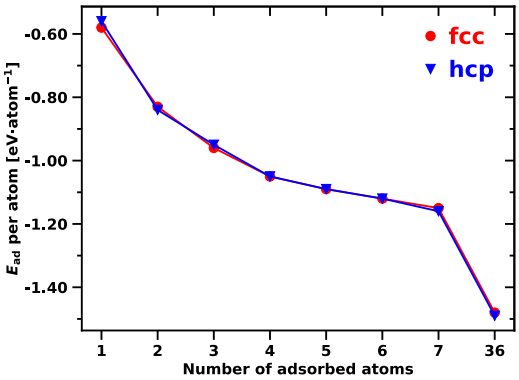

Figure S5. Adsorption energies per atom for islands of different sizes adsorbed in *fcc* and *hcp* positions on 6x6 Mg(0001). From a heptamer onwards, islands in *hcp* positions are more stable. Trimers, pentamers, and hexamers may form different conformations, with the most thermodynamically stable conformation used for the plot. 36 atoms correspond to a full monolayer.

Table S9. Adsorption energies per atoms for islands of different sizes absorbed in *fcc* and *hcp* positions on 6x6 Mg(0001). The last column shows the stacking fault energy $\Delta E_{\mathrm{ad}} = E_{\mathrm{ad},fcc} - E_{\mathrm{ad},hcp}$. Units are given in eV·atom^{-1}.

Island size	*fcc* E_{ad} per atom	*hcp* E_{ad} per atom	Stacking-fault energy ΔE_{ad}
1	-0.58	-0.56	-0.02
2	-0.83*	-0.84**	0.01
3	-0.96, -0.93	-0.95, -0.93	-0.01
4	-1.05	-1.05	0.00
5	-1.09, -1.07	-1.09. -1.07	0.00
6	-1.12, -1.10, -1.08	-1.12, -1.10, -1.09	0.00
7	-1.15	-1.16	0.01
36 (Full monolayer)	-1.48	-1.49	0.01

*** Both adsorbates are in *bridge*-like positions as shown in** Error! Reference source not found.**a.**

**** Adsorbates are in a *fcc* and a *hcp* position, respectively as shown in** Error! Reference source not found.**b.**

Table S10. Pre-exponential factors ν, activation energies E_a, rate constants $k_{@RT}$, and activation temperatures T_a for forward and backward various self-diffusion processes from PBE calculations on Mg(0001). The values are given in 10^{12} Hz, eV, Hz, and K respectively.

System	Path	Pathway	ν^{for}	E_a^{for}	$k_{@RT}^{for}$	T_a^{for}	ν^{rev}	E_a^{rev}	$k_{@RT}^{rev}$	T_a^{rev}
Dimer	Merge	$D_0 \leftrightarrow D_1$	-	0.00	-	0	-	0.49	-	194
		$D_2 \leftrightarrow D_3$	-	0.00	-	2	-	0.46	-	183
	Concerted	$CD_0 \leftrightarrow CD_1$	0.7	0.07	1.3E+11	30	2.2	0.07	4.1E+10	29
		$CD_0 \leftrightarrow CD_2$	0.4	0.01	5.4E+11	6	0.9	0.01	2.2E+11	5
Trimer	Merge	$T_0 \leftrightarrow T_1$	-	0.00	-	1	-	0.64	-	254
	Concerted	$CT_0 \leftrightarrow CT_1$	9.2	0.02	3.8E+10	7	3.8	0.12	4.5E+12	46
	Linear	$TL_0 \leftrightarrow TL_2$	2.3	0.01	1.1E+05	6	10.4	0.47	1.3E+12	180
		$TL_1 \leftrightarrow TL_2$	1.5	0.02	3.3E+04	7	2.3	0.46	7.3E+11	186
		$TL_3 \leftrightarrow TL_5$	1.5	0.00	5.3E+03	1	0.6	0.47	1.3E+12	201
		$TL_4 \leftrightarrow TL_5$	1.2	0.01	6.9E+03	3	0.6	0.46	9.1E+11	198
		$TL_6 \leftrightarrow TL_8$	0.7	0.01	1.8E+04	3	4.3	0.49	5.8E+11	194
		$TL_7 \leftrightarrow TL_8$	0.9	0.02	1.7E+04	8	4.0	0.49	4.1E+11	195
	Interchange	$TI_0 \leftrightarrow TI_1$	2.6	0.06	5.2E+10	24	39.8	0.17	2.5E+11	62
		$TI_0 \leftrightarrow TI_2$	0.4	0.07	1.3E+09	30	3.8	0.20	2.3E+10	81
Step-edge	[11$\bar{2}$0]-step	$S_0 \leftrightarrow S_1$	1.8	0.03	1.3E+09	12	19.0	0.70	1.1E+09	267
		$S_1 \leftrightarrow S_2$	6.4	0.22	1.3E+09	85	6.4	0.22	1.1E+09	85
	[$\bar{1}\bar{1}$20]-step	$S_3 \leftrightarrow S_4$	1.1	0.02	5.2E+09	7	5.5	0.63	5.2E+09	247
		$S_4 \leftrightarrow S_5$	1.9	0.15	5.2E+09	61	1.9	0.15	5.2E+09	61
Step-vacancy	[11$\bar{2}$0]-step	$SV_0 \leftrightarrow SV_1$	0.6	0.03	2.8E-07	12	19.4	1.15	2.0E+11	438
	[$\bar{1}\bar{1}$20]-step	$SV_2 \leftrightarrow SV_3$	0.4	0.02	3.9E-08	10	54.1	1.23	1.7E+11	451
Kink	[11$\bar{2}$0]-step	$K_0 \leftrightarrow K_1$	9.4	0.45	1.8E+05	174	2.8	0.17	2.9E+09	70
		$K_0 \leftrightarrow K_2$	21.4	0.91	4.1E-03	346	1.5	0.02	7.4E+11	7
		$K_0 \leftrightarrow K_3$	4.9	0.51	8.7E+03	202	3.4	0.29	3.5E+07	117
	[$\bar{1}\bar{1}$20]-step	$K_4 \leftrightarrow K_5$	8.3	0.46	8.7E+04	181	3.0	0.12	2.8E+10	48
		$K_4 \leftrightarrow K_6$	17.9	0.92	2.6E-03	350	0.4	0.01	3.2E+11	3
		$K_4 \leftrightarrow K_7$	5.4	0.56	1.1E+03	223	2.2	0.22	3.1E+08	92
Inner-corner	60° corner: [11$\bar{2}$0]-step	$IC_0 \leftrightarrow IC_1$	11.2	0.63	1.5E+02	244	4.7	0.10	9.7E+10	39
	60° corner: [$\bar{1}\bar{1}$20]-step	$IC_2 \leftrightarrow IC_3$	13.9	0.62	3.4E+02	237	4.1	0.08	2.0E+11	30
	120° corner	$IC_4 \leftrightarrow IC_5$	6.8	0.43	3.1E+05	168	5.2	0.18	3.8E+09	72
		$IC_4 \leftrightarrow IC_6$	5.6	0.43	2.1E+05	171	2.4	0.10	4.1E+10	42
Outer-corner	240° corner	$OC_0 \leftrightarrow OC_1$	0.7	0.29	1.2E+08	125	2.6	0.22	1.5E+12	88
		$OC_0 \leftrightarrow OC_1$ (Ex.)	8.6	0.41	9.3E+05	158	9.1	0.33	2.1E+07	128
	300° corner: [11$\bar{2}$0]-step	$OC_2 \leftrightarrow OC_3$ $OC_5 \leftrightarrow OC_4$	1.0	0.24	9.5E+07	99	4.0	0.00	3.5E+12	1
		$OC_3 \leftrightarrow OC_4$	1.3	0.03	3.4E+11	14	1.6	0.03	4.2E+11	14
		$OC_2 \leftrightarrow OC_5$ (Ex.)	8.0	0.32	3.1E+07	123	7.8	0.32	3.0E+07	123

	300° corner: [$\bar{1}\bar{1}$20]-step	$OC_6 \leftrightarrow OC_7$ $OC_8 \leftrightarrow OC_7$	0.2	0.20	7.2E+07	89	2.0	0.03	7.4E+11	10
		$OC_6 \leftrightarrow OC_8$ (Ex.)	1.5	0.16	2.7E+09	66	2.2	0.16	4.0E+09	65
Step-down	**[11$\bar{2}$0]-step**	$E_0 \leftrightarrow E_1$	2.0	0.09	1.5E+00	38	13.6	0.75	5.2E+10	289
		$E_0 \leftrightarrow E_1$ (Ex.)	2.4	0.01	7.0E+01	2	21.5	0.67	1.9E+12	253
	[$\bar{1}\bar{1}$20]-step	$E_2 \leftrightarrow E_3$	0.8	0.16	7.5E+00	67	8.5	0.70	1.6E+09	273
		$E_2 \leftrightarrow E_3$ (Ex.)	-	0.02	-	6	-	0.56	-	222
Step-down (dimer)	**[11$\bar{2}$0]-step**	$ED_0 \leftrightarrow ED_1$	6.9	0.58	2.1E+00	226	10.1	0.74	8.9E+02	286
		$ED_0 \leftrightarrow ED_1$ (Ex.)	4.4	0.21	2.7E+06	85	7.6	0.38	9.9E+08	147
	[$\bar{1}\bar{1}$20]-step	$ED_2 \leftrightarrow ED_3$	15.1	0.67	4.7E+00	256	2.6	0.68	4.6E+01	277
		$ED_2 \leftrightarrow ED_3$ (Ex.)	3.0	0.11	8.2E+09	44	3.2	0.15	4.1E+10	61
Upper-step	**[11$\bar{2}$0]-step**	$US_0 \leftrightarrow US_1$	1.7	0.02	3.1E+11	6	1.7	0.01	1.2E+12	2
		$US_1 \leftrightarrow US_2$	1.7	0.01	1.2E+12	4	0.8	0.03	3.1E+11	11
		$US_2 \leftrightarrow US_3$	0.9	0.02	4.9E+11	6	1.3	0.02	7.2E+11	6
	[$\bar{1}\bar{1}$20]-step	$US_4 \leftrightarrow US_5$	0.8	0.00	2.9E+11	1	2.9	0.03	2.1E+12	12
		$US_5 \leftrightarrow US_6$	2.2	0.00	2.1E+12	0	0.6	0.02	2.9E+11	7

S13

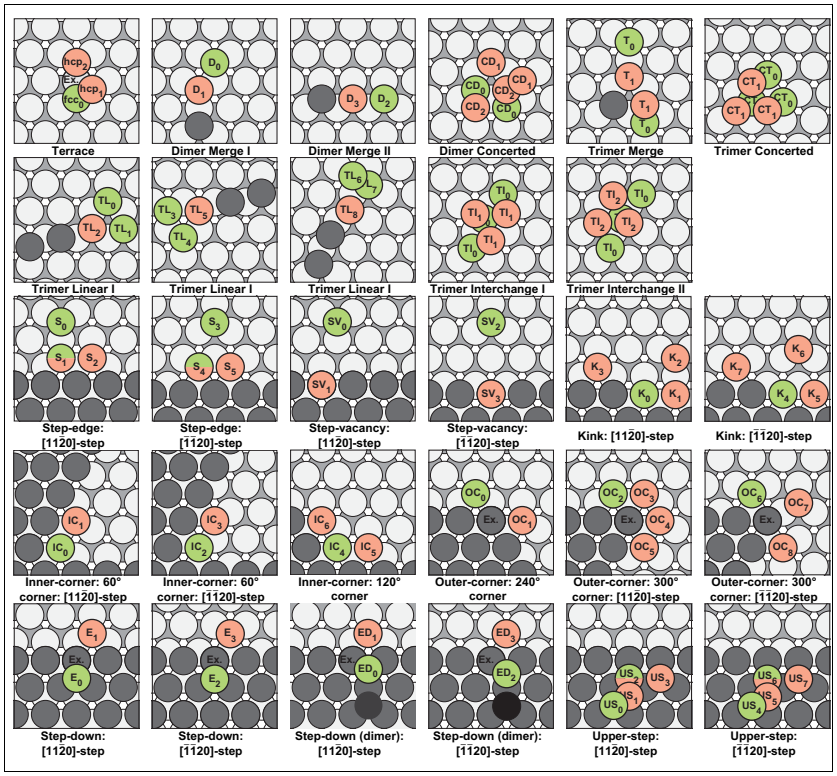

Figure S6. Schematic representation of all investigated diffusion pathways on Mg(0001).

Dimer: Merge 1

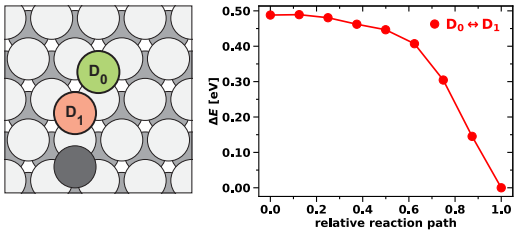

Pathway	E_a^{for}	E_a^{rev}
$D_0 \leftrightarrow D_1$	0.00	0.49

Dimer: Merge 2

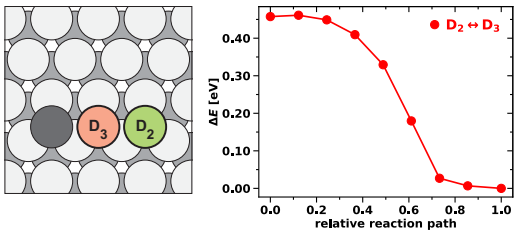

Pathway	E_a^{for}	E_a^{rev}
$D_2 \leftrightarrow D_3$	0.00	0.46

Dimer: Concerted

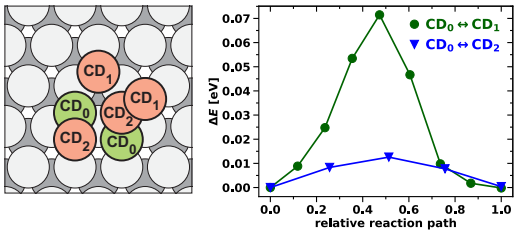

Pathway	E_a^{for}	E_a^{rev}
$CD_0 \leftrightarrow CD_1$	0.07	0.07
$CD_0 \leftrightarrow CD_2$	0.01	0.01

Trimer: Merge

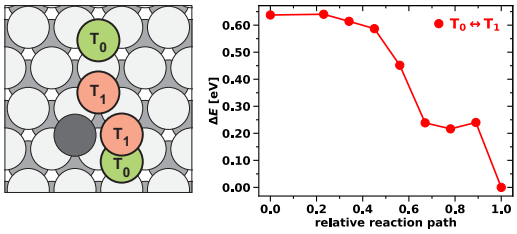

Pathway	E_a^{for}	E_a^{rev}
$T_0 \leftrightarrow T_1$	0.00	0.64

S15

Trimer: Concerted

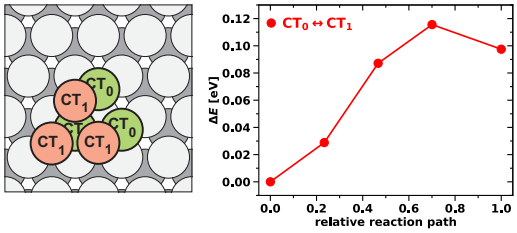

Pathway	E_a^{for}	E_a^{rev}
$CT_0 \leftrightarrow CT_1$	0.02	0.12

Trimer: Linear 1

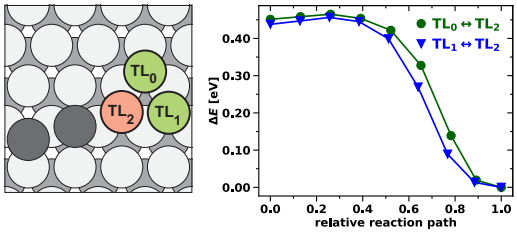

Pathway	E_a^{for}	E_a^{rev}
$TL_0 \leftrightarrow TL_2$	0.01	0.47
$TL_1 \leftrightarrow TL_2$	0.02	0.46

Trimer: Linear 2

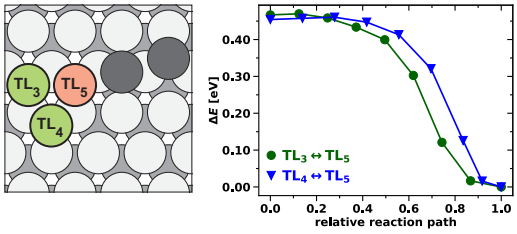

Pathway	E_a^{for}	E_a^{rev}
$TL_3 \leftrightarrow TL_5$	0.00	0.47
$TL_4 \leftrightarrow TL_5$	0.01	0.46

Trimer: Linear 3

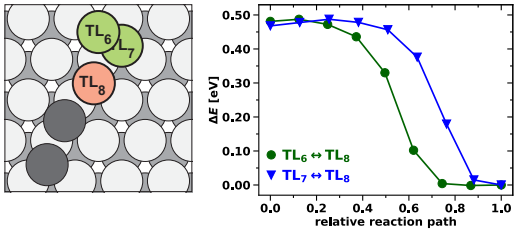

Pathway	E_a^{for}	E_a^{rev}
$TL_6 \leftrightarrow TL_8$	0.01	0.49
$TL_7 \leftrightarrow TL_8$	0.02	0.49

S16

Trimer: Interchange 1

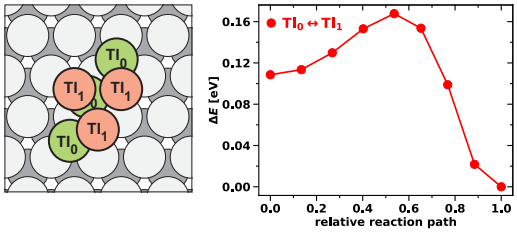

Pathway	E_a^{for}	E_a^{rev}
$Tl_0 \leftrightarrow Tl_1$	0.06	0.17

Trimer: Interchange 2

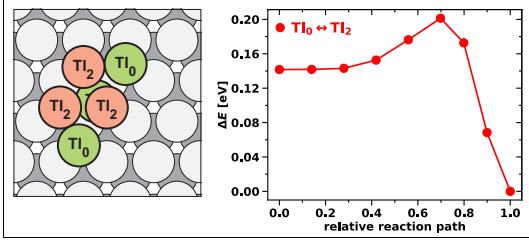

Pathway	E_a^{for}	E_a^{rev}
$Tl_0 \leftrightarrow Tl_2$	0.07	0.20

S17

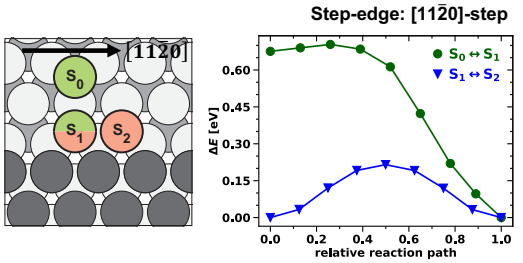

Pathway	E_a^{for}	E_a^{rev}
$S_0 \leftrightarrow S_1$	0.03	0.70
$S_1 \leftrightarrow S_2$	0.22	0.22

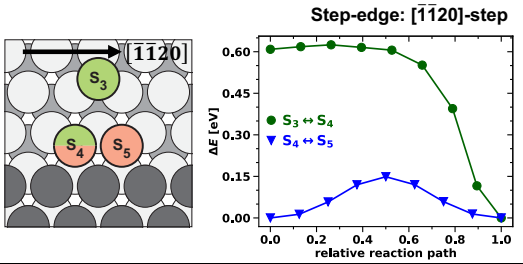

Pathway	E_a^{for}	E_a^{rev}
$S_3 \leftrightarrow S_4$	0.02	0.63
$S_4 \leftrightarrow S_5$	0.15	0.15

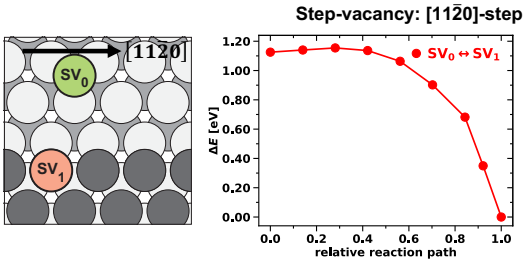

Pathway	E_a^{for}	E_a^{rev}
$SV_0 \leftrightarrow SV_1$	0.03	1.15

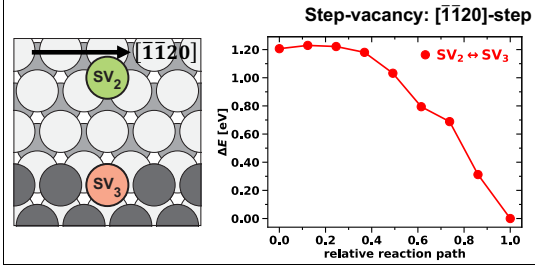

Pathway	E_a^{for}	E_a^{rev}
$SV_2 \leftrightarrow SV_3$	0.02	1.23

S18

Kink: [11$\bar{2}$0]-step

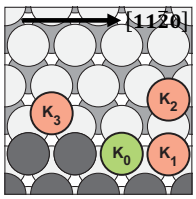

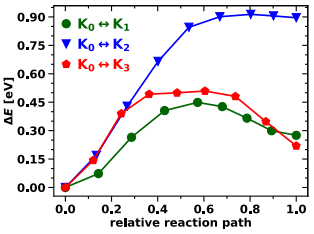

Pathway	E_a^{for}	E_a^{rev}
$K_0 \leftrightarrow K_1$	0.45	0.17
$K_0 \leftrightarrow K_2$	0.91	0.02
$K_0 \leftrightarrow K_3$	0.51	0.29

Kink: [$\bar{1}\bar{1}$20]-step

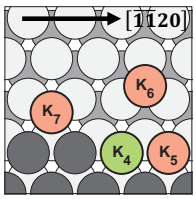

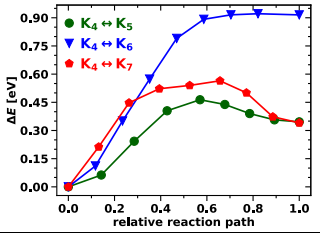

Pathway	E_a^{for}	E_a^{rev}
$K_4 \leftrightarrow K_5$	0.46	0.12
$K_4 \leftrightarrow K_6$	0.92	0.01
$K_4 \leftrightarrow K_7$	0.56	0.22

Inner-corner: 60° corner: [11$\bar{2}$0]-step

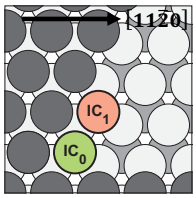

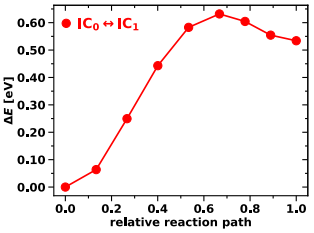

Pathway	E_a^{for}	E_a^{rev}
$IC_0 \leftrightarrow IC_1$	0.63	0.10

Inner-corner: 60° corner: [$\bar{1}\bar{1}$20]-step

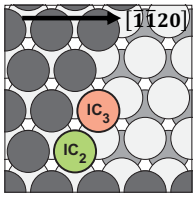

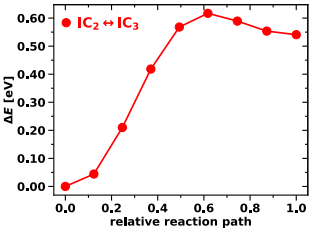

Pathway	E_a^{for}	E_a^{rev}
$IC_2 \leftrightarrow IC_3$	0.62	0.08

S19

Inner-corner: 120° corner

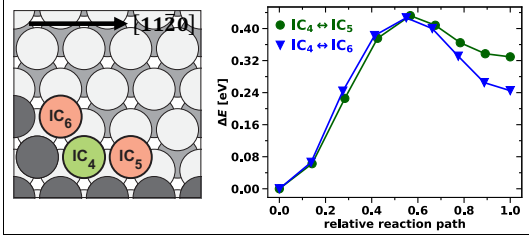

Pathway	E_a^{for}	E_a^{rev}
$IC_4 \leftrightarrow IC_5$	0.43	0.18
$IC_4 \leftrightarrow IC_6$	0.43	0.10

Outer-corner: 240° corner

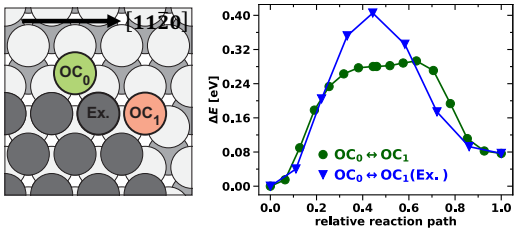

Pathway	E_a^{for}	E_a^{rev}
$OC_0 \leftrightarrow OC_1$	0.29	0.22
$OC_0 \leftrightarrow OC_1$ (Ex.)	0.41	0.33

Outer-corner: 300° corner: [11$\bar{2}$0]-step

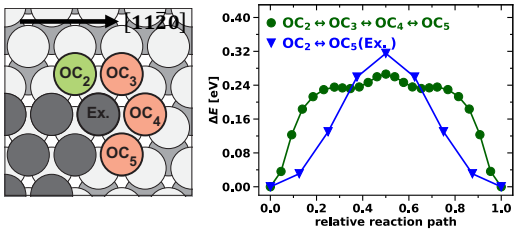

Pathway	E_a^{for}	E_a^{rev}
$OC_2 \leftrightarrow OC_3$ / $OC_5 \leftrightarrow OC_4$	0.24	0.00
$OC_3 \leftrightarrow OC_4$	0.03	0.03
$OC_2 \leftrightarrow OC_5$ (Ex.)	0.32	0.32

Outer-corner: 300° corner: [$\bar{1}\bar{1}$20]-step

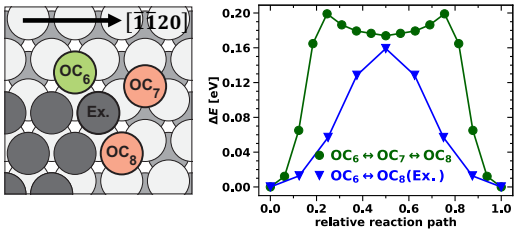

Pathway	E_a^{for}	E_a^{rev}
$OC_6 \leftrightarrow OC_7$ / $OC_8 \leftrightarrow OC_7$	0.20	0.03
$OC_6 \leftrightarrow OC_8$ (Ex.)	0.16	0.16

S20

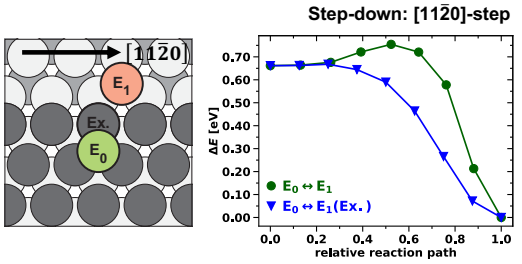

Pathway	E_a^{for}	E_a^{rev}
$E_0 \leftrightarrow E_1$	0.09	0.75
$E_0 \leftrightarrow E_1$ (Ex.)	0.01	0.67

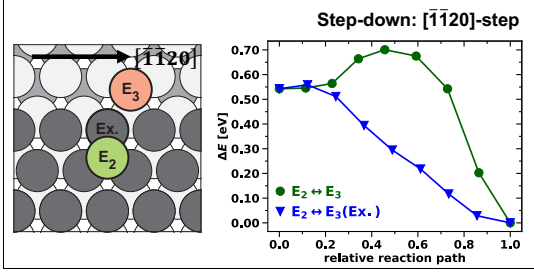

Pathway	E_a^{for}	E_a^{rev}
$E_2 \leftrightarrow E_3$	0.16	0.70
$E_2 \leftrightarrow E_3$ (Ex.)	0.02	0.56

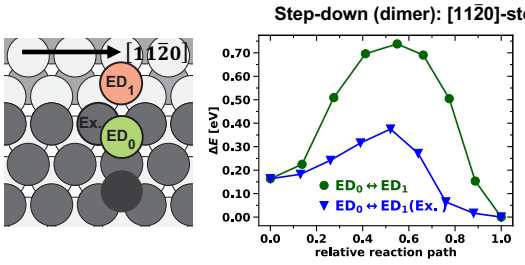

Pathway	E_a^{for}	E_a^{rev}
$ED_0 \leftrightarrow ED_1$	0.58	0.74
$ED_0 \leftrightarrow ED_1$ (Ex.)	0.21	0.38

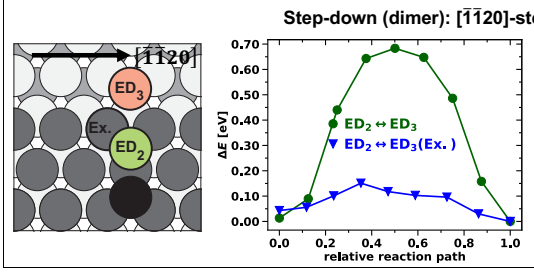

Pathway	E_a^{for}	E_a^{rev}
$ED_2 \leftrightarrow ED_3$	0.67	0.68
$ED_2 \leftrightarrow ED_3$ (Ex.)	0.11	0.15

S21

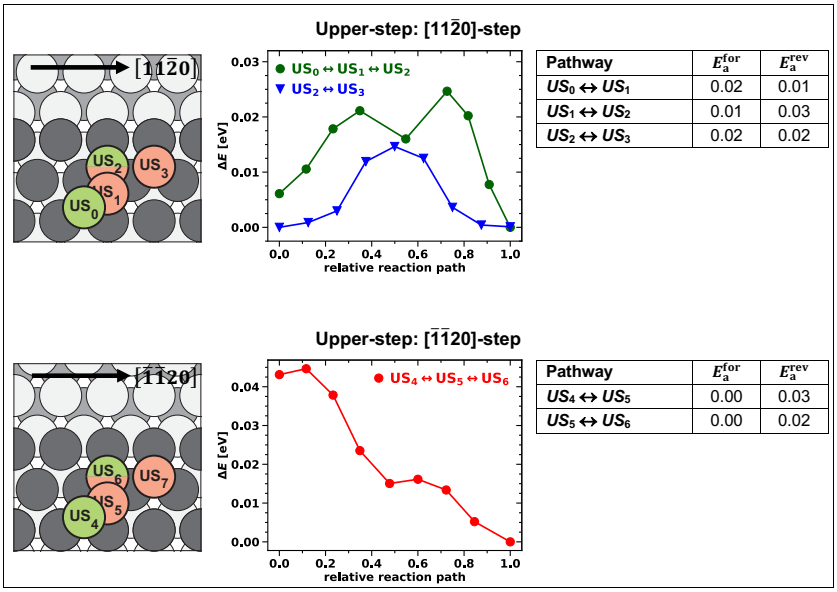

Pathway	E_a^{for}	E_a^{rev}
$US_0 \leftrightarrow US_1$	0.02	0.01
$US_1 \leftrightarrow US_2$	0.01	0.03
$US_2 \leftrightarrow US_3$	0.02	0.02

Pathway	E_a^{for}	E_a^{rev}
$US_4 \leftrightarrow US_5$	0.00	0.03
$US_5 \leftrightarrow US_6$	0.00	0.02

Figure S7. Schematic representation, energy profile and PBE activation energies E_a of self-diffusion processes studied on Mg(0001). Green-colored atoms mark the initial, while red-colored atoms mark the final positions. The values are given in eV.

Table S11. Pre-exponential factors ν, activation energies E_a, rate constants $k_{@RT}$, and activation temperatures T_a for forward and backward various self-diffusion processes from PBE calculations on Mg(10$\bar{1}$1). The values are given in 10^{12} Hertz, eV, Hz, and K, respectively.

System	Path	Pathway	ν^{for}	E_a^{for}	$k_{@RT}^{for}$	T_a^{for}	ν^{rev}	E_a^{rev}	$k_{@RT}^{rev}$	T_a^{rev}
Dimer	Merge	$d_0 \leftrightarrow d_1$	11.6	0.25	5.0E+08	98	23.6	0.58	2.6E+03	218
		$d_2 \leftrightarrow d_3$	4.8	0.19	2.8E+09	75	2.6	0.13	1.5E+10	53
		$d_3 \leftrightarrow d_1$	2.4	0.15	6.0E+09	61	10.6	0.51	2.0E+04	197
		$d_4 \leftrightarrow d_1$	10.2	0.37	5.2E+06	142	11.9	0.67	3.2E+01	259
	Concerted	$cd_0 \leftrightarrow cd_1$	19.0	0.54	1.0E+04	205	18.9	0.54	1.0E+04	205
Trimer	Merge	$t_0 \leftrightarrow t_1$	5.6	0.26	2.3E+08	103	13.1	0.58	1.2E+03	223
		$t_2 \leftrightarrow t_3$	7.8	0.19	4.6E+09	73	4.1	0.20	1.3E+09	82
		$t_3 \leftrightarrow t_1$	3.3	0.27	7.6E+07	109	11.0	0.54	5.7E+03	209
		$t_4 \leftrightarrow t_5$	8.1	0.31	3.5E+07	122	6.3	0.57	9.3E+02	225
		$t_5 \leftrightarrow t_1$	1.6	0.24	1.4E+08	98	4.9	0.28	8.4E+07	110
Step-edge	[$\bar{1}$2$\bar{1}$0]A-step	$s_0 \leftrightarrow s_1$	9.6	0.35	1.1E+07	134	9.9	0.59	6.8E+02	229
		$s_1 \leftrightarrow s_2$	2.7	0.13	1.8E+10	51	4.1	0.13	2.8E+10	50
	[$\bar{1}$2$\bar{1}$0]B-step	$s_3 \leftrightarrow s_4$	9.3	0.44	2.6E+05	171	6.8	0.73	2.3E+00	285
		$s_4 \leftrightarrow s_5$	3.7	0.16	8.0E+09	62	3.4	0.16	7.3E+09	62
	[1$\bar{2}$10]A-step	$s_6 \leftrightarrow s_7$	6.8	0.14	2.5E+10	56	0.1	0.18	1.1E+08	81
		$s_7 \leftrightarrow s_8$	1.0	0.01	6.3E+11	5	0.6	0.01	4.1E+11	5
	[1$\bar{2}$10]B-step	$s_9 \leftrightarrow s_{10}$	4.5	0.36	2.7E+06	144	15.6	0.95	7.5E-04	363
		$s_{10} \leftrightarrow s_{11}$	10.2	0.40	1.2E+06	156	11.3	0.40	1.3E+06	156
	[10$\bar{1}$2]-step	$s_{12} \leftrightarrow s_{13}$	18.5	0.18	1.5E+10	68	46.2	0.71	3.4E+01	260
		$s_{13} \leftrightarrow s_{14}$	6.8	0.45	1.3E+05	177	7.4	0.45	1.3E+05	176
Step-down	[$\bar{1}$2$\bar{1}$0]A-step	$e_0 \leftrightarrow e_1$	10.2	0.44	3.1E+05	169	10.3	0.67	3.8E+01	258
		$e_0 \leftrightarrow e_2$ (Ex.)	4.1	0.11	5.5E+10	44	3.9	0.34	6.0E+06	135
	[$\bar{1}$2$\bar{1}$0]B-step	$e_3 \leftrightarrow e_4$	8.3	0.43	3.3E+05	168	13.7	0.75	1.7E+00	288
		$e_3 \leftrightarrow e_4$ (Ex.)	5.4	0.26	1.8E+08	103	7.2	0.58	7.1E+02	228
	[1$\bar{2}$10]A-step	$e_5 \leftrightarrow e_6$	6.0	0.29	7.3E+07	113	2.4	0.04	4.9E+11	16
		$e_6 \leftrightarrow e_7$	3.5	0.12	3.3E+10	47	1.3	0.42	7.8E+04	175
		$e_5 \leftrightarrow e_7$ (Ex.)	9.9	0.47	8.6E+04	182	1.6	0.53	1.5E+03	217
	[1$\bar{2}$10]B-step	$e_8 \leftrightarrow e_9$	6.9	0.44	1.7E+05	174	11.0	0.96	3.6E-04	371
		$e_8 \leftrightarrow e_{10}$ (Ex.)	3.3	0.07	1.9E+11	29	8.4	0.59	6.5E+02	229
	[10$\bar{1}$2]-step	$e_{11} \leftrightarrow e_{12}$	18.7	0.38	5.5E+06	144	21.6	0.89	1.2E-02	336
		$e_{11} \leftrightarrow e_{12}$ (Ex.)	6.8	0.20	2.8E+09	77	12.5	0.71	9.4E+00	271

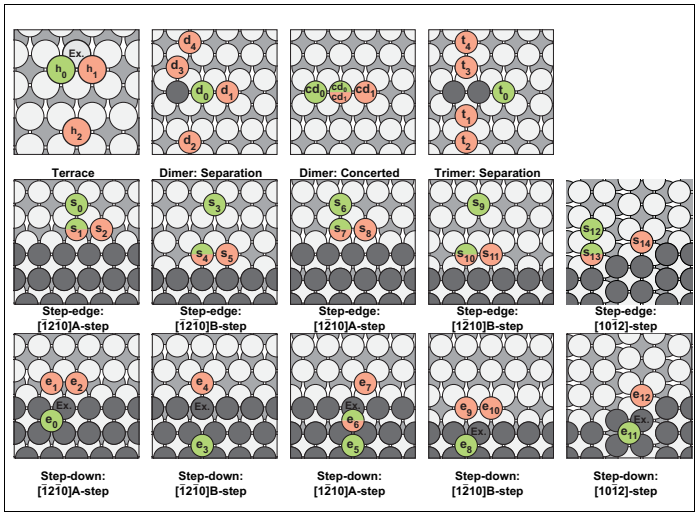

Figure S8. Schematic representation of all investigated diffusion pathways on Mg(10$\bar{1}$1).

Dimer: Merge

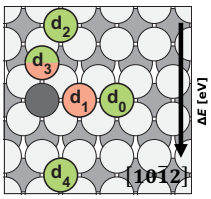

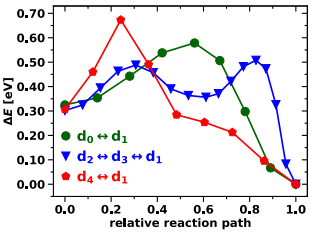

Pathway	E_a^{for}	E_a^{rev}
$d_0 \leftrightarrow d_1$	0.25	0.58
$d_2 \leftrightarrow d_3$	0.19	0.13
$d_3 \leftrightarrow d_1$	0.15	0.51
$d_4 \leftrightarrow d_1$	0.37	0.67

Dimer: Concerted

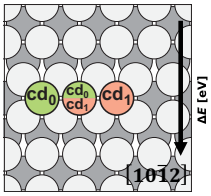

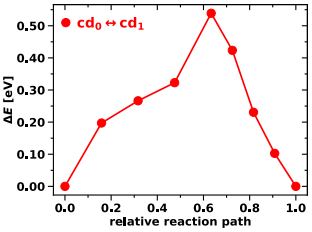

Pathway	E_a^{for}	E_a^{rev}
$cd_0 \leftrightarrow cd_1$	0.54	0.54

Trimer: Merge

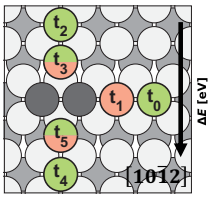

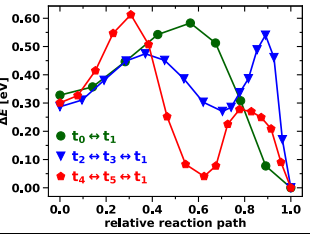

Pathway	E_a^{for}	E_a^{rev}
$t_0 \leftrightarrow t_1$	0.26	0.58
$t_2 \leftrightarrow t_3$	0.19	0.20
$t_3 \leftrightarrow t_1$	0.27	0.54
$t_4 \leftrightarrow t_5$	0.31	0.57
$t_5 \leftrightarrow t_1$	0.24	0.28

S25

Step-edge: [$\bar{1}2\bar{1}0$]A-step

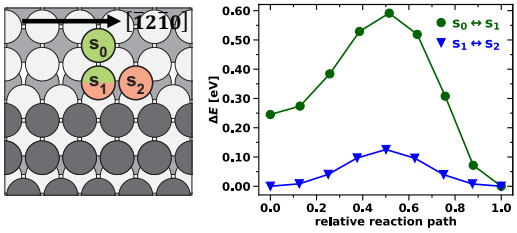

Pathway	E_a^{for}	E_a^{rev}
$s_0 \leftrightarrow s_1$	0.35	0.59
$s_1 \leftrightarrow s_2$	0.13	0.13

Step-edge: [$\bar{1}2\bar{1}0$]B-step

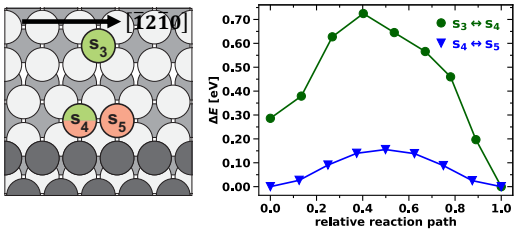

Pathway	E_a^{for}	E_a^{rev}
$s_3 \leftrightarrow s_4$	0.44	0.73
$s_4 \leftrightarrow s_5$	0.16	0.16

Step-edge: [1$\bar{2}$10]A-step

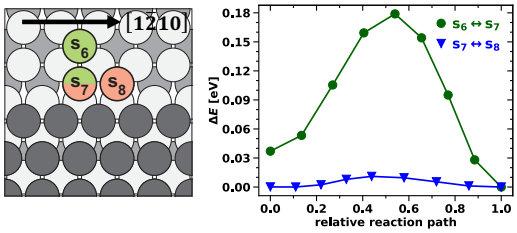

Pathway	E_a^{for}	E_a^{rev}
$s_6 \leftrightarrow s_7$	0.14	0.18
$s_7 \leftrightarrow s_8$	0.01	0.01

Step-edge: [1$\bar{2}$10]B-step

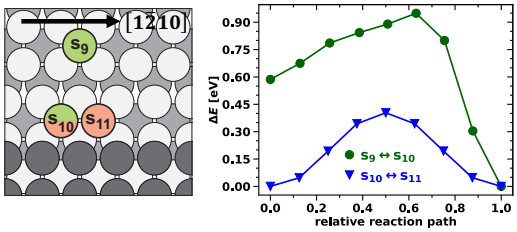

Pathway	E_a^{for}	E_a^{rev}
$s_9 \leftrightarrow s_{10}$	0.36	0.95
$s_{10} \leftrightarrow s_{11}$	0.40	0.40

S26

Step-edge: [10$\bar{1}$2]-step

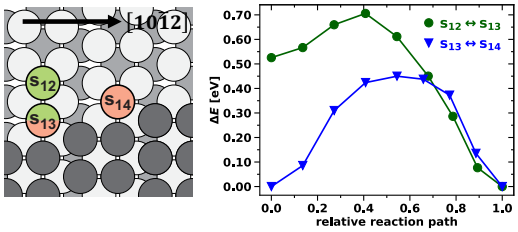

Pathway	E_a^{for}	E_a^{rev}
$s_{12} \leftrightarrow s_{13}$	0.18	0.71
$s_{13} \leftrightarrow s_{14}$	0.45	0.45

Step-down: [$\bar{1}$2$\bar{1}$0]A-step

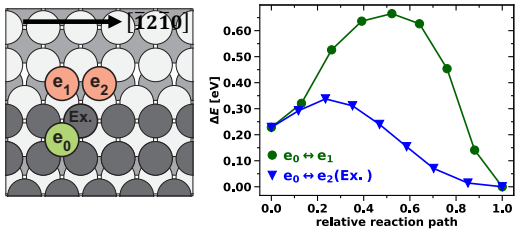

Pathway	E_a^{for}	E_a^{rev}
$e_0 \leftrightarrow e_1$	0.44	0.67
$e_0 \leftrightarrow e_2$ (Ex.)	0.11	0.34

Step-down: [$\bar{1}$2$\bar{1}$0]B-step

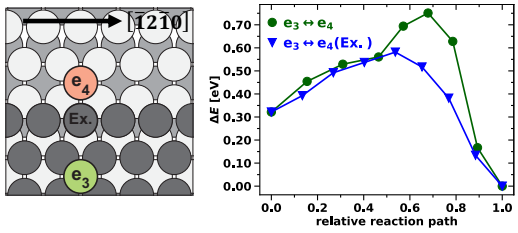

Pathway	E_a^{for}	E_a^{rev}
$e_3 \leftrightarrow e_4$	0.43	0.75
$e_3 \leftrightarrow e_4$ (Ex.)	0.26	0.58

Step-down: [1$\bar{2}$$\bar{1}$0]A-step

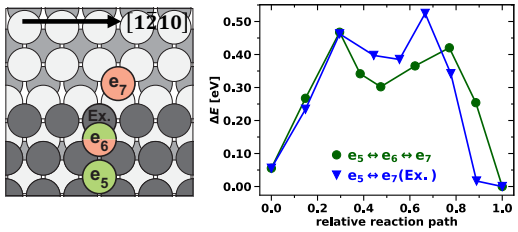

Pathway	E_a^{for}	E_a^{rev}
$e_5 \leftrightarrow e_6$	0.29	0.04
$e_6 \leftrightarrow e_7$	0.12	0.42
$e_5 \leftrightarrow e_7$ (Ex.)	0.47	0.53

S27

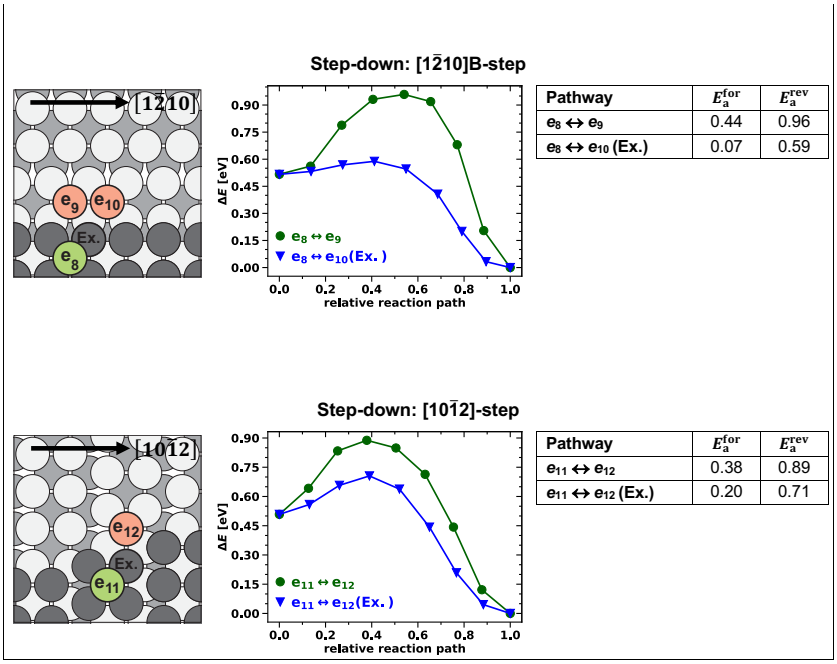

Pathway	E_a^{for}	E_a^{rev}
$e_8 \leftrightarrow e_9$	0.44	0.96
$e_8 \leftrightarrow e_{10}$ (Ex.)	0.07	0.59

Pathway	E_a^{for}	E_a^{rev}
$e_{11} \leftrightarrow e_{12}$	0.38	0.89
$e_{11} \leftrightarrow e_{12}$ (Ex.)	0.20	0.71

Figure S9. Schematic representation, energy profile and PBE activation energies E_a of self-diffusion processes studied on Mg(10$\bar{1}$1). Green-colored atoms mark the initial, while red-colored atoms mark the final positions. The values are given in eV.

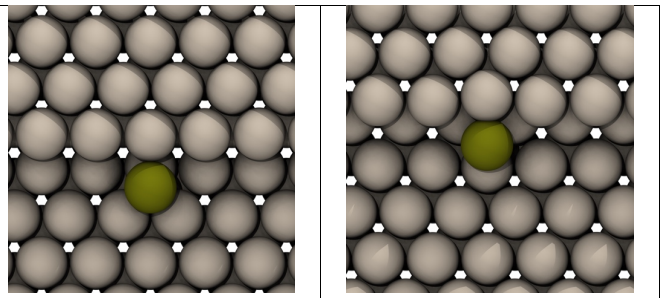

Step-edge: [11$\bar{2}$0]-step (TS) | Step-edge: [$\bar{1}\bar{1}$20]-step (TS)

Figure S10. Transition states of step-edge diffusion pathways along [11$\bar{2}$0]- and [$\bar{1}\bar{1}$20]-steps steps. In the TS of the [$\bar{1}\bar{1}$20]-step, the nearest neighbor atom in the edge row pulls slightly back, leaving a pocket for the diffusing atom (green) to settle in a stabilized *fcc*-like position.

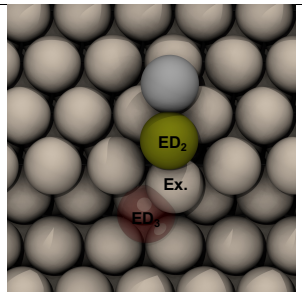

Figure S11. Transition state of step-down (dimer) diffusion pathway along the [$\bar{1}\bar{1}$20]-step. The second atom (gray) follows the diffusing atom (green) into the *fcc* position above the exchange atom. This maintains the dimer conformation until beyond the TS and lowers the activation energy of the process.

References

[1] J. A. Moriarty, A. K. McMahan, *Phys. Rev. Lett.* **1982**, *48*, 809–812.

[2] A. K. McMahan, J. A. Moriarty, *Phys. Rev. B* **1983**, *27*, 3235–3251.

[3] J. A. Moriarty, J. D. Althoff, Phys. Rev. B **1995**, *51*, 5609–5616.

[4] H. Olijnyk, W. B. Holzapfel, *Phys. Rev. B* **1985**, *31*, 4682–4683.

[5] D. Errandonea, Y. Meng, D. Husermann, T. Uchida, *J. Phys.: Condens. Matter* **2003**, *15*, 1277–1289.

[6] G. W. Stinton, S. G. MacLeod, H. Cynn, D. Errandonea, W. J. Evans, J. E. Proctor, Y. Meng, M. I. McMahon, *Phys. Rev. B* **2014**, *90*, 134105.

[7] C. Kittel, *Introduction to Solid State Physics*, *8th ed.*, John Wiley & Sons, New York, **2004**.

[8] A. B. Alchagirov, J. P. Perdew, J. C. Boettger, R. C. Albers, C. Fiolhais, *Phys. Rev. B* **2001**, *63*, 224115.

[9] A. Kopač Lautar, D. Kopač, T. Rejec, T. Bančič, R. Dominko, *Phys. Chem. Chem. Phys.* **2019**, *21*, 2434–2442.

[10] M. Jäckle, A. Groß, *J. Chem. Phys.* **2014**, *141*, 174710.

[11] D. Stottmeister, A. Groß, *ChemSusChem* **2020**, *13*, 3147–3153.

[12] M. Alcántara Ortigoza, M. Aminpour, T. S. Rahman, *Surf. Sci.* **2015**, *632*, 14–19.

[13] E. Wachowicz, A. Kiejna, *J. Phys.: Condens. Matter* **2001**, *13*, 10767–10776.

[14] D. P. Ji, Q. Zhu, S. Q. Wang, *Surf. Sci.* **2016**, *651*, 137–146.

[15] J.-J. Tang, X.-B. Yang, L. OuYang, M. Zhu, Y.-J. Zhao, *J. Phys. D: Appl. Phys.* **2014**, *47*, 115305.

[16] I. T. Røe, S. M. Selbach, S. K. Schnell, *J. Phys. Chem. Lett.* **2020**, 2891–2895.

[17] A. B. Alchagirov, J. P. Perdew, J. C. Boettger, R. C. Albers, C. Fiolhais, *Phys. Rev. B* **2003**, *67*, 026103.

[18] R. Tran, Z. Xu, B. Radhakrishnan, D. Winston, W. Sun, K. A. Persson, S. P. Ong, *Sci. Data* **2016**, *3*, 160080.

[19] C. G. Johansen, H. Huang, T. M. Lu, *Comput. Mater. Sci.* **2009**, *47*, 121–127.

[20] B. J. Keene, *Int. Mater. Rev.* **1993**, *38*, 157–192.

[21] X.-Y. Liu, J. B. Adams, F. Ercolessi, J. A. Moriarty, *Modell. Simul. Mater. Sci. Eng.* **1996**, *4*, 293–303.

[22] D. Y. Sun, M. I. Mendelev, C. A. Becker, K. Kudin, T. Haxhimali, M. Asta, J. J. Hoyt, A. Karma, D. J. Srolovitz, *Phys. Rev. B* **2006**, *73*, 024116.

[23] M. Alcántara Ortigoza, M. Aminpour, T. S. Rahman, *Phys. Rev. B* **2015**, *91*, 115401.

4.2 Development of an Mg/O ReaxFF Potential and Passivation of the Magnesium Anode by Oxygen Impurities in Magnesium-Ion Batteries

The following article is reprinted without changes from Florian Fiesinger, Daniel Gaissmaier, Matthias van den Borg, Julian Beßner, Adri C. T. van Duin, Timo Jacob: Development of an Mg/O ReaxFF Potential and Passivation of the Magnesium Anode by Oxygen Impurities in Magnesium-Ion Batteries, *ChemSusChem* **2023**, *16*, e202201821, published by Wiley-VCH GmbH as an open access article (https://doi.org/10.1002/cssc.202201821) under the terms of the Creative Commons Attribution License CC BY-NC-ND 4.0 (https://creativecommons.org/licenses/by-nc-nd/4.0/), which permits sharing, copying, and redistributing of the material in any medium or format.[27] ©2022 The authors.

Author Contributions: Florian Fiesinger performed all the calculations except of the force field training of the magnesium–magnesium interactions which was performed by Daniel Gaissmaier. Florian Fiesinger analyzed and discussed all results together with Daniel Gaissmaier, Matthias van den Borg, and Julian Beßner. Adri C. T. van Duin and Timo Jacob supervised the research. The initial manuscript draft was written by Florian Fiesinger and all authors commented on the manuscript.

Check for updates

ChemSusChem

Research Article
doi.org/10.1002/cssc.202201821

Chemistry Europe
European Chemical Societies Publishing

www.chemsuschem.org

Development of a Mg/O ReaxFF Potential to describe the Passivation Processes in Magnesium-Ion Batteries**

Florian Fiesinger,[a] Daniel Gaissmaier,[a, b, c] Matthias van den Borg,[a] Julian Beßner,[a] Adri C. T. van Duin,[d] and Timo Jacob*[a, b, c]

One of the key challenges preventing the breakthrough of magnesium-ion batteries (MIB) is the formation of a passivating boundary layer at the Mg anode. To describe the initial steps of Mg anode degradation by O_2 impurities, a Mg/O ReaxFF (force field for reactive systems) parameter set was developed capable of accurately modeling the bulk, surface, adsorption, and diffusion properties of metallic Mg and the salt MgO. It is shown that O_2 immediately dissociates upon first contact with the Mg anode (modeled as Mg(0001), Mg(10$\bar{1}$0)A, and Mg(10$\bar{1}$1)), heating the surface to several 1000 K. The high temperature assists the further oxidation and forms a rock salt interphase intersected by several grain boundaries. Among the Mg surface terminations, Mg(10$\bar{1}$0)A is the most reactive, forming an MgO layer with a thickness of up to 25 Å. The trained force field can be used to model the ongoing reactions in Mg–air batteries but also to study the oxidation of magnesium metal in general.

Introduction

The search for new energy storage technologies to promote electromobility and reduce global warming is one of the greatest challenges of our time. Magnesium-ion batteries (MIB) are attracting increasing attention as an alternative to conventional lithium-ion batteries (LIB) due to the unique properties of magnesium metal anodes, such as high volumetric capacity, low cost, and safe operation.[1–5] However, mass market adoption of MIBs is currently hindered by significant challenges. One of the biggest challenges is the formation of a passivating interface on the Mg surface which is impermeable to Mg cations and leads to battery failure.[6–8] Sun et al. have identified three reasons for Mg degradation in a recent review article.[9]

First, Mg has a higher charge density due to its bi-valency, which leads not only to stronger coordination with solvent molecules and salt anions but also facilitates solvent decomposition at the anode.[10] For example, Lu et al. have shown that the salt anion ClO_4 is chemically reduced at the Mg anode in carbonate-containing solvents, forming a solid-electrolyte interface (SEI) consisting of Mg-halides, MgO, $Mg(OH)_2$, $MgCO_3$, and $Mg(ROCO_2)_2$.[11]

Second, short circuits are induced by non-uniform Mg growth, which can be further subdivided into hemispherical,[12] porous,[13] or dendritic[14] growth morphologies.[9] Hemispherical 3D particles with different shapes have been detected in TFSI-based electrolytes as a function of the applied current density.[12] In an $Mg(TFSI)_2$ salt electrolyte with $MgCl_2$ as additive, continuous stripping and plating leads to fracturing and reformation of the SEI layer, resulting in large effective current densities at the respective fracture sites and inhomogeneous Mg deposition.[13] Through this mechanism, hemispherical deposits are further degraded to porous morphologies and trapped sediments that are irreversibly lost for cycling. The most extreme form of non-uniform Mg growth is the formation of dendrites, which occurs much less frequently at the Mg anode than in the Li equivalent. So far, dendrites have been detected only for a 0.5 mol dm^{-3} solution of MeMgCl in THF at a current density of 0.921 mA cm^{-2}.[14]

Third, corrosion of the Mg surface upon contact with ambient air leads to the formation of inorganic compounds such as MgO and $Mg(OH)_2$ at the interface.[9] During fabrication, transport, or storage of the Mg anode, contact with impurities such as O_2 or H_2O can hardly be avoided. In addition, traces of water in the electrolytes or oxygen residues under inert gas conditions can also lead to passivation.[15,16] According to Connell et al., impurities contribute even more to passivation than decomposition products of electrolytes.[17]

To study in detail the initial steps of the Mg anode passivation by oxygen impurities, we apply ReaxFF, a bond-order based reactive force field method capable of large-scale

[a] F. Fiesinger, Dr. D. Gaissmaier, M. van den Borg, J. Beßner, Prof. Dr. T. Jacob
Institute of Electrochemistry, Ulm University, Albert-Einstein-Allee 47, 89081 Ulm, Germany
E-mail: timo.jacob@uni-ulm.de
[b] Dr. D. Gaissmaier, Prof. Dr. T. Jacob
Helmholtz-Institute Ulm (HIU) for Electrochemical Energy Storage, Helmholtzstr. 11, 89081 Ulm, Germany
[c] Dr. D. Gaissmaier, Prof. Dr. T. Jacob
Karlsruhe Institute of Technology (KIT), P.O. Box 3640, 76021 Karlsruhe, Germany
[d] Prof. Dr. A. C. T. van Duin
Department of Mechanical and Nuclear Engineering, Pennsylvania State University, University Park, PA 16801, USA

[**] A previous version of this manuscript has been deposited on a preprint server (https://doi.org/10.5281/zenodo.7074790)

Supporting information for this article is available on the WWW under https://doi.org/10.1002/cssc.202201821

This publication is part of a collection of papers from contributors to the 7th Ertl Symposium on Catalysis in Electrochemistry (Gwangju, South Korea, October 26–29, 2022). Please visit chemsuschem.org/collections to view all contributions.

© 2022 The Authors. ChemSusChem published by Wiley-VCH GmbH. This is an open access article under the terms of the Creative Commons Attribution Non-Commercial NoDerivs License, which permits use and distribution in any medium, provided the original work is properly cited, the use is non-commercial and no modifications or adaptations are made.

© 2022 The Authors. ChemSusChem published by Wiley-VCH GmbH

ChemSusChem
Research Article
doi.org/10.1002/cssc.202201821
Chemistry Europe
European Chemical Societies Publishing

18645964, 2023, 3, Downloaded from https://chemistry-europe.onlinelibrary.wiley.com/doi/10.1002/cssc.202201821 by Cochrane Germany, Wiley Online Library on [11/05/2023]. See the Terms and Conditions (https://onlinelibrary.wiley.com/terms-and-conditions) on Wiley Online Library for rules of use; OA articles are governed by the applicable Creative Commons License

molecular dynamics simulations (cf. computational details).[53,54] ReaxFF has proven valuable for studying battery materials. For example, Islam et al. developed a ReaxFF potential for amorphous sulfur cathodes, allowing the group to model the volume expansion and associated strain hardening during lithiation.[18] In addition, the authors studied reductive decomposition pathways of ethylene carbonate (EC) using the eReaxFF method, which can explicitly describe electrons in a pseudoclassical manner.[19,20] The study demonstrated electron transfer from Li to EC to trigger ring-opening to form the Li^+/EC^- radical, and predicted possible radical termination products which were also detected experimentally. O'Hearn et al. trained a force field for Li/O systems with the goal of improving the description of brittle fractures in Li_2O slabs.[21] Although the force field was not directly trained for battery application, it should be able to describe oxidation processes at the Li anode. Recently, force field parameters for the study of lithium and sodium metal anodes were trained by Gaissmaier et al.[22] Ostadhossein et al. developed a Li/Si/O/Al force field to study lithium diffusion in silica anodes[23] and Bedrov et al. trained parameters for an ethylene carbonate description to investigate possible reactions of closed and open ring EC radical anions.[24] Moreover, Shin et al. investigated the ionic conductivity of Li in the Na super ionic conductor (NASICON)-type solid-state electrolyte $Li_{1-x}Al_xTi_{2-x}(PO_4)_3$.[25] A complete battery setup consisting of a sulfur cathode, a carbon nanotube anode and tetra(ethylene glycol) dimethyl ether as electrolyte was simulated by Islam et al.[26] One of the latest battery ReaxFF force fields was trained by Hossain et al. to study the influence of Li atoms and cations on organic compounds such as ethylene carbonate, ethyl methyl carbonate, vinylene carbonate, and $LiPF_6$ salts.[27] Thereby, different parameter sets were trained for the Li cation and the atom and its interchange was simulated by a Monte Carlo type replacement. The group found that only the neutral Li atom could trigger ring opening, while the Li cation was inactive.

The oxidation of magnesium is not only of central importance in battery science but also in automotive and aerospace research.[28] There are many studies trying to understand and explain magnesium corrosion in a metallurgical context.[29–32] Thus, Mg/O ReaxFF parameters could also be beneficial to these research areas and further promote corrosion studies.

Until now, no suitable Mg/O parameters have been available to describe the passivation at the Mg anode. So far, only Cheung et al. have trained force field parameters for magnesium hydride systems[33] or Iype et al. to describe $MgSO_4$ hydrates.[34] Additional parameters for Mg/O are available in a peptide force field developed by Zhu et al., whose training set was however limited to the bulk phases of Mg and MgO.[35] The parameters were recently reused by Yeon et al. to study magnesium aluminosilicate glasses, and the training set was extended to include additional bulk phases, heats of formation, and bond scans for the Mg/O description.[36]

The goal of the present study is to describe the initial steps of Mg anode degradation by oxygen impurities. To this end, we trained a reactive ReaxFF Mg/O force field that can accurately describe the properties of metallic Mg and MgO. The comprehensive training set included a variety of bulk, surface, and adsorption energies as well as diffusion barriers calculated at the level of density functional theory (DFT). In addition, we demonstrated the applicability of our force field by first completely oxidizing a Mg particle in a grand-canonical Monte Carlo (GCMC) simulation and then recrystallizing it into the thermodynamically stable rock salt structure by simulated thermal annealing at 2000 K in a subsequent molecular dynamics (MD) simulation.

Results and Discussion

The following section first compares the DFT training data with the force field optimization results. In this context, we discuss the performance and limitations of the obtained ReaxFF parameters. We subsequently demonstrate the functionality of the force field by oxidizing a Mg nanoparticle in a GCMC simulation and then recrystallizing it into the thermodynamically stable rock salt structure in a subsequent MD simulation. Afterwards, we simulate and discuss the first steps of Mg anode passivation. All fitted ReaxFF force field parameters for the Mg/O interactions are given in the Supporting Information.

Magnesium-magnesium interactions

The first milestone of ReaxFF parameter training for the Mg/Mg metal interactions was to reproduce the bulk properties of Mg. Therefore, lattice constants, cohesive energies [(Eq. (3)], and bulk moduli of the crystal phases hexagonal close-packed (hcp), face centered cubic (fcc), body centered cubic (bcc), β-tungsten type (a15), and simple cubic (sc) were introduced to the training set. Figure 1 and Table 1 compare the DFT training data and the results obtained with the fitted ReaxFF force field. We only trained bonding but excluded off-diagonal, valence, or torsion parameters for the Mg/Mg interactions, which means that first, the ratio (a_0/c_0) of the lattice constants a_0 and c_0 in the hcp unit cell always corresponds with $(8/3)^{1/2}$ to the ideal value of a closed-packed crystal, and second, the hcp and fcc cohesive energy will be identical.[37]

The lattice constants of the experimentally present[39] hcp crystal phase at ambient conditions are accurately reproduced by ReaxFF (a_0: both 3.18 Å, c_0: 5.20 Å *vs.* 5.21 Å), which is also true for the cohesive energy (both 1.50 eV) and bulk modulus (38.5 GPa *vs.* 36.5 GPa). The cohesive energy, in particular, is an important measure to describe bond strengths, and was therefore weighted more strongly during the training process; it varies at most by 0.01 eV for all crystal phases. This is also reflected in the relative stability between the crystal phases, which are in good agreement. ReaxFF slightly overestimates the bulk modulus for all crystal phases. This behavior is illustrated in the equation of state (EOS) curves presented in Figure 1 and is a result of an increase of the ReaxFF energy values at higher volumes.

In addition, we trained surface energies of the low index surfaces Mg(0001), Mg(10$\bar{1}$0)A, Mg(10$\bar{1}$0)B, Mg(10$\bar{1}$1), Mg(10$\bar{2}$0),

© 2022 The Authors. ChemSusChem published by Wiley-VCH GmbH

ChemSusChem
Research Article
doi.org/10.1002/cssc.202201821
Chemistry Europe
European Chemical Societies Publishing

18645964, 2023, 3, Downloaded from https://chemistry-europe.onlinelibrary.wiley.com/doi/10.1002/cssc.202201821 by Cochrane Germany, Wiley Online Library on [11/05/2023]. See the Terms and Conditions (https://onlinelibrary.wiley.com/terms-and-conditions) on Wiley Online Library for rules of use; OA articles are governed by the applicable Creative Commons License

Table 1. Lattice constants a_0 and c_0, bulk modulus B_0, and cohesive energies E_{coh} calculated with Equation (3) for the Mg bulk crystal phases hcp, fcc, bcc, a15, and sc determined in ReaxFF and DFT. For the hcp phase, the experimental constants of Kittel were adopted and are given for comparison.[39]

Structure	Method	a_0 [Å]	c_0 [Å]	B_0 [GPa]	E_{coh} [eV]
hcp – $P6_3/mmc$	ReaxFF	3.18	5.20	38.5	1.50
	DFT[38]	3.18	5.21	36.5	1.50
	experiment[39]	3.21	5.21	35.4	1.51
fcc – $Fm\bar{3}m$	ReaxFF	4.50	–	42.9	1.50
	DFT[38]	4.52	–	35.9	1.49
bcc – $Im\bar{3}m$	ReaxFF	3.53	–	42.4	1.49
	DFT[38]	3.57	–	35.3	1.48
a15 – $Pm\bar{3}n$	ReaxFF	5.72	–	41.2	1.45
	DFT[38]	5.72	–	34.7	1.46
sc – $Pm\bar{3}m$	ReaxFF	2.96	–	28.7	1.11
	DFT[38]	3.02	–	23.2	1.12

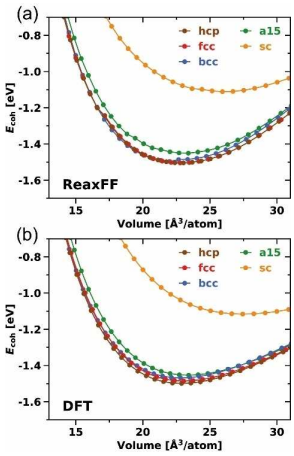

Figure 1. Equations of state (EOS) for bulk Mg crystal phases calculated with a) the trained ReaxFF force field and b) DFT.[38]

and Mg(10$\bar{2}$1), which were calculated using Equation (6). According to DFT calculations, Mg(0001) is the most stable Mg surface, followed by the surfaces Mg(10$\bar{1}$0)A and Mg(10$\bar{1}$1).[38] This trend is reproduced by the trained ReaxFF force field as illustrated in Table 2. The surface energy of Mg(0001) (31.6 meV Å^{-2} *vs.* 33.9 meV Å^{-2}) is reproduced most accurately with an error below 10%; however, this structure was also weighted most strongly during force field training. In general, the trained ReaxFF force field slightly underestimates all absolute surface energies.

The calculated surface fractions in the Wulff construction (Table 3) were only indirectly part of the training set via the surface energies and can therefore be seen as a validation measure. Mg(10$\bar{1}$1) has the largest area percentage (56.9% *vs.* 48.6%) in a Mg nanoparticle, followed by Mg(10$\bar{1}$0)A (23.9% *vs.* 27.9%) and Mg(0001) (19.2% *vs.* 23.7%). The absolute values deviate up to 10%, but the relative ratios agree. It is important to note that when studying Mg metal anodes, the surface Mg(10$\bar{1}$1) should be considered equally as Mg(0001).[38] Despite its higher surface energy compared to Mg(0001), it has by far the largest area percentage in the Wulff construction, which is correctly reproduced in ReaxFF.

We further included adsorption energies of atomic Mg on different sites on Mg(0001), Mg(10$\bar{1}$0)A, and Mg(10$\bar{1}$1) into the training set, calculated using Equation (7). Schematic representations of the underlying structures are shown in Figure S3. Adsorption energy results obtained with ReaxFF and DFT are compared in Table 4. It is noticeable that all adsorption energies for Mg(0001) are significantly overestimated by ≈0.2 eV. Moreover, according to DFT, adsorption at the fcc site is considered to be 0.02 eV more stable than at the hcp site.[38] However, it is impossible to distinguish between the two adsorption sites in ReaxFF without using angular terms or increasing the bond order cutoff, as already explained in the case of the cohesive energy of the hcp and fcc crystals. Besides, the relative stability sequence of the adsorption sites on Mg(0001) is well reproduced. For example, the fcc and meta-stable ontop positions differ by 0.13 eV in ReaxFF and DFT. Additionally, the relative absorption energy trends between different surfaces are

Table 2. Comparison of Mg surface energy results γ calculated with ReaxFF and DFT. The surface energy was obtained using Equation (6).

Surface	γ [meV Å^{-2}] ReaxFF	DFT[38]
Mg(0001)	31.6	33.9
Mg(10$\bar{1}$0)A	34.1	40.3
Mg(10$\bar{1}$0)B	46.4	55.5
Mg(10$\bar{1}$1)	34.3	40.9
Mg(11$\bar{2}$0)	39.9	47.1
Mg(11$\bar{2}$1)	41.4	48.7

Table 3. Calculated area fractions of Mg(0001), Mg(10$\bar{1}$0)A, and Mg(10$\bar{1}$1) in a Mg nanoparticle. The Wulff construction[40] and the area fractions were obtained using the Python package WulffPack from surface energies calculated with ReaxFF and DFT from Table 2.[41]

Surface	Area fraction [%] ReaxFF	DFT[38]
Mg(0001)	19.2	23.7
Mg(10$\bar{1}$0)A	23.9	27.9
Mg(10$\bar{1}$1)	56.9	48.6

© 2022 The Authors. ChemSusChem published by Wiley-VCH GmbH

ChemSusChem
Research Article
doi.org/10.1002/cssc.202201821
Chemistry Europe
European Chemical Societies Publishing

Table 4. Adsorption energies E_{ad} of a Mg adatom on Mg(0001), Mg(10$\bar{1}$0)A, and Mg(10$\bar{1}$1) calculated with ReaxFF and DFT using Equation (7).

Surface	Adsorption site	E_{ad} [eV] ReaxFF	DFT[38]
Mg(0001)	fcc	−0.80	−0.58
	hcp	−0.80	−0.56
	bridge[a]	−0.79	−0.56
	ontop[a]	−0.57	−0.45
Mg(10$\bar{1}$0)A	ontop-bottom	−1.06	−1.00
	bidge-bottom[a]	−1.05	−0.97
	ontop-up[a]	−0.35	−0.46
	bridge-up[a]	−0.58	−0.58
Mg(10$\bar{1}$1)	hollow	−1.03	−0.97

[a] Site not stable, relaxation of the adatoms was constrained in the *x* and *y* direction.

described well by ReaxFF. The ontop-bottom position on Mg(10$\bar{1}$0)A has the highest adsorption energy (−1.06 eV *vs.* −1.00 eV), followed by the hollow position on Mg(10$\bar{1}$1) (−1.03 eV *vs.* −0.97 eV), and the fcc site on Mg(0001) (−0.80 eV *vs.*−0.58 eV).

To obtain a smooth potential energy surface (PES), which is key to performing meaningful MD simulations, we added activation energies of selected self-diffusion processes to the training set, calculated using Equation (8). Our goal was to introduce a diverse spectrum of different magnesium conformations but also of transition states into the training set. For the latter, we included terrace self-diffusion barriers on Mg(0001), Mg(10$\bar{1}$0)A, and Mg(10$\bar{1}$1) (Figure 2, Table 5), but also additional diffusion processes of the terrace-step-kink (TSK) model[42] (like dimer, trimer, step-edge, kink, inner-corner, outer-corner, step-down on Mg(0001) and dimer, trimer on Mg(10$\bar{1}$1)). To keep this section compact, we discuss only the performance of the terrace self-diffusion barriers in the main text but refer to the Supporting Information for the additional diffusion processes (Figure S4, Table S1 for Mg(0001); Figure S5, Table S2 for Mg-(10$\bar{1}$1)). Overall, the trained force field reproduces the reference DFT activation energies of 32 of the 37 processes to an accuracy of $|\triangle E_a| \leq 0.2$ eV. As a necessary trade-off, the remaining 5 diffusion barriers, which include exchange terrace self-diffusion, dimer formation, or the step-down diffusion process on Mg-(0001), show larger deviations. The trained ReaxFF force field describes all hopping terrace self-diffusion processes within 0.1 eV accuracy but struggles to describe the corresponding exchange processes ($\triangle|E_a| \geq 0.3$ eV). In an exchange process, the diffusing atom takes the place of a surface atom, which in turn is pushed to its destination. However, since these processes have much higher barriers than the hopping processes, they are of less importance for an accurate description of surface mobility. In general, terrace self-diffusion on Mg(0001) (Figure 2a) has almost no barrier, which is also the case for diffusion within a channel on Mg(10$\bar{1}$0)A (Figure 2b).[38] In contrast, the activation energy for diffusion across a channel is several times higher, which is in the same order of magnitude as diffusion on Mg(10$\bar{1}$1) (Figure 2c).

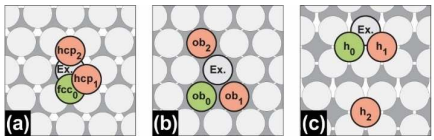

Figure 2. Overview and schematic representation of trained terrace self-diffusion processes on a) Mg(0001), b) Mg(10$\bar{1}$0)A, and c) Mg(10$\bar{1}$1). Green atoms mark the initial, while red atoms mark the final position. The label Ex. marks the exchanged surface atom. Reproduced from Ref. [38] Copyright (2022), with permission from Wiley-VCH.

Magnesium-oxygen interactions

Our training focuses on introducing EOS curves for the MgO crystal phases rock salt, wurtzite, zincblende, cesium chloride, and hcp to the training set for the Mg/O interactions. This selection of structures represents different coordination environments, bond distances, and geometries to provide a broad overview of the configurational space. Each EOS was constructed from eleven data points. The rock salt structure was weighted most strongly during training as this represents the preferred structure of MgO at ambient conditions.[43] Figure 3 compares the DFT reference EOS with the ReaxFF data, which are in excellent agreement. In particular, the transitions from rock salt to the hcp (22 Å^3 to 24 Å^3) and wurtzite (>24 Å^3) structures in the high volume region are well reproduced. The EOS for cesium chloride and rock salt exhibit a significant flattening in the ReaxFF method in general (Figure 3a) due to the exponentially decreasing bond order at long bond lengths. However, since the affected structures constitute high energy

Table 5. Activation energies E_a calculated with ReaxFF and DFT using Equation (8) for forward and backward terrace self-diffusion processes on Mg(0001), Mg(10$\bar{1}$0)A, and Mg(10$\bar{1}$1).[38]

Surface	Pathway	E_a^{for} [eV] ReaxFF	DFT[38]	$\lvert\Delta E_a^{for}\rvert$ [eV]	E_a^{rev} [eV] ReaxFF	DFT[38]	$\lvert\Delta E_a^{for}\rvert$ [eV]
Mg(0001)	$fcc_0 \leftrightarrow hcp_1$	0.01	0.02	0.01	0.01	0.01	0.00
	$fcc_0 \leftrightarrow hcp_2$ (Ex.)	1.20	0.74	0.46	1.19	0.72	0.47
Mg(10$\bar{1}$0)A	$ob_0 \leftrightarrow ob_1$	0.02	0.02	0.00	0.02	0.02	0.00
	$ob_0 \leftrightarrow ob_2$	0.49	0.42	0.07	0.49	0.42	0.07
	$ob_0 \leftrightarrow ob_2$ (Ex.)	0.78	0.46	0.32	0.78	0.46	0.32
Mg(10$\bar{1}$1)	$h_0 \leftrightarrow h_1$	0.39	0.30	0.09	0.39	0.30	0.09
	$h_0 \leftrightarrow h_1$ (Ex.)	1.00	0.59	0.41	1.00	0.59	0.41
	$h_0 \leftrightarrow h_2$	0.41	0.42	0.01	0.41	0.42	0.01

© 2022 The Authors. ChemSusChem published by Wiley-VCH GmbH

18645964, 2023, 3, Downloaded from https://chemistry-europe.onlinelibrary.wiley.com/doi/10.1002/cssc.202201821 by Cochrane Germany, Wiley Online Library on [11/05/2023]. See the Terms and Conditions (https://onlinelibrary.wiley.com/terms-and-conditions) on Wiley Online Library for rules of use; OA articles are governed by the applicable Creative Commons License

ChemSusChem
Research Article
doi.org/10.1002/cssc.202201821
Chemistry Europe
European Chemical Societies Publishing

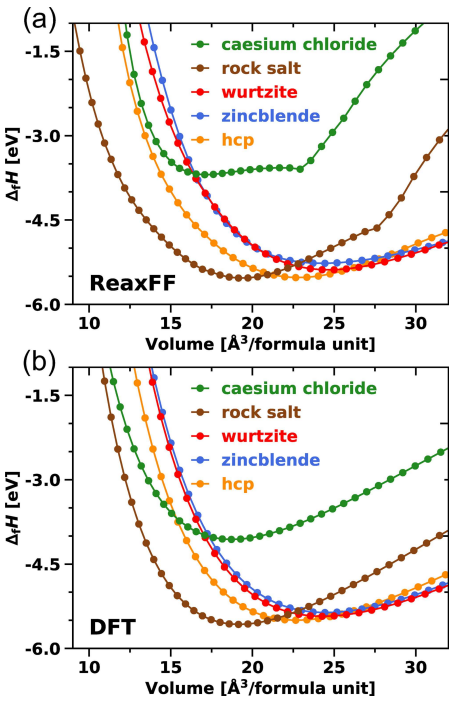

Figure 3. Equations of state (EOS) for MgO crystal phases calculated with a) the trained ReaxFF force field and b) DFT

phases that are not sampled in simulations of MgO at ambient conditions, the impact of this methodological limitation on the intended scope of simulations with the trained force field is deemed negligible. The corresponding indicator, the heat of formation $\triangle_f H$ [Eq. (4)], is reproduced for all structures with a relative error smaller than 10% as shown in Table 6. The rock salt structure is calculated to give the lowest heat of formation with −5.49 eV with the trained force field compared to −5.57 eV in DFT. Furthermore, the relative stability sequence of all crystal phases is correctly reproduced as well.

We incorporated the vacancy energy E_v [Eq. (5)] of an oxygen atom in the rock salt bulk structure with a low weighting in the force field training to use it as a validation measure for the obtained bonding, off-diagonal, and valance parameters. The vacancy energy calculated with the force field equals −6.82 eV and deviates very slightly from the DFT reference (−6.71 eV). The lattice constants and bulk moduli were only indirectly included in the force field training via the volume-energy data points. In particular, the lattice constants deviate from the DFT values by at most 0.02 Å for the rock salt, wurtzite, zincblende, and hcp structures. The bulk modulus for the energetically favored rock salt structure is best described with less than 2% error, while the other structures (wurtzite, zincblende, hcp) deviate around 5% to 12%. The cesium chloride structure, which is energetically unfavorable at ambient conditions, shows the largest deviation from the DFT reference data but constitutes the only experimentally confirmed structure, along with the rock salt phase.[43] However, the transition occurs at an extremely high pressure of 0.36 TPa.

Surface energy results γ were trained only for the stoichiometric surfaces MgO(100) and Mg(110), since it is difficult to calculate the surface energy for the non-stoichiometric surface MgO(111) (cf. Table 7). Either the stoichiometric structure has different terminations (oxygen-rich on the one side, magnesium-rich on the other side), or it is impossible to reference the symmetric structure against the bulk energy. Reuter and Scheffler stated in this context that "in a purely electrostatic model in which all oxygen ions would be in their bulk formal oxidation state, polar surfaces would be charged and should thus exhibit an infinite surface energy".[46] The surface energy results for MgO(100) and MgO(110) were calculated using Equation (6) and are shown in Table 7.

While the trained force field underestimates the DFT surface energy in case of all Mg surfaces, both MgO surfaces are overestimated as shown in Table 7. On the other hand, the experimental surface energy (64.9 meV Å^{-2}) for MgO(100) at 0 K

Table 6. Lattice constants a_0 and c_0, bulk moduli B_0, heats of formation $\triangle_f H$ and oxygen vacancy energies E_v for the MgO crystal phases rock salt, wurtzite, zincblende, hcp, and cesium chloride determined in ReaxFF and DFT. $\triangle_f H$ and E_v were calculated using Equations (4) and (5). The experimental constants for the rock salt structure were adopted from Refs. [44] and [45].

Structure	Method	a_0 [Å]	c_0 [Å]	B_0 [GPa]	$\triangle_f H$ [eV]	E_v [eV]
rock salt – $Fm\bar{3}m$	ReaxFF	4.26		157.5	−5.49	−6.82
	DFT	4.25		154.6	−5.57	−6.71
	experiment[44,45]	4.21		155.0	−6.24	
wurtzite – $P\,6_3mc$	ReaxFF	3.33	5.13	103.6	−5.34	
	DFT	3.31	5.11	117.4	−5.43	
zincblende – $F\,\bar{4}3m$	ReaxFF	4.60		122.4	−5.23	
	DFT	4.61		117.4	−5.36	
hcp – $P\,6_3/mmc$	ReaxFF	3.52	4.23	116.3	−5.48	
	DFT	3.52	4.23	128.0	−5.50	
cesium chloride – $Pm\bar{3}m$	ReaxFF	2.59		210.4	−3.68	
	DFT	2.65		142.2	−4.06	

© 2022 The Authors. ChemSusChem published by Wiley-VCH GmbH

18645964, 2023, 3, Downloaded from https://chemistry-europe.onlinelibrary.wiley.com/doi/10.1002/cssc.202201821 by Cochrane Germany, Wiley Online Library on [11/05/2023]. See the Terms and Conditions (https://onlinelibrary.wiley.com/terms-and-conditions) on Wiley Online Library for rules of use; OA articles are governed by the applicable Creative Commons License

ChemSusChem
Research Article
doi.org/10.1002/cssc.202201821
Chemistry Europe
European Chemical Societies Publishing

Table 7. Calculated [Eq. (6)] and experimental surface energies γ of MgO(100) and Mg(110).

Surface	Method	γ [meV Å^{-2}]
MgO(100)	ReaxFF	71.4
	DFT	55.5
	experiment	64.9[a]; 71.8[b]
MgO(110)	ReaxFF	117.7
	DFT	135.0

[a] At 0 K.[47] [b] At 298 K.[48]

lies in between the values determined with ReaxFF (71.4 meV Å^{-2}) and DFT (55.5 meV Å^{-2}), respectively.[47]

In addition to bulk and surface energies for MgO, we trained oxygen adsorption energies for the surfaces Mg(0001), Mg(10$\bar{1}$0)A, and Mg(10$\bar{1}$1) to diversify the training data for the Mg/O parameters. Schematic illustrations of the adsorption sites are shown in Figure S6 and a comparison of the oxygen adsorption energy results obtained with ReaxFF and DFT is summarized in Table 8.

According to DFT, the tetrahedral position tet-1 between the first and second surface layer is the most stable adsorption site on Mg(0001), which is in agreement with the results of Francis and Taylor.[49] However, our adsorption energy of −4.42 eV is significantly less exothermic (*vs.* −7.69 eV[49]), which is due to the group's chosen oxygen reference, a single oxygen atom in the gas phase, while we use half of the energy of an O_2 molecule. In agreement with Francis and Taylor, we find that hcp adsorption sites are unstable in DFT; an atom placed there relaxes, in the case of Mg(0001), to the tet-1 position. With the trained ReaxFF force field, the hcp sites are stable but, similar to fcc sites, the corresponding adsorption energy is less exothermic compared to the tet-1 site with −4.02 eV and −4.01 eV for Mg(0001), respectively. A potential reason for the decreased adsorption energy could be the smaller coordination number. While four magnesium atoms surround the oxygen atom for the tetrahedral (tet) positions, there are only three surrounding atoms present for the fcc and hcp sites. The tet-3 site on Mg(0001) was identified as a meta-stable position with an energy of −3.79 eV in DFT but is calculated to be unstable with the force field. The most stable adsorption positions calculated with the force field are octahedral (oct) sites coordinated by six Mg atoms with −4.64 eV on Mg(0001), −4.69 eV on Mg(10$\bar{1}$0)A, and −4.62 eV on Mg(10$\bar{1}$1), while DFT predicts this site to be less stable compared to tet sites. During training, it became clear that a trade-off would be required between the accurate description of the relative stability sequences of the adsorption sites and that of the bulk phases. If we assigned a higher weight to the adsorption energy values, the Mg–O–Mg equilibrium angle changed in tandem, which in the most extreme case caused the wurtzite structure to be more stable than the rock salt phase. We ultimately decided to constrain the Mg–O–Mg equilibrium angle at 180 , thereby placing more weight on the accurate reproduction of the bulk phases.

Table 8. Oxygen adsorption energies E_{ad} on Mg(0001), Mg(10$\bar{1}$0)A, and Mg(10$\bar{1}$1) calculated with ReaxFF and DFT using Equation (7).

Surface	Adsorption site	E_{ad} [eV] ReaxFF	DFT
Mg(0001)	fcc	−4.01	−4.03
	hcp	−4.02	–
	tet-1	−4.36	−4.42
	tet-2	−4.33	−4.30
	tet-3[a]	–	−3.79
	oct	−4.64	−3.92
	sub-tet-1	−4.44	−4.26
	sub-tet-2	−4.45	−4.28
	sub-oct	−4.66	−4.05
Mg(10$\bar{1}$0)A	fcc	−4.04	−4.07
	hcp	−3.96	–
	tet	−4.53	−4.43
	bdg	–	−4.14
	oct	−4.69	−4.09
Mg(10$\bar{1}$1)	fcc	−3.93	−4.21
	hcp	−3.94	–
	tet-1	−4.45	−4.31
	tet-2	−4.36	−4.20
	tet-3	−4.46	−4.34
	tet-4[a]	–	−3.90
	oct	−4.62	−3.94
	hlw	−4.44	−4.25

[a] Adsorption site is metastable.

Furthermore, we trained the thermodynamic stability of subsurface (sub) adsorption positions between the second and third surface layers on Mg(0001). While in DFT, the tet positions in deeper surface layers become thermodynamically less stable (−4.26 eV/−4.28 eV *vs.* −4.42 eV/−4.30 eV), the opposite trend is calculated with the force field (−4.44 eV/−4.45 eV *vs.* −4.36 eV/−4.33 eV). With the force field, the sub-oct position shows nearly the same adsorption energy (−4.66 eV) compared to an adsorption site just below the surface (−4.64 eV). In the DFT reference data, the site further away from the surface is more stable (−4.05 eV *vs.* −3.92 eV). In summary, DFT calculations suggest that on Mg(0001), the adsorption sites in between the first and second surface layers are the most stable. With the trained force field, diffusion to deeper layers is calculated to be more favorable from a thermodynamic point of view.

Finally, the activation barriers calculated using Equation (8) for the diffusion process between the oct adsorption site and its subsurface equivalent sub-oct on Mg(0001) were part of the training set (Figure 4). According to our DFT calculations, an oxygen atom must overcome a barrier of 0.68 eV to diffuse from an oct position to a subsurface site and 0.81 eV to diffuse

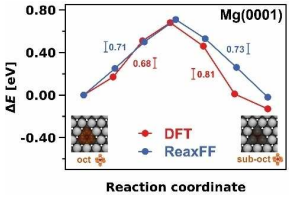

Figure 4. Comparison of the diffusion pathway from the oct to the subsurface oct site on Mg(0001) calculated with DFT and ReaxFF.

© 2022 The Authors. ChemSusChem published by Wiley-VCH GmbH

18645964, 2023, 3, Downloaded from https://chemistry-europe.onlinelibrary.wiley.com/doi/10.1002/cssc.202201821 by Cochrane Germany, Wiley Online Library on [11/05/2023]. See the Terms and Conditions (https://onlinelibrary.wiley.com/terms-and-conditions) on Wiley Online Library for rules of use; OA articles are governed by the applicable Creative Commons License

ChemSusChem
Research Article
doi.org/10.1002/cssc.202201821
Chemistry Europe
European Chemical Societies Publishing

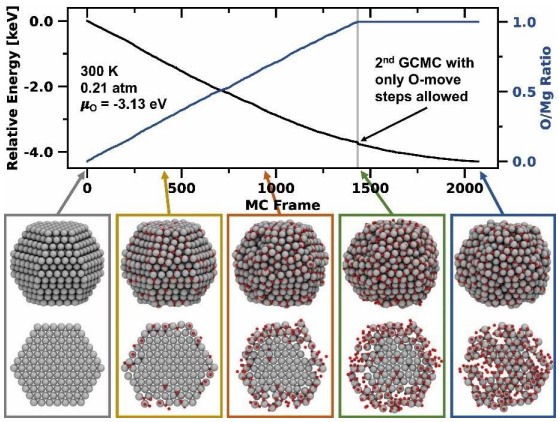

Figure 5. Grand-canonical Monte Carlo simulation showing the oxidation of an equilibrium-shaped Mg_{978} nanoparticle at 300 K and 0.21 atm first up to and then at an O/Mg ratio of 1.0. Oxidation first occurs on the surface oct sites and subsequently penetrates the particle's core.

back. The corresponding barriers in ReaxFF are 0.71 eV and 0.73 eV and thus agree well. We calculated additional oxygen diffusion barriers for Mg(0001), Mg(10$\bar{1}$0)A, and Mg(10$\bar{1}$1) to validate the obtained parameters, which were not part of the training set. The performance of these diffusion processes is discussed in the Supporting Information (Figures S7, S8, and S9; Tables S3, S4, and S5.

Grand-canonical Monte Carlo simulations of the oxidation of a magnesium nanoparticle

As initial test cases we applied the trained Mg/O potential in two subsequent GCMC simulations to investigate the thermodynamic oxidation behavior of a Mg nanoparticle. Therefore, we started with a clean, equilibrium-shaped Mg_{978} nanoparticle and inserted in the first GCMC simulation oxygen atoms up to an O/Mg ratio of 1.0. As shown in Figure 5, oxygen is mainly inserted at the particle's surface during early stages of the simulation. Note that especially oct sites are populated first and that the surface starts to reshape into the rock salt structure. Upon reaching an O/Mg ratio of 1.0, the particle is not yet fully oxidized to the core – as shown in the cross-section of the particle images in Figure 5 – but a series of non-dissociated O_2 molecules is adsorbed on the surface. As the simulation continues, the surface is covered with more and more O_2 molecules but complete oxidation to the core was not achieved even after 10 000 iterations (see Figure S10). Thus, to accelerate the process, we decided to perform a second GCMC simulation, using a nanoparticle with an O/Mg ratio of 1.0 as the input structure from the first GCMC simulation. In 20 000 additional iterations, we allowed only O-move steps but prohibited further oxygen atoms from being inserted or removed. As a result, now oxygen diffusion processes lead to oxidation of the particle's core. The final structure contains many patterns of the rock salt structure, which spread out in different spatial directions. Furthermore, grain boundaries are formed that make the particle appear amorphous. In summary, we show that a magnesium particle generated from Wulff construction oxidizes first at the surface oct sites from a thermodynamic point of view. Further oxygen adsorption is also thermodynamically favored despite the formed surface oxide layers. The fully oxidized particle exhibits an amorphous structure with rock salt structure elements but many grain boundaries.

Molecular dynamics simulation of the recrystallization of a magnesium oxide nanoparticle

We subsequently carried out an MD simulation to recrystallize the particle obtained from the GCMC simulations. To this end, we performed a simulated thermal annealing procedure where we first heated the particle to 2000 K at a rate of 80 K ps^{-1}, maintained the temperature for 75 ps, and then slowly cooled the system down to 1 K at a rate of 16 K ps^{-1}, as shown in Figure 6. The maximum temperature of 2000 K allowed for ample but non-destructive mobility of atoms in the particle. At even higher temperatures, within the simulation time evaporation of small MgO clusters (about ten atoms) was observed and the nanoparticle became unstable. The recrystallization process took place between 25 ps and 100 ps at 2000 K, which is signified by a decrease of the relative energy in Figure 6. While the kinetic energy of the system remains constant in this range (temperature $\hat{=}$ kinetic energy), the potential energy decreases due to the rearrangement process. The final structure of the MgO particle becomes visible after the cooling phase is

© 2022 The Authors. ChemSusChem published by Wiley-VCH GmbH

18645964, 2023, 3, Downloaded from https://chemistry-europe.onlinelibrary.wiley.com/doi/10.1002/cssc.202201821 by Cochrane Germany, Wiley Online Library on [11/05/2023]. See the Terms and Conditions (https://onlinelibrary.wiley.com/terms-and-conditions) on Wiley Online Library for rules of use; OA articles are governed by the applicable Creative Commons License

ChemSusChem
Research Article
doi.org/10.1002/cssc.202201821
Chemistry Europe
European Chemical Societies Publishing

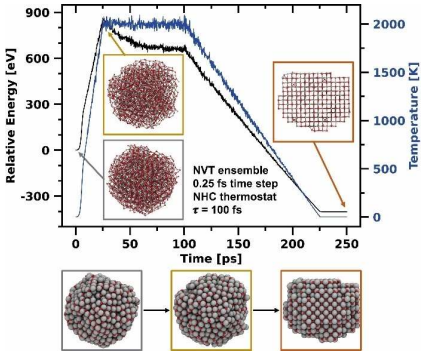

Figure 6. *NVT* simulation showing the recrystallization of an amorphous Mg nanoparticle into the rock salt structure by simulated thermal annealing at 2000 K.

completed. The particle has assumed rock salt structure and the initially round particle now has a cubic shape. In simulations with smaller periods than 75 ps at 2000 K, the recrystallization process was not yet complete and grain boundaries were present in the particle, even though the rock salt phase was already clearly apparent.

Molecular dynamics simulation of the passivation of the magnesium anode

Contact of the Mg anode with oxygen impurities, traces of water, or decomposition products of the electrolyte results in an interface layer impermeable to Mg cations, leading to battery failure.[9] To investigate the initial steps of Mg anode passivation, we performed MD simulations of Mg(0001), Mg-(10$\bar{1}$0)A, and Mg(10$\bar{1}$1) surfaces in contact with an oxygen atmosphere. A weakly coupled Nosé-Hoover (NHC) thermostat set to 300 K was applied only to the ten innermost layers of the Mg slab to avoid quenching of surface reactions and to prevent surface melting which would otherwise have to be compensated by adding an inefficiently large number of surface layers. For Mg(0001), the energy evolution, average temperature in the simulation box, and snapshots at distinct time points are shown in Figure 7. Analogous results for Mg(10$\bar{1}$0)A and Mg(10$\bar{1}$1) are presented in the Supporting Information (Figures S11 and S12). Since the average temperature inside the cell is insufficient to understand the processes taking place at the surface, we divided the *z*-axis into 500 equally sized sections and calculated the temperature of all atoms inside the corresponding box. In this way, we obtained a temperature profile along the *z*-axis to calculate the surface temperature T_{surf}. This compartmentalization also allowed us to analyze the individual temperature profiles of the oxygen atmosphere, the Mg/O interface, and bulk magnesium (Figures S14, S15, and S16).

The first oxygen molecules hitting the metal surface instantaneously dissociate and heat the surface to several 1000 K within the first 0.1 ns. On Mg(0001), the high temperature causes short-term detachment of individual MgO clusters, which later readsorb on the surface. In addition, the elevated temperature causes high mobility at the interface, leading to surface recrystallization into the rock salt structure. However, the structures observed in this simulation are significantly more disordered compared to the recrystallized MgO particle (Figure 7), showing a multitude of grain boundaries connecting several rock salt phase domains. The peak of the average temperature is reached at about 0.4 ns. From this point on, the thermostat extracts kinetic energy at a higher rate than the rate

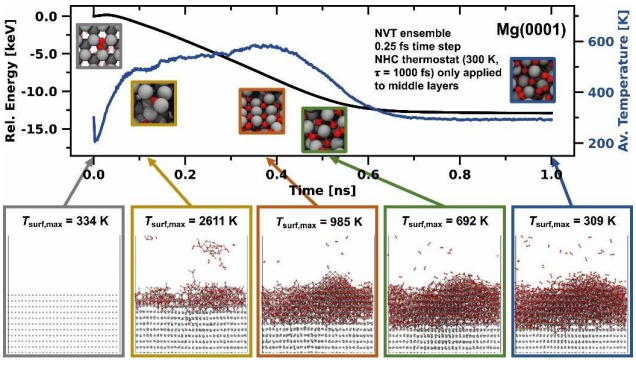

Figure 7. *NVT* simulation of the oxidation behavior of Mg(0001) at 300 K and an O_2 partial pressure 10 atm. Upon contact of the first O_2 molecules, the surface heats to several 1000 K. The high temperature fosters the formation of a rock salt interphase structure on top of the Mg anode. The maximum surface temperature $T_{surf,max}$ was determined from the temperature profiles in Figure S14.

© 2022 The Authors. ChemSusChem published by Wiley-VCH GmbH

18645964, 2023, 3, Downloaded from https://chemistry-europe.onlinelibrary.wiley.com/doi/10.1002/cssc.202201821 by Cochrane Germany, Wiley Online Library on [11/05/2023]. See the Terms and Conditions (https://onlinelibrary.wiley.com/terms-and-conditions) on Wiley Online Library for rules of use; OA articles are governed by the applicable Creative Commons License

ChemSusChem
Research Article
doi.org/10.1002/cssc.202201821
Chemistry Europe
European Chemical Societies Publishing

18645364, 2023, 3, Downloaded from https://chemistry-europe.onlinelibrary.wiley.com/doi/10.1002/cssc.202201821 by Cochrane Germany, Wiley Online Library on [11/05/2023]. See the Terms and Conditions (https://onlinelibrary.wiley.com/terms-and-conditions) on Wiley Online Library for rules of use; OA articles are governed by the applicable Creative Commons License

at which MgO formation releases energy. Nevertheless, the temperature at the surface of $T_{surf,max} = 985$ K remains significantly higher than in the bulk phase of the cell (Figure S14). At about 0.75 ns, equilibrium is reached, and MgO formation at the interface is complete, as underlined by molecular composition analysis (Figure S13). The number of intact O_2 molecules in the atmosphere or adsorbed on the surface remains constant, which is also true for O-atoms bound in the MgO boundary phase. Similar trends as for Mg(0001) are also observed in simulations with Mg(10$\bar{1}$0)A and Mg(10$\bar{1}$1) surfaces in contact with oxygen; in fact, we found these surfaces to be even more reactive. The relative energy decreases the most for Mg(10$\bar{1}$0)A surface model and the oxidation penetrates the deepest, likely due to the more open surface structure. Over the course of oxidation, the average temperature reaches the highest values for Mg(10$\bar{1}$0)A and remains on a plateau for the longest time before decreasing again (Figure S15). Similarly, molecular composition analysis in Figure S13 shows that on Mg(10$\bar{1}$0)A, most O_2 molecules were decomposed and bound in the MgO phase, followed by Mg(10$\bar{1}$1) and finally Mg(0001) (Figure S13). This trend aligns with the relative surface energies, where Mg(10$\bar{1}$0)A and Mg(10$\bar{1}$1) surfaces are less stable than Mg(0001) (see Table 2).

Fournier et al. experimentally studied the oxidation of magnesium by exposing Mg to a pure oxygen atmosphere at 20 kPa and determined an MgO layer thickness of 260 Å at 300 K (170 Å at 150 K) for a 15 min exposure time.[29] A simulation over such a long time is currently impossible with the ReaxFF method. Our simulation covers the first nanosecond and describes the initial contact of O_2 with the Mg surface. The thickness of the MgO resulting from our simulations constitute about one-tenth of the overall surface thickness (Mg(0001) ≈ 20 Å, Mg(10$\bar{1}$0)A ≈ 25 Å, Mg(10$\bar{1}$1) ≈ 21 Å). Larger oxide layer thickness could likely be observed by using significantly more surface layers, and by turning off the thermostat which dampens oxygen mobility increasingly the deeper that oxygen atoms penetrate into the slab. Fournier et al. also suggested that the surface oxide growth at 300 K follows an inverse logarithmic law. This is consistent with our observations that after initial contact, the surface is heated to such an extent that oxidation to deeper layers is facilitated. However, once the first oxide layer is formed and the surface temperature has normalized, diffusion of oxygen bound in the MgO interphase into deeper surface layers is likely the rate-determining step.[32]

Conclusion

In this work, we developed a reactive force field description for Mg/O systems for the ReaxFF framework. Magnesium-magnesium interactions were obtained using the *KVIK* optimization routine designed explicitly for metallic systems, while magnesium-oxygen interactions were trained using the successive one-parameter parabolic interpolation (SOPPI) optimizer. As a result, the force field can reliably reproduce the bulk, surface, adsorption, and diffusion properties of both metallic Mg and the MgO salt.

We first showed in a GCMC simulation that, from a thermodynamic point of view, a Mg nanoparticle (here 978 atoms) is first oxidized at surface oct sites. The structure obtained at the end of the simulation is mostly amorphous with individual domains showing rock salt ordering, separated by grain boundaries. For complete transformation to the rock salt structure, the particle must be heated to 2000 K in an MD simulation for at least 75 ps. If the thermal annealing is performed at too low temperatures or the system is cooled down too quickly, grain boundaries remain visible.

We further showed the effects of oxygen impurities on Mg surfaces. We demonstrated that O_2 immediately dissociates upon first contact with the Mg surface, heating the surface to several 1000 K. The high temperature catalyzes further oxidation and causes the formation of rock salt phases separated by grain boundaries. Among the Mg surfaces, Mg(1010)A is the most reactive, forming an MgO layer with a thickness of up to 25 Å.

The future goal is to extend the presented force field by Mg/H and Mg/C parameters to obtain a full magnesium electrolyte description to model the initial steps of SEI formation in Mg batteries. For the moment, our trained force field offers the opportunity to study the passivation and oxidation of metallic Mg in more detail or to investigate the ongoing reactions in Mg-air batteries.[50–52]

Computational Details

The ReaxFF reactive force field method

ReaxFF is a reactive force field method introduced by van Duin et al. that can model bond breakages and formations without explicitly describing the system's electronic structure.[53,54] To this end, ReaxFF employs an empirical approach that first translates the inter-atomic distance across all atoms into a continuous bond-order function BO_{ij}, which is further divided into σ (BO_{ij}^{σ}), π (BO_{ij}^{π}), and ππ ($BO_{ij}^{\pi\pi}$) bond contributions [Eq. (1)]. The continuity of the function provides constant differentiability of the energy landscape, which is necessary to calculate the forces acting on the atoms. Thus, ReaxFF enables to accurately describe bond transitions and long-distance covalent interactions which are necessary to account for transition states and reaction barriers.[55] The bond-order formalism is defined as:

$$\begin{aligned} BO_{ij} &= BO_{ij}^{\sigma} + BO_{ij}^{\pi} + BO_{ij}^{\pi\pi} \\ &= \exp\left[p_{bo1}\left(\frac{r_{ij}}{r_0^{\sigma}}\right)^{p_{bo2}}\right] + \exp\left[p_{bo3}\left(\frac{r_{ij}}{r_0^{\pi}}\right)^{p_{bo4}}\right] \\ &+ \exp\left[p_{bo5}\left(\frac{r_{ij}}{r_0^{\pi\pi}}\right)^{p_{bo6}}\right] \end{aligned} \quad (1)$$

where BO_{ij} is the total bond-order between two atoms i and j, r_{ij} is the inter-atomic distance, r_0 are the equilibrium bond distances of the σ, π, and $\pi\pi$ bonds, and p_{bo1} to p_{bo6} are empirical parameters. Thereupon, the system's total energy E_{system} is calculated using Equation (2), which is composed of several bond-order dependent energy terms like the binding energy E_{bond}, three-body angular E_{angle} and four-body torsional energy E_{tors}, and penalty energy terms for over E_{over} and under coordination E_{under}. Non-bond-order dependent

© 2022 The Authors. ChemSusChem published by Wiley-VCH GmbH

ChemSusChem
Research Article
doi.org/10.1002/cssc.202201821
Chemistry Europe
European Chemical Societies Publishing

18645964, 2023, 3, Downloaded from https://chemistry-europe.onlinelibrary.wiley.com/doi/10.1002/cssc.202201821 by Cochrane Germany, Wiley Online Library on [11/05/2023]. See the Terms and Conditions (https://onlinelibrary.wiley.com/terms-and-conditions) on Wiley Online Library for rules of use; OA articles are governed by the applicable Creative Commons License

energy terms are the electrostatic Coulomb energy $E_{Coulomb}$ and the dispersive van der Waals interactions $E_{vdWaals}$:

$$E_{system} = E_{bond} + E_{angle} + E_{tors} + E_{over} + E_{under} + E_{vdWaals} + E_{Coulomb} + E_{specific} \quad (2)$$

The last energy term $E_{specific}$ summarizes energy contributions that were not relevant to our force field, such as hydrogen bonding or the energy correction in conjugated systems. For a detailed description of the energy terms, we refer to the Supporting Information in the work of Chenoweth et al.[54] To calculate the non-bond-order dependent Coulomb energy, we applied the polarizable charge approach electron equilibration method (EEM) developed by Mortier et al., which provides a good description of metallic systems.[56] Moreover, we do not consider compressed systems in which EEM can lead to unrealistically high Coulomb attractions.[53]

ReaxFF force field training

The training set for the Mg/Mg and Mg/O parameters was entirely composed of quantum chemical calculations. The Mg/Mg parameters were trained against data from our previous publication,[38] while the Mg/O training data is presented in this work. The O/O parameters were adapted from the battery electrolyte force field from Hossain et al.[27] The Mg/Mg parameters were trained using the *KVIK* optimization routine, which was developed in particular for fast and accurate training of metal ReaxFF force fields.[22] After each optimization cycle, all structures are rescaled with the optimal lattice constant. Otherwise, stresses in the unit cell can significantly affect adsorption energy results or diffusion barriers as Stottmeister and Groß showed. [57] The Mg/O parameters, on the other hand, were trained with the classical successive one-parameter parabolic interpolation (SOPPI).[58] In general, every optimizer has strengths and weaknesses with no guarantee of getting to the global minimum on the first try.[59] Instead, the training process involves many consecutive training cycles, in which the weighting of the training data is continuously adjusted.

The cohesive energies E_{coh} for the following Mg crystal phases hcp, fcc, bcc, a15, and sc were calculated by Equation (3):

$$E_{coh} = -\frac{1}{N}\left(E_{Mg}^{bulk} - N \cdot E_{Mg}^{atom}\right) \quad (3)$$

where E_{Mg}^{bulk} is the energy of the Mg bulk crystal structure, E_{Mg}^{atom} is the energy of an isolated Mg atom and N is the amount of Mg atoms in the corresponding bulk unit cell.

In contrast, the heats of formation $\triangle_f H$ for the MgO crystal phases rock salt, wurtzite, zincblende, cesium chloride, and hcp were obtained as follows:

$$\Delta_f H = \frac{1}{N}\left(E_{MgO}^{bulk} - N \cdot E_{Mg,hcp}^{bulk} - \frac{N}{2}\left(E_{O_2}^{gas} - E_{O_2}^{ZPE}\right)\right) \quad (4)$$

where E_{MgO}^{bulk} is the bulk energy of the MgO crystal phase, $E_{Mg,hcp}^{bulk}$ is the bulk energy of hcp Mg per Mg atom, $E_{O_2}^{gas}$ is the gas-phase energy of one oxygen molecule, $E_{O_2}^{ZPE}$ is the vibrational zero point energy within the harmonic normal approximation, and N is the amount of MgO fragments within the MgO crystal phase.

The bulk modulus was obtained with the jellium equation of state[60,61] and the vacancy energy E_v was calculated in a (2×2×2) MgO rock salt unit cell with the following equation:

$$E_v = E_{(MgO)_{32}}^{bulk} - E_{Mg_{32}O_{31}}^{bulk} - \frac{E_{O_2}^{gas}}{2} \quad (5)$$

where $E_{(MgO)_{32}}^{bulk}$ is the bulk energy of the rock salt structure, $E_{Mg_{32}O_{31}}^{bulk}$ is the bulk energy of the rock salt structure with one missing oxygen atom and $E_{O_2}^{gas}$ is the gas-phase energy of one oxygen molecule.

The surface energy γ was determined as shown below:

$$\gamma = \frac{1}{2A}\left(E^{slab} - N \cdot E^{bulk}\right) \quad (6)$$

where E^{slab} is the energy of the surface slab, E^{bulk} is the bulk energy per Mg atom/MgO fragment, N is the amount of Mg atoms/MgO fragments in the slab, and A is the surface slab area. The area A has to be multiplied by two because of the symmetric slab configuration. The Wulff construction[40] and the area fractions were obtained using the Python package WulffPack.[41]

The adsorption energies E_{ad} were calculated by subtracting the energy of the slab E^{slab} and the adsorbate $E^{adsorbate}$ from the energy of the relaxed structure E^{tot} containing the slab and the adsorbate. For a magnesium adsorbate, $E^{adsorbate}$ equaled the energy of an isolated Mg atom E^{atom} and for an oxygen adsorbate $E^{adsorbate}$ corresponded to half of the energy of an O_2 molecule $\frac{E_{O_2}^{gas}}{2}$:

$$E_{ad} = E^{tot} - E^{slab} - E^{adsorbate} \quad (7)$$

The activation energy $E_a^{for/rev}$ equaled the energy difference between a stable adsorption position $E_{IS/FS}$ and the transition state energy E_{TS} of a diffusion process from (forward or to (reverse) this position:

$$E_a^{for/rev} = E_{TS} - E_{IS/FS} \quad (8)$$

DFT calculations

All first principles calculations to obtain the training set for the parameterization of the Mg/O parameters were performed with the periodic plane-wave DFT code Vienna *ab initio* simulation package (VASP).[62,63] The description of the core electrons was carried out using the projector augmented wave (PAW) method where the Mg 2*s* and O 2*s*4*p* electrons were considered as valence electrons.[64,65] The exchange and correlation energy was described using the Perdew, Burke, and Enzerhof (PBE) functional following the generalized gradient approximation (GGA) approach.[66] After a detailed convergence study, we chose the cutoff energy to be 500 eV (Figure S1a) and the *k*-points sampling using a gamma-centered mesh (due to the hexagonal symmetry of hcp Mg) with a minimum grid density of 0.14 $Å^{-1}$ (Figure S1b). We also ensured that the number of *k*-points in one direction was always rounded up to the next odd integer. To provide consistency with the Mg/Mg training set, we used Gaussian smearing with a width of 0.1 eV for the one-electron states as we did for metallic magnesium.[38] The convergence criterion for the electronic self-consistent field (SCF) was set to a maximum energy difference of 1×10^{-5} eV between two consecutive minimization cycles, and the norms of all forces had to be less than 1×10^{-3} eV $Å^{-1}$. Surface energy results were calculated using (1×1) cells with a minimum thickness of 20 Å and an equally large vacuum region. Oxygen adsorption energy results and diffusion barriers were calculated on (4×4) Mg(0001), (4×2) Mg(10$\bar{1}$0)A, and (4×2) Mg(10$\bar{1}$1) periodic surface models with six

© 2022 The Authors. ChemSusChem published by Wiley-VCH GmbH

ChemSusChem
Research Article
doi.org/10.1002/cssc.202201821
Chemistry Europe
European Chemical Societies Publishing

surface layers where the coordinates of the lowest two layers were constrained to simulate bulk behavior. To find the transition state, we applied the climbing image nudged elastic band (CI-NEB) method as implemented in the transition state tools for VASP (VTST) package.[67,68] Here, we used five images to represent the minimum energy path (MEP), each separated by a spring constant of 5.0 eV Å^{-2}. We used the image-dependent pair potential (IDPP) as the initial estimate for the MEP to achieve faster convergence.[69,70] To confirm stable adsorption positions and transition states, we determined the vibrational frequencies of the diffusing atom and its nearest neighbor atoms along the diffusion path. Stable adsorption sites were required to have no imaginary frequency while transition states must have exactly one imaginary frequency due to a maximum in the potential energy surface in one direction. To calculate harmonic normal modes, we used the dynamical matrix method from the VTST package where the respective atoms were displaced by 0.001 Å in each direction. To this end, we increased the electronic and ionic convergence criteria to 1×10^{-8} eV and 1×10^{-8} eV Å^{-1}, respectively.

ReaxFF grand-canonical Monte Carlo simulations

We used the GCMC algorithm implemented in the AMS driver program,[71] originally developed by Senftle et al. as an extension for standalone ReaxFF.[72] In a $TV\mu_O N_{Mg}$ ensemble, the algorithm randomly decides whether an oxygen atom should be (1) inserted, (2) removed, or (3) displaced in the system. The coordinates for the insertion and displacement steps are chosen randomly. The algorithm places atoms further than 1.85 Å to the nearest atom to prevent a Coulomb collapse (excessive Coulomb attraction) but closer than 3.0 Å to achieve faster convergence. Subsequently, the system's geometry is relaxed until the norms of all forces were less than 0.1 eV Å^{-1} or the maximum number of steps (1000) was reached.[73] Finally, the probabilities from Equations (9), (10), and (11) decided whether the executed Monte Carlo (MC) step is accepted or rejected:

$$p_{\text{insert}}^{\text{accept}} = \min\left[1, \frac{V}{\Lambda^3(N+1)} \cdot \exp(-\beta[E_2 - E_1 - \mu_O(T,P)])\right] \quad (9)$$

$$p_{\text{remove}}^{\text{accept}} = \min\left[1, \frac{N\Lambda^3}{V} \cdot \exp(-\beta[E_2 - E_1 + \mu_O(T,P)])\right] \quad (10)$$

$$p_{\text{displace}}^{\text{accept}} = \min[1, \exp(-\beta[E_2 - E_1])] \quad (11)$$

In Equations (9), (10), and (11), N is equal to the the number of exchangeable particles in the system before the MC move, V is the volume of the system, Λ corresponds to the thermal de Brogli wavelength of the exchanged particle, β equals the Boltzmann factor ($\beta = 1/k_bT$), and E_1 and E_2 are the potential energy values of the system before and after the MC move. The chemical potential of the single oxygen atom is set to be $\mu_O = 3.13$ eV and was calculated under ambient conditions at 300 K and 0.21 atm using Equation (12):

$$\mu_O(T,P) = \frac{1}{2}\left[\mu_{O_2,\text{exp}}(T,P^0) + k_bT\ln\left(\frac{P}{P^0}\right)\right] - E_{O_2,\text{diss}} \quad (12)$$

which is half the experimental chemical potential of an O_2 molecule minus its zero-Kelvin bond dissociation energy $E_{O_2,\text{diss}}$. The experimental oxygen chemical potential was determined via the Showmate equation using parameters from the thermochemical tables of the NIST-JANAF.[74] The bond dissociation energy of the O_2 molecule ($E_{O_2,\text{diss}} = 5.59$ eV) was calculated using ReaxFF.

The input structure of the Mg nanoparticle was obtained using the Python package WulffPack.[41] The surface energies calculated with ReaxFF presented in Table 2 served as input to generate a 978 atom-sized particle in a 100 Å × 100 Å × 100 Å simulation box.

ReaxFF molecular dynamics simulations

MD simulations were performed within the AMS driver program[71] using the Velocity-Verlet algorithm with a time step of 0.25 fs.[75] The geometry of the system was optimized before each MD simulation until the norms of all forces on all atoms were below 0.1 eV Å^{-1} to avoid simulation artifacts due to high-energy starting configurations.

We performed the recrystallization of the MgO particle in an *NVT* ensemble using a NHC thermostat with a time constant τ of 100 fs. The initial geometry corresponded to the MgO particle obtained by the GCMC simulations, shown in the blue box in Figure 5. Simulations of the Mg anode used (16×16) Mg(0001), (16×8) Mg(10$\bar{1}$0)A and (16×8) Mg(10$\bar{1}\bar{1}$) periodic surface model systems with 60 layers for 1 ns (≙4 000 000 iterations with 0.25 fs time step). On each side of the surface slab was a vacuum of 2000 Å thickness filled with 5504 O_2 molecules whose atomic configurations were generated using the PACKMOL software.[76] We calculated the number of O_2 molecules using the ideal gas law at 300 K at ten times atmospheric pressure (10 atm). The initial velocities of all atoms followed a Maxwell-Boltzmann distribution for 300 K. Furthermore, we applied a weakly coupled NHC thermostat (τ = 1000 fs) to the ten innermost Mg layers at 300 K to provide a heat sink for the reaction heat generated at the surface. The choice to use a heat sink region constitutes a compromise: in simulations without a thermostat, the Mg surface heated far beyond its melting temperature due to the strongly exothermic oxidation reaction taking place and evaporation was observed. The number of surface layers required to serve as a heat sink to compensate for this effect is computationally inefficient. In contrast, applying the thermostat to all atoms quenches the surface reactions altogether. With the thermostat layer used here, the surface heats up to several 1000 K for a short time upon first contact of the bare Mg surface with oxygen but the surface remains intact. An illustration of the cell setup and the simulation settings used are given in Figure S2.

Author Contributions

F.F. performed all the calculations except of the force field training of the magnesium-magnesium interactions which was performed by D.G. F.F. analyzed and discussed all results together with D.G., M.B., and J.B. A.C.T.v.D. and T.J. supervised the research. The manuscript was written by F.F. and all authors commented on the manuscript.

Acknowledgements

This work contributes to the research performed at the Center for Electrochemical Energy Storage Ulm-Karlsruhe (CELEST) and was partly funded by the German Research Foundation (DFG) under Project-ID 390874152 (POLiS Cluster of Excellence). Further support through the DFG-research unit FOR-5065 (ELSICS) under Project-ID 428906592 is gratefully acknowledged. The authors acknowledge support by the state of Baden-Württemberg through bwHPC and

© 2022 The Authors. ChemSusChem published by Wiley-VCH GmbH

18645964, 2023, 3, Downloaded from https://chemistry-europe.onlinelibrary.wiley.com/doi/10.1002/cssc.202201821 by Cochrane Germany, Wiley Online Library on [11/05/2023]. See the Terms and Conditions (https://onlinelibrary.wiley.com/terms-and-conditions) on Wiley Online Library for rules of use; OA articles are governed by the applicable Creative Commons License

ChemSusChem
Research Article
doi.org/10.1002/cssc.202201821
Chemistry Europe
European Chemical Societies Publishing

18645964, 2023, 3, Downloaded from https://chemistry-europe.onlinelibrary.wiley.com/doi/10.1002/cssc.202201821 by Cochrane Germany, Wiley Online Library on [11/05/2023]. See the Terms and Conditions (https://onlinelibrary.wiley.com/terms-and-conditions) on Wiley Online Library for rules of use; OA articles are governed by the applicable Creative Commons License

the DFG through grant no INST 40/575-1 FUGG (JUSTUS 2 cluster). F.F. sincerely thanks Dr. Björn Kirchhoff and Dr. Christoph Jung for helpful discussions and comments on the manuscript. A.C.T.v.D. acknowledges funding from a grant from the U.S. Army Research Laboratory through the Collaborative Research Alliance (CRA) for Multi-Scale Multidisciplinary Modeling of Electronic Materials (MSME) under Cooperative Agreement No. W911NF-12-2-0023. Open Access funding enabled and organized by Projekt DEAL.

Conflict of Interest

The authors declare no conflict of interest.

Data Availability Statement

The data that support the findings of this study are openly available in zenodo at https://doi.org/10.5281/zenodo.7074790. Furthermore, the *KVIK* optimization routine is openly available in the GitHub repository at https://github.com/shk11/KVIKOptimizer.

Keywords: batteries · magnesium · multi-scale modeling · passivation · ReaxFF

[1] Y. Liang, H. Dong, D. Aurbach, Y. Yao, *Nat. Energy* **2020**, *5*, 646.
[2] P. Bonnick, J. Muldoon, *Adv. Funct. Mater.* **2020**, *30*, 1.
[3] F. Liu, T. Wang, X. Liu, L. Fan, *Adv. Energy Mater.* **2021**, *11*, 2000787.
[4] J. Song, E. Sahadeo, M. Noked, S. B. Lee, *J. Phys. Chem. Lett.* **2016**, *7*, 1736.
[5] D. Li, Y. Yuan, J. Liu, M. Fichtner, F. Pan, *J. Magnesium Alloys* **2020**, *8*, 963.
[6] Z. Liang, C. Ban, *Angew. Chem. Int. Ed.* **2021**, *60*, 11036.
[7] J. Shi, J. Zhang, J. Guo, J. Lu, *Nanoscale Horiz.* **2020**, *5*, 1467.
[8] R. Attias, M. Salama, B. Hirsch, Y. Goffer, D. Aurbach, *Joule* **2019**, *3*, 27.
[9] Y. Sun, F. Ai, Y. Lu, *Small* **2022**, *18*, 2200009.
[10] N. N. Rajput, X. Qu, N. Sa, A. K. Burrell, K. A. Persson, *J. Am. Chem. Soc.* **2015**, *137*, 3411.
[11] Z. Lu, A. Schechter, M. Moshkovich, D. Aurbach, *J. Electroanal. Chem.* **1999**, *466*, 203.
[12] J. Eaves-Rathert, K. Moyer, M. Zohair, C. L. Pint, *Joule* **2020**, *4*, 1324.
[13] H. D. Yoo, S.-D. Han, I. L. Bolotin, G. M. Nolis, R. D. Bayliss, A. K. Burrell, J. T. Vaughey, J. Cabana, *Langmuir* **2017**, *33*, 9398.
[14] R. Davidson, A. Verma, D. Santos, F. Hao, C. Fincher, S. Xiang, J. Van Buskirk, K. Xie, M. Pharr, P. P. Mukherjee, S. Banerjee, *ACS Energy Lett.* **2019**, *4*, 375.
[15] M. van den Borg, D. Gaissmaier, E. Knobbe, D. Fantauzzi, T. Jacob, *Appl. Surf. Sci.* **2021**, *555*, 149447.
[16] M. van den Borg, D. Gaissmaier, D. Fantauzzi, E. Knobbe, T. Jacob, *ChemSusChem* **2022**, *15*, e2021017.
[17] J. G. Connell, B. Genorio, P. P. Lopes, D. Strmcnik, V. R. Stamenkovic, N. M. Markovic, *Chem. Mater.* **2016**, *28*, 8268.
[18] M. M. Islam, A. Ostadhossein, O. Borodin, A. T. Yeates, W. W. Tipton, R. G. Hennig, N. Kumar, A. C. T. van Duin, *Phys. Chem. Chem. Phys.* **2015**, *17*, 3383.
[19] M. M. Islam, A. C. T. van Duin, *J. Phys. Chem. C* **2016**, *120*, 27128.
[20] M. M. Islam, G. Kolesov, T. Verstraelen, E. Kaxiras, A. C. T. van Duin, *J. Chem. Theory Comput.* **2016**, *12*, 3463.
[21] K. A. O'Hearn, M. W. Swift, J. Liu, I. Magoulas, P. Piecuch, A. C. T. van Duin, H. M. Aktulga, Y. Qi, *J. Chem. Phys.* **2020**, *153*, 084107.
[22] D. Gaissmaier, M. van den Borg, D. Fantauzzi, T. Jacob, *ChemRxiv preprint* **2022**, DOI: 10.26434/chemrxiv-2022-lrsjd-v2.
[23] A. Ostadhossein, S.-Y. Kim, E. D. Cubuk, Y. Qi, A. C. T. van Duin, *J. Phys. Chem. A* **2016**, *120*, 2114.
[24] D. Bedrov, G. D. Smith, A. C. T. van Duin, *J. Phys. Chem. A* **2012**, *116*, 2978.
[25] Y. K. Shin, M. Y. Sengul, A. S. M. Jonayat, W. Lee, E. D. Gomez, C. A. Randall, A. C. T. v. Duin, *Phys. Chem. Chem. Phys.* **2018**, *20*, 22134.
[26] M. M. Islam, V. S. Bryantsev, A. C. T. van Duin, *J. Electrochem. Soc.* **2014**, *161*, E3009.
[27] M. J. Hossain, G. Pawar, B. Liaw, K. L. Gering, E. J. Dufek, A. C. T. van Duin, *J. Chem. Phys.* **2020**, *152*, 184301.
[28] G. Song, A. Atrens, *Adv. Eng. Mater.* **2003**, *5*, 837.
[29] V. Fournier, P. Marcus, I. Olefjord, *Surf. Interface Anal.* **2002**, *34*, 494.
[30] G. Song, A. Atrens, *Adv. Eng. Mater.* **2007**, *9*, 177.
[31] Q. Tan, A. Atrens, N. Mo, M.-X. Zhang, *Corros. Sci.* **2016**, *112*, 734.
[32] H. Nie, M. Schoenitz, E. L. Dreizin, *J. Phys. Chem. C* **2016**, *120*, 974.
[33] S. Cheung, W.-Q. Deng, A. C. T. van Duin, W. A. Goddard, *J. Phys. Chem. A* **2005**, *109*, 851.
[34] E. Iype, M. Hütter, A. P. J. Jansen, S. V. Nedea, C. C. M. Rindt, *J. Comput. Chem.* **2013**, *34*, 1143.
[35] R. Zhu, F. Janetzko, Y. Zhang, A. C. T. van Duin, W. A. Goddard, D. R. Salahub, *Theor. Chem. Acc.* **2008**, *120*, 479.
[36] J. Yeon, S. C. Chowdhury, C. M. Daksha, J. W. Gillespie, *J. Phys. Chem. C* **2021**, *125*, 18380.
[37] D. Raymand, A. C. van Duin, M. Baudin, K. Hermansson, *Surf. Sci.* **2008**, *602*, 1020.
[38] F. Fiesinger, D. Gaissmaier, M. van den Borg, T. Jacob, *ChemSusChem* **2022**, *15*, e202200414.
[39] C. Kittel, *Introduction to Solid State Physics, 8th Edition*, Wiley, Hoboken **2004**.
[40] G. Wulff, *Kristallogr.* **1901**, *34*, 449.
[41] J. Rahm, P. Erhart, *J. Open Source Softw.* **2020**, *5*, 1944.
[42] W. K. Burton, N. Cabrera, F. C. Frank, *Phil. Trans. R. Soc. A* **1951**, *243*, 299.
[43] R. S. McWilliams, D. K. Spaulding, J. H. Eggert, P. M. Celliers, D. G. Hicks, R. F. Smith, G. W. Collins, R. Jeanloz, *Science* **2012**, *338*, 1330.
[44] M. J. L. Sangster, G. Peckham, D. H. Saunderson, *J. Phys. C* **1970**, *3*, 1026.
[45] D. Lide, *CRC Handbook of Chemistry and Physics, 90th Edition*, CRC Press, Boca Raton **2009**.
[46] K. Reuter, M. Scheffler, *Phys. Rev. B* **2001**, *65*, 035406.
[47] G. Jura, C. W. Garland, *J. Am. Chem. Soc.* **1952**, *74*, 6033.
[48] A. R. C. Westwood, D. L. Goldheim, *J. Appl. Phys.* **1963**, *34*, 3335.
[49] M. F. Francis, C. D. Taylor, *Phys. Rev. B* **2013**, *87*, 075450.
[50] C. Li, Y. Sun, F. Gebert, S. Chou, *Adv. Energy Mater.* **2017**, *7*, 1700869.
[51] Y.-T. Lu, A. R. Neale, C.-C. Hu, L. J. Hardwick, *Front. Energy Res.* **2021**, *8*.
[52] L. J. Hardwick, C. P. De León, *Johnson Matthey Technol. Rev.* **2018**, *62*, 134.
[53] A. C. T. van Duin, S. Dasgupta, F. Lorant, W. A. Goddard, *J. Phys. Chem. A* **2001**, *105*, 9396.
[54] K. Chenoweth, A. C. T. van Duin, W. A. Goddard, *J. Phys. Chem. A* **2008**, *112*, 1040.
[55] T. P. Senftle, S. Hong, M. M. Islam, S. B. Kylasa, Y. Zheng, Y. K. Shin, C. Junkermeier, R. EngelHerbert, M. J. Janik, H. M. Aktulga, T. Verstraelen, A. Grama, A. C. Van Duin, *npj Comput. Mater.* **2016**, *2*, 15011.
[56] W. J. Mortier, S. K. Ghosh, S. Shankar, *J. Am. Chem. Soc.* **1986**, *108*, 4315.
[57] D. Stottmeister, A. Groß, *ChemSusChem* **2020**, *13*, 3147.
[58] A. C. T. van Duin, J. M. A. Baas, B. van de Graaf, *J. Chem. Soc. Faraday Trans.* **1994**, *90*, 2881.
[59] G. Shchygol, A. Yakovlev, T. Trnka, A. C. T. van Duin, T. Verstraelen, *J. Chem. Theory Comput.* **2019**, *15*, 6799.
[60] A. B. Alchagirov, J. P. Perdew, J. C. Boettger, R. C. Albers, C. Fiolhais, *Phys. Rev. B* **2001**, *63*, 224115.
[61] A. B. Alchagirov, J. P. Perdew, J. C. Boettger, R. C. Albers, C. Fiolhais, *Phys. Rev. B* **2003**, *67*, 026103.
[62] G. Kresse, J. Furthmüller, *Phys. Rev. B* **1996**, *54*, 11169.
[63] G. Kresse, J. Furthmüller, *Comput. Mater. Sci.* **1996**, *6*, 15.
[64] P. E. Blöchl, *Phys. Rev. B* **1994**, *50*, 17953.
[65] D. Joubert, *Phys. Rev. B: Condens. Matter Mater. Phys.* **1999**, *59*, 1758.
[66] J. P. Perdew, K. Burke, M. Ernzerhof, *Phys. Rev. Lett.* **1996**, *77*, 3865.
[67] G. Henkelman, H. Jónsson, *J. Chem. Phys.* **2000**, *113*, 9978.
[68] G. Henkelman, B. P. Uberuaga, H. Jónsson, *J. Chem. Phys.* **2000**, *113*, 9901.
[69] S. Smidstrup, A. Pedersen, K. Stokbro, H. Jónsson, *J. Chem. Phys.* **2014**, *140*, 214106.
[70] A. Hjorth Larsen, J. Jørgen Mortensen, J. Blomqvist, I.E. Castelli, R. Christensen, M. Dułak, J. Friis, M. N. Groves, B. Hammer, C. Hargus, E. D. Hermes, P. C. Jennings, P. Bjerre Jensen, J. Kermode, J. R. Kitchin, E. Leonhard Kolsbjerg, J. Kubal, K. Kaasbjerg, S. Lysgaard, J. Bergmann Maronsson, T. Maxson, T. Olsen, L. Pastewka, A. Peterson, C.

© 2022 The Authors. ChemSusChem published by Wiley-VCH GmbH

ChemSusChem
Research Article
doi.org/10.1002/cssc.202201821
Chemistry Europe
European Chemical Societies Publishing

Rostgaard, J. Schiøtz, O. Schütt, M. Strange, K. S. Thygesen, T. Vegge, L. Vilhelmsen, M. Walter, Z. Zeng, K. W. Jacobsen, *J. Phys. Condens. Matter* **2017**, *29*, 273002.
[71] R. Rüger, M. Franchini, T. Trnka, A. Yakovlev, E. van Lenthe, P. Philipsen, T. van Vuren, B. Klumpers, T. Soini, AMS 2021, SCM, Vrije Universiteit, Amsterdam (The Netherlands) **2021**.
[72] T. P. Senftle, R. J. Meyer, M. J. Janik, A. C. T. van Duin, *J. Chem. Phys.* **2013**, *139*, 044109.
[73] E. Bitzek, P. Koskinen, F. Gähler, M. Moseler, P. Gumbsch, *Phys. Rev. Lett.* **2006**, *97*, 170201.
[74] M. W. Chase, *NIST-JANAF Thermochemical Tables, 4th Edition*, American Institute of Physics, College Park **1998**.
[75] L. Verlet, *Phys. Rev.* **1967**, *159*, 98.
[76] L. Martínez, R. Andrade, E. G. Birgin, J. M. Martínez, *J. Comput. Chem.* **2009**, *30*, 2157.

Manuscript received: September 26, 2022
Revised manuscript received: November 7, 2022
Accepted manuscript online: November 8, 2022
Version of record online: January 16, 2023

© 2022 The Authors. ChemSusChem published by Wiley-VCH GmbH

18645964, 2023, 3, Downloaded from https://chemistry-europe.onlinelibrary.wiley.com/doi/10.1002/cssc.202201821 by Cochrane Germany, Wiley Online Library on [11/05/2023]. See the Terms and Conditions (https://onlinelibrary.wiley.com/terms-and-conditions) on Wiley Online Library for rules of use; OA articles are governed by the applicable Creative Commons License

ChemSusChem

Supporting Information

Development of a Mg/O ReaxFF Potential to describe the Passivation Processes in Magnesium-Ion Batteries**

Florian Fiesinger, Daniel Gaissmaier, Matthias van den Borg, Julian Beßner, Adri C. T. van Duin, and Timo Jacob*This publication is part of a collection of papers from contributors to the 7th Ertl Symposium on Catalysis in Electrochemistry (Gwangju, South Korea, October 26–29, 2022). Please visit to view all contributions.© 2022 The Authors. ChemSusChem published by Wiley-VCH GmbH. This is an open access article under the terms of the Creative Commons Attribution Non-Commercial NoDerivs License, which permits use and distribution in any medium, provided the original work is properly cited, the use is non-commercial and no modifications or adaptations are made.

Mg/O force field file

```
Reactive MD-force field: F. Fiesinger (2022) - Mg/O FF
 39          ! Number of general parameters
   50.0000 !p_boc1 Eq(4c): Overcoordination parame
    9.5469 !p_boc2 Eq(4d): Overcoordination parame
   26.5405 !p_coa2 Eq(15): Valency angle conjugati
    1.7224 !p_trip4 Eq(20): Triple bond stabilisat
    6.8702 !p_trip3 Eq(20): Triple bond stabilisat
   60.4850 !k_c2 Eq(19): C2-correction
    1.0588 !p_ovun6 Eq(12): Undercoordination
    4.6000 !p_trip2 Eq(20): Triple bond stabilisat
   12.1176 !p_ovun7 Eq(12): Undercoordination
   13.3056 !p_ovun8 Eq(12): Undercoordination
  -30.5044 !p_trip1 Eq(20): Triple bond stabilizat
    0.0000 !Lower Taper-radius (must be 0)
   10.0000 !R_cut Eq(21): Upper Taper-radius
    2.8793 !p_fe1 Eq(6a): Fe dimer correction
   15.0000 !p_val6 Eq(13c): Valency undercoordinat
    6.0891 !p_lp1 Eq(8): Lone pair param
    1.0563 !p_val9 Eq(13f): Valency angle exponent
    2.0384 !p_val10 Eq(13g): Valency angle paramet
    6.1431 !p_fe2 Eq(6a): Fe dimer correction
    6.9290 !p_pen2 Eq(14a): Double bond/angle para
    0.3989 !p_pen3 Eq(14a): Double bond/angle para
    3.9954 !p_pen4 Eq(14a): Double bond/angle para
   -2.4837 !p_fe3 Eq(6a): Fe dimer correction
    5.7796 !p_tor2 Eq(16b): Torsion/BO parameter
   10.0000 !p_tor3 Eq(16c): Torsion overcoordinati
    1.9487 !p_tor4 Eq(16c): Torsion overcoordinati
   -1.2327 !p_elho Eq(26a): electron-hole interact
    2.1645 !p_cot2 Eq(17b): Conjugation if tors13=
    1.5591 !p_vdW1 Eq(23b): vdWaals shielding
    0.0010 !Cutoff for bond order (*100)
    2.1365 !p_coa4 Eq(15): Valency angle conjugati
    0.6991 !p_ovun4 Eq(11b): Over/Undercoordinatio
   50.0000 !p_ovun3 Eq(11b): Over/Undercoordinatio
    1.8512 !p_val8 Eq(13d): Valency/lone pair para
    0.5000 !X_soft Eq(25): ACKS2 softness for X_ij
   20.0000 !d Eq(23d): Scale factor in lg-dispersi
    5.0000 !p_val Eq(27): Gauss exponent for elect
    0.0000 !1 Eq(13e): disable undecoord in val an
    2.6962 !p_coa3 Eq(15): Valency angle conjugati
 2     ! Nr of atoms; cov.r; valency;a.m;Rvdw;Evdw;gammaEEM;cov.r2;#
         alfa;gammavdW;valency;Eunder;Eover;chiEEM;etaEEM;n.u.
         cov r3;Elp;Heat inc.;bo131;bo132;bo133;softcut;n.u.
         ov/un;val1;n.u.;val3,vval4
O     1.2450    2.0000   15.9990    2.3890    0.1000    1.0898    1.0548    6.0000
      9.7300   13.8449    4.0000   37.5000  116.0768    8.5000    8.3122    2.0000
      0.9049    0.4056   59.0626    3.5027    0.7640    0.0021    0.9745    0.0000
     -3.5500    2.9000    1.0493    4.0000    2.9225    1.3000    0.2000   13.0000
Mg    1.8315    2.0000   24.3050    2.2464    0.1806    0.7404    1.0000    2.0000
     10.9186   27.1205    3.0000   38.0000    0.0000    0.6422    5.4853    0.0000
     -1.3000    0.0000  220.0000   49.9248    0.3370    0.0000    0.0000    0.0000
     -2.5000    2.3663    1.0564    6.0000    2.9663    2.4500    1.0000   40.0000
 3     ! Nr of bonds; Edis1;LPpen;n.u.;pbe1;pbo5;13corr;pbo6
                      pbe2;pbo3;pbo4;n.u.;pbo1;pbo2;ovcorr
 1   1 142.2858  145.0000   50.8293    0.2506   -0.1000    1.0000   29.7503    0.6051
         0.3451   -0.1055    9.0000    1.0000   -0.1225    5.5000    1.0000    0.0000
 1   2  53.7362    0.0000   43.3991    0.4817   -0.3000    1.0000   36.0000    0.0667
         0.4678   -0.2000    8.4994    1.0000   -0.1486    8.8494    1.0000   24.4461
 2   2  25.1797    0.0000    0.0000    0.6249   -0.2050    0.0000   16.0000    0.2618
         0.7684   -0.2000   10.0000    1.0000   -0.2374    3.2858    0.0000    0.0000
 1     ! Nr of off-diagonal terms; Ediss;Ro;gamma;rsigma;rpi;rpi2
 1   2    1.0196    1.1711   13.4732    1.9128   -1.0000   -1.0000
 5     ! Nr of angles;at1;at2;at3;Thetao,o;ka;kb;pv1;pv2
```

```
1   1   1   80.7324   30.4554    0.9953    0.0000    1.6310   50.0000    1.0783
1   2   1    0.0000   21.1509    1.9901    0.0000    1.0311    0.0000    2.2855
2   1   2   90.0000    5.7293    0.5286    0.0000    1.6966    0.0000    1.3853
1   1   2   16.1468    4.6234    1.5549    0.0000    1.0488    0.0000    1.0830
1   2   2   21.8146    6.1011    0.5672    0.0000    2.1986    0.0000    1.5074
3     ! Nr of torsions;at1;at2;at3;at4;;V1;V2;V3;V2(BO);vconj;n.u;n
1   1   1   1   -2.5000    0.0100    1.0000   -9.0000   -0.0100    0.0000    0.0000
0   1   1   0    0.5511   25.4150    1.1330   -5.1903   -1.0000    0.0000    0.0000
2   1   1   2    0.4381   23.9911    1.2283   -5.1903   -1.0000    0.0000    0.0000
0     ! Nr of hydrogen bonds;at1;at2;at3;Rhb;Dehb;vhb1
```

S2

Computational details

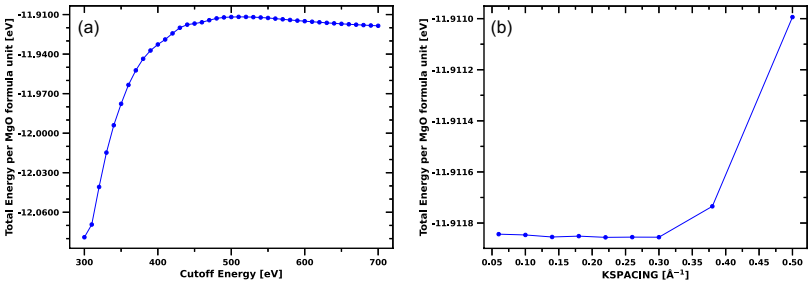

Figure S1: Convergence studies of the a) cutoff energy (ENCUT Tag) and b) grid density of k-points (KSPACING Tag) for the MgO bulk structure.

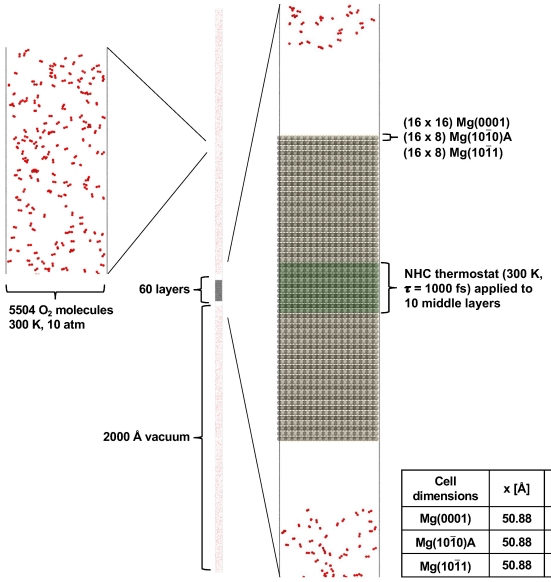

Cell dimensions	x [Å]	y [Å]	z [Å]
Mg(0001)	50.88	44.06	4153.40
Mg(10$\bar{1}$0)A	50.88	41.60	4167.07
Mg(10$\bar{1}\bar{1}$)	50.88	47.07	4148.05

Figure S2: Cell dimensions and simulation settings used to model passivation of the magnesium anode.

Mg adsorption on Mg(0001), Mg$(10\bar{1}0)$A, and Mg$(10\bar{1}1)$

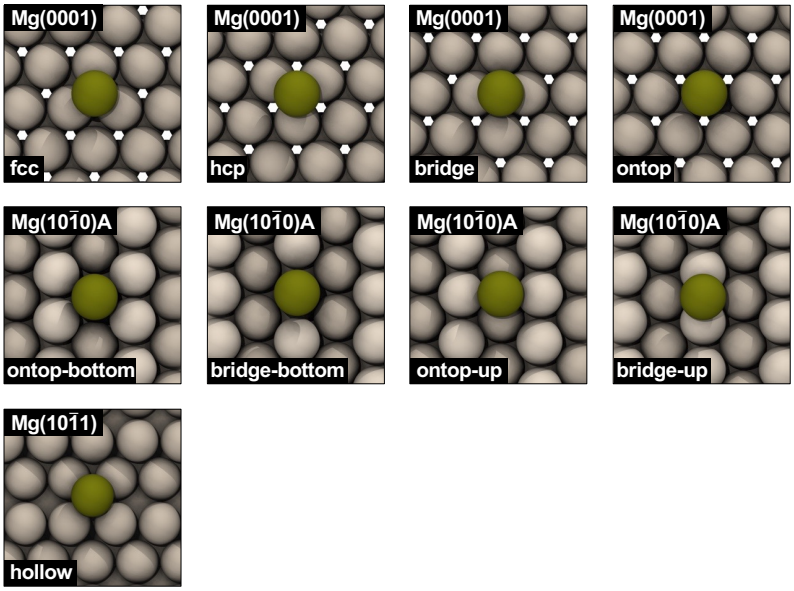

Figure S3: Schematic illustration of Mg adsorption sites on Mg(0001), Mg$(10\bar{1}0)$A, and Mg$(10\bar{1}1)$. The green-colored atom is the magnesium adsorbate, and the gray-colored atoms are surface atoms. Adapted from Ref. [1] Copyright (2022), with permission from Wiley-VCH.

Mg diffusion processes on Mg(0001)

A detailed comparison of the activation energy results calculated with ReaxFF and DFT is provided in Table S1. We previously showed that Mg dimer formation on Mg(0001) occurs barrier-free and that its cleavage is associated with a barrier that is several times larger (Figure S4a and S4b).[1] The trained ReaxFF force field reproduces this trend only qualitatively: the barriers for dimer formation are shallow (0.11 eV and 0.12 eV) but so are the reverse barriers (0.28 eV and 0.29 eV). A similar overestimation occurs for the diffusion of a Mg atom towards a $[11\bar{2}0]$-directed step-edge (0.22 eV *vs.* 0.03 eV; Figure S4c) but diffusion along the step-edge is accurately reproduced (both 0.22 eV; Figure S4c and S4d). The trained ReaxFF force field describes the kink processes well (Figure S4e and S4f), both when the atom leaves the site towards the terrace (0.72 eV *vs.* 0.91 eV/ 0.92 eV) and along the step-edge (0.44 eV/ 0.47 eV *vs.* 0.45 eV/ 0.46 eV). Analogous to the dimer systems, the force field underestimates the barriers for bond breaking (0.43 eV/ 0.46 eV *vs.* 0.63 eV/ 0.62 eV) for inner-corner processes (Figure S4g and S4h) but overestimates bond formation barriers (0.21 eV/ 0.25 eV *vs.* 0.10 eV/ 0.08 eV). Precisely as in DFT, the exchange process at a 240° outer-corner (Figure S4k) exhibits a higher barrier than diffusion around the corner with the trained force field. However, unlike in the DFT reference data set, the OC_1 site is thermodynamically more stable than the OC_0 site. Furthermore, with the force field, the exchange processes are much better reproduced at the 300° outer-corners (Figure S4i and S4j) than at the terrace, even though the barriers are still slightly overestimated. Finally, DFT predicts an almost barrier-free descent via the exchange process on $[11\bar{2}0]$- and $[\bar{1}\bar{1}20]$-steps (0.01 eV/ 0.02 eV; Figure S4l and S4m).[1] Because the force field overestimates the exchange processes in general, the barriers to descent are generally higher (0.27 eV/ 0.13 eV). The activation barriers for the ascent, on the other hand, are well reproduced for hopping and exchange processes ($\Delta|E_a| \leq 0.1$ eV).

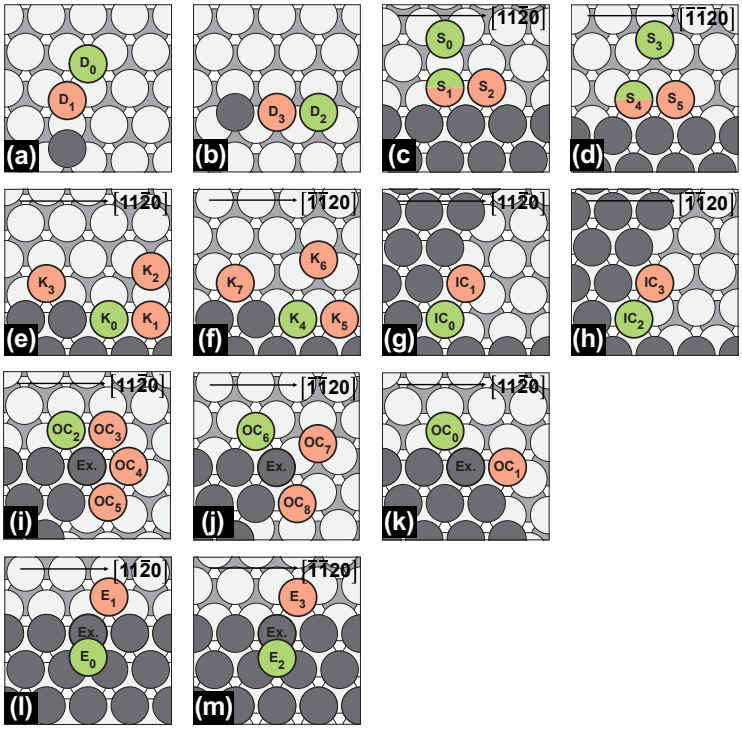

Figure S4: Overview and schematic representation of trained self-diffusion processes on Mg(0001): a) dimer I, b) dimer II, c) step-edge [11$\bar{2}$0]-step, d) step-edge [$\bar{1}$1$\bar{2}$0]-step, e) kink [11$\bar{2}$0]-step, f) kink [$\bar{1}$1$\bar{2}$0]-step, g) 60° inner-corner [11$\bar{2}$0]-step, h) 60° inner-corner [$\bar{1}$1$\bar{2}$0]-step, i) 300° outer-corner [11$\bar{2}$0]-step, j) 300° outer-corner [$\bar{1}$1$\bar{2}$0]-step k) 240° outer-corner, l) step-down [11$\bar{2}$0]-step, m) step-down [$\bar{1}$1$\bar{2}$0]-step. Green atoms mark the initial, while red atoms mark the final position. Adapted from Ref. [1] Copyright (2022), with permission from Wiley-VCH.

Table S1: Comparison of activation energies E_a in eV calculated with ReaxFF and DFT using Equation (8) for forward and backward self-diffusion processes on Mg(0001). DFT reference activation energy values were adopted from Fiesinger et al.[1]

Mg(0001)	Pathway	$E_{a,ReaxFF}^{for}$	$E_{a,DFT}^{for}$	$\lvert\Delta E_a^{for}\rvert$	$E_{a,ReaxFF}^{rev}$	$E_{a,DFT}^{rev}$	$\lvert\Delta E_a^{rev}\rvert$
dimer	$D_0 \leftrightarrow D_1$	0.11	0.00	0.11	0.28	0.49	0.21
	$D_2 \leftrightarrow D_3$	0.12	0.00	0.12	0.29	0.46	0.17
step-edge	$S_0 \leftrightarrow S_1$	0.22	0.03	0.19	0.69	0.70	0.01
	$S_1 \leftrightarrow S_2$	0.22	0.22	0.00	0.22	0.22	0.00
	$S_3 \leftrightarrow S_4$	0.10	0.02	0.08	0.50	0.63	0.13
	$S_4 \leftrightarrow S_5$	0.26	0.15	0.11	0.26	0.15	0.11
kink	$K_0 \leftrightarrow K_1$	0.44	0.45	0.01	0.21	0.17	0.04
	$K_0 \leftrightarrow K_2$	0.72	0.91	0.19	0.01	0.02	0.01
	$K_4 \leftrightarrow K_5$	0.47	0.46	0.01	0.25	0.12	0.13
	$K_4 \leftrightarrow K_6$	0.72	0.92	0.20	0.01	0.01	0.00
inner-corner	$IC_0 \leftrightarrow IC_1$	0.43	0.63	0.20	0.21	0.10	0.11
	$IC_2 \leftrightarrow IC_3$	0.46	0.62	0.16	0.25	0.08	0.17
outer-corner	$OC_0 \leftrightarrow OC_1$	0.30	0.29	0.01	0.32	0.22	0.10
	$OC_0 \leftrightarrow OC_1$ (Ex.)	0.51	0.41	0.10	0.52	0.33	0.19
	$OC_2 \leftrightarrow OC_5$ (Ex.)	0.37	0.32	0.05	0.37	0.32	0.05
	$OC_6 \leftrightarrow OC_8$ (Ex.)	0.24	0.16	0.08	0.24	0.16	0.08
step-down	$E_0 \leftrightarrow E_1$	0.27	0.09	0.18	0.72	0.75	0.03
	$E_0 \leftrightarrow E_1$ (Ex.)	0.31	0.01	0.30	0.77	0.67	0.10
	$E_2 \leftrightarrow E_3$	0.27	0.16	0.11	0.73	0.70	0.03
	$E_2 \leftrightarrow E_3$ (Ex.)	0.13	0.02	0.11	0.59	0.56	0.03

Mg diffusion processes on Mg$(10\bar{1}1)$

A detailed comparison of the activation energy results calculated with ReaxFF and DFT is provided in Table S2. On Mg$(10\bar{1}1)$, the dimer and trimer processes within a channel ($d_0 \leftrightarrow d_1$, $t_0 \leftrightarrow t_1$) are well reproduced by the force field (Figure S5). In contrast to DFT, however, two separated monomers are calculated to be thermodynamically more stable than the dimer in the $d_2 \leftrightarrow d_3$ process. A similar trend is calculated for the trimers. In DFT, a linear trimer structure is the most thermodynamically stable; with the force field, a triangular trimer with the third atom at position t_5 is preferred. Nevertheless, all trimer barriers are reproduced in ReaxFF with a maximum deviation of $\Delta|E_a| = 0.11\,\text{eV}$.

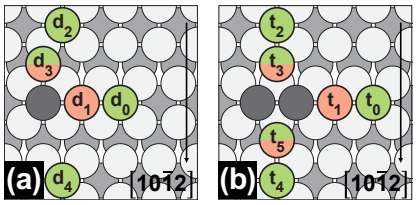

Figure S5: Overview and schematic representation of trained self-diffusion processes on Mg$(10\bar{1}1)$: a) Dimer, b) Trimer. Green atoms mark the initial, while red atoms mark the final position. Adapted from Ref. [1] Copyright (2022), with permission from Wiley-VCH.

Table S2: Comparison of activation energies E_a in eV calculated with ReaxFF and DFT using Equation (8) for forward and backward self-diffusion processes on Mg$(10\bar{1}1)$. DFT reference activation energy values were adopted from Fiesinger et al.[1]

Mg$(10\bar{1}1)$	Pathway	$E_{a,\text{ReaxFF}}^{\text{for}}$	$E_{a,\text{DFT}}^{\text{for}}$	$\lvert\Delta E_a^{\text{for}}\rvert$	$E_{a,\text{ReaxFF}}^{\text{rev}}$	$E_{a,\text{DFT}}^{\text{rev}}$	$\lvert\Delta E_a^{\text{rev}}\rvert$
dimer	$d_0 \leftrightarrow d_1$	0.37	0.25	0.12	0.63	0.58	0.05
	$d_2 \leftrightarrow d_3$	0.20	0.19	0.01	0.22	0.13	0.09
	$d_3 \leftrightarrow d_1$	0.22	0.15	0.07	0.45	0.51	0.06
	$d_4 \leftrightarrow d_1$	0.39	0.37	0.02	0.64	0.67	0.03
trimer	$t_0 \leftrightarrow t_1$	0.37	0.26	0.11	0.62	0.58	0.04
	$t_2 \leftrightarrow t_3$	0.19	0.19	0.00	0.29	0.20	0.09
	$t_3 \leftrightarrow t_1$	0.32	0.27	0.05	0.46	0.54	0.08
	$t_4 \leftrightarrow t_5$	0.36	0.31	0.05	0.66	0.57	0.09
	$t_5 \leftrightarrow t_1$	0.33	0.24	0.09	0.27	0.28	0.01

O adsorption on Mg(0001), Mg$(10\bar{1}0)$A, and Mg$(10\bar{1}1)$

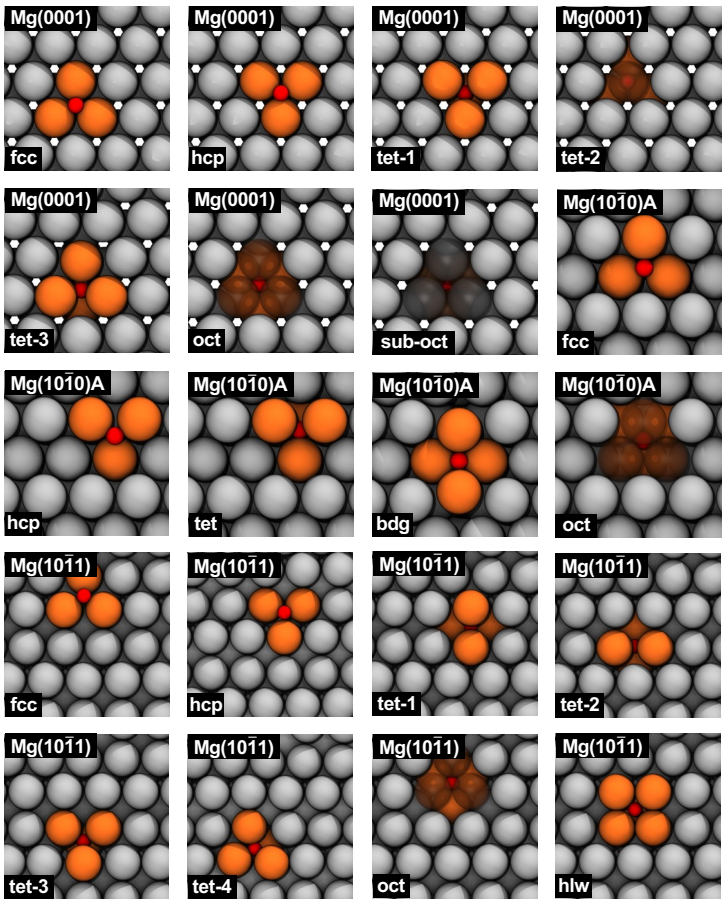

Figure S6: Schematic illustration of oxygen adsorption sites on on Mg(0001), Mg$(10\bar{1}0)$A, and Mg$(10\bar{1}1)$. The red-colored atom is the oxygen adsorbate, gray-colored atoms are surface atoms, and orange-colored atoms are surface atoms which coordinate to the oxygen adsorbate.

O diffusion processes on Mg(0001)

According to DFT, an oxygen atom diffuses on Mg(0001) (Table S3) in a zigzag route first from the fcc site by overcoming a barrier of 0.41 eV to the thermodynamically most stable tet-1 position (Figure S7c). From there, the oxygen atom moves to the oct position via the meta-stable tet-3 site with an activation energy of 0.72 eV. Finally, the oxygen atom overcomes 0.37 eV to reach the tet-2 position. In calculations with the trained force field, an oxygen atom adsorbed at the fcc position diffuses vertically down to the oct position overcoming a barrier of 0.20 eV (Figure S7a), or from the hcp to the tet-1 site overcoming 0.17 eV (Figure S7b), thereby underestimating the barrier by 50 % compared to DFT. The diffusion barriers within the surface are the same magnitude as the DFT barriers, with 0.54 eV from the tet-1 to the oct and 0.81 eV from the oct to the tet-2 site, respectively.

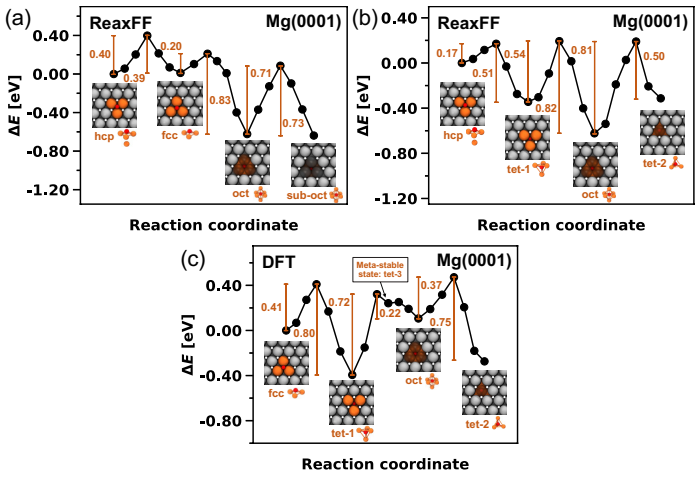

Figure S7: Diffusion profiles of an oxygen atom on Mg(0001) calculated with ReaxFF a) from the hcp to the fcc over the oct to the sub-oct site, b) from the hcp to the tet-1 over the oct to the tet-2 site, and with DFT c) from the fcc to the tet-1 over the oct to the tet-2 site.

O diffusion processes on Mg$(10\bar{1}0)$A

On Mg$(10\bar{1}0)$A (Table S4), oxygen atom diffusion as calculated with DFT is associated with only minor barriers of 0.12 eV/ 0.05 eV for diffusion between the bdg and the fcc sites (Figure S8c). With the trained force field, a barrier of 0.10 eV is calculated for diffusion between two fcc sites (Figure S8b). This result constitutes a significant deviation between DFT and the force field. While in DFT, the bdg position is stable, it corresponds to a transition state on the force field's potential energy surface. Similar to Mg(0001), the barrier from the oct to the

Table S3: Comparison of activation energies E_a in eV calculated using Equation (8) for forward and backward O-diffusion on Mg(0001) for ReaxFF and DFT.

Mg(0001)	$E^{for}_{a,ReaxFF}$	$E^{for}_{a,DFT}$	$E^{rev}_{a,ReaxFF}$	$E^{rev}_{a,DFT}$
hcp ↔ fcc	0.40	-	0.39	-
fcc ↔ oct	0.20	-	0.83	-
oct ↔ sub-oct	0.71	0.68	0.73	0.81
hcp ↔ tet-1	0.17	-	0.51	-
tet-1 ↔ oct	0.54	-	0.82	-
oct ↔ tet-2	0.81	0.37	0.50	0.75
fcc ↔ tet-1	-	0.41	-	0.80
tet-1 ↔ tet-3	-	0.72	-	0.08
tet-3 ↔ oct	-	0.01	-	0.15

tet position (0.72 eV) is higher than in the reverse direction (0.56 eV) calculated with the force field, while in DFT, the sequence is reversed (0.41 eV and 0.74 eV). For the force field, the low barrier of (0.05 eV) for diffusion from the hcp to the tet position, located below the first surface layer (Figure S8a), constitutes another deviation. In DFT, we calculated no barrier, causing the oxygen to relax directly to the tet position.

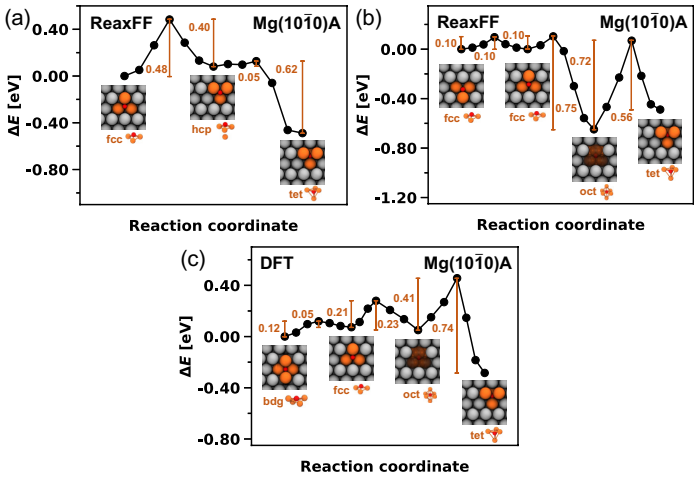

Figure S8: Diffusion profiles of an oxygen atom on Mg(10$\bar{1}$0)A calculated with ReaxFF a) from the fcc over the hcp to the tet site, b) from one fcc to the next fcc over the oct to the tet site, and with DFT c) from the bdg to the fcc over the oct to the tet site.

Table S4: Comparison of activation energies E_a in eV calculated using Equation (8) for forward and backward O-diffusion on Mg($10\bar{1}0$) for ReaxFF and DFT.

Mg($10\bar{1}0$)	$E_{a,ReaxFF}^{for}$	$E_{a,DFT}^{for}$	$E_{a,ReaxFF}^{rev}$	$E_{a,DFT}^{rev}$
fcc ↔ hcp	0.48	-	0.40	-
hcp ↔ tet	0.05	-	0.62	-
fcc ↔ fcc	0.10	-	0.10	-
bdg ↔ fcc	-	0.12	-	0.05
fcc ↔ oct	0.10	0.21	0.75	0.23
oct ↔ tet	0.72	0.41	0.56	0.74

O diffusion processes on Mg($10\bar{1}1$)

The oxygen atom diffusion barriers on Mg($10\bar{1}1$) are in agreement with the DFT reference activation energy (Table S5). E.g., the diffusion path from the hlw position via the tet-2 site (0.59 eV *vs.* 0.54 eV) to the tet-3 site (0.16 eV *vs.* 0.05 eV), as well as the reverse direction (0.25 eV *vs.* 0.19 eV for tet-3 to tet-2 and 0.51 eV *vs.* 0.49 eV for tet-2 to hlw), is accurately reproduced by the force field (cf. Figure S9b and S9d). However, differences emerge due to the overestimated thermodynamic stability of the oct position calculated by the force field. The diffusion of an oxygen atom from the tet-3 site (0.45 eV) or from the fcc to the oct site (0.13 eV) is highly preferred over its counterpart when calculations are performed with the force field (0.62 eV and 0.82 eV). In DFT, this sequence is reversed, and low barriers are associated with diffusion from the oct to the tet-3 site (0.16 eV) or the fcc position (0.11 eV). Equally of interest is the diffusion pathway for an oxygen atom at the hlw position coordinated by five Mg atoms towards the fcc or oct sites. While in the DFT, the oxygen atom significantly prefers to diffuse to the fcc position (0.66 eV), the trained force field predicts diffusion to the oct position (0.66 eV) (cf. Figure S9a and S9c).

Table S5: Comparison of activation energies E_a in eV calculated using Equation (8) for forward and backward O-diffusion on Mg($10\bar{1}1$) for ReaxFF and DFT.

Mg($10\bar{1}1$)	$E_{a,ReaxFF}^{for}$	$E_{a,DFT}^{for}$	$E_{a,ReaxFF}^{rev}$	$E_{a,DFT}^{rev}$
fcc ↔ oct	0.10	0.38	0.82	0.11
oct ↔ hlw	0.84	-	0.66	-
hlw ↔ tet-1	0.53	0.42	0.54	0.48
fcc ↔ hlw	-	0.62	-	0.66
hlw ↔ tet-2	0.59	0.54	0.51	0.49
tet-2 ↔ tet-3	0.16	0.05	0.25	0.19
tet-3 ↔ oct	0.45	-	0.62	-
tet-3 ↔ tet-4	-	0.56	-	0.12
tet-4 ↔ oct	-	0.07	-	0.11

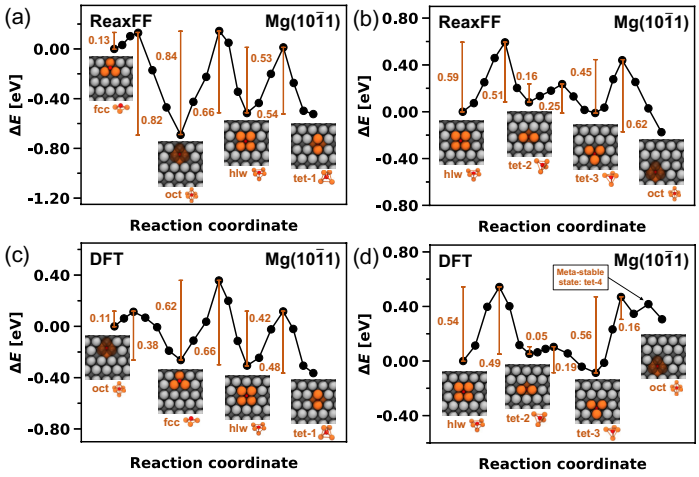

Figure S9: Diffusion profiles of an oxygen atom on Mg(10$\bar{1}$1) calculated with ReaxFF a) from the fcc to the oct over the hlw to the tet-1 site and b) from the hlw to the tet-2 over the tet-3 to the oct site and with DFT c) from the oct to the fcc over the hlw to the tet-1 site and d) from hlw to the tet-2 over the tet-3 to the oct site.

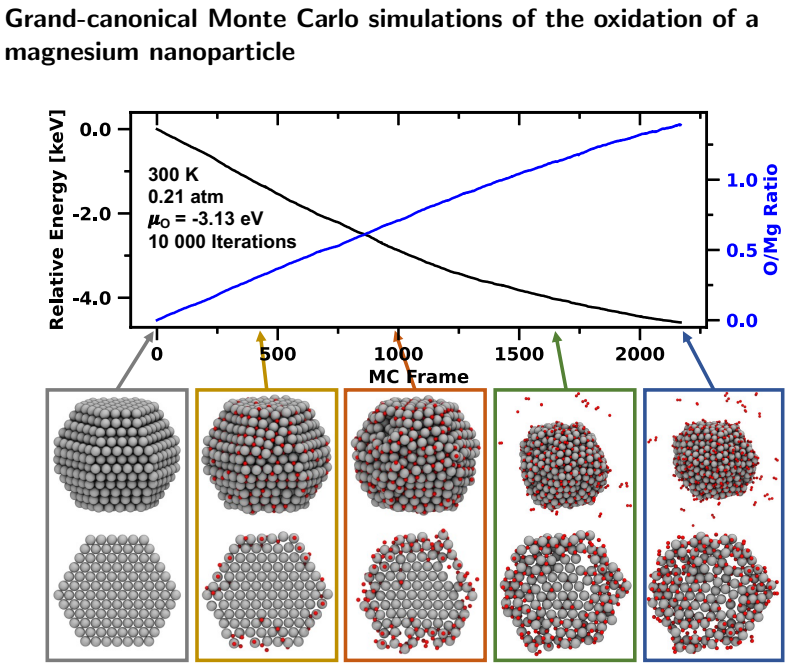

Figure S10: Grand-canonical Monte Carlo simulation showing the oxidation of an equilibrium-shaped Mg_{978} nanoparticle at 300 K and 0.21 atm. Initially, oxidation occurs at the surface but does not penetrate the particle's core. Instead, oxygen molecules are formed in the gas phase.

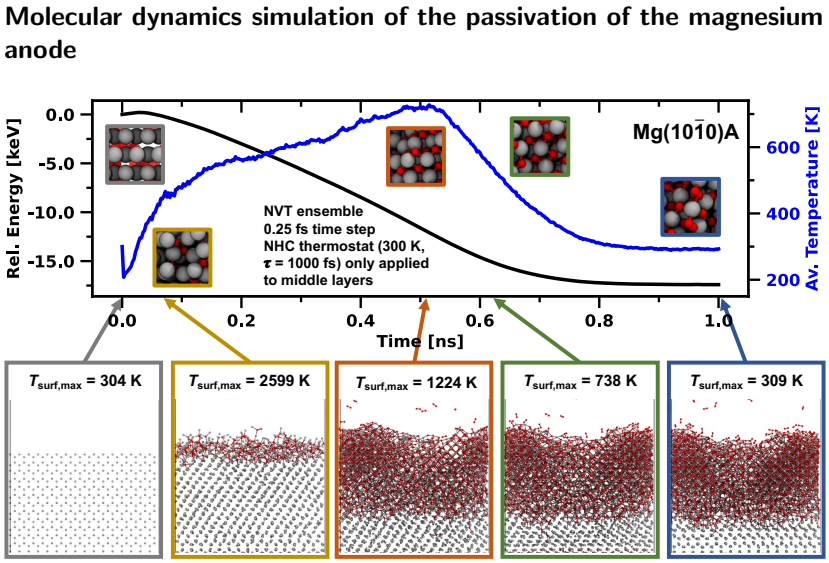

Figure S11: *NVT* simulation showing the oxidation behavior of Mg(10$\bar{1}$0)A at 300 K at 10 atm O_2 pressure. Upon contact of the first O_2 molecules, the surface heats up to several 1000 K. The high temperature fosters the formation of an rocksalt interphase on top of the Mg anode. The maximum surface temperature $T_{surf,max}$ was determined from the temperature profiles in Figure S15.

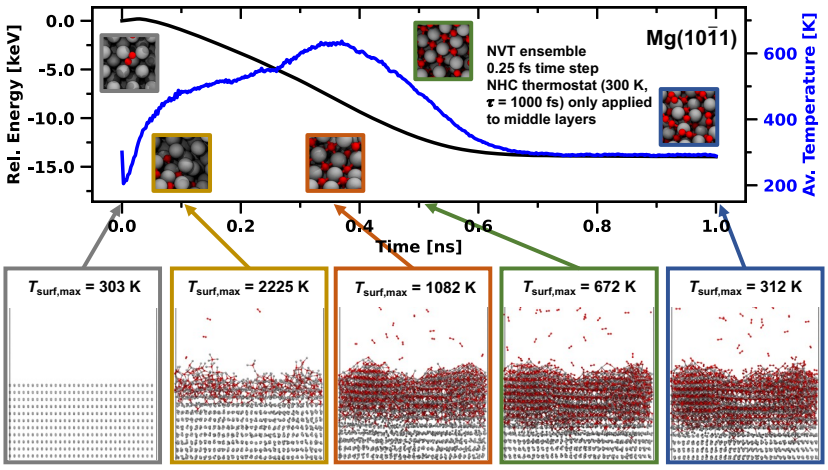

Figure S12: *NVT* simulation showing the oxidation behavior of Mg(10$\bar{1}$1) at 300 K at 10 atm O_2 pressure. Upon contact of the first O_2 molecules, the surface heats up to several 1000 K. The high temperature fosters the formation of an rocksalt interphase on top of the Mg anode. The maximum surface temperature $T_{surf,max}$ was determined from the temperature profiles in Figure S16.

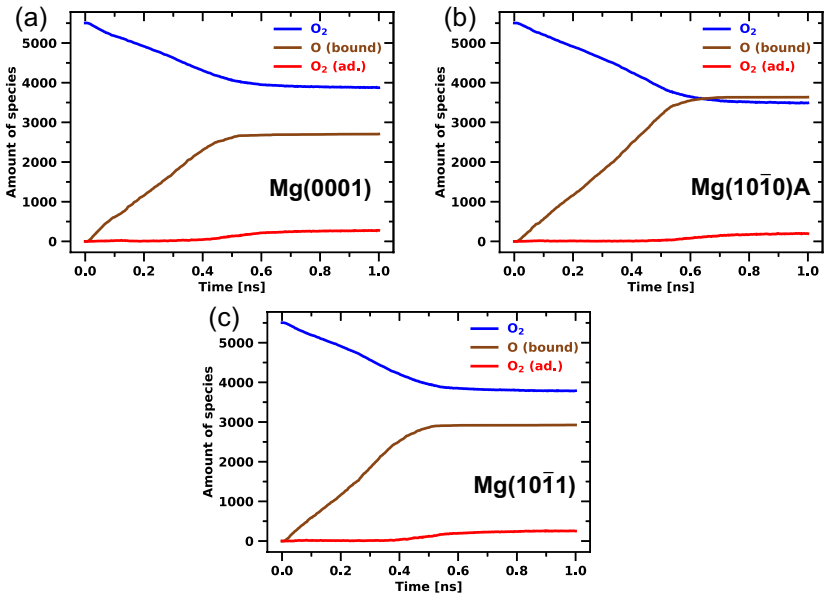

Figure S13: Analysis of the composition of molecular oxygen in the atmosphere O_2, adsorbed oxygen on the Mg surface O_2 (ad.), and bound oxygen atoms in the Mg bulk O (bound) for the NVT calculations on (a) Mg(0001), (b) Mg(10$\bar{1}$0)A, and (c) Mg(10$\bar{1}$1). Oxygen was counted as being in the atmosphere when two oxygen atoms were closer than 1.5 Å, but both were more than 2.45 Å away from a Mg bulk atom; they were considered adsorbed if two oxygen atoms were closer than 1.5 Å and one was closer than 2.45 Å from a Mg bulk atom or bound if one oxygen atom was closer than 2.45 Å to a Mg bulk atom but farther than 2.45 Å from the nearest oxygen atom.

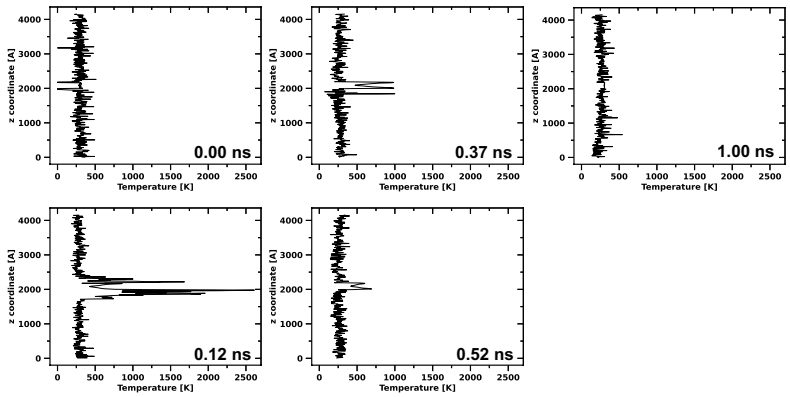

Figure S14: Temperature profiles along the z-axis from the selected snapshots in the colored boxes from the NVT calculation on Mg(0001) in Figure 7. The z-axis was divided into 500 equally sized sections, and the temperature of all atoms inside the corresponding box was calculated time-averaged over all MD steps since the previous snapshot. See documentation from SCM about Molecular Dynamics on https://www.scm.com/doc/AMS/Tasks/Molecular_Dynamics.html (accessed: August 2022).

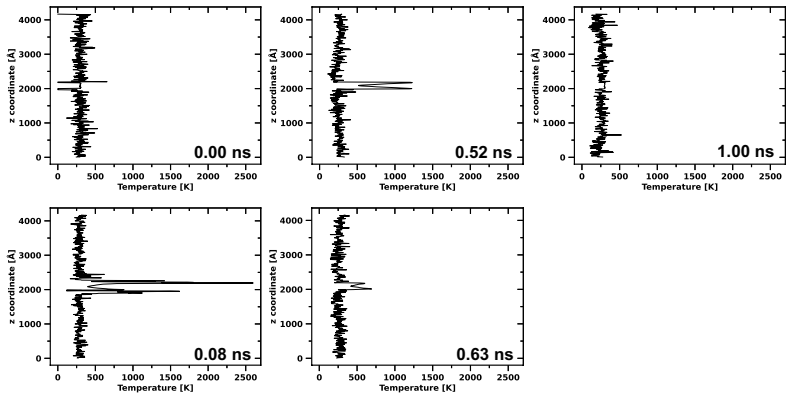

Figure S15: Temperature profiles along the z-axis from the selected snapshots in the colored boxes from the NVT calculation on Mg($10\bar{1}0$)A in Figure S11. The z-axis was divided into 500 equally sized sections, and the temperature of all atoms inside the corresponding box was calculated time-averaged over all MD steps since the previous snapshot. See documentation from SCM about Molecular Dynamics on https://www.scm.com/doc/AMS/Tasks/Molecular_Dynamics.html (accessed: August 2022).

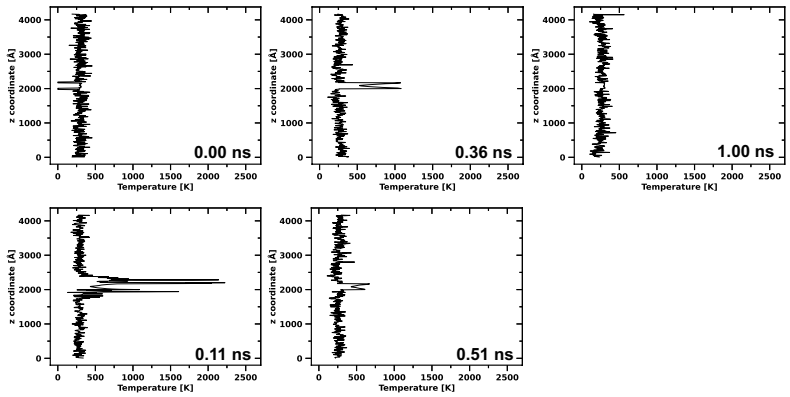

Figure S16: Temperature profiles along the z-axis from the selected snapshots in the colored boxes from the NVT calculation on Mg($10\bar{1}1$) in Figure S12. The z-axis was divided into 500 equally sized sections, and the temperature of all atoms inside the corresponding box was calculated time-averaged over all MD steps since the previous snapshot. See documentation from SCM about Molecular Dynamics on https://www.scm.com/doc/AMS/Tasks/Molecular_Dynamics.html (accessed: August 2022).

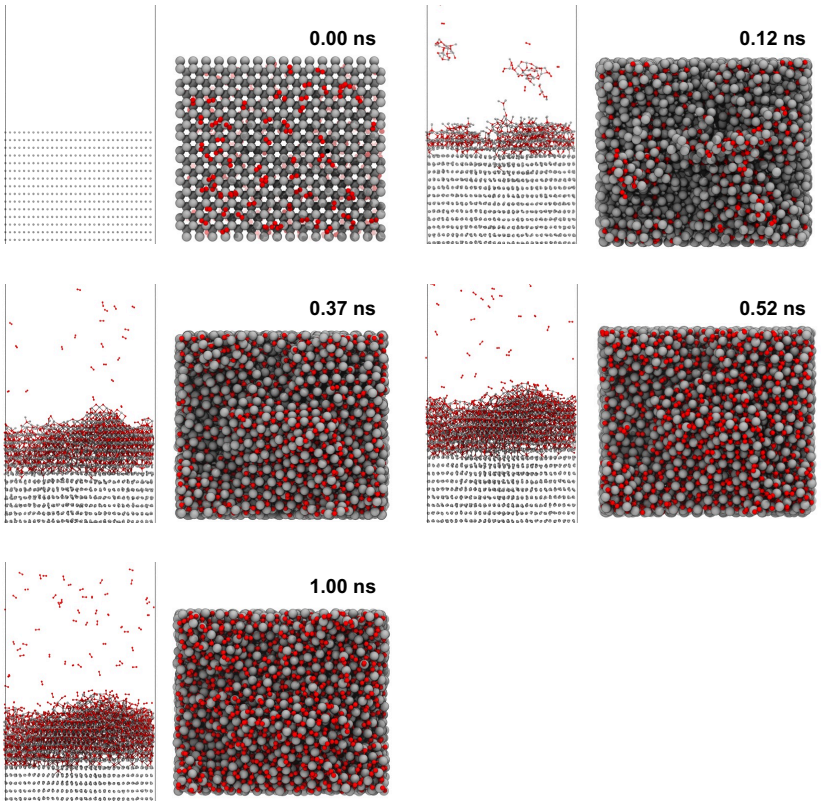

Figure S17: Enlarged images of the side and top views of the selected snapshots in the colored boxes from the NVT calculation on Mg(0001) in Figure 7.

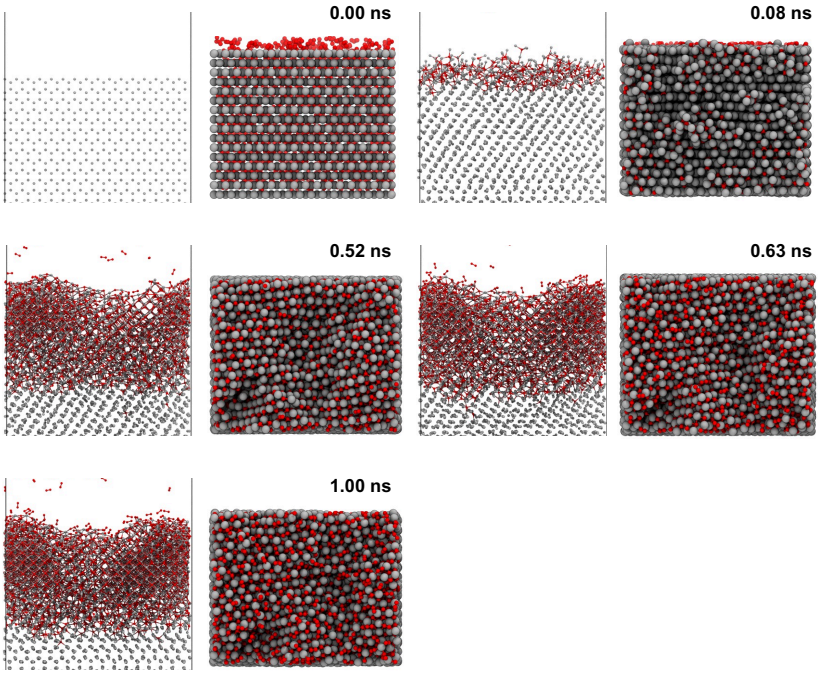

Figure S18: Enlarged images of the side and top views of the selected snapshots in the colored boxes from the NVT calculation on Mg($10\bar{1}0$)A in Figure S11.

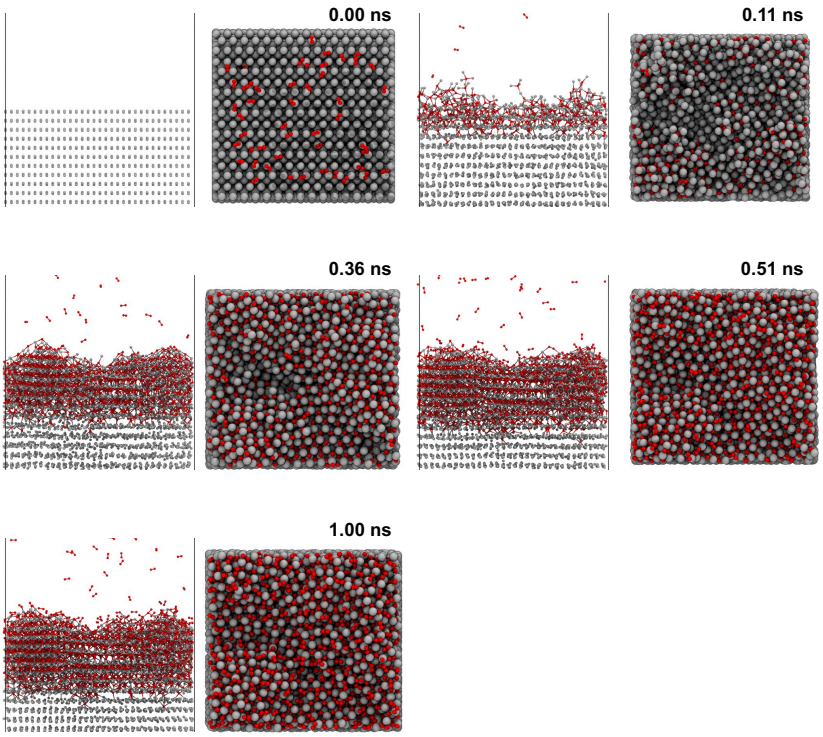

Figure S19: Enlarged images of the side and top views of the selected snapshots in the colored boxes from the NVT calculation on Mg($10\bar{1}1$) in Figure S12.

References

[1] F. Fiesinger, D. Gaissmaier, M. van den Borg, T. Jacob, *ChemSusChem* **2022**, *15*, e202200414.

4.3 Suitability of Carbazolyl Hauser and Turbo-Hauser Bases as Magnesium-Based Electrolytes

The following article is reprinted without changes from Philipp Schüler, Simon Sengupta, Steve Zaubitzer, Florian Fiesinger, Saustin Dongmo, Helmar Görls, Margret Wohlfahrt-Mehrens, Matthias van den Borg, Daniel Gaissmaier, Sven Krieck, Mario Marinaro, Timo Jacob, Matthias Westerhausen: Suitability of Carbazolyl Hauser and Turbo-Hauser Bases as Magnesium-Based Electrolytes, *Eur. J. Inorg. Chem.* **2022**, e202200149, published by Wiley-VCH GmbH as an open access article (`https://doi.org/10.1002/ejic.202200149`) under the terms of the Creative Commons Attribution License CC BY-NC-ND 4.0 (`https://creativecommons.org/licenses/by-nc-nd/4.0/`), which permits sharing, copying, and redistributing of the material in any medium or format.[33] ©2022 The authors.

Author Contributions: Philipp Schüler and Simon Sengupta synthesized the electrolyte, performed the crystal structure determination, and collected all NMR data, which they analyzed together with Helmar Görls, Sven Krieck, and Matthias Westerhausen. Steve Zaubitzer and Saustin Dongmo conducted the electrochemical measurements, XRD characterizations, and analyzed together with Mario Marinaro. Florian Fiesinger performed all the calculations and analyzed together with Daniel Gaissmaier, Matthias van den Borg, and Timo Jacob. Margret Wohlfahrt-Mehrens, Mario Marinaro, Timo Jacob, and Matthias Westerhausen supervised the research. The manuscript was written through contributions of all authors. All authors discussed the results and commented on the manuscript.

EurJIC
European Journal of Inorganic Chemistry

Research Article
doi.org/10.1002/ejic.202200149

Chemistry Europe
European Chemical Societies Publishing

www.eurjic.org

Suitability of Carbazolyl Hauser and Turbo-Hauser Bases as Magnesium-Based Electrolytes

Philipp Schüler[+],[a] Simon Sengupta[+],[a] Steve Zaubitzer,[b] Florian Fiesinger,[c] Saustin Dongmo,[b] Helmar Görls,[a] Margret Wohlfahrt-Mehrens,[b, d] Matthias van den Borg,[c] Daniel Gaissmaier,[c, d, e] Sven Krieck,[a] Mario Marinaro,[b] Timo Jacob,[c, d, e] and Matthias Westerhausen*[a]

Lithium-ion batteries pose certain drawbacks and alternatives are highly demanded. Requirements such as low corrosiveness, electrochemical stability and suitable electrolytes can be met by magnesium-ion batteries. Metalation of carbazole with Mg in THF in the presence of ethyl bromide yields the sparingly soluble Hauser base [(thf)$_3$Mg(Carb)Br] (**1**) which shows a Schlenk-type equilibrium with formation of [(thf)$_3$Mg(Carb)$_2$] and [(thf)$_4$MgBr$_2$]. A THF solution of **1** shows a low overpotential and a good cyclability of electrodeposition/-stripping of Mg on a Cu current collector. An improved performance is achieved with the turbo-Hauser bases [(thf)(Carb)Mg(μ-Br/X)$_2$Li(thf)$_2$] (X = Br (**2**) and Cl (**3**)) which show a significantly higher solubility in ethereal solvents. The THF solvation energies increase from (thf)$_x$MgBr$_2$ over (thf)$_x$Mg(Carb)Br to (thf)$_x$Mg(Carb)$_2$ for an equal number x of ligated THF molecules.

Introduction

Hauser bases are magnesium amide bases that have been described firstly by Hauser and Walker in 1947.[1] These bases represent valuable and often chemoselective metalation reagents.[2] Commonly Hauser bases R$_2$N–Mg(L)–X crystallize as dimeric complexes with bridging halide[3] or amido ligands.[3b,4] In solution, quite complex temperature-dependent Schlenk-type equilibria between mono- and dinuclear complexes on the one hand and homo- and heteroleptic compounds on the other have been elucidated for *i*Pr$_2$N–MgCl in THF solution based on DOSY-NMR experiments.[5] The addition of lithium halide produces the turbo-Hauser bases (Knochel-Hauser reagents) of the general type R$_2$N–MgCl·LiCl with enhanced reactivity and chemoselectivity.[6] Expectedly, equilibria between diverse species have been observed in solution by DOSY-NMR spectroscopy.[5,7] The preparation of these turbo-Hauser bases proceeds smoothly by deprotonation of secondary amines with Grignard reagents in the presence of lithium halide or with turbo-Grignard reagents such as *i*PrMgCl·LiCl.[8]

Besides the widely used application of Hauser and turbo-Hauser bases as selective metalation reagents, we are interested in magnesium batteries.[9] Not only the nature of the electrodes[10] plays an important role, but also the electrolyte causes challenges that have to be addressed beyond aqueous systems.[11]

The realization of zero-emission is one of the greatest challenges of our generation. For the transformation from classical fossil-based transportation to a fully electrical one, lithium-ion-batteries (LIBs) are nowadays the only choice due to their outstanding energy performance. Nevertheless, raw materials for LIBs are not available in unlimited quantities and therefore might not cover the increasing demand for electrochemical storage.[12] Furthermore, dendrite growth at the surface of Li metal and side reactions with the electrolyte pose challenges.[13] This has led scientists around the world to search for alternatives to today's established technologies.[14] Magnesium (Mg) possesses the highest volumetric capacity (3833 mAh cm^{-3}) compared to calcium (Ca) (2073 mAh cm^{-3}), lithium (Li) (2062 mAh cm^{-3}), and sodium (Na) (1128 mAh cm^{-3}) and furthermore, the high abundance makes a Mg-based battery as a promising candidate to opening up the post-lithium age. Since the realization of the first Mg battery by

[a] *P. Schüler,[+] S. Sengupta,[+] Dr. H. Görls, Dr. S. Krieck, Prof. Dr. M. Westerhausen*
Institute of Inorganic and Analytical Chemistry
Friedrich Schiller University Jena (FSU)
Humboldtstraße 8, 07743 Jena, Germany
E-mail: m.we@uni-jena.de
www.westerhausen.uni-jena.de
[b] *S. Zaubitzer, Dr. S. Dongmo, Dr. M. Wohlfahrt-Mehrens, Dr. M. Marinaro*
Zentrum für Sonnenenergie und Wasserstoff-Forschung Baden-Württemberg
Helmholtzstraße 8, 89081 Ulm, Germany
[c] *F. Fiesinger, M. van den Borg, D. Gaissmaier, T. Jacob*
Institute of Electrochemistry
University Ulm
Albert-Einstein-Allee 47, 89081 Ulm, Germany
[d] *Dr. M. Wohlfahrt-Mehrens, D. Gaissmaier, T. Jacob*
Helmholtz Institute Ulm (HIU) Electrochemical Energy Storage
Helmholtzstraße 11, 89081 Ulm, Germany
[e] *D. Gaissmaier, T. Jacob*
Karlsruhe Institute of Technology (KIT)
P.O. Box 3640, D-76021 Karlsruhe, Germany
[+] *These authors contributed equally to this publication.*

Supporting information for this article is available on the WWW under https://doi.org/10.1002/ejic.202200149

© 2022 The Authors. European Journal of Inorganic Chemistry published by Wiley-VCH GmbH. This is an open access article under the terms of the Creative Commons Attribution Non-Commercial NoDerivs License, which permits use and distribution in any medium, provided the original work is properly cited, the use is non-commercial and no modifications or adaptations are made.

© 2022 The Authors. European Journal of Inorganic Chemistry published by Wiley-VCH GmbH

10990682c, 2022, 17, Downloaded from https://chemistry-europe.onlinelibrary.wiley.com/doi/10.1002/ejic.202200149 by KIT, der Universitat Ulm, Wiley Online Library on [21/10/2022]. See the Terms and Conditions (https://onlinelibrary.wiley.com/terms-and-conditions) on Wiley Online Library for rules of use; OA articles are governed by the applicable Creative Commons License

EurJIC
European Journal of Inorganic Chemistry

Research Article
doi.org/10.1002/ejic.202200149

Chemistry Europe
European Chemical Societies Publishing

10990682c, 2022, 17, Downloaded from https://chemistry-europe.onlinelibrary.wiley.com/doi/10.1002/ejic.202200149 by KIT der Universitat Ulm, Wiley Online Library on [21/10/2022]. See the Terms and Conditions (https://onlinelibrary.wiley.com/terms-and-conditions) on Wiley Online Library for rules of use; OA articles are governed by the applicable Creative Commons License

using a Chevrel Phase (CP) as cathode and moreover the compatibility with a sulfur (S) cathode, the research activities onto the development of Mg-based electrolytes and appropriate electrolyte compatible electrode materials have been increased over time.[15]

Results and Discussion

Synthesis of Carbazolyl Magnesium Bromide

For the use as an electrolyte in magnesium batteries, specific requirements must be fulfilled such as low corrosiveness, electrochemical stability, straightforward synthesis, and high solubility in suitable solvents. Therefore, we studied the carbazolyl Hauser and turbo-Hauser bases. The direct magnesiation of carbazole by magnesium turnings is impossible. Therefore, we applied the *in-situ* Grignard metalation method (*i*GMM)[16] and added ethyl bromide to a suspension of carbazole and magnesium turnings in THF at room temperature as depicted in Scheme 1. Toward the end of the metalation reaction, carbazolyl magnesium bromide [(thf)$_3$Mg(Carb)Br] (**1**) crystallized from the reaction mixture in the shape of slightly greenish blocks. A Schlenk-type equilibrium between heteroleptic CarbMgBr on the one hand and homoleptic Mg(Carb)$_2$ and MgBr$_2$ on the other was observed in [D$_8$]THF solution by NMR spectroscopy (cf. Figures S1-S4). DOSY-NMR experiments verify the mononuclear nature of the magnesium amide complexes (cf. Figure S5).

The *i*GMM was performed in the presence of LiBr and of LiCl yielding the corresponding heterobimetallic turbo-Hauser bases as shown in Scheme 1 (for NMR cf. Figures S6-S10 and Figure S12). DOSY-NMR investigations supported the composition of 1:1 adducts of the type (Carb)MgLiBrX (X = Br (**2**), Cl (**3**)) (cf. Figure S11). The solubility significantly increased in the order **1** < **2** < **3**, and in fact, crystalline [(thf)$_3$Mg(Carb)Br] (**1**) is very sparingly soluble even in ethereal solvents.

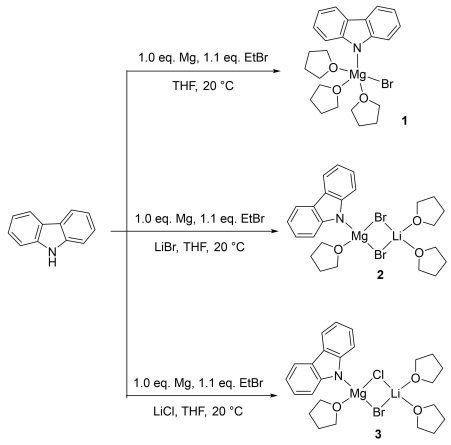

Scheme 1. Synthesis of thf adducts of the carbazolyl magnesium bromide (**1**, carbazolyl Hauser base) as well as its lithium bromide (**2**) and lithium chloride (**3**) adducts (carbazolyl turbo-Hauser bases).

Solid-State Structure

The molecular structure and atom labeling scheme of [(thf)$_3$Mg(Carb)Br] (**1**) are depicted in Figure 1. The magnesium atom Mg1 is in a trigonal bipyramidal environment with the two thf ligands of O1 and O3 in apical positions. The Mg1–N1 bond length of 204.5(3) pm is significantly larger than the Mg-N distances in dinuclear [(TMP)Mg(thf)(μ-Cl)]$_2$ (198.1(2) pm) and [(thf)$_2$Li(μ-Cl)$_2$Mg(thf)(TMP)] (195.58(14) pm)[3b] which is primarily a consequence of the larger coordination number of the magnesium center.

Electrochemical Study

Efficient metal deposition and stripping are crucial for operating metal-based batteries. Therefore, the reversibility of the electrodeposition and electro-stripping of Mg metal in the novel carbazolyl-based electrolyte was investigated using cyclic voltammetry (CV). Figure 2a shows the features of electrodeposition/-stripping of Mg metal on a Cu current collector. At cycle #10, the over-potential for Mg deposition was −330 mV

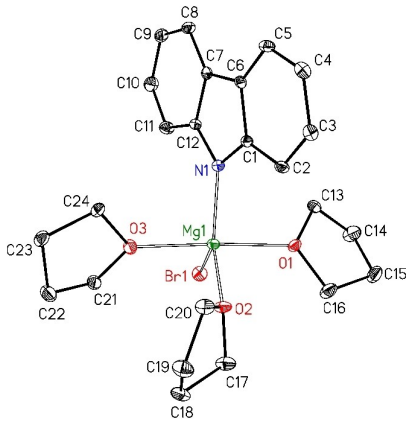

Figure 1. Molecular structure and atom labelling scheme of [(thf)$_3$Mg(Carb)Br] (**1**). The ellipsoids represent a probability of 30%, H atoms are neglected for the sake of clarity. Selected bond lengths (pm): Mg1–N1 204.5(3), Mg1–Br1 250.81(11), Mg1–O1 209.6(2), Mg1–O2 206.5(2), Mg1–O3 213.1(2); bond angles (deg.) at Mg1: N1—Mg1—Br1 125.65(9), N1–Mg1–O1 89.49(10), N1–Mg1–O2 120.62(11), N1–Mg1–O3 91.65(10), O1–Mg1–O2 87.44(10), O1–Mg1–O3 173.87(11), O1–Mg1–Br1 91.89(7), O2–Mg1–O3 86.80(10), O2–Mg1–Br1 113.72(8), O3–Mg1–Br1 92.34(7).

© 2022 The Authors. European Journal of Inorganic Chemistry published by Wiley-VCH GmbH

EurJIC
European Journal of Inorganic Chemistry

Research Article
doi.org/10.1002/ejic.202200149

Chemistry Europe
European Chemical Societies Publishing

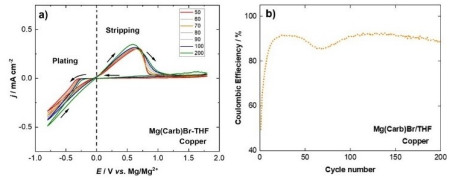

Figure 2. (a) Cyclic voltammograms of magnesium electro-deposition/electro-stripping on a Cu current collector using 0.26 M [$(thf)_3$Mg(Carb)Br] (**1**) in THF. Scan rate: 10 mV s^{-1}. RE/CE: Magnesium metal. (b) Respective Coulombic efficiency from cyclic voltammetry measurement.

vs. Mg/Mg^{2+} and further decreases down to −220 mV *vs.* Mg/Mg^{2+} at cycle #200th. The low over-potential and cyclability is a substantial improvement over the borate-based $Mg[B(hfip)_4]_2$/DME (~400 mV) and $B(OMgCl)_3$/Triglyme and Triglyme/THF (> 500 mV) electrolytes.[17] The Coulombic efficiency for the electro-deposition/-stripping process of Mg metal is close to 91 % (cf. Figure 2b).

This novel electrolyte formulation shows an increase in the electrolyte stability of 500 mV as in contrast to the reported stabilities of 1.5 V for Grignard-based electrolytes; it is for copper and stainless steel more than 2 V (cf. Figure S18).[18] The electrochemical performance in terms of cathodic and anodic current densities, which corresponds to the electro-deposition/-stripping process, respectively, and efficiency can be further improved with the addition of LiCl (cf. Figure S19). This might be due to the activation of the Mg surface by the chlorine-anion or either to the formation of a Li-contained Solid Electrolyte Interface (SEI).[19] The electro-deposited material on Cu current collector was characterized by XRD and SEM techniques. Figure 3b shows the XRD pattern of Mg metal deposited on the Cu current collector. The reflection patterns can be clearly assigned to a hexagonal Mg structure and to the Cu current collector (substrate).[20] Figure 3a shows that the Mg electro-deposited as compact particles with different orientations. Elemental analysis of the deposited material via EDX measurement confirmed the XRD findings of deposited Mg (cf. SI Figure S20).

The morphology of the electro-deposited Mg is influenced by the electrolyte composition. In the presence of LiCl, the Mg electro-deposited patchier (cf. Figure S21).

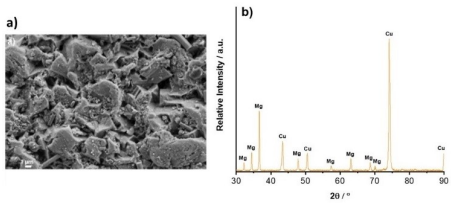

Figure 3. (a) Scanning electron micrograph of electro-deposited magnesium on copper current collector (magnification = 10.000-fold). (b) Respective XRD patterns of the electro-deposited magnesium obtained after chronopotentiometry at −0.6 mA cm^{-2}.

Computational Study

Density functional theory (DFT) calculations were performed to determine the solvation energies and Mulliken charges for $(thf)_x$MgCarbBr, $(thf)_x$Mg$(Carb)_2$, and $(thf)_x$MgBr_2 at different degrees of solvation ($x \triangleq$ number of coordinated THF molecules). As the degree of solvation increases, the structure of the electrolyte changes from a linear ($x = 0$) via a trigonal-planar ($x = 1$) to a tetrahedral ($x = 2$) via a trigonal-bipyramidal ($x = 3$) to an octahedral complex ($x = 4$), as shown in Table S1 (see Supporting Information). Table 1 summarizes the energy gain per additional THF molecule ($E_{solv,gain}$) as well as the cumulative solvation energy ($E_{solv,cum}$) for the corresponding conformation. The contribution to the solvation energetics per additional THF decreases, as expected, with an increasing degree of solvation. For example, the gain in solvation energy for Mg(Carb)Br is −148 kJ·mol^{-1} for the first, −125 kJ·mol^{-1} for the second, −94 kJ·mol^{-1} for the third, and −64 kJ·mol^{-1} for the fourth THF molecule. The cumulative solvation energies for a given degree of solvation are the highest for Mg$(Carb)_2$, followed by Mg(Carb)Br and $MgBr_2$. Following this order, the cumulative solvation energies for 3 coordinated THF molecules are −403 kJ·mol^{-1}, −367 kJ·mol^{-1}, and −336 kJ·mol^{-1}, respectively. This finding already indicates that the bromide ligand provides more negative charge to the Mg cation than the carbazolyl group, which would explain the stronger bonding between the central magnesium cation and the oxygen of THF for Mg$(Carb)_2$. We further see that the HOMO and LUMO energy levels increase (i.e. become less negative) with higher solvation degrees, as shown in Table 2. Since lower HOMO levels of the electrolyte correspond to better anodic stability, we expect a diminished oxidative stability with increasing THF solvation.[21]

The Mulliken charge analysis for MgCarbBr in Figure 4 indicates a decrease in negative charge on the THF oxygen atoms of approximately 4 % per additional THF molecule. This is caused by the lower individual contribution of each THF to donate negative charge to the magnesium cation. An increasing

Table 1. Solvation energy gain $E_{solv,gain}$ and cumulative solvation energy $E_{solv,cum}$ in kJ·mol^{-1} of heteroleptic $(thf)_x$MgCarbBr and homoleptic $(thf)_x$Mg$(Carb)_2$, as well as $(thf)_x$MgBr_2 at varying degrees of solvation (x = number of ligated THF molecules). Due to steric effects, a maximum of 3 THF molecules could be coordinated to Mg$(Carb)_2$. The total energies used for calculating $E_{solv,gain}$ and $E_{solv,cum}$ are given in Table S2 (see Supporting Information).

x	$(thf)_x$Mg(Carb)Br		$(thf)_x$Mg$(Carb)_2$		$(thf)_x$MgBr_2	
	$E_{solv,gain}$	$E_{solv,cum}$	$E_{solv,gain}$	$E_{solv,cum}$	$E_{solv,gain}$	$E_{solv,cum}$
1	−148	−148	−164	−164	−132	−132
2	−125	−273	−147	−311	−117	−249
3	−94	−367	−92	−403	−87	−336
4	−63	−430	–	–	−79	−414

© 2022 The Authors. European Journal of Inorganic Chemistry published by Wiley-VCH GmbH

10990682c, 2022, 17, Downloaded from https://chemistry-europe.onlinelibrary.wiley.com/doi/10.1002/ejic.202200149 by KIT-Universitat Ulm, Wiley Online Library on [21/10/2022]. See the Terms and Conditions (https://onlinelibrary.wiley.com/terms-and-conditions) on Wiley Online Library for rules of use; OA articles are governed by the applicable Creative Commons License

EurJIC
European Journal of Inorganic Chemistry

Research Article
doi.org/10.1002/ejic.202200149

Chemistry Europe
European Chemical Societies Publishing

10990682c, 2022, 17, Downloaded from https://chemistry-europe.onlinelibrary.wiley.com/doi/10.1002/ejic.202200149 by KIT-Der Universitaet Ulm, Wiley Online Library on [21/10/2022]. See the Terms and Conditions (https://onlinelibrary.wiley.com/terms-and-conditions) on Wiley Online Library for rules of use; OA articles are governed by the applicable Creative Commons License

Table 2. HOMO and LUMO energy levels in eV of heteroleptic $(thf)_xMgCarbBr$ and homoleptic $(thf)_xMg(Carb)_2$, as well as $(thf)_xMgBr_2$ at varying degrees of solvation (x = number of ligated THF molecules).

x	$(thf)_xMg(Carb)Br$		$(thf)_xMg(Carb)_2$		$(thf)_xMgBr_2$	
	E_{HOMO}	E_{LUMO}	E_{HOMO}	E_{LUMO}	E_{HOMO}	E_{LUMO}
1	−6.34	−0.62	−6.01	−0.64	−8.28	−0.22
2	−5.88	−0.13	−5.91	−0.22	−7.69	0.61
3	−5.74	−0.06	−5.79	−0.15	−7.31	0.78
4	−5.63	0.08	–	–	−6.81	0.89

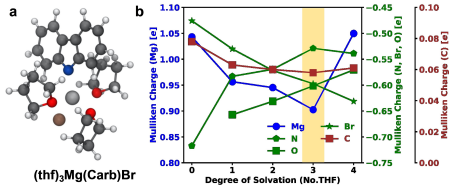

Figure 4. (a) Molecular structure of $(thf)_3Mg(Carb)Br$ calculated with DFT. (b) Respective Mulliken charges for Mg, N, Br, O and C at different solvation degrees. The charges for O are averaged over the oxygen atoms of the THFs. The same applies to the charges of the C atoms, which are averaged over the carbon atoms of the carbazolyl group. The yellow area marks the most probable degree of solvation according to NMR. Number of ligated THF molecules is in perfect agreement with NMR results. Calculated bond lengths of $(thf)_3Mg(Carb)Br$ (DFT) are also in agreement with X-ray structure results (pm): Mg1–N1 203.6, Mg1–Br1 247.3, Mg1–O1 216.5, Mg1–O2 210.8, Mg1–O3 219.6; bond angles (deg.) at Mg1: N1–Mg1–Br1 127.0, N1–Mg1–O1 88.4, N1–Mg1–O2 126.8, N1–Mg1–O3 91.5, O1–Mg1–O2 82.3, O1–Mg1–O3 166.7, O1–Mg1–Br1 94.4, O2–Mg1–O3 87.2, O2–Mg1–Br1 105.9, O3–Mg1–Br1 96.2.

degree of solvation is also associated with steric effects. In case of the bromine ligand in $(thf)_xMg(Carb)Br$, the Mg–Br bond increases (232.3 < 236.4 < 241.6 < 247.3 < 262.5 pm, for x = 0–4), resulting in about 10% less charge being transferred from bromine to magnesium per additional THF molecule. The Mg–N bond distance also increases upon solvation (192.4 < 198.0 < 199.8 < 203.6 < 212.1 pm, for x = 0–4), although the negative charge on the nitrogen atom decreases ($-0.71e < -0.58e < -0.57e < -0.53e < -0.52e$, for x = 0–4). The free-electron pairs of the THF oxygen atoms cause a negative charge transfer from the nitrogen electrons into the aromatic system of the carbazolyl group due to electrostatic repulsions. That is consistent with the averaged positive charge on the aromatic carbon atoms decreasing by approximately 10% with the first THF molecule and an additional 4% with each subsequent THF molecule. The charge on the magnesium cation remains largely constant but shows a minimum positive charge in the trigonal bipyramidal structure, which was experimentally determined by NMR spectroscopy. For the sake of completeness, the Mulliken charges of homoleptic $(thf)_xMg(Carb)_2$ and $(thf)_xMgBr_2$ may be found in the Supporting Information (Figure S22, Figure S23, and Table S3).

Conclusion

The *in-situ* Grignard metalation method (*i*GMM) of carbazole, i.e. the metalation of carbazole by Mg in the presence of ethyl bromide in THF, allows to prepare the slightly green Hauser base $[(thf)_3Mg(Carb)Br]$ (**1**) which is only sparingly soluble. A Schlenk-type equilibrium is operative leading to the formation of homoleptic $[(thf)_3Mg(Carb)_2]$ and $[(thf)_4MgBr_2]$. Quantum chemical calculations show preferred coordination numbers and increasing solvation energies in the series $(thf)_xMgBr_2 < (thf)_xMg(Carb)Br < (thf)_xMg(Carb)_2$ for an equal number x of ligated THF molecules. If the *i*GMM is performed in the presence of lithium halide, the heterobimetallic turbo-Hauser bases $[(thf)(Carb)Mg(\mu\text{-}Br/X)_2Li(thf)_2]$ (X = Br (**2**) and Cl (**3**)) form as has been verified by DOSY NMR spectroscopy. A THF solution of **1** shows a low over-potential and a good cyclability of electro-deposition/-stripping of Mg on a Cu current collector. An improved performance is achieved with the heterobimetallic turbo-Hauser bases $[(thf)(Carb)Mg(\mu\text{-}Br/Cl)_2Li(thf)_2]$.

Experimental Section

General information. All manipulations were carried out under an inert nitrogen atmosphere using standard Schlenk techniques, if not otherwise stated. The solvents were dried over KOH and subsequently distilled over sodium/benzophenone under a nitrogen atmosphere prior to use. All substrates were purchased from Alfa Aesar, abcr, Sigma Aldrich or TCI and used without further purification. The yields given are not optimized. Purity of the compounds was verified by NMR spectroscopy. Deuterated solvents were dried over sodium, distilled, degassed, and stored under nitrogen over sodium. ^{1}H, ^{29}Si and $^{13}C\{^{1}H\}$ NMR spectra were recorded on Bruker Avance III 400 (BBO, BBFO probes), Avance III HD 500 (BBO Prodigy probe) or Avance III HD 600 (TCI cryo probe) spectrometers. Chemical shifts are reported in parts per million relatively to $SiMe_4$ (^{1}H, ^{13}C) as an external standard referenced to the solvents residual proton signal using xiref AU program for ^{7}Li-NMR spectra. DOSY-NMR spectra were measured using the ledbpgp2 s standard pulse sequence. Molar masses in solution were calculated using the ECC-DOSY method.[22] ASAP-HSQC-spectra and ASAP-HSQC-DEPT-spectra were recorded using the published pulse sequences.[23]

*Synthesis of [(thf)$_3$CarbMgBr] (**1**).* Carbazole (4.93 g, 29.6 mmol, 1 eq.) and magnesium granules (0.79 g, 32.6 mmol, 1.1 eq.) were suspended in THF (60 mL). EtBr (2.22 mL, 6.0 mmol, 1 eq.) was added dropwise over 30 minutes and the reaction mixture was stirred at room temperature for 2 h. Titration of a hydrolysed aliquot with sulfuric acid (0.1 N) against phenolphthalein showed 88% yield. Almost after completion of the reaction the product crystallized spontaneously. The precipitate was collected by filtration (G3 frit) and dried under reduced pressure. $[(thf)_3MgCarbBr]$ (11.96 g, 24,3 mmol, 82%) was obtained as slightly green blocks. IR (ATR): 2981 (w), 2892 (w), 1619(w), 1493 (m), 1294 (m), 911 (m) cm^{-1}, m.p. = 138–143 C. In $[D_8]$THF solution a Schlenk-type equilibrium was observed. *Physical data of [(thf)$_3$Mg(Carb)Br] (**1**):* ^{1}H NMR ($[D_8]$THF, 297 K, 400 MHz): δ = 8.00 (d, J = 7.64 Hz, 2H), 7.73 (d, J = 8.16 Hz, 2H), 7.20 (t, J = 7.54 Hz, 2H), 6.92 (t, J = 7.33 Hz, 2H) ppm, ^{13}C NMR ($[D_8]$THF, 297 K, 101 MHz): δ = 150.0, 123.0, 119.0, 114.6, 113.6, ^{1}H DOSY ($[D_8]$THF, 297 K, 400 MHz): $D_{Ref,THF} = 2.43 \cdot 10^{-9}$ m^2/s, $D_{[(thf)4MgCarbBr} = 7.42 \cdot 10^{-10}$ m^2/s, $MW_{calc} = 590$ g mol^{-1}, $MW_{found} = 589$ g mol^{-1}, Δ = 0%. *Physical data of [(thf)MgCarb$_2$]:* ^{1}H NMR

© 2022 The Authors. European Journal of Inorganic Chemistry published by Wiley-VCH GmbH

EurJIC
European Journal of Inorganic Chemistry

Research Article
doi.org/10.1002/ejic.202200149

Chemistry Europe
European Chemical Societies Publishing

10990682c, 2022, 17, Downloaded from https://chemistry-europe.onlinelibrary.wiley.com/doi/10.1002/ejic.202200149 by KIT-Der Universitaet Ulm, Wiley Online Library on [21/10/2022]. See the Terms and Conditions (https://onlinelibrary.wiley.com/terms-and-conditions) on Wiley Online Library for rules of use; OA articles are governed by the applicable Creative Commons License

([D$_8$]THF, 297 K, 400 MHz): δ = 8.09 (d, J = 7.68 Hz, 2H), 7.60 (d, J = 8.20 Hz, 2H), 7.15 (t, J = 7.44 Hz, 2H), 6.97 (t, J = 7.30 Hz, 2H) ppm, ^{13}C NMR ([D$_8$]THF, 297 K, 101 MHz): δ = 150.0, 119.2, 118.4, 114.9, 114.0 ppm, ^{1}H DOSY ([D$_8$]THF, 297 K, 400 MHz): $D_{Ref,THF}$ = $2.43 \cdot 10^{-9}$ m^2 s^{-1}, $D_{[(thf)MgCarb2}$ = $8.50 \cdot 10^{-10}$ m^2 s^{-1}, MW_{calc} = 436 g mol^{-1}, MW_{found} = 467 g mol^{-1}, Δ = −7 %.

*Synthesis of [(thf)CarbMg(μ-Cl/Br)$_2$Li(thf)$_2$] (**2**).* NMR-scale: Carbazole (20 mg, 120 μmol,1 eq.), magnesium turnings (3 mg, 120 μmol, 1 eq.) and LiCl (4 mg, 0.8 eq. 96 μmol) were suspended in 550 μL of [D$_8$]THF. EtBr (9 μL, 1 eq.) was added, and the Young tube was sealed. After a few minutes gas evolution was observed and after 3 h gas evolution ceased. During this time, a yellow-green solution formed. Physical data of **2**: ^{1}H NMR ([D$_8$]THF, 233 K, 400 MHz): δ = 7.95, (d, J = 6.3 Hz, 4H), 7.07 (t, J = 7.36, 8.94 Hz, 2H), 6.81 (t, J = 6.84, 9.47 Hz, 2H) ppm, ^{13}C NMR ([D$_8$]THF, 233 K, 101 MHz): δ = 150.7, 122.2, 118.4, 115.9, 113.7 ppm, ^{7}Li NMR ([D$_8$]THF, 233 K, 155.5 MHz): δ = −0.05 (s) ppm, ^{1}H DOSY ([D$_8$]THF, 297 K, 400 MHz): $D_{Ref,THF}$ = $2.19 \cdot 10^{-9}$ m^2 s^{-1}, $D_{[(thf)CarbMg-μ-Cl,Br-Li(thf)2]}$ = $7.02 \cdot 10^{-10}$ m^2 s^{-1}, MW_{calc} = 553 g mol^{-1}, MW_{found} = 539 g mol^{-1}, Δ = 2 %.

*Synthesis of [(thf)CarbMg-μ-Br$_2$-Li(thf)$_2$] (**3**).* LiBr (1.58 g, 18,19 mmol, 1 eq.), Mg granules (440 mg, 18.19 mmol, 1 eq.) and carbazole (3.04 g, 18.19 mmol, 1 eq.) were suspended in 30 mL of THF and cooled to 10 C. EtBr (1.4 mL, 18.19 mmol, 1 eq.) was added in two portions and the reaction mixture was stirred for 2 h at room temperature. Physical data of **3**: ^{1}H NMR ([D$_8$]THF, 297 K, 400 MHz): δ = 7.93 (d, J = 7.7 Hz, 1H), 7.86 (d, J = 8.2 Hz, 1H), 7.19–7.07 (m, 1H), 6.90–6.80 (m, 1H), 3.65 (s, THF), 1.79 (s, THF) ppm, ^{13}C NMR ([D$_8$]THF, 297 K, 101 MHz): δ = 150.2, 125.1, 124.9, 122.7, 119.7, 118.6, 118.3, 114.2, 114.2, 110.5 ppm, ^{7}Li NMR ([D$_8$]THF, 297 K, 155.5 MHz): δ = 0.35 ppm, ^{1}H DOSY ([D$_8$]THF, 297 K, 400 MHz): $D_{Ref,Si(SiMe3)4}$ = $9.39 \cdot 10^{-10}$ m^2 s^{-1}, $D_{[(thf)CarbMg-μ-Br2-Li(thf)2]}$ = $6.37 \cdot 10^{-10}$ m^2 s^{-1}, MW_{calc} = 573 g mol^{-1}, MW_{found} = 581 g mol^{-1}, Δ = 1 %.

Crystal Structure Determination of 1. The intensity data for **1** were collected on a Nonius KappaCCD diffractometer using graphite-monochromated Mo-K$_\alpha$ radiation. Data were corrected for Lorentz and polarization effects; absorption was taken into account on a semi-empirical basis using multiple-scans.[24–26] The structures were solved by direct methods (SHELXS[27]) and refined by full-matrix least squares techniques against F_o^2 (SHELXL-2018).[28] All hydrogen atoms were located by difference Fourier synthesis and refined isotropically. All non-hydrogen atoms were refined anisotropically.[28] The program packages XP[29] and POV-Ray[30] were used for structure representations. Crystal and refinement data for **1**: $C_{24}H_{32}BrMgNO_3$, M = 486.72 g mol^{-1}, colorless prism, size 0.108 × 0.102 × 0.088 mm^3, monoclinic, space group $P2_1/n$, a = 11.3856(2), b = 14.5083(4), c = 14.3729(4) Å, β = 107.130(1) , V = 2268.88(10) Å^3, T = −140 C, Z = 4, $\rho_{calcd.}$ = 1.425 g cm^{-3}, μ (Mo-K$_\alpha$) = 18.65 cm^{-1}, multi-scan, $trans_{min}$: 0.6939, $trans_{max}$: 0.7456, F(000) = 1016, 16569 reflections in h(−14/14), k(−18/18), l(−18/18), measured in the range 2.042 ≤ Θ ≤ 27.484 , completeness Θmax = 99.8 %, 5171 independent reflections, R_{int} = 0.0573, 4228 reflections with $F_o > 4\sigma(F_o)$, 399 parameters, 0 restraints, $R1_{obs}$ = 0.0484, wR^2_{obs} = 0.1002, $R1_{all}$ = 0.0646, wR^2_{all} = 0.1091, GOOF = 1.078, largest difference peak and hole: 0.588/−0.625 e Å^{-3}.

Electrochemical Characterization. Copper foil (99.95 %, *thickness* = 0.01 mm, Schlenk), magnesium foil (99.95 %, *thickness* = 0.15 mm, Goodfellow) and magnesium wire (99.99 %, *d* = 1 mm, Goodfellow) were used as working, counter and reference electrodes, respectively. Prior to use, the copper foil was dried under vacuum at 120 C. To remove the thin native oxide layer from the magnesium current collector the surface was polished with sandpaper (1200 micron). The electrochemical measurements were performed inside a glovebox in a three-electrode configuration using EL-Cell ECC-Ref cells conducted to a BioLogic VMP3 potentiostat. Magnesium and Copper foil used as counter and working electrode (*d* = 18 mm) and a piece of magnesium wire was used as reference electrode, respectively. A glass fiber used as separator (1.55 mm thick, ECC-01-0021-C/L, EL-Cell) used as reservoir for Mg electrolyte (450 μL). Cyclic voltammetry experiments were run in a potential range between −0.8 V to 1.8 V *vs.* Mg/Mg^{2+} at a scan rate of 10 mV s^{-1}. Mg was electro-deposited onto copper current collector using chronopotentiometry at a fixed current density of −0.6 mA cm^{-2}.

Ex-situ Analysis. X-ray diffraction (XRD) and scanning electron microscopy (SEM) were applied to characterize the morphology of the electrodeposited Mg on the current collector. XRD pattern was recorded using an air-dome sample holder in a single scan between 10 and 90 in 0.02 2θ increments on a Bruker AXS D8 Discover using Cu–Kα radiation, a Ni-monochromator and a LYNXEYE 2D energy dispersive detector. The SEM images have been obtained with a LEO 1530 VP microscope with an acceleration of 5.0 kV and a secondary electron detector.

Computational Details. All electrolyte structures were generated using the Amsterdam Modelling Suite and pre-optimized with the semi-empirical MOPAC engine.[31] Spin unrestricted, non-relativistic first principle geometry optimizations were subsequently performed within the Amsterdam Density Functional (ADF) framework, using slater type orbitals (STOs) with a triple-ζ polarized (TZP), all-electron basis set and the meta hybrid exchange correlation functional MN15 as part of the LibXC library.[32] Convergence criteria were chosen to be $2.6 \cdot 10^{-3}$ kJ · mol^{-1} for the energy difference between two consecutive self-consistent field (SCF) cycles and 2.6 kJ · mol^{-1} · Å^{-1} for the forces during geometry optimization. The gain in solvation energy per additional THF $E_{solv,gain}$ was calculated for $(thf)_xMg(Carb)Br$, $(thf)_xMg(Carb)_2$, and $(thf)_xMgBr_2$ using equation 1, where x equals the number of coordinated THF solvent molecules.

$$E_{solv,\ gain} = E^{(thf)_x Electrolyte} - E^{(thf)_{(x-1)} Electrolyte} - E^{thf} \quad (1)$$

In addition, the cumulative solvation energy for a given conformation was determined by equation 2:

$$E_{solv,\ cum} = \sum_{(thf)_1}^{(thf)_x} E^{(thf)_x Electrolyte}_{solv,\ gain} \quad (2)$$

Atomic charges were obtained by the Mulliken charge analysis.[33]

Supporting Information (see footnote on the first page of this article)

Experimental details, analytical methods as well as NMR spectra and theoretical data (pdf format). Crystallographic data (excluding structure factors) has been deposited with the Cambridge Crystallographic Data Centre as supplementary publication CCDC-2142703 for **1**. Copies of the data can be obtained free of charge on application to CCDC, 12 Union Road, Cambridge CB2 1EZ, UK [E- mail: deposit@ccdc.cam.ac.uk].

Deposition Number 2142703 (for **1**) contains the supplementary crystallographic data for this paper. These data are provided free of charge by the joint Cambridge Crystallographic Data Centre and Fachinformationszentrum Karlsruhe Access Structures service www.ccdc.cam.ac.uk/structures.

© 2022 The Authors. European Journal of Inorganic Chemistry published by Wiley-VCH GmbH

EurJIC
European Journal of Inorganic Chemistry

Research Article
doi.org/10.1002/ejic.202200149

Chemistry Europe
European Chemical Societies Publishing

10990682c, 2022, 17, Downloaded from https://chemistry-europe.onlinelibrary.wiley.com/doi/10.1002/ejic.202200149 by KIT-Bibliothek, Wiley Online Library on [21/10/2022]. See the Terms and Conditions (https://onlinelibrary.wiley.com/terms-and-conditions) on Wiley Online Library for rules of use; OA articles are governed by the applicable Creative Commons License

Acknowledgements

We acknowledge the valuable support of the NMR service platform (www.nmr.uni-jena.de/) of the Faculty of Chemistry and Earth Sciences of the Friedrich Schiller University Jena, Germany. P. Schüler is very grateful to the German Environment Foundation (Deutsche Bundesstiftung Umwelt, DBU, grant no. 20018/578) for a generous Ph.D. grant. This work contributes to the research performed at CELEST (Center for Electrochemical Energy Storage Ulm-Karlsruhe) and was partly funded by the German Research Foundation (DFG) under Project ID 390874152 (POLiS Cluster of Excellence). The authors acknowledge support by the state of Baden-Württemberg through bwHPC and the German Research Foundation (DFG) through grant no INST 40/575-1 FUGG (JUSTUS 2 cluster). Open Access funding enabled and organized by Projekt DEAL.

Conflict of Interest

The authors declare no conflict of interest.

Data Availability Statement

The data that support the findings of this study are available in the supplementary material of this article.

Keywords: Batteries · Electrolytes · Hauser bases · Magnesium · Structure elucidation · Turbo-Hauser bases

[1] a) C. R. Hauser, H. G. Walker, *J. Am. Chem. Soc.* **1947**, *69*, 295–297; b) C. R. Hauser, C. R. Hance, *J. Am. Chem. Soc.* **1951**, *73*, 5846–5848.
[2] a) B. Haag, M. Mosrin, H. Ila, V. Malakhov, P. Knochel, *Angew. Chem. Int. Ed.* **2011**, *50*, 9794–9824; *Angew. Chem.* **2011**, *123*, 9968–9999; b) A. Kremsmair, J. H. Harenberg, K. Schwärzer, A. Hess, P. Knochel, *Chem. Sci.* **2021**, *12*, 6011–6019.
[3] a) K.-C. Yang, C.-C. Chang, J.-Y. Huang, C.-C. Lin, G.-H. Lee, Y. Wang, M. Y. Chiang, *J. Organomet. Chem.* **2002**, *648*, 176–187; b) P. García-Álvarez, D. V. Graham, E. Hevia, A. R. Kennedy, J. Klett, R. E. Mulvey, C. T. O'Hara, *Angew. Chem. Int. Ed.* **2008**, *47*, 8079–8081; *Angew. Chem.* **2008**, *120*, 8199–8201.
[4] a) A. S. Batsanov, P. D. Bolton, R. C. B. Copley, M. G. Davidson, J. A. K. Howard, C. Lustig, R. D. Price, *J. Organomet. Chem.* **1998**, *550*, 445–448; b) D. R. Armstrong, P. Garcá-Álvarez, A. R. Kennedy, R. E. Mulvey, J. A. Parkinson, *Angew. Chem. Int. Ed.* **2010**, *49*, 3185–3188; *Angew. Chem.* **2010**, *122*, 3253–3256.
[5] R. Neufeld, T. L. Teuteberg, R. Herbst-Irmer, R. A. Mata, D. Stalke, *J. Am. Chem. Soc.* **2016**, *138*, 4796–4806.
[6] Selected recent examples demonstrate the scope of these turbo-Hauser bases: a) A. Castelló-Micó, J. Nafe, K. Higashida, K. Karaghiosoff, M. Gingras, P. Knochel, *Org. Lett.* **2017**, *19*, 360–363; b) M. Balkenhohl, R. Greiner, I. S. Makarov, B. Heinz, K. Karaghiosoff, H. Zipse, P. Knochel, *Chem. Eur. J.* **2017**, *23*, 13046–13050; c) A. Castelló-Micó, P. Knochel, *Synthesis* **2018**, *50*, 155–169; d) M. Balkenhohl, B. Salgues, T. Hirai, K. Karaghiosoff, P. Knochel, *Org. Lett.* **2018**, *20*, 3114–3118; e) M. Baenziger, S. Eswaran, Y. Jiang, G. Kasinathan, *Synthesis* **2019**, *51*, 1649–1654; f) K. Schwärzer, C. P. Tüllmann, S. Graßl, B. Górski, C. E. Brocklehurst, P. Knochel, *Org. Lett.* **2020**, *22*, 1899–1902.
[7] R. Neufeld, D. Stalke, *Chem. Eur. J.* **2016**, *22*, 12624–12628.
[8] R. L.-Y. Bao, R. Zhao, L. Shi, *Chem. Commun.* **2015**, *51*, 6884–6900.
[9] S. Dongmo, S. Zaubitzer, P. Schüler, S. Krieck, L. Jörissen, M. Wohlfahrt-Mehrens, M. Westerhausen, M. Marinaro, *ChemSusChem* **2020**, *13*, 3530–3538.
[10] M. Mao, T. Gao, S. Hou, C. Wang, *Chem. Soc. Rev.* **2018**, *47*, 8804–8841.
[11] J. Muldoon, C. B. Bucur, T. Gregory, *Chem. Rev.* **2014**, *114*, 11683–11720.
[12] M. Marinaro, D. Bresser, E. Beyer, P. Faguy, K. Hosoi, H. Li, J. Sakovica, K. Amine, M. Wohlfahrt-Mertens, S. Passerini, *J. Power Sources* **2020**, *459*, 228073.
[13] A. Mauger, C. M. Julien, *Inorganics* **2022**, *10*, 5.
[14] a) M. Armand, J.-M. Tarascon, *Nature* **2008**, *451* (7179), 652–657; b) M. R. Palacin, *Acc. Mater. Res.* **2021**, *2*, 319–326.
[15] a) D. Aurbach, Z. Lu, A. Schechter, Y. Gofer, H. Gizbar, R. Turgemann, Y. Cohen, *Nature* **2000**, *407* (6805), 724–727; b) H. S. Kim, T. S. Arthur, G. D. Allred, J. Zajicek, J. G. Newman, A. E. Rodnyansky, A. G. Oliver, W. C. Boggess, J. Muldoon, *Nat. Commun.* **2011**, *2* (1), 426–427; c) R. Dominiko, J. Bitenc, R. Berthelot, M. Gauthier, G. Pagot, V. Di Noto, *J. Power Sources* **2020**, *478*; d) Y. Liang, H. Dong, D. Aurbach, Y. Yao, *Nat. Energy* **2020**, *5* (9), 646–656; e) Q. Guo, W. Zeng, S.-L. Liu, Y.-Q. Li, J.-Y. Xu, Y. Wang, *Rare Met.* **2021**, *40* (2), 290–308; f) F. Maroni, S. Dongmo, C. Gauckler, M. Marinaro, M. Wohlfahrt-Mertens, *Batteries & Supercaps* **2021**, *4*, 1–32.
[16] S. Krieck, P. Schüler, J. M. Peschel, M. Westerhausen, *Synthesis* **2019**, *51*, 1115–1122.
[17] a) Z. Zhao-Karger, M. Gil Bardaji, O. Fuhr, M. Fichtner, *J. Mater. Chem. A* **2017**, *5* (22), 10815–10820; b) K. Sato, G. Mori, T. Kiyosu, T. Yaji, K. Nakanishi, T. Otha, K. Okamoto, Y. Orikasa, *Sci. Rep.* **2020**, *10* (1), 7362.
[18] A. Ponrouch, M. R. Palacín, *Phil. Trans. R. Soc. A* **2019**, *377*, 20180297.
[19] a) K. Tang, A. Du, S. Dong, Z. Cui, X. Liu, C. Lu, J. Zhao, X. Zhou, G. Cui, *Adv. Mater.* **2020**, *32* (6), 1904987; b) S. S. Kim, K. A. See, *ACS Appl. Mater. Interfaces* **2021**, *13* (1), 671–680.
[20] H. E. Swanson, E. Tatge, *Natl. Bur. Stand. Rep.* **1953**, (ICDD PDF No. 00–004-0770).
[21] a) Z. Li, O. Fuhr, M. Fichtner, Z. Zhao-Karger, *Energy Environ. Sci.* **2019**, *12*, 3496–3501; b) A. J. Crowe, K. K. Stringham, B. M. Bartlett, *ACS Appl. Mater. Interfaces* **2016**, *8*, 23060–23065; c) W. Ren, D. Wu, Y. NuLi, D. Zhang, Y. Yang, Y. Wang, J. Yang, J. Wang, *ACS Energy Lett.* **2021**, *6*, 3212–3220.
[22] R. Neufeld, D. Stalke, *Chem. Sci.* **2015**, *6*, 3354–3364.
[23] a) D. Schulze-Sünnighausen, J. Becker, B. Luy, *J. Am. Chem. Soc.* **2014**, *136*, 1242–1245; b) D. Schulze-Sünnighausen, J. Becker, M. R. M. Koos, B. Luy, *J. Magn. Reson.* **2017**, *281*, 151–161.
[24] R. Hooft: COLLECT, Data Collection Software; Nonius B. V., Netherlands, **1998**.
[25] Z. Otwinowski, W. Minor, in *Methods in Enzymology* (Eds. C. W. Carter, R. M. Sweet), vol. *276*, part A, Academic Press, San Diego, USA, **1997**, pp. 307–326.
[26] L. Krause, R. Herbst-Irmer, G. M. Sheldrick, D. Stalke, *J. Appl. Crystallogr.* **2015**, *48*, 3–10.
[27] G. M. Sheldrick, *Acta Crystallogr. Sect. A* **2015**, *71*, 3–8.
[28] G. M. Sheldrick, *Acta Crystallogr. Sect. C* **2015**, *71*, 3–8.
[29] XP, Siemens Analytical X-ray Instruments Inc., Karlsruhe, Germany, **1990**; Madison, WI, USA, **1994**.
[30] POV-Ray, Persistence of Vision Raytracer, Victoria, Australia, **2007**.
[31] a) AMS 2020, SCM, Theoretical Chemistry, Vrije Universiteit, Amsterdam, The Netherlands, http://www.scm.com. **2020**; b) J. J. P. Stewart, *J. Mol. Model.* **2013**, *19*, 1–32; c) AMS 2020 MOPAC: MOPAC Engine based on the MOPAC2016 source code (J. P. James, http://OpenMOPAC.net).
[32] a) G. te Velde, F. M. Bickelhaupt, E. J. Baerends, C. Fonseca Guerra, S. J. A. van Gisbergen, J. G. Snijders, T. Ziegler, *J. Comput. Chem.* **2001**, *22*, 931–967; b) ADF 2020, SCM, Theoretical Chemistry, Vrije Universiteit, Amsterdam, The Netherlands, http://www.scm.com. **2020**; c) D. P. Chong, E. Van Lenthe, S. Van Gisbergen, E. J. J. Baerends, *Comput. Chem.* **2004**, *25*, 1030–1036; d) H. S. Yu, X. He, S. L. Li, D. G. Truhlar, *Chem. Sci.* **2016**, *7*, 5032–5051; e) S. Lehtola, C. Steigemann, M. J. T. Oliveira, M. A. L. Marques, *SoftwareX* **2018**, *7*, 1–5.
[33] R. S. Mulliken, *J. Chem. Phys.* **1955**, *23*, 1833–1840.

Manuscript received: March 9, 2022
Revised manuscript received: March 15, 2022
Accepted manuscript online: March 16, 2022

© 2022 The Authors. European Journal of Inorganic Chemistry published by Wiley-VCH GmbH

European Journal of Inorganic Chemistry

Supporting Information

Suitability of Carbazolyl Hauser and Turbo-Hauser Bases as Magnesium-Based Electrolytes

Philipp Schüler[+], Simon Sengupta[+], Steve Zaubitzer, Florian Fiesinger, Saustin Dongmo, Helmar Görls, Margret Wohlfahrt-Mehrens, Matthias van den Borg, Daniel Gaissmaier, Sven Krieck, Mario Marinaro, Timo Jacob, and Matthias Westerhausen*

Contents

Analytical details S1
Analytical Details of [(thf)$_3$MgCarbBr] (**1**) S1
Analytical Details of [(thf)MgCarb-μ-(Cl, Br)-Li(thf)$_2$] S4
Analytical Details of (thf)$_3$MgCarbBr + LiBr S8
Electrochemical details S11
Computational details S13

Analytical details

Analytical Details of [(thf)$_3$MgCarbBr] (**1**)

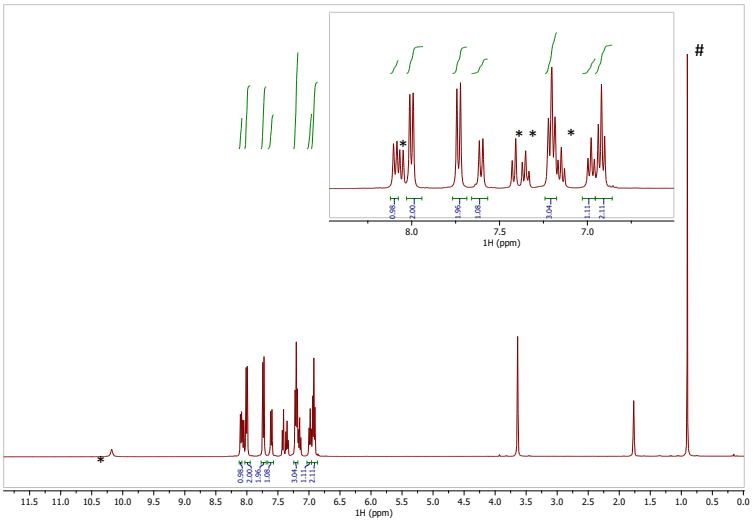

Figure S1: ^{1}H NMR spectrum (400 MHz, [D$_8$]THF, 297 K) of [(thf)$_3$Mg(Carb)Br] (*CarbH, # ethane).

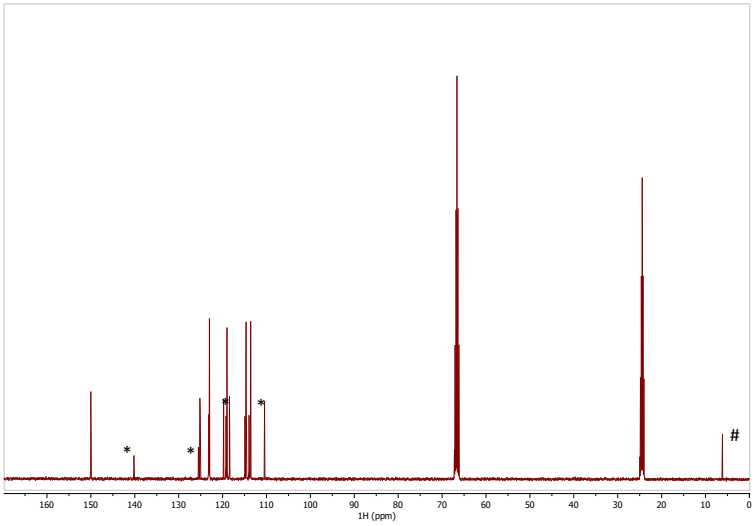

Figure S2: $^{13}C\{^{1}H\}$ NMR spectrum (101 MHz, $[D_8]THF$, 297 K) of $[(thf)_3Mg(Carb)Br]$ (*CarbH, # ethane).

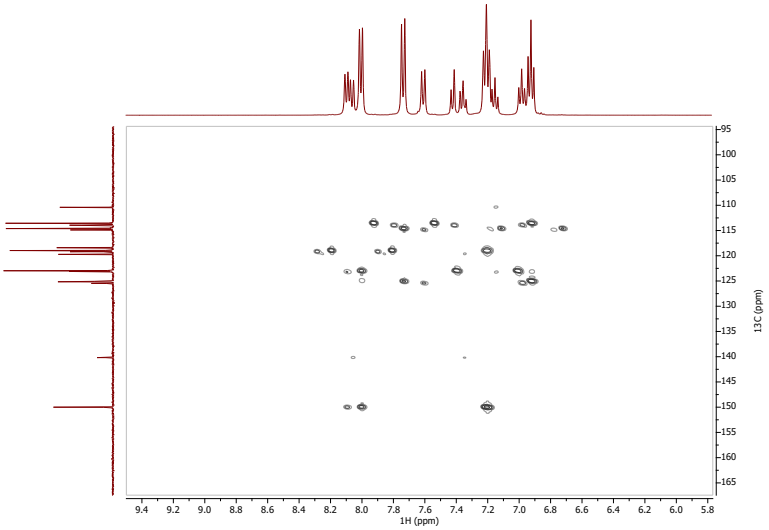

Figure S3: $^{1}H,^{13}C$-HMBC NMR spectrum (400 MHz, $[D_8]THF$, 297 K) of $[(thf)_3Mg(Carb)Br]$ (aromatic region).

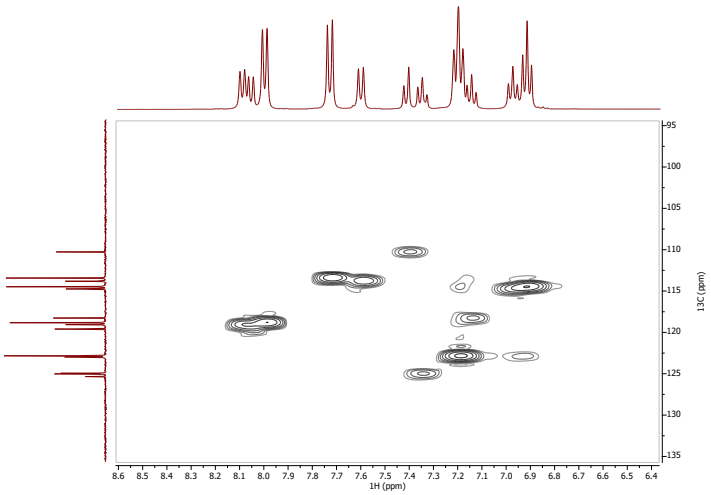

Figure S4: $^{1}H,^{13}C$-ASAP-HSQC NMR spectrum (400 MHz, $[D_8]$THF, 297 K) of $[(thf)_3Mg(Carb)Br]$ (aromatic region).

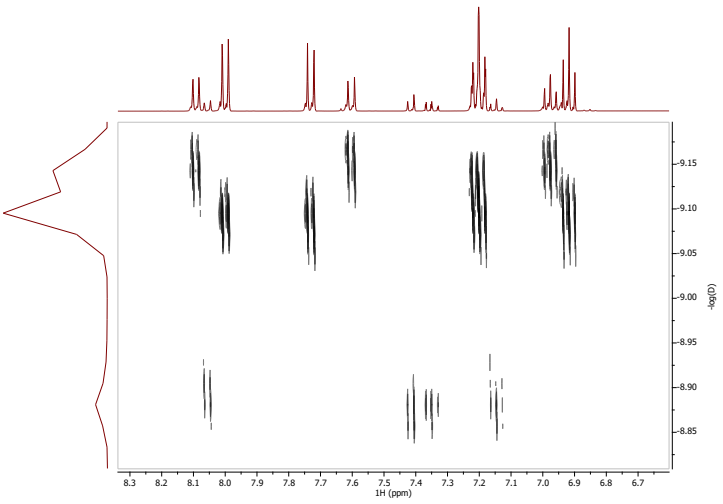

Figure S5: ^{1}H-DOSY NMR spectrum (400 MHz, $[D_8]$THF, 297 K) of $[(thf)_3Mg(Carb)Br]$ (aromatic region).

Analytical Details of [(thf)Mg(Carb)(μ-Cl/Br)$_2$Li(thf)$_2$] (**2**)

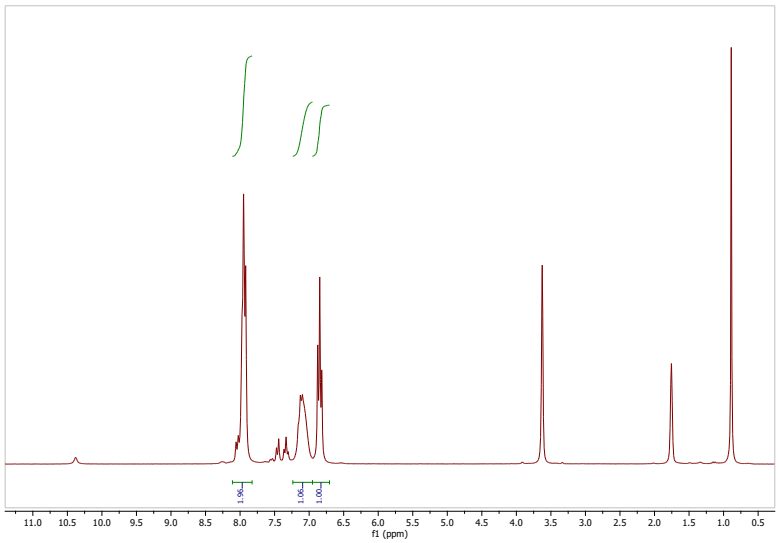

Figure S6: ^{1}H NMR spectrum (400 MHz, [D$_8$]THF, 297 K) of [(thf)Mg(Carb)(μ-Cl/Br)$_2$Li(thf)$_2$].

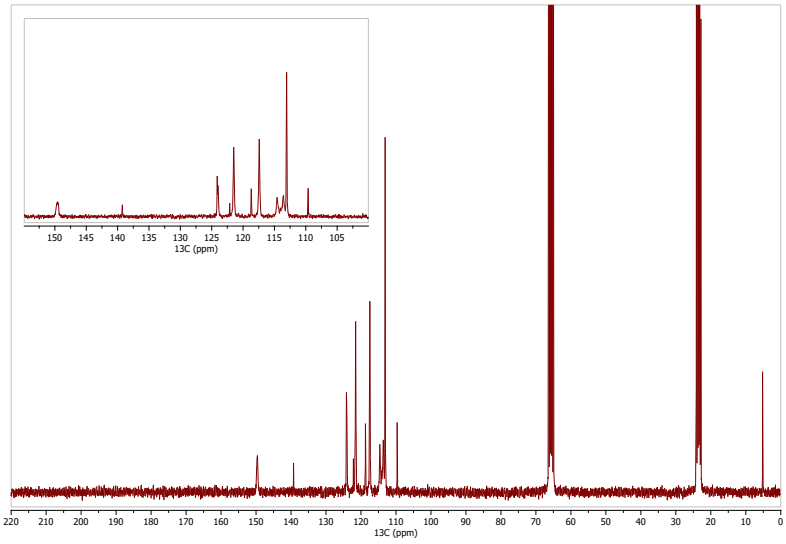

Figure S7: ^{13}C{^{1}H} NMR spectrum (101 MHz, [D$_8$]THF, 297 K) of [(thf)Mg(Carb)(μ-Cl/Br)$_2$Li(thf)$_2$].

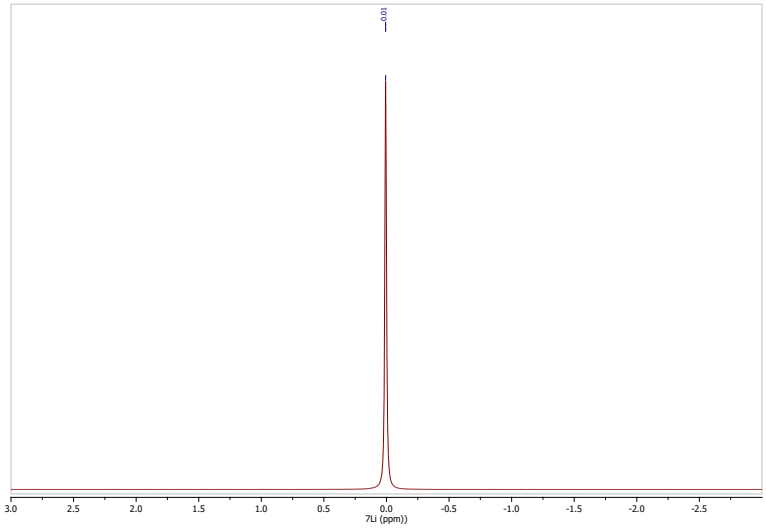

Figure S8: ^{7}Li NMR spectrum (155.5 MHz, [D_8]THF, 297 K) of [(thf)Mg(Carb)(μ-Cl/Br)$_2$Li(thf)$_2$].

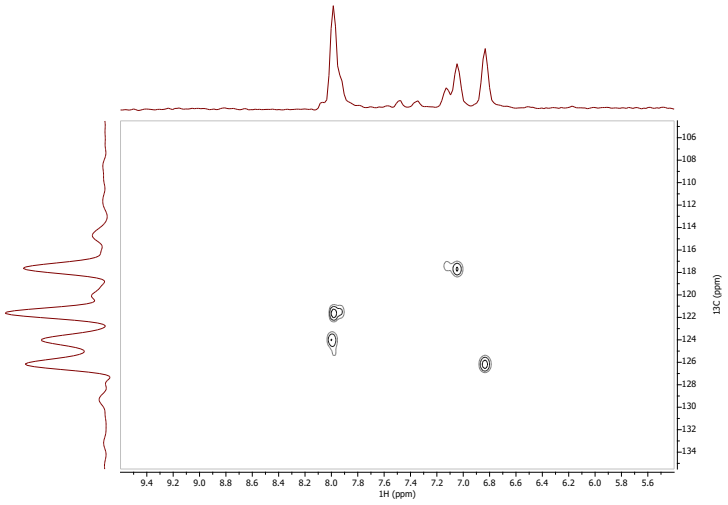

Figure S9: HSQC NMR spectrum (400 MHz, [D_8]THF, 297 K) of [(thf)Mg(Carb)(μ-Cl/Br)$_2$Li(thf)$_2$].

S5

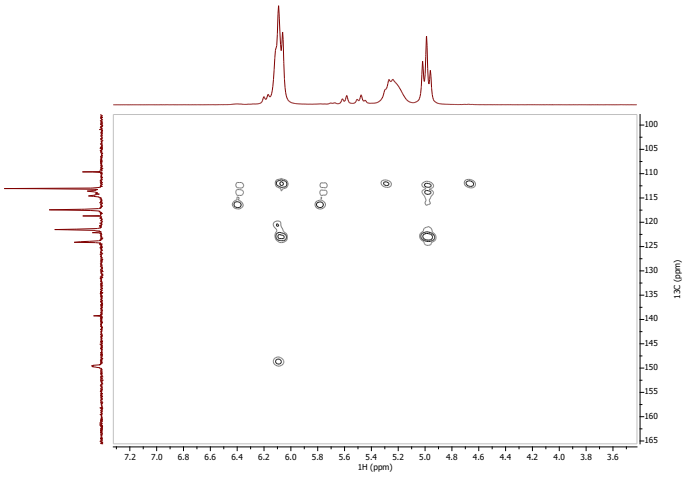

Figure S10: HMBC NMR spectrum (400 MHz, $[D_8]$THF, 297 K) of $[(thf)Mg(Carb)(\mu\text{-}Cl/Br)_2Li(thf)_2]$.

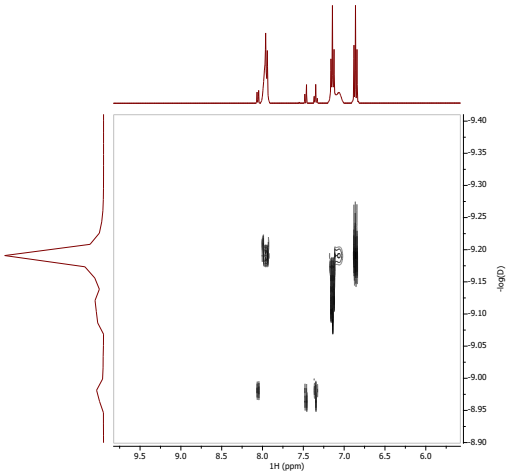

Figure S11: DOSY NMR spectrum (400 MHz, $[D_8]$THF, 297 K) of $[(thf)Mg(Carb)(\mu\text{-}Cl/Br)_2Li(thf)_2]$.

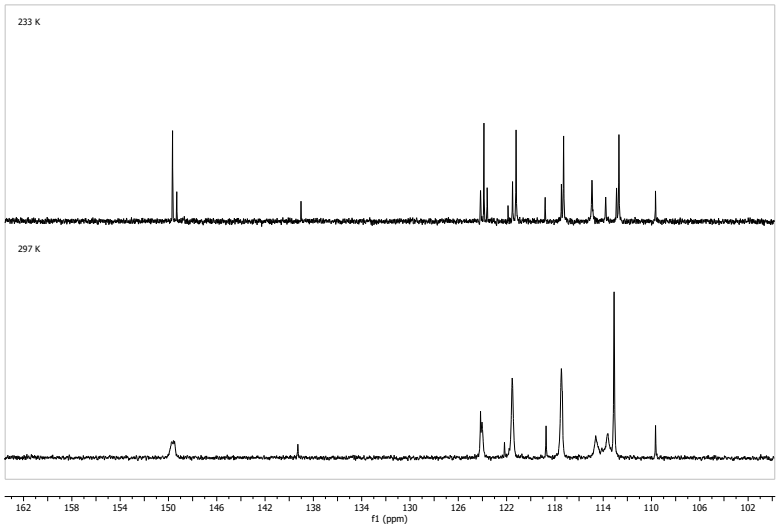

Figure S12: Temperature dependent ^{13}C NMR spectra (101 MHz, $[D_8]THF$, 297 K) of $[(thf)Mg(Carb)(\mu\text{-}Cl/Br)_2Li(thf)_2]$.

Analytical Details of $(thf)_3Mg(Carb)Br + LiBr$

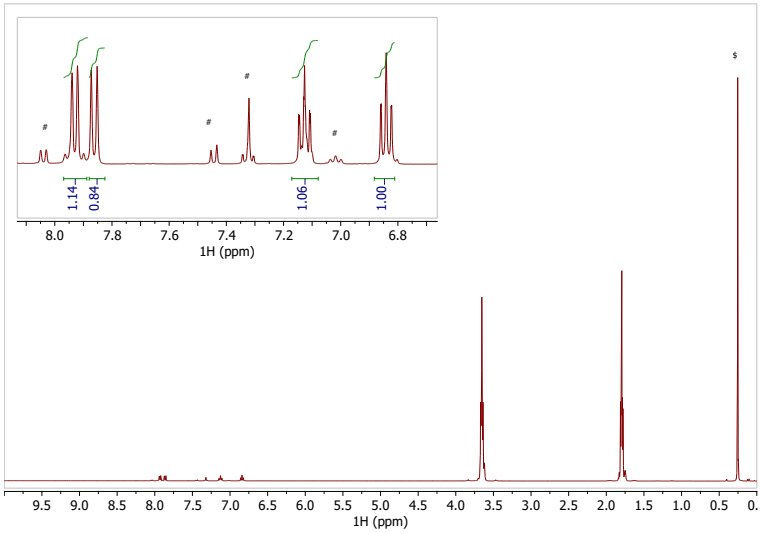

Figure S13: ^{1}H NMR spectrum (400 MHz, $[D_8]THF$, 297 K) of $[(thf)Mg(Carb)(\mu\text{-}Br)_2Li(thf)_2]$ (#-carbazole, $-Si(SiMe_3)_4$).

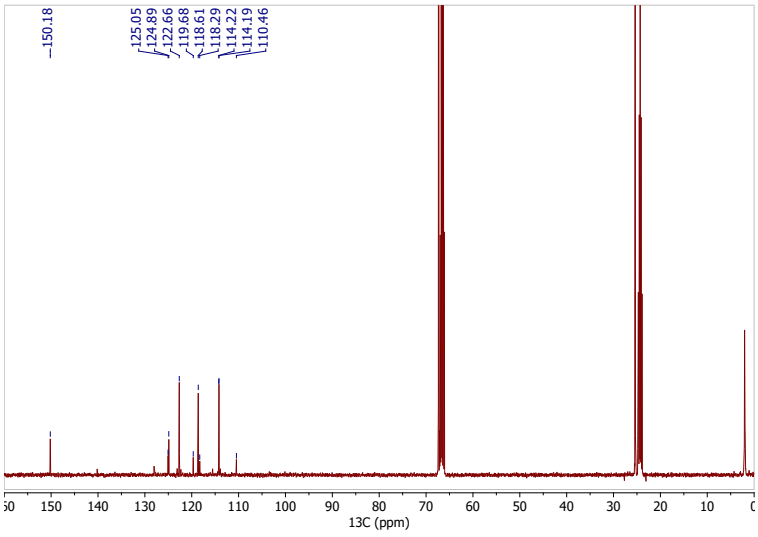

Figure S14: $^{13}C\{^{1}H\}$ NMR spectrum (101 MHz, $[D_8]THF$, 297 K) of $[(thf)Mg(Carb)(\mu\text{-}Br)_2Li(thf)_2]$.

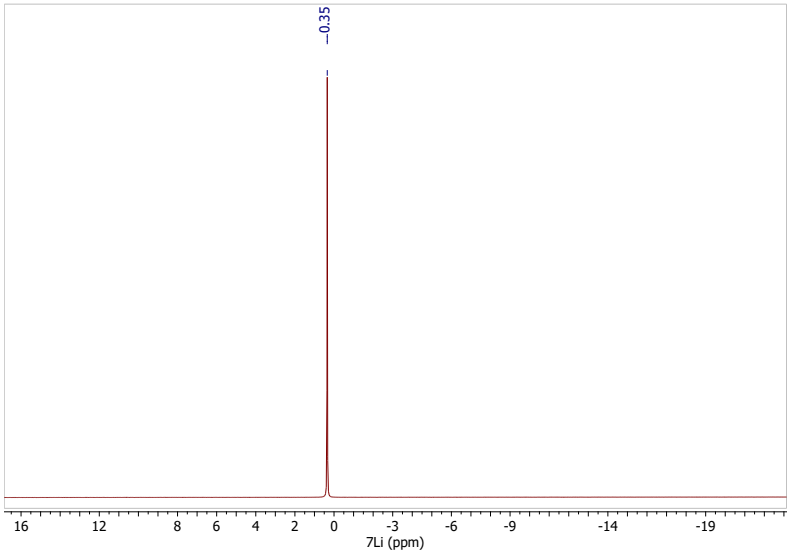

Figure S15: ^{7}Li NMR spectrum (101 MHz, [D$_8$]THF, 297 K) of [(thf)Mg(Carb)(μ-Br)$_2$Li(thf)$_2$].

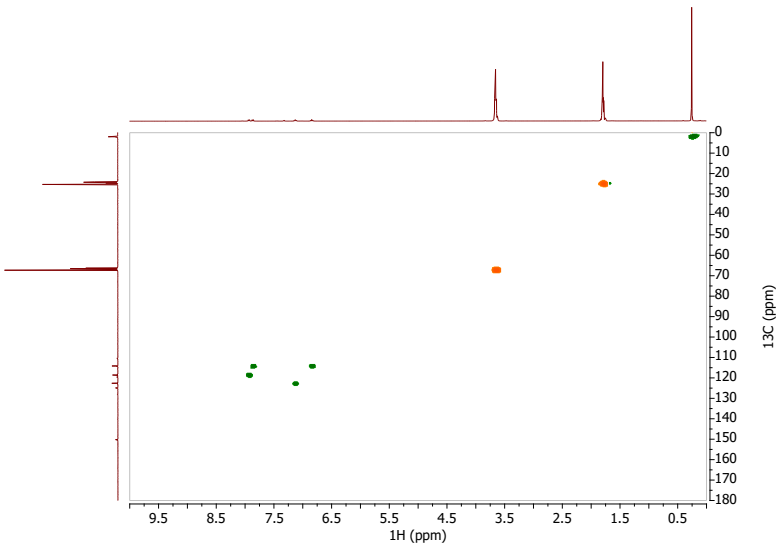

Figure S16: HSQC-DEPT NMR spectrum (400 MHz, [D$_8$]THF, 297 K) of [(thf)Mg(Carb)(μ-Br)$_2$Li(thf)$_2$].

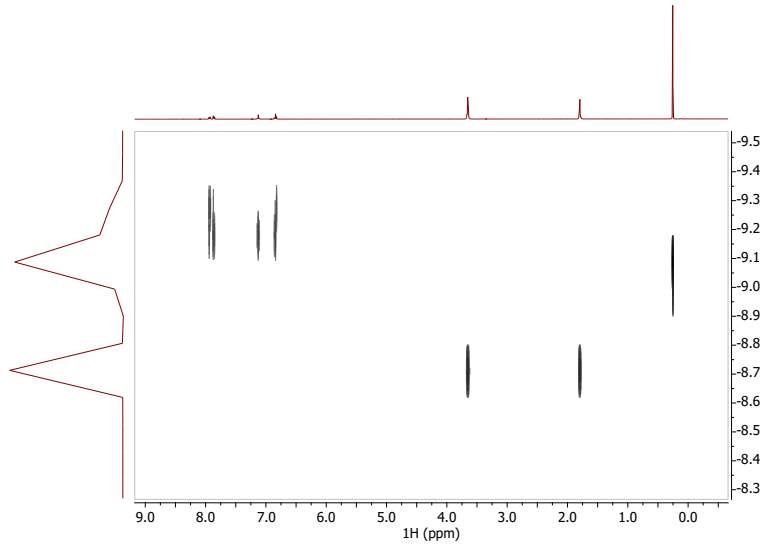

Figure S17: ^{1}H-DOSY NMR spectrum (400 MHz, [D$_8$]THF, 297 K) of [(thf)Mg(Carb)(μ-Br)$_2$Li(thf)$_2$].

Electrochemical details

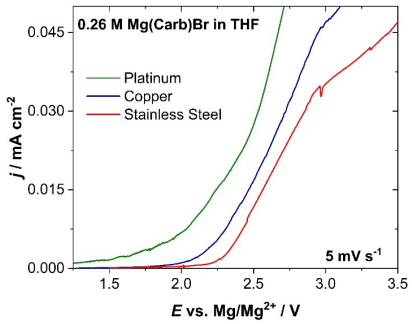

Figure S18: Linear sweep voltammetry of a 0.26 M Mg(Carb)Br in THF electrolyte on a platinum (green), copper (blue) and stainless steel (red) electrode, in a three-electrode setup with Mg as counter and reference electrodes. Sweep rate 5 mV s^{-1}.

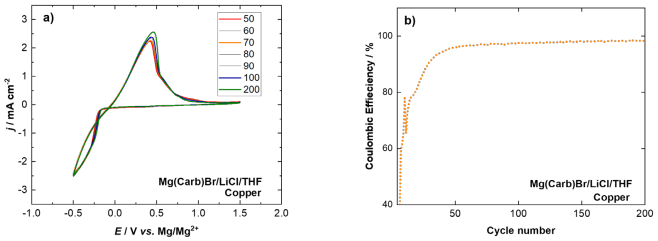

Figure S19: a) Cyclic voltammograms of magnesium electro-deposition/electro-stripping of a 0.41 M Mg(Carb)Br/LiCl-THF electrolyte solution using a copper current collector. Scan rate: 10 mV s^{-1}. RE/CE: Magnesium metal. b) Respective Coloumbic efficiency from cyclic voltammetry measurement.

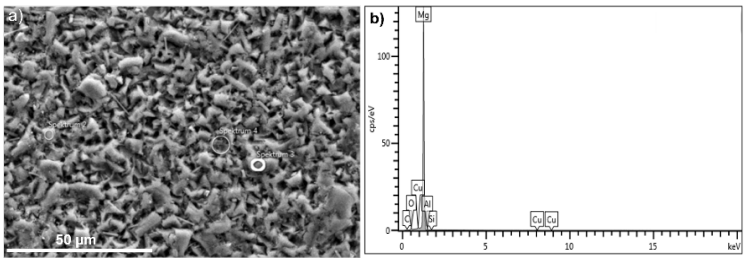

Figure S20: a) SEM image of the electro-deposited magnesium onto a copper current collector after chronopentiometry at a current density of -0.6 mA cm^{-2} using a 0.26 M Mg(Carb)Br/THF electrolyte. b) Respective elemental composition plot of the electro- deposited material.

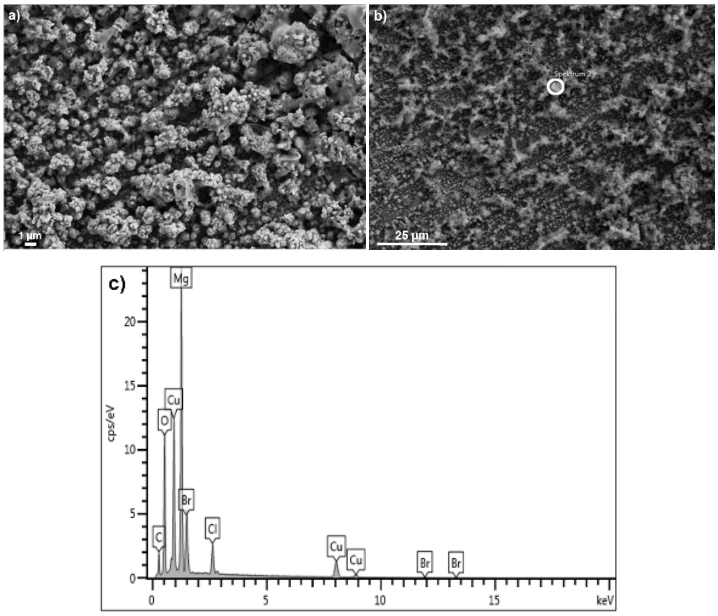

Figure S21: a) Scanning electron micrographs of electro-deposited magnesium on copper current collector after chronopotentiometry at a current density of -0.6 mA cm^{-2} using a 0.41 M Mg(Carb)Br/LiCl-THF electrolyte. b) Investigated area for the SEM-EDX analysis of the electro-deposited magnesium. c) Respective elemental composition plot of the electro- deposited material.

Computational details

Table S1: Geometries of $(thf)_xMgCarbBr$, $(thf)_xMg(Carb)_2$, and $(thf)_xMgBr_2$ at different degrees of solvation ($x \triangleq$ number of coordinated THFs). As the degree of solvation increases, the structure of the electrolyte changes from a linear ($x = 0$) via a trigonal-planar ($x = 1$) to a tetrahedral ($x = 2$) via a trigonal-bipyramidal ($x = 3$) to an octahedral complex ($x = 4$). Due to steric effects, a maximum of 3 THFs could be coordinated to $Mg(Carb)_2$. Color codes are light grey for Mg, brown for Br, blue for N, red for O, dark grey for C and white for H.

x **# of THF (geometry)**	**$(thf)_xMg(Carb)Br$**	**$(thf)_xMg(Carb)_2$**	**$(thf)_xMgBr_2$**
0 (linear)	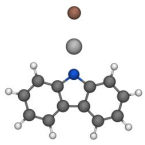	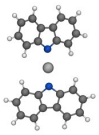	
1 (trigonal-planar)	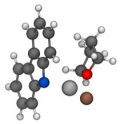		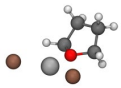
2 (tetrahedral)	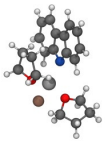	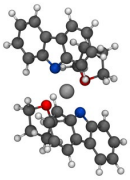	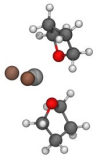
3 (trigonal-bipyramidal)	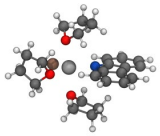		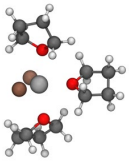
4 (octahedral)	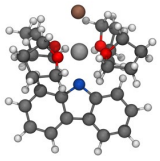	-	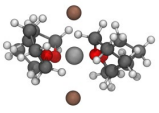

Table S2: Detailed total energies of $(thf)_xMgCarbBr$, $(thf)_xMg(Carb)_2$, and $(thf)_xMgBr_2$ at different degrees of solvation (x ≙ number of coordinated THFs) involved in the calculation of the solvation energy gain $E_{solv,gain}$ and cumulative solvation energy $E_{solv,cum}$ in kJ·mol^{-1}. The total reference energy of THF E^{thf} equals -9.111 kJ·mol^{-1}.

x # of THF	$(thf)_xMg(Carb)Br$	$(thf)_xMg(Carb)_2$	$(thf)_xMgBr_2$
0	-18.646	-36.250	-1.041
1	-27.805	-45.425	-10.184
2	-36.941	-54.583	-19.313
3	-46.047	-63.687	-28.411
4	-55.121	-	-37.501

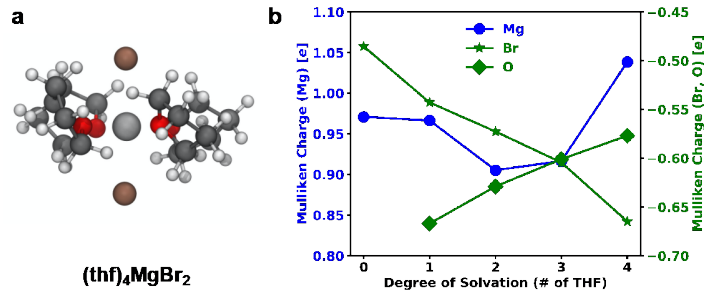

Figure S22: a) Molecular structure of $(thf)_4MgBr_2$ calculated with DFT. b) Mulliken charges for Mg, Br and O for $(thf)_xMgBr_2$ at different solvation degrees. The charges for O are averaged over the oxygen atoms of the THFs. The same applies to the charges of the Br atoms, which are averaged over the two bromine ligands.

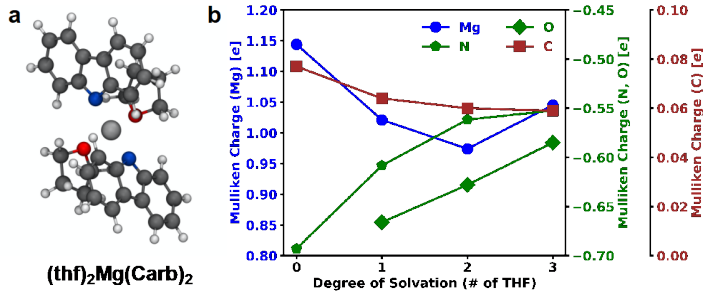

Figure S23: a) Molecular structure of $(thf)_2Mg(Carb)_2$ calculated with DFT. b) Mulliken charges for Mg, N, O, and C for $(thf)_xMg(Carb)_2$ at different solvation degrees. The charges for O are averaged over the oxygen atoms of the THFs. The same applies to the charges of the N and the C atoms, which are averaged over the carbon and nitrogen atoms of the carbazolyl groups.

Table S3: Detailed Mulliken atomic charges of $(thf)_xMgCarbBr$, $(thf)_xMg(Carb)_2$, and $(thf)_xMgBr_2$ at different degrees of solvation (x ≙ number of coordinated THFs) in elementary charge e (≙ $1.602 \cdot 10^{-19}$ C). The charges for O are averaged over the oxygen atoms of the THFs. The charges for C are averaged over the carbon atoms of the carbazolyl groups. The charges of N and Br are averaged if applicable.

x **# of THF**	**Mg**	**N**	**Br**	**O**	**C**
$(thf)_xMg(Carb)Br$					
0	1.043	-0.717	-0.476	-	0.078
1	0.957	-0.583	-0.530	-0.657	0.063
2	0.945	-0.570	-0.572	-0.631	0.060
3	0.903	-0.529	-0.597	-0.602	0.058
4	1.092	-0.523	-0.672	-0.575	0.056
$(thf)_xMg(Carb)_2$					
0	1.144	-0.693	-	-	0.077
1	1.021	-0.608	-	-0.666	0.064
2	0.974	-0.562	-	-0.628	0.060
3	1.045	-0.552	-	-0.585	0.059
$(thf)_xMgBr_2$					
0	0.971	-	-0.485	-	-
1	0.966	-	-0.543	-0.667	-
2	0.905	-	-0.573	-0.629	-
3	0.917	-	-0.604	-0.601	-
4	1.039	-	-0.665	-0.577	-

4.4 A Novel and Highly Effcient Indolyl-Based Electrolyte for Mg Batteries

The following article is reprinted without changes from Steve Zaubitzer, Saustin Dongmo, Philipp Schüler, Sven Krieck, Florian Fiesinger, Daniel Gaissmaier, Matthias van den Borg, Timo Jacob, Matthias Westerhausen, Margret Wohlfahrt-Mehrens, Mario Marinaro: A Novel and Highly Efficient Indolyl-Based Electrolyte for Mg Batteries, *Energy Technol.* **2022**, *10*, 2200440 (`https://doi.org/10.1002/ente.202200440`), with the permission of Wiley-VCH GmbH.[34] ©2022 Wiley-VCH GmbH.

Author Contributions: Steve Zaubitzer and Saustin Dongmo conducted the electrochemical measurements, XRD characterizations, and analyzed together with Mario Marinaro. Philipp Schüler synthesized the electrolyte, collected all of the NMR data, and analyzed together with Sven Krieck and Matthias Westerhausen. Florian Fiesinger performed all the calculations and analyzed together with Daniel Gaissmaier, Matthias van den Borg, and Timo Jacob. Mario Marinaro, Matthias Westerhausen, Timo Jacob, and Margret Wohlfahrt-Mehrens supervised the research. The manuscript was written through contributions of all authors. All authors discussed the results and commented on the manuscript.

Check for updates

RESEARCH ARTICLE

Energy Technology
Generation, Conversion, Storage, Distribution
www.entechnol.de

A Novel and Highly Efficient Indolyl-Based Electrolyte for Mg Batteries

*Steve Zaubitzer, Saustin Dongmo, Philipp Schüler, Sven Krieck, Florian Fiesinger, Daniel Gaissmaier, Matthias van den Borg, Timo Jacob, Matthias Westerhausen, Margret Wohlfahrt-Mehrens, and Mario Marinaro**

Magnesium-based batteries are one of the most promising candidates as postlithium electrochemical energy storage devices. Despite considerable research progress, suitable electrolytes supporting long-term reversible stripping/deposition of magnesium metal in a low content or halide-free electrolyte are still of great interest. Moreover, the electrolytes should possess certain properties to be a good match with candidate cathode materials. Herein, the electrochemical performance of a novel indolyl-based electrolyte is presented. Theoretical modeling combined with NMR analysis identifies the magnesium species in the electrolyte. Reversible stripping/deposition of Mg metal in indolyl-based electrolyte shows long-term cycling with high coulombic efficiency of >99.5% and yields dendrite-free magnesium deposition in compact and smooth layers. The X-ray diffraction shows different preferential structural orientations depending on the electrode substrate. Finally, a proof-of-concept Mg‖Mo_6S_8 full cell using the newly developed electrolyte is proposed.

1. Introduction

Lithium-ion batteries (LIBs) have an impact on our daily life since the turn of the nineties as the most important and widespread electrochemical energy storage systems. Nowadays, there is a continuously growing demand for higher energy density storage devices and for new sustainable battery technologies.[1] Moreover, the development and implementation of new sustainable energy systems could become the ultimate bridge to a definitive energy transition, addressing increasingly pressing climate change problems. Magnesium (Mg) possesses the highest volumetric capacity (3850 mAh cm^{-3}) compared to Li (2060 mAh cm^{-3}), Na (1130 mAh cm^{-3}), and Ca (2050 mAh cm^{-3}), which makes a Mg metal-based battery cell a promising candidate to envision a future shift of the current battery field to a postlithium age.[2,3] Moreover, depending on the experimental conditions, electrodeposition of metallic Mg can be free of dendrites.[2,4–7] Abundancy, low cost, and eco-friendliness are additional appealing features that render Mg metal an attractive choice.[2,3,5–9] The first proof-of-concept of a rechargeable Mg metal battery was demonstrated by Aurbach et al., with the most impressive cycle life ever reported so far.[10] Stripping and deposition of a magnesium metal anode were enabled for >3500 cycles using a Chevrel phase (CP) cathode.[11] The organomagnesium chloroaluminate complex, $Mg(AlCl_2BuEt)_2$/tetrahydrofuran (THF) was used as electrolyte, even if it presents now well-known corrosivity of the current collector and a limited anodic stability.[12] The electrolyte contained Grignard reagents, making it nucleophilic in nature, and thus unsuitable for electrophilic-type cathode materials.[13] This remarkable breakthrough of the first Mg battery prototype ignited a great interest in the development of suitable electrolytes and cathodes to improve the cell voltage. Intensive research has been carried out on the development of new electrolytes, which can enable reversible deposition and stripping at low overpotentials, are noncorrosive and nonnucleophilic in nature, possess high anodic stability, and are easy-to-make. However, the strategy to design compatible electrolytes that fulfill all these requirements seems not to be an easy task. A good compromise was found in the hexamethyldisilazide magnesium chloride (HMDSMgCl) electrolyte, as the addition of aluminum chloride ($AlCl_3$) improved the anodic stability up to 3.6 V versus Mg/Mg^{2+} on Pt.[14] Worth noting that a high ratio of $AlCl_3$ Lewis acid and/or $MgCl_2$ in (HMDS)MgCl-based electrolytes leads not only to higher anodic stability but also to high Mg deposition

S. Zaubitzer, S. Dongmo, M. Wohlfahrt-Mehrens, M. Marinaro
Zentrum für Sonnenenergie und Wasserstoff-Forschung
Baden-Württemberg
89081 Ulm, Germany
E-mail: mario.marinaro@zsw-bw.de

P. Schüler, S. Krieck, M. Westerhausen
Institute of Inorganic and Analytical Chemistry
Friedrich-Schiller University Jena
07743 Jena, Germany

F. Fiesinger, D. Gaissmaier, M. van den Borg, T. Jacob
Institute of Electrochemistry
Ulm University
89081 Ulm, Germany

D. Gaissmaier, T. Jacob, M. Wohlfahrt-Mehrens
Helmholtz Institute Ulm (HIU) Electrochemical Energy Storage
Helmholtz Str. 11, D-89081 Ulm, Germany

D. Gaissmaier, T. Jacob
Karlsruhe Institute of Technology (KIT)
76021 Karlsruhe, Germany

The ORCID identification number(s) for the author(s) of this article can be found under https://doi.org/10.1002/ente.202200440.

DOI: 10.1002/ente.202200440

 © 2022 Wiley-VCH GmbH

21944296, 2022, 8, Downloaded from https://onlinelibrary.wiley.com/doi/10.1002/ente.202200440 by KIZ der Universitat Ulm, Wiley Online Library on [21/10/2022]. See the Terms and Conditions (https://onlinelibrary.wiley.com/terms-and-conditions) on Wiley Online Library for rules of use; OA articles are governed by the applicable Creative Commons License

ADVANCED SCIENCE NEWS
www.advancedsciencenews.com

Energy Technology
Generation, Conversion, Storage, Distribution
www.entechnol.de

21944296, 2022, 8, Downloaded from https://onlinelibrary.wiley.com/doi/10.1002/ente.202200440 by KIT-Der Universitat Ulm, Wiley Online Library on [21/10/2022]. See the Terms and Conditions (https://onlinelibrary.wiley.com/terms-and-conditions) on Wiley Online Library for rules of use; OA articles are governed by the applicable Creative Commons License

overpotential (up to 500 mV).[15] Moreover, during reversible deposition of Mg metal using (HMDS)MgCl-based electrolyte formulation less than 100 cycles were reported, even in a full cell $Mg \| Mo_6S_8$, considered as a state-of-art of Mg batteries.[15] The introduction of the all-inorganic magnesium aluminum chloride (MACC) in THF or glyme electrolyte came shortly after as a breath of fresh air toward suitable Mg electrolytes. But still they are corrosive due to the high content of chloride ions[15] and the electrodeposited Mg layer also contains aluminum and chlorine.[16,17] Halide-free boron-centered carborane $Mg(CB_{11}H_{12})_2$/tetraglyme (TG) and the tetrakis(hexafluoroisopropyloxy)borate $Mg[B(hfip)_4]_2$/1,2-dimethoxyethane (DME) state-of-the-art electrolytes offer a high anodic stability ≈3.90 V and 4.30 V versus Mg/Mg^{2+} on stainless steel (SS) and, due to the weakly coordinated anion, good ionic conductivities.[18,19] Further improvements are, however, needed in terms of coulombic efficiency (≈94.4% and 98.0% for 0.4 M $Mg(CB_{11}H_{12})_2$/TG and 0.6 M $Mg[B(hfip)_4]_2$/DME, respectively) cycling stability (up to 100 cycles reported for both types of electrolytes) and easier synthesis approaches .[15,20–23] An additional challenge arises in the quest for a suitable cathode material.[24] Intercalation of Mg^{2+} cations using metal oxide, sulfur, and selenide-based cathode materials presents many hurdles, owing to the high charge density of the Mg^{2+} divalent cation, leading to sluggish kinetics, which require high energies during desolvation processes at the electrode/electrolyte interface and during solid-state diffusion. Polyanionic structures are becoming more and more popular as cathode materials for Mg-batteries due to a strong inductive effect, which reduces the interaction with the guest Mg^{2+} cation.[24–26] Conversion-type cathodes, such as sulfur (S), appear to be a possible alternative, owing to a comparable volumetric capacity when paired with a magnesium metal anode (3459 mAh cm^{-3}) and do not require a highly anodically stable electrolyte (up to ≈2.5 V vs Mg/Mg^{2+}).[27,28] However, so far, the full proof-of-concept of a working Mg–sulfur battery using the state-of-art $Mg[B(hfip)_4]_2$/DME electrolyte showed 80% of capacity loss after 100 cycles,[21] owing to the incompatibility with the electrolyte and a poor cyclability of the Mg anode.[21,29] Therefore, an electrolyte allowing a prolonged stable cyclability of a Mg anode will be a step forward toward a practical Mg–S battery. To achieve this goal, we recently developed a nonnucleophilic HMDS-based electrolyte enabling a prolonged metal anode cycling, with a low halide content, and possessing relatively good anodic stability, required for Mg–S battery.[30] The impact on the electrochemical performance by using halides strongly depends on the nature of the halide. So far, chloride has been the halide of choice for most formulations. However, it has been demonstrated that long-term cycling at high coulombic efficiencies can be achieved by using bromide instead of chloride,[30] thus having a less corrosive environment.

In this work, we report a novel nonnucleophilic (indolyl) magnesium bromide electrolyte (Mg(Ind)Br). The in situ-Grignard metalation synthesis route yields one major Mg species. NMR spectroscopy characterization results are in line with theoretical simulations. Long-term reversible Mg deposition/stripping investigations show high coulombic efficiencies and low overpotentials without any addition of Lewis acids or halide-based additives. Furthermore, in a full cell setup the electrolyte allows the intercalation and deintercalation of Mg^{2+} with a CP as cathode.

2. Results and Discussion

2.1. Magnesium Speciation Analysis and Modeling

Mg(Ind)Br was prepared using the in situ-Grignard metalation method (*i*GMM)[31] starting from Mg metal, indole, and ethyl bromide. This highly efficient low costs (cf., Table S1, Supporting Information), one-pot reaction (yield up to >95%) provides an excellent synthetic route and allows preparing highly concentrated solutions. The solution structure was elucidated using standard NMR techniques (Figure S1–S5, Supporting Information) in combination with ECC-DOSY[32] (Figure S6 and S7, Supporting Information) to determine the molar mass. In a Schlenk-type equilibrium, amido-magnesium halides typically coexist in solution with the corresponding homoleptic species [Equation (1)]. Surprisingly, only one set of NMR resonances was observed in THF solution hinting toward the formation of the heteroleptic complex $[([D_8]THF)_4\,Mg(Ind)Br]$, as shown in Figure S5, Supporting Information, (M_W: calc.: 541, found: 541 g mol^{-1}, $\Delta = 0\%$). The ^{25}Mg NMR spectrum showed a broad singlet ($\delta = 4.7$ ppm, $\omega = 288$ Hz) and based on linewidth broadening an asymmetric coordination sphere of the quadrupolar metal ion can be assumed.

Density functional theory (DFT) calculations were performed to confirm the NMR data as well as to determine solution structure and solvation energies of the various species involved in the Mg(Ind)Br-based electrolyte equilibria. As described in the literature, Mg cations are mostly coordinated in a sixfold octahedral environment,[33–35] although fourfold and fivefold coordination structures were also found depending on the bulkiness of ligated Lewis bases.[36,37] In the case of the electrolyte studied in this work, the central Mg cation is arranged in an octahedral environment with the counterions located in *trans* positions due to electrostatic reasons (cf., **Figure 1**). We found the highest solvation energy (E_{solv}) for Mg(Ind)Br with −481 kJ mol^{-1} followed by $MgBr_2$ and $Mg(Ind)_2$ with solvation energies of −473 and −472 kJ·mol^{-1}, respectively (cf., **Table 1**). The solvation energies of the considered species are almost identical with a maximum solvation energy difference (ΔE_solv) of 9 kJ mol^{-1} between Mg(Ind)Br and $Mg(Ind)_2$. The narrow solvation energy range is consistent with the observed Mulliken atomic charges of the Mg atom, which are (with values between 0.97 and 1.11e, depending on the electrolyte species and degree of solvation) very similar; the atomic charges of the THF oxygen atoms are even closer between −0.57 and −0.60e (Table S3–S5, Supporting Information). The average solvation energies per THF molecule (see Table 1) in the first solvation shell vary between −108 and −104 kJ·mol^{-1}, which is comparable with the calculated value of −98 kJ·mol^{-1} from Wan et al. for their tetra-coordinated dichloromagnesium complex.[36] As shown in Figure 1, a Schlenk-type equilibrium reaction takes place between two Mg(Ind)Br molecules on one side and one $Mg(Ind)_2$ + one $MgBr_2$ species on the other side [Equation (1)]

 © 2022 Wiley-VCH GmbH

ADVANCED SCIENCE NEWS
www.advancedsciencenews.com

Energy Technology
Generation, Conversion, Storage, Distribution
www.entechnol.de

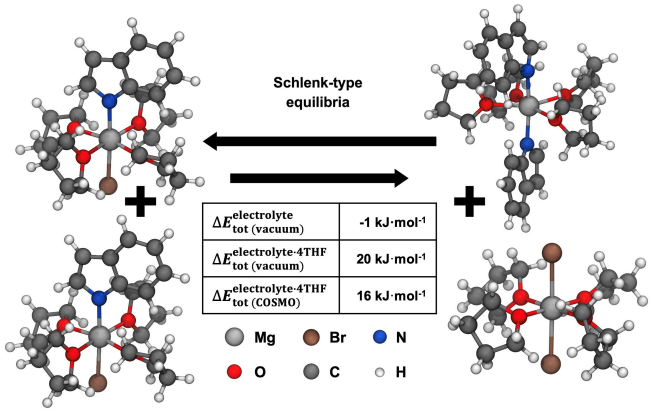

Figure 1. Schlenk-type equilibrium of the Mg(Ind)Br-based electrolyte. The first solvation shell consisting of four THF molecules was included explicitly, while additional THF solvation was considered implicitly using the conductor like screening model (COSMO).[61] Two Mg(Ind)Br molecules are by 16 kJ·mol^{-1} (20 kJ·mol^{-1} in case of only explicit THF solvation, 1 kJ mol^{-1} in case of no solvation) thermodynamically more favorable compared to the educts $Mg(Ind)_2 + MgBr_2$, indicating the position of the equilibrium shifted to the left side in line with the NMR analysis. The energy difference is defined as $\Delta E_{tot} = (E_{tot}^{Mg(Ind)_2} + E_{tot}^{MgBr_2}) - 2 \cdot E_{tot}^{Mg(Ind)Br}$.

Table 1. Calculated solvation energies (E_{solv}) for Mg(Ind)Br, $MgBr_2$ and $Mg(Ind)_2$ in THF using Equation (2), (3), and (4). The first solvation layer is included explicitly; further THF solvation is described via the implicit solvation model COSMO.[61] The solvation energy difference (ΔE_{solv}) is given for $MgBr_2$, and $Mg(Ind)_2$ with respect to Mg(Ind)Br which has the highest solvation energy with –481 kJ mol^{-1}. The average solvation energy per THF molecule is calculated for the first solvation shell as E_{solv} per THF $= E_{explicit}/4$.

kJ · mol^{-1}	E_{solv}	ΔE_{solv}	E_{solv} per THF
Mg(Ind)Br·4THF	–481		–108
$MgBr_2$·4THF	–473	8	–104
$Mg(Ind)_2$·4THF	–472	9	–108

$$2(thf)_4Mg(Ind)Br \rightleftharpoons (thf)_4MgBr_2 + (thf)_4Mg(Ind)_2 \quad (1)$$

To determine the equilibrium of this reaction, the total energies of both sides of the reaction have been evaluated. The two Mg(Ind)Br molecules are thermodynamically favored by 16 kJ mol^{-1} (20 kJ mol^{-1} in case of Mg^{2+} ions only solvated by four explicit THF molecules) compared to the educts $Mg(Ind)_2 + MgBr_2$. This finding attests that the equilibrium should slightly be shifted in favor of the heteroleptic complexes, which is in agreement with the obtained NMR results. However, the small energy difference also suggests a fast equilibrium between the heteroleptic and homoleptic species in THF solution. Without solvation, the equilibrium is almost balanced ($\Delta E_{tot\,(vacuum)}^{electrolyte} = -1$ kJ mol^{-1}), which reveals the important role of the THF solvent in the equilibrium reaction.

2.2. Electrochemical Performance and Electrode-Dependency of Mg deposition

Deposition/stripping is one of the key steps for a successfully operating metal-based battery. To evaluate the electrochemical reversibility of the metal deposition and dissolution in the indolyl-based electrolyte, we first performed cyclic voltammetry (CV) measurements.

Figure 2A–D shows the typical features of electrochemical reversible deposition and dissolution of Mg metal. The feasibility of the magnesium deposition/dissolution was evaluated on different metal substrates, i.e., copper (Cu), nickel (Ni), SS, and platinum (Pt). Despite the similar shapes of the CVs, the onset for the Mg deposition indicated a substrate-dependent process. At cycle #10, the overpotential for Mg deposition was −185 mV (Cu), −190 mV (Pt), ≈−220 mV (Al), −225 mV (Ni), and ≈ −250 mV for SS. The low overpotentials for the Mg electrodeposition (less than 200 mV on Cu and Pt) are comparable to the reported values of the Mg(HMDS)Br-based electrolyte obtained with the same sweep rate.[28] Current density of ≈2 mA cm^{-2} on Pt, SS, Ni and −1.5 mA cm^{-2} for Cu were reached at the cutoff potential of −0.8 V versus Mg/Mg^{2+}, respectively, at CV cycle #10. Cathodic current density values increased for Cu, Pt, SS and remained constant in the case of Ni electrode, at cycle #200. This casts a hint toward substrate-dependent processes that can slightly influence the electrochemical performance. Atomic force microscopy (AFM) (**Figure 3**) investigations of the Cu electrode roughness before and after cycling showed that this increase cannot be directly linked to an increased active surface of the working electrode because the changes in surface roughness (fresh: $R_z = 0.48 \pm 0.12$ µm,

© 2022 Wiley-VCH GmbH

21944296, 2022, 8, Downloaded from https://onlinelibrary.wiley.com/doi/10.1002/ente.202200440 by KIZ der Universitat Ulm, Wiley Online Library on [21/10/2022]. See the Terms and Conditions (https://onlinelibrary.wiley.com/terms-and-conditions) on Wiley Online Library for rules of use; OA articles are governed by the applicable Creative Commons License

ADVANCED SCIENCE NEWS
www.advancedsciencenews.com

Energy Technology
Generation, Conversion, Storage, Distribution
www.entechnol.de

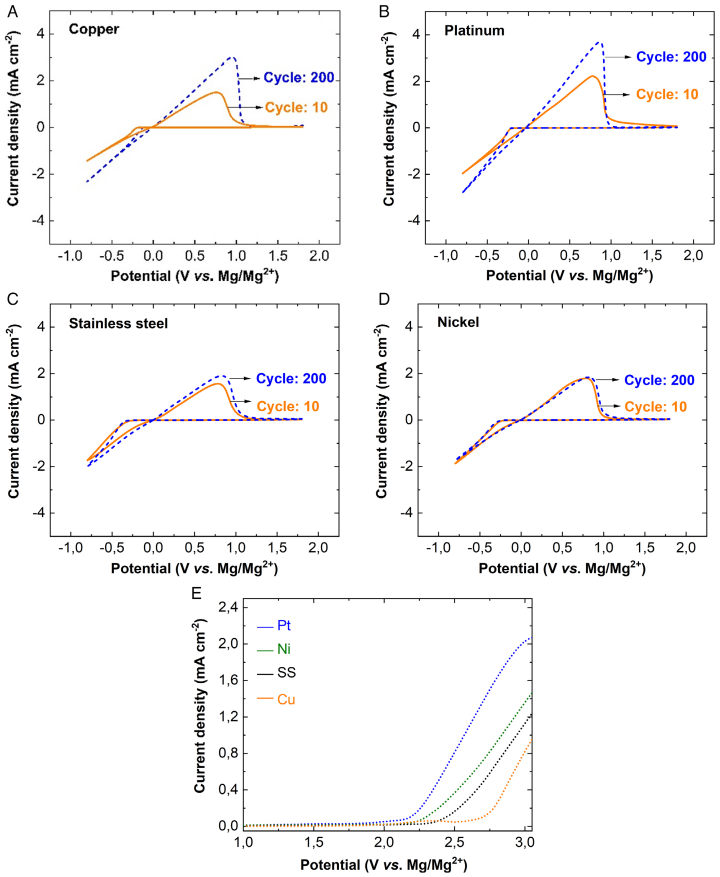

Figure 2. Cyclic voltammograms of the Mg electrodeposition and electrostripping process using 0.6 M Mg(Ind)Br in THF as electrolyte at various current collectors: A) Cu, B) Pt, C) SS, and D) Ni. Sweep rate of 10 mV s^{-1}. E) Linear sweep voltammograms at a sweep rate of 5 mV s^{-1}. All the electrochemical measurements were performed in a three-electrode setup with Mg as counter and reference electrodes.

cycled: $R_z = 0.52 \pm 0.9$ µm) are relatively small (cf., Figure S8 and S9, Supporting Information, for Pt, SS, and Ni, respectively). The anodic stability on different substrates was determined by linear sweep voltammetry (LSV). Figure 2E presents the anodic stabilities at a scan rate of 5 mV s^{-1} and demonstrates comparatively good anodic stability on Cu (≈2.2 V vs Mg/Mg^{2+}), Ni (2.3 V vs Mg/Mg^{2+}), and SS (2.4 V vs Mg/Mg^{2+}), similar to the reported values for nitrogen-based magnesium electrolytes containing strong Lewis-acid like aluminum chloride ($AlCl_3$)[38] and moreover an improvement in the electrolyte stability of approximately 400 mV compared to the all-phenyl-complex and MACC electrolytes obtained on a SS current collector and same sweep rate.[39] It is known that the anodic stability of nitrogen-based Mg electrolytes is governed by the N—Mg bond and can be improved through the stabilization of the bond by using a strong Lewis acid like $AlCl_3$.[38] However, this could not be extended to the Mg(Ind)Br electrolyte, where an increase of current densities was observed due to the increase of the electrolyte conductivity from 0.46 mS cm^{-1} (without $AlCl_3$) to 0.70 mS cm^{-1} (with 10 mol% $AlCl_3$), as shown in Figure S10, Supporting Information. The

 © 2022 Wiley-VCH GmbH

21944296, 2022, 8, Downloaded from https://onlinelibrary.wiley.com/doi/10.1002/ente.202200440 by KIT-Der Universitat Ulm, Wiley Online Library on [21/10/2022]. See the Terms and Conditions (https://onlinelibrary.wiley.com/terms-and-conditions) on Wiley Online Library for rules of use; OA articles are governed by the applicable Creative Commons License

ADVANCED SCIENCE NEWS
www.advancedsciencenews.com

Energy Technology
Generation, Conversion, Storage, Distribution
www.entechnol.de

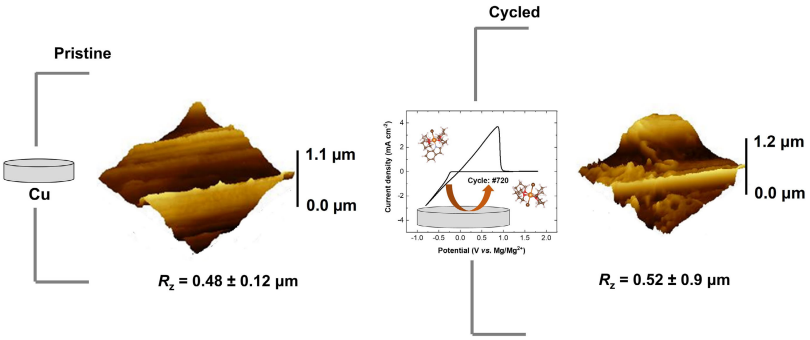

Figure 3. AFM characterization of the surface roughness of pristine and cycled Cu electrode.

addition of higher amounts of $AlCl_3$ yielded gel-type electrolytes and magnesium chloride ($MgCl_2$) or magnesium bromide ($MgBr_2$) does not dissolve in Mg(Ind)Br-THF electrolyte.

Long-term cycling at high coulombic efficiency can be a reliable indicator of stability and cyclability of electrolyte with the Mg metal anode and can be used to assess the electrochemical performance of novel electrolytes.[30] For an accurate determination of the coulombic efficiency during the reversible Mg deposition/stripping process, chronopotentiometry technique was applied.[40] **Figure 4**A shows the galvanostatic cycling of the indolyl-based electrolyte on Cu substrate at 0.8 mA cm^{-2} current density, with a timescale of 30 min during Mg deposition, and 0.8 V (vs Mg/Mg^{2+}) cutoff potential during stripping. The corresponding coulombic efficiencies up to cycle #700 are reported in Figure 4B. A remarkable coulombic efficiency of 99.5% is obtained during long-term cycling. This result is even more meaningful when compared with the available literature, which usually shows a cyclability of only 500 cycles, but nevertheless reported for a lower current density of about 0.5 mA cm^{-2}.[41–43] This long-term stable cycling demonstrates a remarkable stability of the electrolyte. A similar performance was observed with Pt, Ni, SS, and Al substrates (cf., Figure S11 and S12, Supporting Information).

The electrodeposited Mg was characterized through scanning electron microscopy (SEM) and X-Ray diffraction (XRD). **Figure 5**A–D shows the XRD patterns of the deposited Mg metal layer on different substrates. The XRD pattern is characterized by sharp reflections which have been assigned to hexagonal Mg[44] (PDF 00-035-0821) and to the metal substrates used as current collectors (Cu, SS, Ni, Pt). In the case of Ni and SS, the patterns of the substrate itself are missing because the deposited Mg layer could be easily removed from the metal substrate. SEM micrographs (**Figure 6**A–E) show different morphologies of electrodeposited Mg. In the case of a Cu electrode (Figure 6A), Mg deposits in regular shapes with different preferential orientations compared to Ni and SS. These observations are consistent if the intensity ratio of the [002]/[101] XRD reflections of the electrodeposited Mg is taken into consideration. This aspect will be discussed in detail in the discussion section. The deposition onto Pt represents an exception, with Mg growth leading to a dense

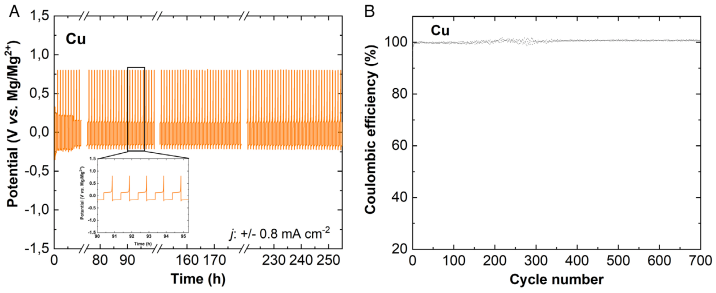

Figure 4. A) Chronopotentiometry cycling at Cu electrode using 0.6 M Mg(Ind)Br in THF at ±0.8 mA cm^{-2} with 30 min time scale during deposition and cutoff potential at 0.8 V during stripping, Mg was used as reference and counter electrode. B) Coulombic efficiencies evaluated after chronopotentiometry measurement.

© 2022 Wiley-VCH GmbH

21944296, 2022, 8, Downloaded from https://onlinelibrary.wiley.com/doi/10.1002/ente.202200440 by KIZ der Universitat Ulm, Wiley Online Library on [21/10/2022]. See the Terms and Conditions (https://onlinelibrary.wiley.com/terms-and-conditions) on Wiley Online Library for rules of use; OA articles are governed by the applicable Creative Commons License

ADVANCED SCIENCE NEWS
www.advancedsciencenews.com

Energy Technology
Generation, Conversion, Storage, Distribution
www.entechnol.de

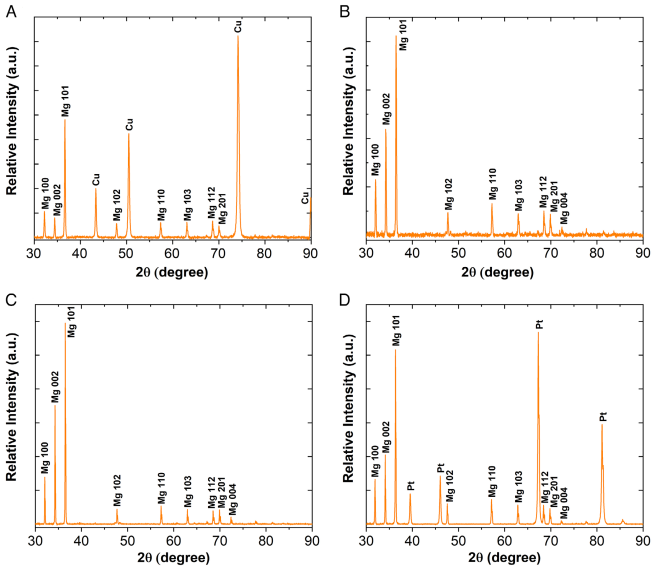

Figure 5. XRD patterns of deposited magnesium layer on A) Cu, B) SS, C) Ni, and D) Pt obtained after chronoamperometry at −350 mV with 3.93 mAh cm^{-2} as limited capacity.

and homogenous layer. SEM images of the Pt-deposited Mg layer are devoid of the current collector because it was found to be easily removable from the substrate after XRD analysis (Figure 6D). From the respective cross-sectional view (Figure 6E), also residual glass fibers on top of the thick Mg layer can be identified.

As a proof-of-concept, a full cell Mg battery with Mo_6S_8 as a cathode and Mg foil as anode was assembled. The resulting charge–discharge profiles of the Mo_6S_8 cathode, using 2 mA g^{-1} as current density, are presented in **Figure 7**A. At cycle #2, a discharge capacity of 40 mAh g^{-1} is achieved and further increases to around 50 mAh g^{-1} at cycle #14 (cf., Figure 7A,C) with a high overall reversibility for the de-/intercalation process (cf., Figure 7D, for the cycling performance, cf., Figure S13A,B, Supporting Information). Such a rise in the capacity during cycling can be assigned to improving the Mg diffusivity in the host material caused by the increasing amount of inserted Mg^{2+} ions in the lattice of the CP.[45] Furthermore, the Mg can also be plated and stripped at the anode side at low overpotentials (cf., Figure 7B).

Also is the solvation environment for the Mg^{2+} ions strongly connected to the de- and intercalation into the CP. The cycling profile shows a slow diffusion kinetics as also reported by Ren *et al.*[42] Nevertheless, besides the similarly shape of the charge-discharge curves for the de-/intercalation of magnesium ions into the host material, the different states of charge are investigated by XRD (cf., Figure S14, Supporting Information) and in good agreement with the data reported in the literature.[46,47]

3. Discussion

Lewis acid salt $AlCl_3$ added in Mg(Ind)Br-THF does not improve the anodic stability of this novel electrolyte formulation (cf., Figure S1C, Supporting Information) as reported for HMDS-based electrolytes.[48] Therefore, an extension to other nitrogen-containing electrolytes cannot be considered in this case. Moreover, the nonnucleophilicity of the benzopyrrole anion is influenced by the solvent. Depending on the solvent, aprotic polar or nonpolar, the benzopyrrole anion can produce a nucleophilic attack or not.[45] This could stand as a starting point to optimize the Mg(Ind)Br by testing the impact of different compatible solvents on the electrochemical performance of the electrolyte at different concentrations. Deposition and stripping processes have been shown to be substrate-dependent processes, affecting the overpotential and current densities of Mg electrodeposition and the preferential orientation of the crystalline structure. A tentative explanation of the substrate dependence can be done considering their intrinsic properties, such as the electronic conductivity and the affinity between Mg and the substrate during the nucleation processes at the atomic scale (surface energy). The impact of the electrolyte interface generated during the deposition process or the generation of new electrochemically active

© 2022 Wiley-VCH GmbH

21944296, 2022, 8, Downloaded from https://onlinelibrary.wiley.com/doi/10.1002/ente.202200440 by KIZ der Universitat Ulm, Wiley Online Library on [21/10/2022]. See the Terms and Conditions (https://onlinelibrary.wiley.com/terms-and-conditions) on Wiley Online Library for rules of use; OA articles are governed by the applicable Creative Commons License

ADVANCED SCIENCE NEWS
www.advancedsciencenews.com

Energy Technology
Generation, Conversion, Storage, Distribution
www.entechnol.de

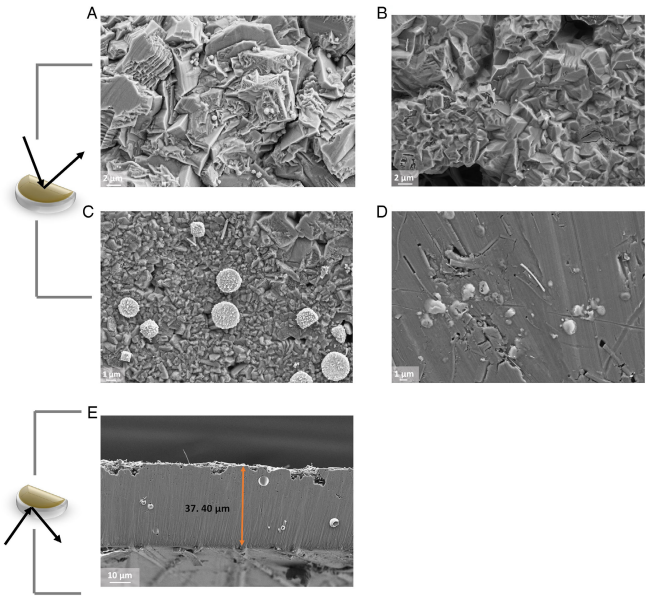

Figure 6. Scanning electron micrographs of deposited magnesium layer on A) Cu electrode, B) (SS), C) Ni, D) Pt, and E) cross-sectional view of pure Mg layer deposited on Pt.

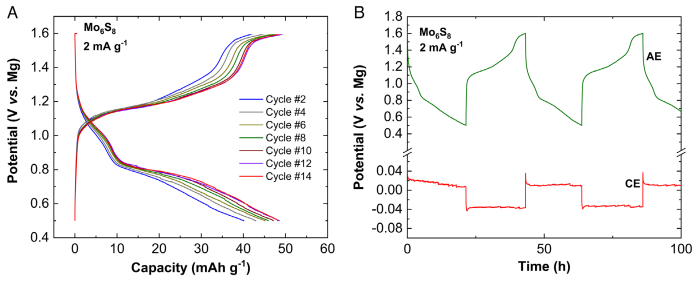

Figure 7. Galvanostatic cycling of the Mg‖0.6 M Mg(Ind)Br/THF‖Mo_6S_8 cell cycled at 2 mA g^{-1} in a three-electrode setup with an Mg quasireference electrode and a cutoff voltage of 0.5–1.6 V. A) Charge/discharge profiles of the Mo_6S_8 working electrode and the B) enlarged graph of the voltage profiles of the Mo_6S_8 working electrode (green) and Mg counter electrode (red).

Mg-species during cycling could eventually explain the increase of current density. The different orientations of a crystalline structure during electrodeposition of Mg on Ni, SS, and Pt operate by minimizing the surface energy, reflected in the high-intensity [002] plane compared to [100]. Cu shows a lower intensity for the respective orientation, and as mentioned above, the surface energy cannot be minimized during crystal growth thus the preferential orientation is along the [100] plane.[49] It has been reported that the high-intensity ratio [002]/[101] indicates that the crystal growth proceeds preferentially along the ab plane and vice versa; a low-intensity ratio indicates a growth along the *c*-axis.[49] The peak ratio increases from Cu (0.17), Ni (1.69), SS (1.90) to Pt (2.5), and it is consistent with the observed morphological differences in the deposited Mg layers. The

© 2022 Wiley-VCH GmbH

21944296, 2022, 8, Downloaded from https://onlinelibrary.wiley.com/doi/10.1002/ente.202200440 by KIZ der Universitat Ulm, Wiley Online Library on [21/10/2022]. See the Terms and Conditions (https://onlinelibrary.wiley.com/terms-and-conditions) on Wiley Online Library for rules of use; OA articles are governed by the applicable Creative Commons License

21944296, 2022, 8, Downloaded from https://onlinelibrary.wiley.com/doi/10.1002/ente.202200440 by RWTH Aachen Universitat Uhn, Wiley Online Library on [21/10/2022]. See the Terms and Conditions (https://onlinelibrary.wiley.com/terms-and-conditions) on Wiley Online Library for rules of use; OA articles are governed by the applicable Creative Commons License

energetically different surface orientations during the crystal growth are presented in the different reflection intensities for the electrodeposited Mg.[50] Furthermore, low intensity for the [002] reflection indicates a low tendency to minimize surface energy[49] during the crystal growth on Cu. Although [101] shows the highest reflection intensity in the XRD pattern, it possesses the highest surface energy compared to the [100] and [002] orientation. These can be explained by the highest area fraction from the [101] orientation in the crystal's equilibrium shape and underpins the theoretical findings of Lautar et al.[50] Mechanistically speaking, the electrodeposition of Mg seems not to be a simple two-electron transfer.[51] It is rather a complicated adsorption process that is influenced by the electrochemically active species.[52] In the case of organomagnesium chloroaluminate electrolytes, the electrochemical-active species in solution comprises a dimeric magnesium–cationic complex $[Mg_2(\mu\text{-}Cl_3)^*6THF]^+$.[53] Analytical approaches such as in situ/operando-X-Ray absorption spectroscopy (XAS) demonstrated that on the electrode surface, the dimeric complex splits into a mononuclear cationic complex $[MgCl^*5THF]^+$.[54] In the case of HMDS-based electrolytes, several active species are present in solution and are subject to a Schlenk-type equilibrium.[27,30] Due to the presence of such equilibria, theoretical forecasts (e.g., DFT-based simulations) become much more complicated. Nevertheless, future works should be conducted to validate the electrochemically active species during the polarization of the electrode, e.g., by in situ-Raman or electrochemical NMR. Furthermore, more details about the nucleation and preferential growth directions are needed and should be investigated, e.g., with electrochemical scanning tunnel microscopy (STM).

4. Conclusions

In summary, we report on the electrochemical performance of a novel electrolyte for Mg-ion batteries containing benzopyrrole and bromide as anions. The high performance through deposition and stripping does not require additional Lewis acids such as $AlCl_3$ or halide-based additives. As suggested by XRD characterization, the deposited magnesium layers present different preferential growth orientations, depending on the substrates. The analysis of Mg species reveals the formation of a Schlenk-type equilibrium. It identifies $(thf)_4$ Mg(Ind)Br as the main bulk species, which is in line with the theoretical calculation of solvation–desolvation energies. Furthermore, this benzopyrrole-based electrolyte allows the de- and intercalation of Mg^{2+} into a CP cathode. Moreover, after long-term cycling, there is no indication of corrosion at the current collector. This electrolyte is very promising for application in the next generation of rechargeable Mg batteries with good electrochemical performance and the one-pot cost-effective synthesis.

5. Experimental Section

Computational Details: The input structures for the electrolytes were generated with the AMS driver program[55] and preoptimized with a modified version of the semiempirical PM7 method[56] as implemented in the MOPAC engine.[57] All first principles geometry optimizations were performed within the Amsterdam Density Functional (ADF)[55] program suite. Spin unrestricted, nonrelativistic calculations were performed using slater-type orbitals (STOs) with triple zeta polarized (TZP), all-electron basis sets[58] and the meta hybrid exchange–correlation functional MN15[59] as part of the LibXC library.[60] Self-consistent field (SCF) convergence was achieved when the energy difference between consecutive SCF cycles was less than 2.6×10^{-3} kJ mol^{-1}, and the geometry was considered as converged when all forces were at least smaller than 2.6 kJ mol^{-1}·Å^{-1}. The THF solvation energy was calculated in a two-step process, with the first solvation shell included explicitly, while additional THF solvation was considered implicitly using the conductor like screening model (COSMO) as implemented in ADF[61] [Equation (2)].

$$E_{solv} = E_{explicit} + E_{implicit} \tag{2}$$

The explicit fraction of THF solvation was calculated by subtracting the total energies of the respective electrolyte species (Mg(Ind)Br, $Mg(Ind)_2$, $MgBr_2$) and the THF molecules from the total energy of the electrolyte with the first solvation shell included [Equation (3)].

$$E_{explicit} = E_{tot\,(vacuum)}^{electrolyte\text{-}4THF} - E_{tot\,(vacuum)}^{electrolyte} - 4 \cdot E_{tot\,(vacuum)}^{THF} \tag{3}$$

The implicit fraction of THF solvation corresponds to the difference in total energy from a COSMO and a vacuum calculation of the electrolyte with the first solvation shell included explicitly [Equation (4)].

$$E_{implicit} = E_{tot\,(COSMO)}^{electrolyte\text{-}4THF} - E_{tot\,(vacuum)}^{electrolyte\text{-}4THF} \tag{4}$$

Detailed absolute energies for the electrolyte species Mg(Ind)Br, $MgBr_2$, and $Mg(Ind)_2$ involved in the calculation of the solvation energy E_{solv} may be found in Table S2, Supporting Information. Atomic charges were determined with the Mulliken charge analysis.[62]

Electrolyte Synthesis and NMR/Mass Spectrometry Characterization: All manipulations were carried out in an inert nitrogen atmosphere using standard Schlenk techniques, if not otherwise noted. The solvents were dried over KOH and subsequently distilled over sodium/benzophenone in a nitrogen atmosphere before use. Deuterated THF was dried over sodium, distilled, degassed, and stored under nitrogen over sodium. All substrates were purchased from Alfa or TCI and used without further purification. The yields given are not optimized. NMR spectra were recorded using a Bruker Avance III 400 MHz and a Bruker Avance III 600 MHz spectrometer. Chemical shifts are reported in parts per million relative to $SiMe_4$ as an external standard referenced to the solvents residual proton signal. Molecular mass analysis via NMR spectroscopy was done using the Stalke method (ECC-DOSY,[32] [D_8]THF as internal standard) and the *ledbgp2s* pulse program. ASAP-HSQC-NMR spectra were recorded using the pulse program published by Luy.[63]

Synthesis of IndMgBr: Magnesium (98%, granular, 0.41 g, 17.1 mmol) and indole (2.00 g, 1 eq., 17.1 mmol) were placed in a Schlenk flask and THF (25 mL) was added. EtBr (1.27 mL, 1 eq., 17.1 mmol) was added in three portions over 1 h. The reaction mixture was stirred for 3 h at room temperature. The solution was decanted from the unreacted magnesium and used without further purification (0.56 M, 83%, 14.1 mmol). The yield was determined by acidimetric titration of a hydrolyzed aliquot. ^{1}H NMR (400 MHz, [D_8]THF, 298 K) $\delta = 6.31$ (s, 1H, H3), 6.69 (t, $J = 7.19$ Hz, 1H, H5), 6.76 (dt, $J = 6.76$, 0.97 Hz, 1H, H6), 7.3 (s, br, H2), 7.40 (d, $J = 7.5$ Hz, H7), 7.50 (d, $J = 7.8$ Hz, H4) ppm. ^{13}C{^{1}H} NMR (101 MHz, [D_8]THF, 298 K) $\delta = 100.5$ (C3), 115.6 (C4), 116.6 (C5), 119.6 (C7), 132.0 (C3a), 135.3 (br, C2), 146.4 (C7a) ppm. ^{25}Mg-NMR (24.5 MHz, [D_8]THF, 297 K) $\delta = 4.7$ ppm (bs, $\omega = 288$ Hz), ^{15}N{^{1}H} NMR (MHz, [D_8]THF, 297 K) $\delta = 181.3$ (s).

Materials and Electrochemical Characterization: Copper foil (99.95%, $d = 0.01$ mm, Schlenk), magnesium foil (99.95%, $d = 0.15$ mm, Goodfellow), and magnesium wire (99.99%, $d = 1$ mm, Goodfellow) were used as working, counter, and reference electrodes, respectively. Furthermore, SS foil ($d = 0.025$ mm, Goodfellow), aluminum foil (Schlenk), nickel foil (99%, $d = 0.1$ mm, Goodfellow), and platinum foil (99.99%, $d = 0.1$ mm, Goodfellow) were used as working electrodes. Prior to use, the copper and aluminum foils were dried under vacuum

 © 2022 Wiley-VCH GmbH

at 120 °C. To remove the thin native oxide layer onto the magnesium current collector, the surface was polished with sandpaper (1200 μm).

The Chevrel cathodes were prepared by homogenization of the powder mixture consisting of 70 wt% Mo_6S_8 (NEI Corporation USA), 20 wt% Super C65, and 10 wt% polyvinylidenfluorid (PVDF, Solvay) in a speed-mixer (DAC 800.2 VAC-P) for 1000 rpm (1 min), 1500 rpm (2 min), and 2000 rpm (2 min). Afterward 20 mL of *N*-methyl-2-pyrrolidon (NMP) was added to the powder and homogenized again each for 1 min at 1000, 1500, and 2000 rpm. The obtained slurry were coated on a copper foil and predried for 2 h at 80 °C. After being cut into $d = 18$ mm discs, the cathode was dried under vacuum at 80 °C for 15 h. The mass loading of CP was around 1.0–1.5 mg cm^{-2}.

The electrochemical measurements were performed inside a glove box using EL-Cell ECC-Ref cells. Cell assembling was done according to the following sequence: working and counter electrodes $d = 18$ mm, a piece of magnesium wire was used as reference electrode. A glass fiber used as separator (1.55 mm thick, ECC-01-0021-C/L, EL-Cell) used as reservoir for Mg electrolyte (450 μL). The electrochemical tests were performed on a BioLogic VMP3 cell test system with BioLogic EC-Lab software V10.32. CV experiments were run in a potential range between −0.8 V and 1.8 V versus Mg/Mg^{2+} at a scan rate of 10 mV s^{-1}. Linear sweep voltammetry (LSV) experiments were performed with copper, nickel, aluminum, SS, and platinum current collectors with a scan rate of 5 mV s^{-1}. Mg was electrodeposited onto the current collectors by using chronoamperometry at a fixed voltage of −350 mV to obtain 3.93 mAh cm^{-2}. Coulombic efficiencies have been calculated from chronopotentiometry experiments carried out at ±0.8 mA cm^{-2} for $t = 30$ min and an upper cut-off of 0.8 V. Ionic conductivities were measured using a Microcell from HC-rhd instruments. It consists of a 4-platinum electrode setup and determines the conductivity by electrochemical impedance spectroscopy (EIS).

AFM Measurements: The topography of an uncycled Cu sample and one after 720 cycles was measured by an AFM (Topometrix Explorer with Anfatec Controller) using a Multi75GD-G cantilever (Budgetsensors, Sofia, Bulgaria). A 50 × 50 μm^2 area of the surface was then measured with a scan rate of 2 Hz.

XRD and SEM-EDX Characterization: XRD and SEM were applied to characterize the morphology of the electrodeposited Mg on the current collector. XRD pattern was recorded using an air-dome sample holder in a single scan between 10° and 90° in 0.02° 2θ increments on a Bruker AXS D8 Discover using Cu Kα radiation, a Ni-monochromator, and a LYNXEYE 2D energy dispersive detector. The SEM images have been obtained with a LEO 1530 VP microscope with an acceleration of 5.0 kV and a secondary electron detector.

Supporting Information

Supporting Information is available from the Wiley Online Library or from the author.

Acknowledgements

This work contributes to the research performed at CELEST (Center for Electrochemical Energy Storage Ulm-Karlsruhe) and was partly funded by the German Research Foundation (DFG) under Project ID 390874152 (POLiS Cluster of Excellence). The authors acknowledge support by the state of Baden-Württemberg through bwHPC and the German Research Foundation (DFG) through grant no. INST 40/575-1 FUGG (JUSTUS 2 cluster). S.Z., S.D., M.W.-M., and M.M. would also like to acknowledge the German Federal Ministry of Education and Research (BMBF) for financial support within the project "LuCaMag" (grant no. 03EK3051D). Additionally, T.J. gratefully acknowledges support by the German Science Foundation through the priority program SPP-2248. P.S. is very grateful to the German Environment Foundation (Deutsche Bundesstiftung Umwelt, DBU, grant no. 20018/578) for a generous Ph.D. grant. The authors acknowledge the valuable support of the NMR and the MS-platform of the Faculty of Chemistry and Earth Sciences of the Friedrich Schiller University Jena, Germany. The authors thank also Dr. Maximilian Eckl for the AFM measurements, Dr. Claudia Pfeiffer for SEM measurements, Dagmar Weihrather-Köstner for ionic conductivity measurements, and Cornelius Gauckler who helped with the preparation of the Chevrel cathode. Finally, the authors thank to Dr. Fabio Maroni who critically read the manuscript and added helpful comments.

Conflict of Interest

The authors declare no conflict of interest.

Author Contributions

S.Z. and S.D. conducted the electrochemical measurements, XRD characterizations, and analyzed together with M.M. P.S. synthesized the electrolyte, collected all of the NMR data, and analyzed together with S.K. and M.W. F.F. performed all the calculations and analyzed together with D.G., M.B., and T.J. M.M., M.W., T.J., and M.W.M. supervised the research. The manuscript was written through contributions of all authors. All authors discussed the results and commented on the manuscript.

Data Availability Statement

The data that support the findings of this study are available from the corresponding author upon reasonable request.

Keywords

aprotic electrolytes, density functional theory, electrochemical metal deposition/dissolution, Mg-batteries, Schlenk-type equilibrium

Received: May 2, 2022
Revised: June 13, 2022
Published online: June 28, 2022

[1] M. Marinaro, D. Bresser, E. Beyer, P. Faguy, K. Hosoi, H. Li, J. Sakovica, K. Amine, M. Wohlfahrt-Mehrens, S. Passerini, *J. Power Sources* **2020**, *459*, 228073.
[2] J. Niu, Z. Zhang, D. Aurbach, *Adv. Energy Mater.* **2020**, *10*, 2000697.
[3] S. Passerini, D. Bresser, A. Moretti, A. Varzi, in *Batteries Present and Future Energy Storage Challenges*, Wiley-VCH, Weinheim **2020**.
[4] N. Sa, B. Pan, A. Saha-Shah, A. A. Hubaud, J. T. Vaughey, L. A. Baker, C. Liao, A. K. Burrell, *ACS Appl. Mater. Interfaces* **2016**, *8*, 16002.
[5] K. Xu, *Chem. Rev.* **2004**, *104*, 4303.
[6] O. Crowther, A. C. West, *J. Electrochem. Soc.* **2008**, *155*, A806.
[7] R. Schwarz, M. Pejic, P. Fischer, M. Marinaro, L. Jörissen, M. Wachtler, *Angew. Chem. Int. Ed.* **2016**, *55*, 14958.
[8] N. N. Greenwood, A. Earnshaw, in *Chemie Der Elemente*, VCH-Verlagsgesellschaft MbH, Weinheim **1988**.
[9] N. Sa, N. N. Rajput, H. Wang, B. Key, M. Ferrandon, V. Srinivasan, K. A. Persson, A. K. Burrell, J. T. Vaughey, *RSC Adv.* **2016**, *6*, 113663.
[10] D. Aurbach, Z. Lu, A. Schechter, Y. Gofer, H. Gizbar, R. Turgeman, Y. Cohen, M. Moshkovich, E. Levi, *Nature* **2000**, *407*, 724.
[11] D. Aurbach, I. Weissman, Y. Gofer, E. Levi, *Chem. Rec.* **2003**, *3*, 61.
[12] Y. Yang, W. Wang, Y. NuLi, J. Yang, J. Wang, *ACS Appl. Mater. Interfaces* **2019**, *11*, 9062.
[13] R. Deivanayagam, B. J. Ingram, R. Shahbazian-Yassar, *Energy Storage Mater.* **2019**, *21*, 136.

 © 2022 Wiley-VCH GmbH

21944296, 2022, 8, Downloaded from https://onlinelibrary.wiley.com/doi/10.1002/ente.202200440 by KIZ der Universitat Ulm, Wiley Online Library on [21/10/2022]. See the Terms and Conditions (https://onlinelibrary.wiley.com/terms-and-conditions) on Wiley Online Library for rules of use; OA articles are governed by the applicable Creative Commons License

[14] Z. Zhao-Karger, X. Zhao, O. Fuhr, M. Fichtner, *RSC Adv.* **2013**, *3*, 16330.
[15] Z. Zhang, S. Dong, Z. Cui, A. Du, G. Li, G. Cui, *Small Methods* **2018**, *2*, 1800020.
[16] R. E. Doe, R. Han, J. Hwang, A. J. Gmitter, I. Shterenberg, H. D. Yoo, N. Pour, D. Aurbach, *Chem. Commun.* **2014**, *50*, 243.
[17] G. Vardar, J. G. Smith, T. Thompson, K. Inagaki, J. Naruse, H. Hiramatsu, A. E. S. Sleightholme, J. Sakamoto, D. J. Siegel, C. W. Monroe, *Chem. Mater.* **2016**, *28*, 7629.
[18] O. Tutusaus, R. Mohtadi, T. S. Arthur, F. Mizuno, E. G. Nelson, Y. V. Sevryugina, *Angew. Chem. Int. Ed.* **2015**, *54*, 7900.
[19] Z. Zhao-Karger, M. E. Gil Bardaji, O. Fuhr, M. Fichtner, *J. Mater. Chem. A* **2017**, *5*, 10815.
[20] H. Shuai, J. Xu, K. Huang, *Coord. Chem. Rev.* **2020**, *422*, 213478.
[21] Z. Zhao-Karger, R. Liu, W. Dai, Z. Li, T. Diemant, B. P. Vinayan, C. Bonatto Minella, X. Yu, A. Manthiram, R. J. Behm, M. Ruben, M. Fichtner, *ACS Energy Lett.* **2018**, *3*, 2005.
[22] J. Luo, Y. Bi, L. Zhang, X. Zhang, T. L. Liu, *Angew. Chem. Int. Ed.* **2019**, *58*, 6967.
[23] T. Mandai, *ACS Appl. Mater. Interfaces* **2020**, *12*, 39135.
[24] F. Maroni, S. Dongmo, C. Gauckler, M. Marinaro, M. Wohlfahrt-Mehrens, *Batter. Supercaps* **2021**, *4*, 1221.
[25] G. Hasegawa, Y. Akiyama, M. Tanaka, R. Ishikawa, H. Akamatsu, Y. Ikuhara, K. Hayashi, *ACS Appl. Energy Mater.* **2020**, *3*, 6824.
[26] S. Dongmo, F. Maroni, C. Gauckler, M. Marinaro, M. Wohlfahrt-Mehrens, *J. Electrochem. Soc.* **2021**, *168*, 120541
[27] H. S. Kim, T. S. Arthur, G. D. Allred, J. Zajicek, J. G. Newman, A. E. Rodnyansky, A. G. Oliver, W. C. Boggess, J. Muldoon, *Nat. Commun.* **2011**, *2*, 426.
[28] Z. Zhao-Karger, R. Liu, W. Dai, Z. Li, T. Diemant, B. P. Vinayan, C. Bonatto Minella, X. Yu, A. Manthiram, R. J. Behm, M. Ruben, M. Fichtner, *ACS Energy Lett.* **2018**, *3*, 2005.
[29] D.-T. Nguyen, R. Horia, A. Y. S. Eng, S.-W. Song, Z. W. Seh, *Mater. Horizons* **2021**, *8*, 830.
[30] S. Dongmo, S. Zaubitzer, P. Schüler, S. Krieck, L. Jörissen, M. Wohlfahrt-Mehrens, M. Westerhausen, M. Marinaro, *ChemSusChem* **2020**, *13*, 3530.
[31] S. Krieck, P. Schüler, J. Peschel, M. Westerhausen, *Synthesis* **2019**, *51*, 1115.
[32] R. Neufeld, D. Stalke, *Chem. Sci.* **2015**, *6*, 3354.
[33] M. Pavlov, P. E. M. Siegbahn, M. Sandström, *J. Phys. Chem. A* **1998**, *102*, 219.
[34] K. Fujii, M. Sogawa, N. Yoshimoto, M. Morita, *J. Phys. Chem. B* **2018**, *122*, 8712.
[35] T. Kimura, K. Fujii, Y. Sato, M. Morita, N. Yoshimoto, *J. Phys. Chem. C* **2015**, *119*, 18911.
[36] L. F. Wan, D. Prendergast, *J. Am. Chem. Soc.* **2014**, *136*, 14456.
[37] P. Schüler, S. Sengupta, S. Zaubitzer, F. Fiesinger, S. Dongmo, H. Görls, M. Wohlfahrt-Mehrens, M. Borg, D. Gaissmaier, S. Krieck, M. Marinaro, T. Jacob, M. Westerhausen, *Eur. J. Inorg. Chem.* **2022**, *2022*.
[38] X. Zhao, Y. Yang, Y. Nuli, D. Li, Y. Wang, X. Xiang, *Chem. Commun.* **2019**, *55*, 6086.
[39] A. L. Lipson, S.-D. Han, B. Pan, K. A. See, A. A. Gewirth, C. Liao, J. T. Vaughey, B. J. Ingram, *J. Electrochem. Soc.* **2016**, *163*, A2253.
[40] Y. Liang, H. Dong, D. Aurbach, Y. Yao, *Nat. Energy* **2020**, *5*, 646.
[41] J. T. Herb, C. A. Nist-Lund, C. B. Arnold, *ACS Energy Lett.* **2016**, *1*, 1227.
[42] W. Ren, D. Wu, Y. NuLi, D. Zhang, Y. Yang, Y. Wang, J. Yang, J. Wang, *ACS Energy Lett.* **2021**, *6*, 3212.
[43] X. Huang, J. Wen, J. Lei, G. Huang, F. Pan, L. Li, *ACS Appl. Mater. Interfaces* **2022**, *14*, 8906.
[44] H. E. Swanson, E. Tatge, Nat. Bur. Stand. Rep. (ICDD PDF No. 00-004-0770), **1953**.
[45] E. Levi, G. Gershinsky, D. Aurbach, O. Isnard, G. Ceder, Chem. Mater. **2009**, *21*, 1390.
[46] M. D. Levi, D. Aurbach, *J. Power Sources* **2005**, *146*, 349.
[47] E. Levi, A. Mitelman, O. Isnard, M. Brunelli, D. Aurbach, *Inorg. Chem.* **2008**, *47*, 1975.
[48] R. Attias, M. Salama, B. Hirsch, Y. Goffer, D. Aurbach, *Joule* **2019**, *3*, 27.
[49] M. Matsui, *J. Power Sources* **2011**, *196*, 7048.
[50] A. Kopač Lautar, D. Kopač, T. Rejec, T. Bančič, R. Dominko, *Phys. Chem. Chem. Phys.* **2019**, *21*, 2434.
[51] K. Ta, K. A. See, A. A. Gewirth, *J. Phys. Chem. C* **2018**, *122*, 13790.
[52] D. Aurbach, A. Schechter, M. Moshkovich, Y. Cohen, *J. Electrochem. Soc.* **2001**, *148*, 1004.
[53] D. Aurbach, H. Gizbar, A. Schechter, O. Chusid, H. E. Gottlieb, Y. Gofer, I. Goldberg, *J. Electrochem. Soc.* **2002**, *149*, 115.
[54] A. Benmayza, M. Ramanathan, T. S. Arthur, M. Matsui, F. Mizuno, J. Guo, P. A. Glans, J. Prakash, *J. Phys. Chem. C* **2013**, *117*, 26881.
[55] R. Rüger, M. Franchini, T. Trnka, A. Yakovlev, E. van Lenthe, P. Philipsen, T. van Vuren, B. Klumpers, T. Soini, *AMS 2020.101, SCM, Theoretical Chemistry*, Vrije Universiteit, Amsterdam, The Netherlands, https://www.scm.com (accessed: June 2022).
[56] J. J. P. Stewart, *J. Mol. Model.* **2013**, *19*, 1.
[57] J. J. P. Stewart, AMS MOPAC 2020, MOPAC Engine based on the MOPAC2016 source code, http://OpenMOPAC.net (accessed: June 2022).
[58] D. P. Chong, E. Van Lenthe, S. Van Gisbergen, E. J. Baerends, *J. Comput. Chem.* **2004**, *25*, 1030.
[59] H. S. Yu, X. He, S. L. Li, D. G. Truhlar, *Chem. Sci.* **2016**, *7*, 5032.
[60] S. Lehtola, C. Steigemann, M. J. T. Oliveira, M. A. L. Marques, *SoftwareX* **2018**, *7*, 1.
[61] C. C. Pye, T. Ziegler, *Theor. Chem. Acc. Theory, Comput. Model.* **1999**, *101*, 396.
[62] R. S. Mulliken, *J. Chem. Phys.* **1955**, *23*, 1833.
[63] D. Schulze-Sünninghausen, J. Becker, B. Luy, *J. Am. Chem. Soc.* **2014**, *136*, 1242.

 © 2022 Wiley-VCH GmbH

21944296, 2022, 8, Downloaded from https://onlinelibrary.wiley.com/doi/10.1002/ente.202200440 by KIZ der Universitat Ulm, Wiley Online Library on [21/10/2022]. See the Terms and Conditions (https://onlinelibrary.wiley.com/terms-and-conditions) on Wiley Online Library for rules of use; OA articles are governed by the applicable Creative Commons License

Supplementary Information

A Novel and Highly Efficient Indolyl-based Electrolyte for Mg-batteries

Steve Zaubitzer[a], Saustin Dongmo[a], Philipp Schüler[b], Sven Krieck[b], Florian Fiesinger[c], Daniel Gaissmaier[c,d,e], Matthias van den Borg[c], Timo Jacob[c,d,e], Matthias Westerhausen[b], Margret Wohlfahrt-Mehrens[a,d], Mario Marinaro[a*]

[a]Zentrum für Sonnenenergie und Wasserstoff-Forschung Baden-Württemberg, Helmholtzstraße 8, D-89081 Ulm, Germany.

[b]Friedrich-Schiller University Jena, Institute of Inorganic and Analytical Chemistry, Humboldtstraße 8, D-07743 Jena, Germany.

[c]Ulm University, Institute of Electrochemistry, Albert-Einstein-Allee 47, D-89081 Ulm, Germany.

[d]Helmholtz Institute Ulm (HIU) Electrochemical Energy Storage, Helmholtz Str. 11, D-89081 Ulm, Germany.

[e]Karlsruhe Institute of Technology (KIT), P.O. Box 3640, D-76021 Karlsruhe, Germany.

Corresponding Author: *mario.marinaro@zsw-bw.de

Supplementary Figures

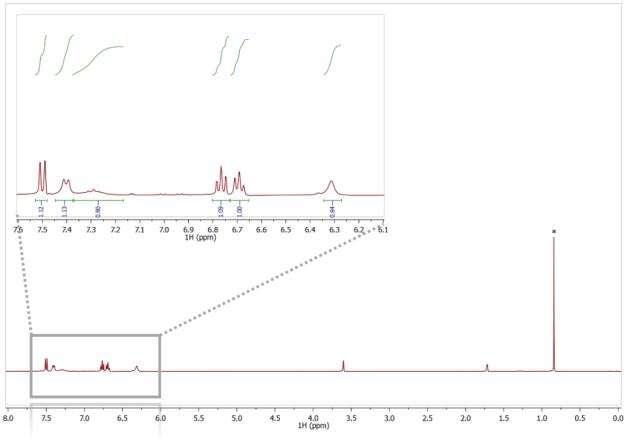

Figure S1 ^{1}H-NMR spectrum (400 MHz, [D_8]-THF, 296 K) of $(thf)_4$IndMgBr (* ethane).

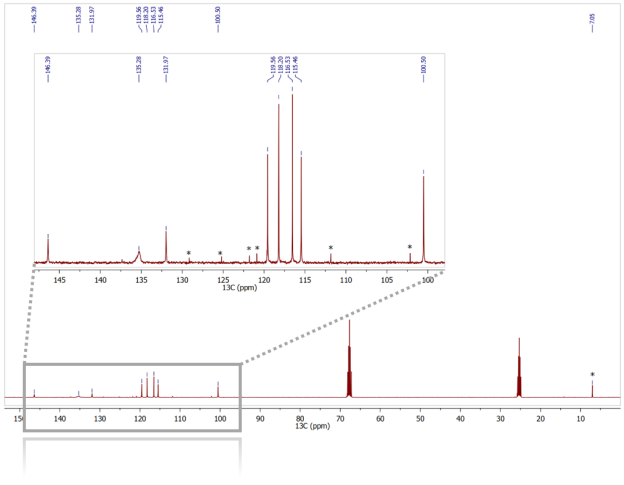

Figure S2 ^{13}C{^{1}H}-NMR spectrum (101 MHz, [D_8]-THF, 296 K) of $(thf)_4$IndMgBr (* ethane, indole).

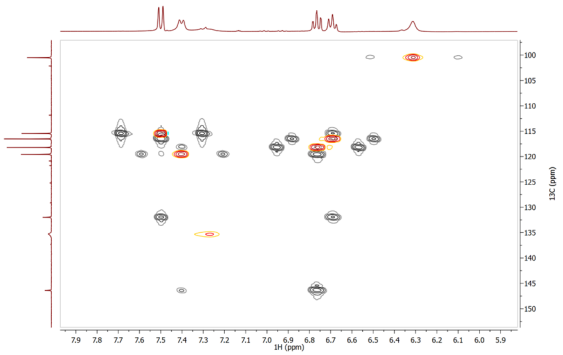

Figure S3 HSQC/HMBC-NMR overlay (400 MHz, [D_8]-THF, 296 K) of $(thf)_4$IndMgBr (* ethane, indole).

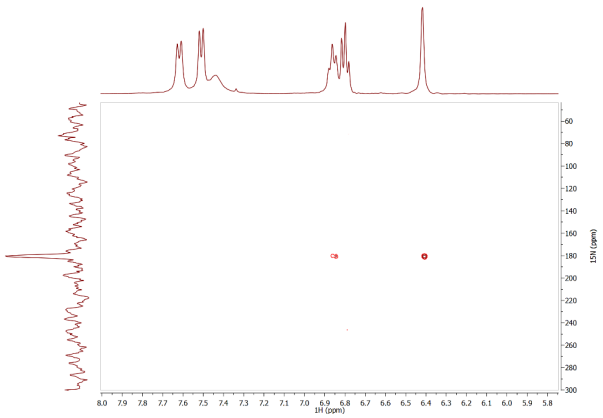

Figure S4 ^{15}N-^{1}H-HMBC (60.82 MHz, [D_8]-THF, 296 K) of $(thf)_4$IndMgBr.

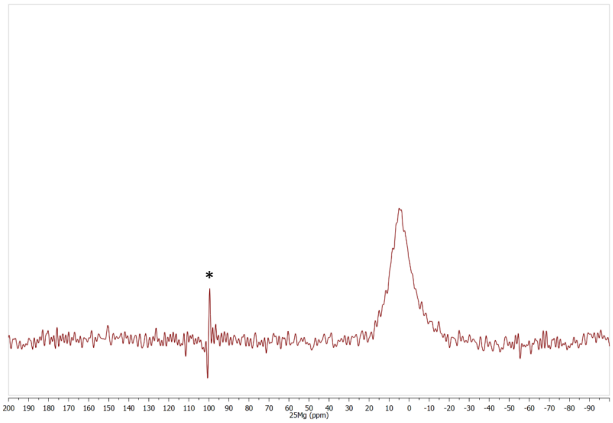

Figure S5 ^{25}Mg-NMR (24.5 MHz, [D_8]-THF, 296 K) of $(thf)_4$IndMgBr (* artefact).

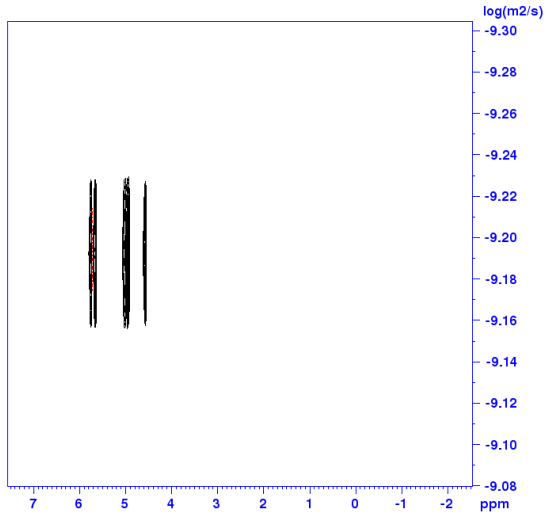

Figure S6 ^{1}H-DOSY-NMR (400 MHz, CD_3CN, 296 K) of $(thf)_4$IndMgBr.

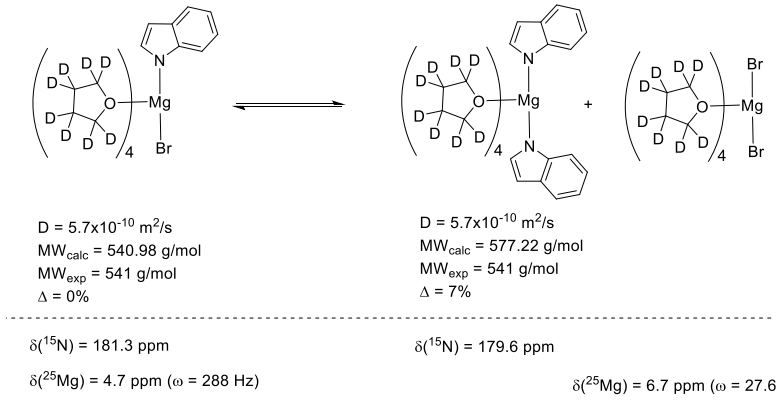

Figure S7 Results from the ECC-DOSY molar weight calculations and comparison of selected chemical shifts of the homoleptic and heteroleptic indolyl species.

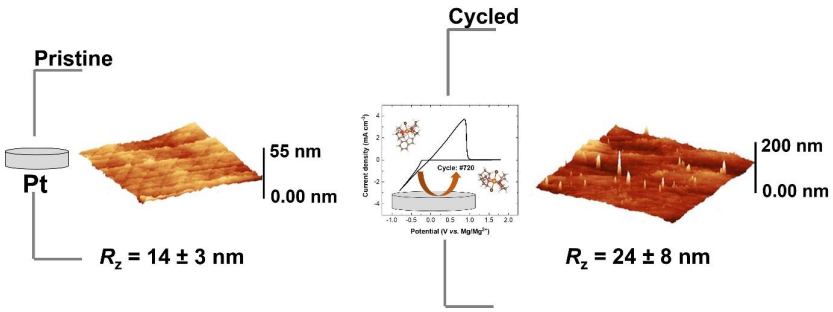

Figure S8 AFM characterization of the surface roughness of pristine and cycled Pt electrode.

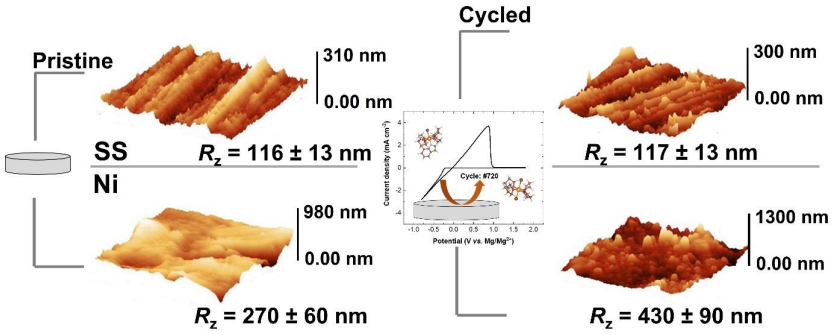

Figure S9 AFM characterization of the surface roughness of pristine and cycled SS and Ni electrode.

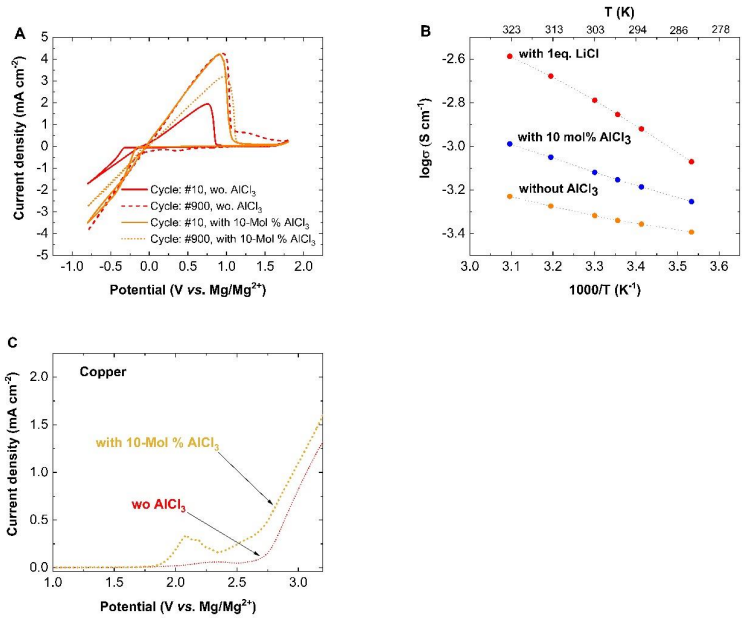

Figure S10 A) Selected cyclic voltammograms of the magnesium electroplating and stripping on Cu without and with addition $AlCl_3$ at a scan rate of 10 mV s^{-1}, Mg as counter and reference electrodes. **B**) Arrhenius plot of the ionic conductivity of a solution of 0.6 M Mg(Ind)Br in THF without (orange dots), with (blue dots) $AlCl_3$ and with (red dots) 1eq. LiCl as additive in a temperature range from 283K to 323K. **C**) Evaluation of the impact of the Lewis acid $AlCl_3$ on the anodic stability. Using a 0.6 M Mg(Ind)Br-THF electrolyte solution without (red dots) and with 10-Mol % $AlCl_3$ (orange dots) as additive. Performed in a three-electrode configuration with Mg as counter and reference electrode, Cu as the working electrode, and by an applied sweep rate of 5 mV s^{-1}.

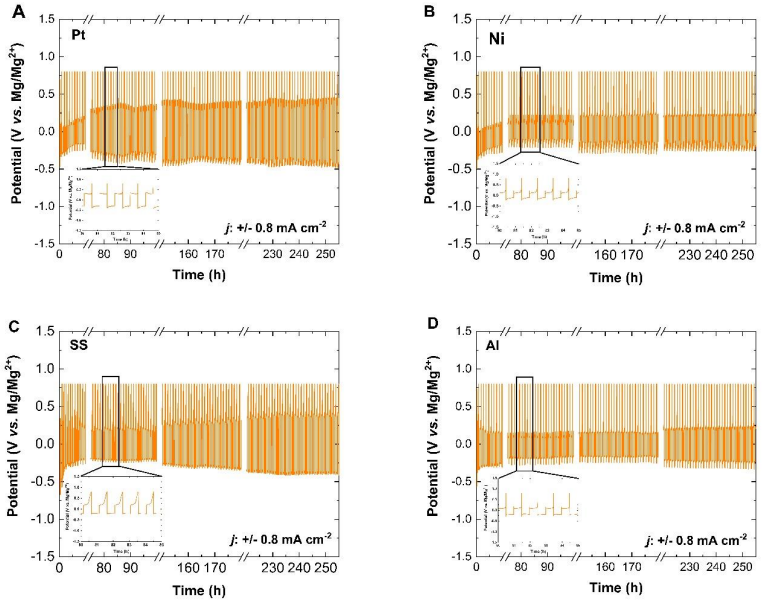

Figure S11 Chronopotentiometry cycling using 0.6 M Mg(Ind)Br in THF at ±0.8 mA cm^{-2} with 30 min time scale during plating and cut-off potential at 0.8 V during stripping, Mg was used as reference and counter electrode and **A**) platinum, **B**) nickel, **C**) stainless steel and **D**) aluminium as a current collector.

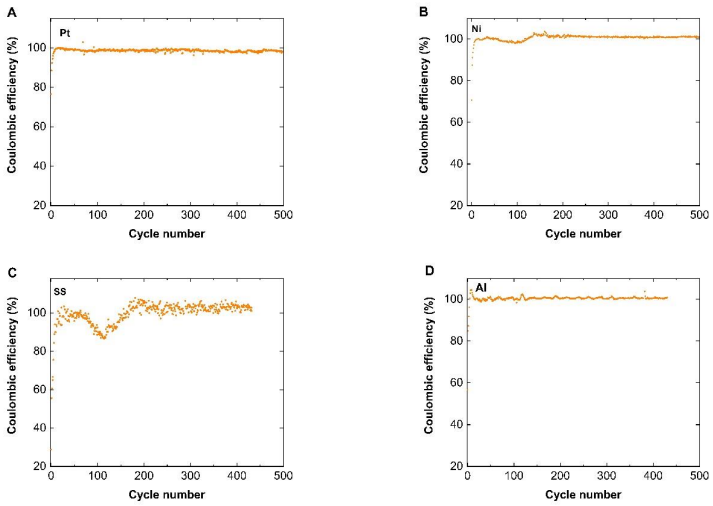

Figure S12 Respective coulombic efficiencies evaluated after chronopotentiometry for **A**) platinum, **B**) nickel, **C**) stainless steel and **D**) aluminium as current collector.

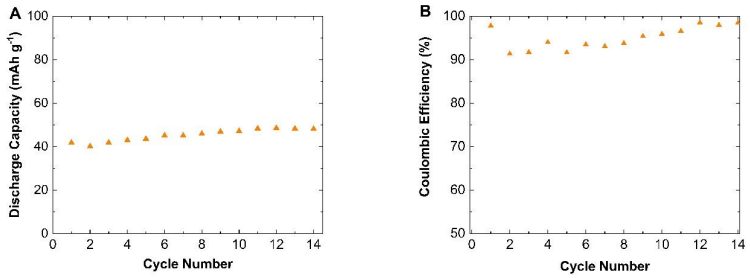

Figure S13 Cycling performance and evaluated Coulombic efficiency obtained for the Mg‖0.6 M Mg(Ind)Br/THF‖Mo_6S_8 cell with an applied current density of 2 mA g^{-1}.

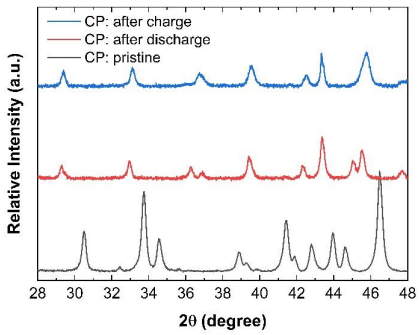

Figure S14 XRD patterns of the Chevrel cathode before (black), after discharge (red) and after charge (blue).

Supplementary Table

Table S1 Table of selected advanced non-nucleophilic magnesium-based electrolytes and the comparison of their electrochemical performance, including the discharge capacity using a Chevrel (Mo_6S_8) cathode. 1 C = 128.8 mA g^{-1}.

Electrolyte	**$\eta_{plating}$ /(mV) / Anodic stability (substrate) / V**	**Discharge capacity /(mAh g^{-1}) @current rate**	**Raw materials**	**Prices of raw materials**	**Price per 100 ml electrolyte**	**Ref.**
0.35 M $(HMDS)_2$-Mg/$AlCl_3$ in DGM	>500 (not specified) / 2.2 (Cu)	~90 @0.08C (30th)	Magnesium-bis(hexamethyldisilazide) Aluminium chloride Diglyme	379€ / 25g (97%, Sigma-Aldrich) 394€ / 25g (99.999%, Sigma-Aldrich) 123€ / 100ml (anh., 99.5%, Sigma-Aldrich)	~456€	[1]
0.5 M $Mg(BH_4)_2$/1 M THFPB in DGM	~200 (50th) / 1.6 (Cu)	~70 @0.2C (100th)	Tris(2H-hexafluoroisopropyl)-borate Magnesiumborhydrid Diglyme	~453€ / 5g (>95%, TCI, Shanghai) 155€ / 1g (95%, Sigma-Aldrich) ~230€ / 1L (anh., 99.5%, Aladdin)	~5330€	[2]
0.25 M $Mg[Al(HFIP)_4]_2$ in DME	~350 (3rd) / 2.2 (Cu)	~45 @0.08C (10th)	Magnesium methoxide 1,1,1,3,3,3-Hexafluoro-2-propanol Trimethylaluminium Tetrahydrofuran 1,2-Dimethoxyethane	0.5 L / 67.9€ (6-10 wt.% in methanol, Sigma-Aldrich) 25g / 67.3€ (Sigmal-Aldrich) 100 mL /86.8€ (2.0 M in hexane, Sigma-Aldrich) 1 L/ 173€ (≥99.9 %, anhydrous, inhibitor-free, Sigma-Aldrich) 250 mL / 145 € (anhydrous, 99.5%, inhibitor-free, Sigma-Aldrich)	~214 €	[3]
0.5 M OMBB in DME	~110 (50th) / ~2.0 (Cu)	~80 @0.1C (5th)	1,2-Dimethoxyethane Tris(hexafluoroisopropyl)-borate Magnesium chloride	250 mL / 145 € (anhydrous, 99.5%, inhibitor-free, Sigma-Aldrich) 5 g / 334€ (95%, TCI) 50 g / 136.20 € (anhydrous, 99.99%, Macklin)	~3600 €	[4]

			Magnesium, powder	100 g / 73.50 € (99.8%, Alfa-Aesar)		
0.3 M $Mg[B(hfip)_4]_2$ in DME	400 (3rd) / 2.6 (Cu)	~48 @0.4C (20th)	Natriumborhydrid Magnesium chloride Diethylether Hexafluoroisopropanol 1,2-Dimethoxyethane	25 g / 37.7 € (≥98 %, Sigma-Aldrich) 100 g / 47.8€ (≥98 %, Sigma-Aldrich) 1 L / 102 € (anhydrous, ≥99.7 %, 1ppm BHT, Sigma-Aldrich) 250 g / 125.5 € (99 %, abcr GmbH) 250 mL / 145 € (anhydrous, 99.5%, inhibitor-free, Sigma-Aldrich)	~165 €	[5]-[6]
0.2 M MBA/0.4 M $MgCl_2$ in THF	not reported / ~1.8 V (Cu)	~88 @0.05C (10th)	Magnesium-bis(diisopropyl)amide Magnesium chloride Tetrahydrofuran	(0.7 M in THF, Sigma-Aldrich), **even not more commercially available** 25 g / 166 € (99.9%, ultradry, powder, Alfa Aesar) Aladdin		[7]
0.25 M MBA-$B(Otfe)_3$ in THF	~500 (not precised) / ~1.6 V (Cu)	~48@0.02 C (12nd)	Magnesium-bis(diisopropyl)amide 2,2,2-Trifluoroethanol Tetrahydrofuran	(0.7 M in THF, Infinity Scientific (Beijing) Co., Ltd. **no price information available** 100g / 30€ (> 99%, TCI, Shanghai) (99.5%, safedry, Adamas-beta) **no price information available**		[8]
0.6 M Mg(Ind)Br in THF	185 (10th) / ~2.2 V (Cu)	~48@ ~0.02C (14th)	Magnesium Indole Tetrahydrofuran Bromethan	100g / 19.3€ (98%, Sigma-Aldrich) 100g / 73.2€ (≥99%, Sigma-Aldrich) 1L / 63.5€ (≥99.9%, 250 ppm BHT as inhibitor, Sigma-Aldrich) 1L / 58.3€ (98%, Sigma-Aldrich)	~14€	**This work**

Table S2 Detailed total energies for the electrolyte species Mg(Ind)Br, $MgBr_2$ and $Mg(Ind)_2$ involved in the calculation of the solvation energy E_{solv}.

$\mathbf{kJ\ mol^{-1}}$	**Mg(Ind)Br**	$\mathbf{MgBr_2}$	$\mathbf{Mg(Ind)_2}$
$E_{tot\ (vacuum)}^{electrolyte\cdot 4THF}$	-49.756	-37.501	-61.991
$E_{tot\ (vacuum)}^{electrolyte}$	-13.277	-1.041	-25.514
$E_{tot\ (vacuum)}^{THF}$	-9.011	-9.011	-9.011
$E_{explicit}$	-434	-415	-432
$E_{tot\ (COSMO)}^{electrolyte\cdot 4THF}$	-49.804	-37.560	-62.032
$E_{tot\ (vacuum)}^{electrolyte\cdot 4THF}$	-49.756	-37.501	-61.991
$E_{implicit}$	-47	-58	-40
E_{solv}	-481	-473	-472

13

Table S3 Calculated atomic charges for Mg(Ind)Br, $MgBr_2$ and $Mg(Ind)_2$ determined with the Mulliken charge analysis[9] without THF solvation.

Partial charges	$\mathbf{Mg(Ind)Br_{(vacuum)}}$	$\mathbf{MgBr_{2\ (vacuum)}}$	$\mathbf{Mg(Ind)_{2\ (vacuum)}}$
Mg	1.03	0.97	1.00
Br	-0.48	-0.49, -0.49	-
N (Ind)	-0.67	-	-0.64, -0.64

Table S4 Calculated atomic charges for Mg(Ind)Br, $MgBr_2$ and $Mg(Ind)_2$ determined with the Mulliken charge analysis[9] with included explicit THF solvation.

Partial charges	$\mathbf{Mg(Ind)Br \cdot 4THF_{(vacuum)}}$	$\mathbf{MgBr_2 \cdot 4THF_{(vacuum)}}$	$\mathbf{Mg(Ind)_2 \cdot 4THF_{(vacuum)}}$
Mg	1.03	1.04	0.99
Br	-0.66	-0.66, -0.67	-
N (Ind)	-0.51	-	-0.50, -0.51
O	-0.58, -0.58, -0.59, -0.59	-0.57, -0.57, -0.58, -0.58	-0.56, -0.57, -0.57, -0.57

Table S5 Calculated atomic charges for Mg(Ind)Br, $MgBr_2$ and $Mg(Ind)_2$ determined with the Mulliken charge analysis[9] with included explicit + implicit THF solvation.

Partial charges	$\mathbf{Mg(Ind)Br \cdot 4THF_{(COSMO)}}$	$\mathbf{MgBr_2 \cdot 4THF_{(COSMO)}}$	$\mathbf{Mg(Ind)_2 \cdot 4THF_{(COSMO)}}$
Mg	1.11	1.07	1.00
Br	-0.76	-0.75, -0.76	-
N (Ind)	-0.49	-	-0.48, -0.49
O	-0.58, -0.59, -0.60, -0.60	-0.58, -0.58, -0.59, -0.60	-0.57, -0.57, -0.57, -0.58

[1] Z. Zhao-Karger, X. Zhao, O. Fuhr, M. Fichtner, *RSC Adv.* **2013**, *3*, 16330.

[2] H. Xu, Z. Zhang, J. Li, L. Qiao, C. Lu, K. Tang, S. Dong, J. Ma, Y. Liu, X. Zhou, G. Cui, *ACS Appl. Mater. Interfaces* **2018**, *10*, 23757–23765.

[3] J. T. Herb, C. A. Nist-Lund, C. B. Arnold, *ACS Energy Lett.* **2016**, *1*, 1227–1232.

[4] A. Du, Z. Zhang, H. Qu, Z. Cui, L. Qiao, L. Wang, J. Chai, T. Lu, S. Dong, T. Dong, H. Xu, X. Zhou, G. Cui, *Energy Environ. Sci.* **2017**, *10*, 2616–2625.

[5] Z. Zhao-Karger, M. E. Gil Bardaji, O. Fuhr, M. Fichtner, *J. Mater. Chem. A* **2017**, *5*, 10815–10820.

[6] Z. Li, T. Diemant, Z. Meng, Y. Xiu, A. Reupert, L. Wang, M. Fichtner, Z. Zhao-Karger, *ACS Appl. Mater. Interfaces* **2021**, *13*, 33123–33132.

[7] Y. Yang, Y. Qiu, Y. NuLi, W. Wang, J. Yang, J. Wang, *J. Mater. Chem. A* **2019**, *7*, 18295–18303.

[8] W. Ren, D. Wu, Y. NuLi, D. Zhang, Y. Yang, Y. Wang, J. Yang, J. Wang, *ACS Energy Lett.* **2021**, 3212–3220.

[9] R. S. Mulliken, *J. Chem. Phys.* **1955**, *23*, 1833–1840.

5 Conclusion

Magnesium-ion batteries are discussed as future alternative to the existing lithium-ion technology. However, mass market adoption is currently hindered by many open research questions on dendrite growth, SEI formation, or finding suitable electrolytes, which need to be investigated and resolved first. This work aimed to contribute to battery research and thus support the future idea of a working magnesium-ion battery. To this end, the main findings of the four preceding papers are summarized below.

First, in chapter 4.1, the atomistic properties of Mg were determined, and the initial stages of surface growth were discussed. DFT calculations confirm the preference of magnesium to crystallize in a hcp crystalline structure at ambient conditions, with surface terminations Mg(0001), Mg($10\bar{1}0$)A, and Mg($10\bar{1}1$) being, in this order, most stable.[23] Interestingly, the surface proportions in a nanocrystal are quite different.[23] According to the Wulff construction, Mg($10\bar{1}1$) has the largest share of the surface with a surface fraction of about 50%, while the remaining area is distributed evenly between Mg(0001) and Mg($10\bar{1}0$)A.[23] The Wulff construction clearly illustrates that diffusion properties must be discussed for all three surfaces collectively and cannot be limited to the thermodynamically most stable surface Mg(0001).[23] Terrace self-diffusion of single atoms runs almost barrier-free on Mg(0001) but with higher activation energy on Mg($10\bar{1}1$).[23] When adsorbates collide on the surfaces, initial dimer, trimer, and cluster structures are formed, which is highly favored due to high attractive interactions between the adsorbates.[23] The small cluster structures can be seen as seeds for further island growth, whose shape on Mg(0001) could be either triangular with only $< \bar{1}\bar{1}22 >$- steps as proposed by Jäckle *et al.*[54] or hexagonal with alternating $< 11\bar{2}2 >$- and $< \bar{1}\bar{1}22 >$-steps at elevated temperatures[108].[23] However, the island pattern should be compact rather than fractal due to low step-edge and corner crossing barriers.[23,58] On Mg($10\bar{1}1$), diffusion barriers are in general higher compared to Mg(0001), but the ratios for bond formation and breakage are closer together.[23] All processes studied on Mg($10\bar{1}1$) can occur at ambient conditions, while on Mg(0001) kink evaporation and the formation of a step-vacancy are not activated at room temperature.[23] The three-dimensional diffusion studies reveal mostly nega-

tive Ehrlich–Schwoebel barriers for all investigated exchange descend processes on Mg(0001) and Mg($10\bar{1}1$), indicating a uniform and smooth surface growth due to a high rate of interlayer mass transport at low deposition rates.[23,58] However, a second adatom significantly increases the descent barriers for hopping and exchange processes, fostering the aggregation of new islands on top of existing islands if the adatom meets another adatom faster than it reaches the step-edge.[23]

Second, in chapter 4.2 a ReaxFF reactive force field description for Mg/O systems was developed.[27] Magnesium–magnesium interactions were obtained using the *KVIK* optimization routine[107] designed explicitly for metallic systems, while magnesium–oxygen interactions were trained using the SOPPI[101] optimizer.[27] As a result, the force field can reliably reproduce the bulk, surface, adsorption, and diffusion properties of both metallic Mg and the MgO salt.[27] A GCMC simulation showed that from a thermodynamic point of view, a Mg nanoparticle is first oxidized at surface octahedral sites.[27] The final structure obtained at the end of the simulation was mostly amorphous with individual domains showing rock salt ordering, separated by grain boundaries.[27] For complete transformation to the rock salt structure, the particle must be heated to 2000 K in an MD simulation for at least 75 ps.[27] If the thermal annealing is performed at too low temperatures or the system is cooled down too quickly, grain boundaries remain visible.[27] Furthermore, MD simulations demonstrated the effects of oxygen impurities on Mg surfaces.[27] O_2 immediately dissociates upon first contact with the Mg surface, heating the surface to several 1000 K.[27] The high temperature catalyzes further oxidation and causes the formation of rock salt phases separated by grain boundaries.[27] Among the Mg surfaces, Mg($10\bar{1}0$)A is the most reactive, forming an MgO layer with a thickness of up to 25 Å.[27]

Third, in Chapter 4.3, a Hauser base $(thf)_3Mg(Carb)Br$ was proposed as electrolyte for MIBs, which is synthesized by the *in-situ* Grignard metallation method (*i*GMM), more precisely by the metallation of carbazole by Mg in the presence of ethyl bromide in THF.[33] The electrolyte is present in Schlenk equilibrium, leading to the formation of homoleptic $(thf)_3Mg(Carb)_2$ and $(thf)_4MgBr_2$ in addition to heteroleptic $(thf)_3Mg(Carb)Br$.[33] DFT calculations were performed to determine the solvation energy and Mulliken charges for $(thf)_xMgCarbBr$, $(thf)_xMg(Carb)_2$, and $(thf)_xMgBr_2$ at different degrees x of solvation.[33] The highest solvation energy is obtained for $Mg(Carb)_2$, followed by Mg(Carb)Br and $MgBr_2$ for an equal number of ligated THF molecules.[33] The degree of solvation affects the coordination structure of the electrolyte, which changes from a linear (x = 0) via a trigonal-planar (x = 1) to a tetrahedral

(x = 2) via a trigonal-bipyramidal (x = 3) to an octahedral enviroment (x = 4).[33] Furthermore, Mulliken charge analysis demonstrated that with increasing solvation, the free electron pairs of THF oxygen atoms cause charge transfer from the nitrogen electrons of the carbazolyl group into its aromatic system due to electrostatic repulsion.[33] Unfortunately, the Coulombic efficiency of the Hauser base is only 91 %, so the electrolyte is most likely inadequate for battery applications.[33]

Fourth, in chapter 4.4, a novel electrolyte Mg(Ind)Br for MIBs containing benzopyrrole and bromide as anions is presented.[34] The cost-effective one-pot synthesis does not require additional Lewis acids such as $AlCl_3$ or halide-based additives and shows no signs of corrosion even after prolonged cycling.[34] Moreover, the electrolyte allows dendrite-free magnesium deposition in compact and smooth layers with a Coulombic efficiency of $>$99.5 %.[34] Like MgCarbBr, the electrolyte is in Schlenk equilibrium, with two Mg(Ind)Br molecules on one side and one $Mg(Ind)_2$ plus one $MgBr_2$ species on the other side.[34] DFT calculations were employed to study which side of the equilibrium is favored and to calculate solvation energy.[34] According to DFT and considering explicit and implicit solvation effects, Mg(Ind)Br species are slightly thermodynamically favored compared to homoleptic counterparts, which is consistent with NMR measurements.[34] In addition, according to DFT, Mg(Ind)Br has the highest solvation energy, followed by $MgBr_2$ and $Mg(Ind)_2$, with only marginal differences between the species.[34] The benzopyrrole-based electrolyte is promising for use in next-generation rechargeable Mg batteries because reversible intercalation of Mg cations into a Chevrel phase cathode is also possible.[34]

Bibliography

[1] Intergovernmental Panel on Climate Change: Global Warming of 1.5°C: An IPCC Special Report on the impacts of global warming of 1.5°C above pre-industrial levels and related global greenhouse gas emission pathways, in the context of strengthening the global response to the threat of climate change, sustainable development, and efforts to eradicate poverty, Summary for Policymakers, **2018**, https://www.ipcc.ch/site/assets/uploads/sites/2/2022/06/SPM_version_report_LR.pdf (accessed: 05/2023).

[2] Intergovernmental Panel on Climate Change: Climate Change 2022: Mitigation of Climate Change, Summary for Policymakers, **2022**, https://www.ipcc.ch/report/ar6/wg3/downloads/report/IPCC_AR6_WGIII_SPM.pdf (accessed: 05/2023).

[3] P. Jaramillo, S. K. Ribeiro, P. Newman, S. Dhar, O. Diemuodeke, T. Kajino, D. Lee, S. Nugroho, X. Ou, A. H. Strømman, J. Whitehead: Transport In IPCC, Climate Change 2022: Mitigation of Climate Change. Contribution of Working Group III to the Sixth Assessment Report of the Intergovernmental Panel on Climate Change, **2022**, https://www.ipcc.ch/report/ar6/wg3/downloads/report/IPCC_AR6_WGIII_Chapter_10.pdf (accessed: 05/2023).

[4] European Parliament: Reducing car emissions: new CO2 targets for cars and vans explained, **2022**, https://www.europarl.europa.eu/news/en/headlines/priorities/climate-change/20180920STO14027/reducing-car-emissions-new-co2-targets-for-cars-and-vans-explained (accessed: 05/2023).

[5] European Commission: Factsheet - The Transport and Mobility Sector, **2020**, https://ec.europa.eu/commission/presscorner/detail/en/fs_20_2350 (accessed: 05/2023).

[6] Eckart Aretz: Ende des Verbrennungsmotors: Norwegen gibt das Tempo vor, **2019**, https://www.tagesschau.de/wirtschaft/verbrennungsmotor-international-101.html (accessed: 05/2023).

[7] Z. P. Cano, D. Banham, S. Ye, A. Hintennach, J. Lu, M. Fowler, Z. Chen: Batteries and fuel cells for emerging electric vehicle markets, *Nat. Energy* **2018**, *3*, 279–289.

[8] International Energy Agency: Global Supply Chains of EV Batteries, **2020**, https://www.iea.org/reports/global-supply-chains-of-ev-batteries (accessed: 05/2023).

[9] European Commission, Joint Research Centre: Critical Raw Materials for Strategic Technologies and Sectors in the EU, **2022**, https://rmis.jrc.ec.europa.eu/uploads/CRMs_for_Strategic_Technologies_and_Sectors_in_the_EU_2020.pdf (accessed: 05/2023).

[10] Z. Guo, S. Zhao, T. Li, D. Su, S. Guo, G. Wang: Recent Advances in Rechargeable Magnesium-Based Batteries for High-Efficiency Energy Storage, *Adv. Energy Mater.* **2020**, *10*, 1903591.

[11] F. Bella, S. De Luca, L. Fagiolari, D. Versaci, J. Amici, C. Francia, S. Bodoardo: An Overview on Anodes for Magnesium Batteries: Challenges towards a Promising Storage Solution for Renewables, *Nanomaterials* **2021**, *11*, 810.

[12] A. Wang, S. Kadam, H. Li, S. Shi, Y. Qi: Review on modeling of the anode solid electrolyte interphase (SEI) for lithium-ion batteries, *npj Comput. Mater.* **2018**, *4*, 15.

[13] Y. Sun, F. Ai, Y.-C. Lu: Electrolyte and Interphase Design for Magnesium Anode: Major Challenges and Perspectives, *Small* **2022**, *18*, 2200009.

[14] J. B. Goodenough, K.-S. Park: The Li-Ion Rechargeable Battery: A Perspective, *J. Am. Chem. Soc.* **2013**, *135*, 1167–1176.

[15] J. B. Goodenough: How we made the Li-ion rechargeable battery: Progress in portable and ubiquitous electronics would not be possible without rechargeable batteries. John B. Goodenough recounts the history of the lithium-ion rechargeable battery, *Nat. Electron.* **2018**, *1*, 204.

[16] M. Armand, J.-M. Tarascon: Building better batteries, *Nature* **2008**, *451*, 652–657.

[17] A. Manthiram: An Outlook on Lithium Ion Battery Technology, *ACS Cent. Sci.* **2017**, *3*, 1063–1069.

[18] A. Manthiram: A reflection on lithium-ion battery cathode chemistry, *Nat. Commun.* **2020**, *11*, 1550.

[19] European Commission: Critical Raw Materials Resilience: Charting a Path towards greater Security and Sustainability, **2020**, `https://eur-lex.europa.eu/legal-content/EN/TXT/PDF/?uri=CELEX:52020DC0474&from=EN` (accessed: 05/2023).

[20] M. Fichtner, Motivation for a Magnesium Battery in: *Magnesium Batteries: Research and Applications*, The Royal Society of Chemistry, **2020**, Chapter 1, pp. 1–16.

[21] J. Song, E. Sahadeo, M. Noked, S. B. Lee: Mapping the Challenges of Magnesium Battery, *J. Phys. Chem. Lett.* **2016**, *7*, 1736–1749.

[22] M. Matsui: Study on electrochemically deposited Mg metal, *J. Power Sources* **2011**, *196*, 7048–7055.

[23] F. Fiesinger, D. Gaissmaier, M. van den Borg, T. Jacob: First-Principles Studies on the Atomistic Properties of Metallic Magnesium as Anode Material in Magnesium-Ion Batteries, *ChemSusChem* **2022**, *15*, e202200414.

[24] M. van den Borg, D. Gaissmaier, E. Knobbe, D. Fantauzzi, T. Jacob: Theoretical studies on the initial oxidation of metallic lithium anodes, *Appl. Surf. Sci.* **2021**, *555*, 149447.

[25] M. van den Borg, D. Gaissmaier, D. Fantauzzi, E. Knobbe, T. Jacob: Atomistic Studies on Water-Induced Lithium Corrosion, *ChemSusChem* **2022**, *15*, e202101765.

[26] J. G. Connell, B. Genorio, P. P. Lopes, D. Strmcnik, V. R. Stamenkovic, N. M. Markovic: Tuning the Reversibility of Mg Anodes via Controlled Surface Passivation by H_2O/Cl^- in Organic Electrolytes, *Chem. Mater.* **2016**, *28*, 8268–8277.

[27] F. Fiesinger, D. Gaissmaier, M. van den Borg, J. Beßner, A. C. T. van Duin, T. Jacob: Development of a Mg/O ReaxFF Potential to describe the Passivation Processes in Magnesium-Ion Batteries**, *ChemSusChem* **2023**, *16*, e202201821.

[28] H. D. Yoo, I. Shterenberg, Y. Gofer, G. Gershinsky, N. Pour, D. Aurbach: Mg rechargeable batteries: an on-going challenge, *Energy Environ. Sci.* **2013**, *6*, 2265.

[29] I. Shterenberg, M. Salama, Y. Gofer, E. Levi, D. Aurbach: The challenge of developing rechargeable magnesium batteries, *MRS Bull.* **2014**, *39*, 453–460.

[30] R. Deivanayagam, B. J. Ingram, R. Shahbazian-Yassar: Progress in development of electrolytes for magnesium batteries, *Energy Storage Mater.* **2019**, *21*, 136–153.

[31] R. Attias, M. Salama, B. Hirsch, Y. Goffer, D. Aurbach: Anode-Electrolyte Interfaces in Secondary Magnesium Batteries, *Joule* **2019**, *3*, 27–52.

[32] Z. Liang, C. Ban: Strategies to Enable Reversible Magnesium Electrochemistry: From Electrolytes to Artificial Solid–Electrolyte Interphases, *Angew. Chem. Int. Ed.* **2021**, *60*, 11036–11047.

[33] P. Schüler, S. Sengupta, S. Zaubitzer, F. Fiesinger, S. Dongmo, H. Görls, M. Wohlfahrt-Mehrens, M. van den Borg, D. Gaissmaier, S. Krieck, M. Marinaro, T. Jacob, M. Westerhausen: Suitability of Carbazolyl Hauser and Turbo-Hauser Bases as Magnesium-Based Electrolytes, *Eur. J. Inorg. Chem.* **2022**, e202200149.

[34] S. Zaubitzer, S. Dongmo, P. Schüler, S. Krieck, F. Fiesinger, D. Gaissmaier, M. van den Borg, T. Jacob, M. Westerhausen, M. Wohlfahrt-Mehrens, M. Marinaro: A Novel and Highly Efficient Indolyl-Based Electrolyte for Mg Batteries, *Energy Technol.* **2022**, *10*, 2200440.

[35] E. Peled: The Electrochemical Behavior of Alkali and Alkaline Earth Metals in Nonaqueous Battery Systems—The Solid Electrolyte Interphase Model, *J. Electrochem. Soc.* **1979**, *126*, 2047–2051.

[36] E. Peled, H. Straze: The Kinetics of the Magnesium Electrode in Thionyl Chloride Solutions, *J. Electrochem. Soc.* **1977**, *124*, 1030–1035.

[37] E. Peled, D. Golodnitsky, G. Ardel: Advanced Model for Solid Electrolyte Interphase Electrodes in Liquid and Polymer Electrolytes, *J. Electrochem. Soc.* **1997**, *144*, L208–L210.

[38] J. B. Goodenough, Y. Kim: Challenges for Rechargeable Li Batteries, *Chem. Mater.* **2010**, *22*, 587–603.

[39] H. Dou, X. Zhao, Y. Zhang, W. Zhao, Y. Yan, Z.-F. Ma, X. Wang, X. Yang: Revisiting the degradation of solid/electrolyte interfaces of magnesium metal anodes: Decisive role of interfacial composition, *Nano Energy* **2021**, *86*, 106087.

[40] S. Shi, P. Lu, Z. Liu, Y. Qi, L. G. Hector, H. Li, S. J. Harris: Direct Calculation of Li-Ion Transport in the Solid Electrolyte Interphase, *J. Am. Chem. Soc.* **2012**, *134*, 15476–15487.

[41] J. Yan, J. Zhang, Y.-C. Su, X.-G. Zhang, B.-J. Xia: A novel perspective on the formation of the solid electrolyte interphase on the graphite electrode for lithium-ion batteries, *Electrochim. Acta* **2010**, *55*, 1785–1794.

[42] K. Ushirogata, K. Sodeyama, Z. Futera, Y. Tateyama, Y. Okuno: Near-Shore Aggregation Mechanism of Electrolyte Decomposition Products to Explain Solid Electrolyte Interphase Formation, *J. Electrochem. Soc.* **2015**, *162*, A2670–A2678.

[43] S. He, J. Luo, T. L. Liu: $MgCl_2/AlCl_3$ electrolytes for reversible Mg deposition/stripping: electrochemical conditioning or not?, *J. Mater. Chem. A* **2017**, *5*, 12718–12722.

[44] J. S. Lowe, D. J. Siegel: Reaction Pathways for Solvent Decomposition on Magnesium Anodes, *J. Phys. Chem. C* **2018**, *122*, 10714–10724.

[45] Y. Yu, A. Baskin, C. Valero-Vidal, N. T. Hahn, Q. Liu, K. R. Zavadil, B. W. Eichhorn, D. Prendergast, E. J. Crumlin: Instability at the Electrode/Electrolyte Interface Induced by Hard Cation Chelation and Nucleophilic Attack, *Chem. Mater.* **2017**, *29*, 8504–8512.

[46] T. J. Seguin, N. T. Hahn, K. R. Zavadil, K. A. Persson: Elucidating Non-aqueous Solvent Stability and Associated Decomposition Mechanisms for Mg Energy Storage Applications From First-Principles, *Front. Chem.* **2019**, *7*, 175.

[47] S.-B. Son, T. Gao, S. P. Harvey, K. X. Steirer, A. Stokes, A. Norman, C. Wang, A. Cresce, K. Xu, C. Ban: An artificial interphase enables reversible magnesium chemistry in carbonate electrolytes, *Nat. Chem.* **2018**, *10*, 532–539.

[48] M. Matsui, H. Kuwata, D. Mori, N. Imanishi, M. Mizuhata: Destabilized Passivation Layer on Magnesium-Based Intermetallics as Potential Anode Active Materials for Magnesium Ion Batteries, *Front. Chem.* **2019**, *7*, 7.

[49] Z. Meng, D. Foix, N. Brun, R. Dedryvère, L. Stievano, M. Morcrette, R. Berthelot: Alloys to Replace Mg Anodes in Efficient and Practical Mg-Ion/Sulfur Batteries, *ACS Energy Lett.* **2019**, *4*, 2040–2044.

[50] N. Singh, T. S. Arthur, C. Ling, M. Matsui, F. Mizuno: A high energy-density tin anode for rechargeable magnesium-ion batteries, *Chem. Commun.* **2013**, *49*, 149–151.

[51] P. Bonnick, J. Muldoon: A Trip to Oz and a Peak Behind the Curtain of Magnesium Batteries, *Adv. Funct. Mater.* **2020**, *30*, 1–15.

[52] D. Li, Y. Yuan, J. Liu, M. Fichtner, F. Pan: A review on current anode materials for rechargeable Mg batteries, *J. Magnesium Alloys* **2020**, *8*, 963–979.

[53] R. Davidson, A. Verma, D. Santos, F. Hao, C. Fincher, S. Xiang, J. Van Buskirk, K. Xie, M. Pharr, P. P. Mukherjee, S. Banerjee: Formation of Magnesium Dendrites during Electrodeposition, *ACS Energy Lett.* **2019**, *4*, 375–376.

[54] M. Jäckle, K. Helmbrecht, M. Smits, D. Stottmeister, A. Groß: Self-diffusion barriers: Possible descriptors for dendrite growth in batteries?, *Energy Environ. Sci.* **2018**, *11*, 3400–3407.

[55] M. Jäckle, A. Groß: Microscopic properties of lithium, sodium, and magnesium battery anode materials related to possible dendrite growth, *J. Chem. Phys.* **2014**, *141*, 174710.

[56] D. Gaissmaier, M. Borg, D. Fantauzzi, T. Jacob: Microscopic Properties of Na and Li—A First Principle Study of Metal Battery Anode Materials, *ChemSusChem* **2020**, *13*, 771–783.

[57] D. Gaissmaier, D. Fantauzzi, T. Jacob: First principles studies of self-diffusion processes on metallic lithium surfaces, *J. Chem. Phys.* **2019**, *150*, 041723.

[58] Z. Zhang, M. G. Lagally: Atomistic Processes in the Early Stages of Thin-Film Growth, *Science* **1997**, *276*, 377–383.

[59] I. T. Røe, S. M. Selbach, S. K. Schnell: Crystal Structure Influences Migration along Li and Mg Surfaces, *J. Phys. Chem. Lett.* **2020**, *11*, 2891–2895.

[60] E. Santos, W. Schmickler: The Crucial Role of Local Excess Charges in Dendrite Growth on Lithium Electrodes, *Angew. Chem. Int. Ed.* **2021**, *60*, 5876–5881.

[61] A. Hagopian, M.-L. Doublet, J.-S. Filhol: Thermodynamic origin of dendrite growth in metal anode batteries, *Energy Environ. Sci.* **2020**, *13*, 5186–5197.

[62] M. Li, C. Wang, Z. Chen, K. Xu, J. Lu: New Concepts in Electrolytes, *Chem. Rev.* **2020**, *120*, 6783–6819.

[63] A. Brenner: Note on the Electrodeposition of Magnesium from an Organic Solution of a Magnesium-Boron Complex, *J. Electrochem. Soc.* **1971**, *118*, 99.

[64] D. Aurbach, Z. Lu, A. Schechter, Y. Gofer, H. Gizbar, R. Turgeman, Y. Cohen, M. Moshkovich, E. Levi: Prototype systems for rechargeable magnesium batteries, *Nature* **2000**, *407*, 724–727.

[65] D. Aurbach, I. Weissman, Y. Gofer, E. Levi: Nonaqueous magnesium electrochemistry and its application in secondary batteries, *Chem. Rec.* **2003**, *3*, 61–73.

[66] N. Pour, Y. Gofer, D. T. Major, D. Aurbach: Structural Analysis of Electrolyte Solutions for Rechargeable Mg Batteries by Stereoscopic Means and DFT Calculations, *J. Am. Chem. Soc.* **2011**, *133*, 6270–6278.

[67] T. D. Gregory, R. J. Hoffman, R. C. Winterton: Nonaqueous Electrochemistry of Magnesium: Applications to Energy Storage, *J. Electrochem. Soc.* **1990**, *137*, 775–780.

[68] Y.-s. Guo, F. Zhang, J. Yang, F.-f. Wang, Y. NuLi, S.-i. Hirano: Boron-based electrolyte solutions with wide electrochemical windows for rechargeable magnesium batteries, *Energy Environ. Sci.* **2012**, *5*, 9100.

[69] A. Du, Z. Zhang, H. Qu, Z. Cui, L. Qiao, L. Wang, J. Chai, T. Lu, S. Dong, T. Dong, H. Xu, X. Zhou, G. Cui: An efficient organic magnesium borate-based electrolyte with non-nucleophilic characteristics for magnesium–sulfur battery, *Energy Environ. Sci.* **2017**, *10*, 2616–2625.

[70] R. Mohtadi, M. Matsui, T. S. Arthur, S. J. Hwang: Magnesium borohydride: From hydrogen storage to magnesium battery, *Angew. Chem. Int. Ed.* **2012**, *51*, 9780–9783.

[71] T. Zhang, Z. Tao, J. Chen: Magnesium–air batteries: from principle to application, *Mater. Horiz.* **2014**, *1*, 196–206.

[72] Z. Zhao-Karger, J. E. Mueller, X. Zhao, O. Fuhr, T. Jacob, M. Fichtner: Novel transmetalation reaction for electrolyte synthesis for rechargeable magnesium batteries, *RSC Adv.* **2014**, *4*, 26924–26927.

[73] Z. Zhao-Karger, X. Zhao, D. Wang, T. Diemant, R. J. Behm, M. Fichtner: Performance Improvement of Magnesium Sulfur Batteries with Modified Non-Nucleophilic Electrolytes, *Adv. Energy Mater.* **2015**, *5*, 1401155.

[74] S. Dongmo, S. Zaubitzer, P. Schüler, S. Krieck, L. Jörissen, M. Wohlfahrt-Mehrens, M. Westerhausen, M. Marinaro: Stripping and Plating a Magnesium Metal Anode in Bromide-Based Non-Nucleophilic Electrolytes, *ChemSusChem* **2020**, *13*, 3530–3538.

[75] R. E. Doe, R. Han, J. Hwang, A. J. Gmitter, I. Shterenberg, H. D. Yoo, N. Pour, D. Aurbach: Novel, electrolyte solutions comprising fully inorganic salts with high anodic stability for rechargeable magnesium batteries, *Chem. Commun.* **2014**, *50*, 243–245.

[76] K. A. See, K. W. Chapman, L. Zhu, K. M. Wiaderek, O. J. Borkiewicz, C. J. Barile, P. J. Chupas, A. A. Gewirth: The Interplay of Al and Mg Speciation in Advanced Mg Battery Electrolyte Solutions, *J. Am. Chem. Soc.* **2016**, *138*, 328–337.

[77] J. E. Mueller, D. Fantauzzi, T. Jacob, Multiscale Modeling of Electrochemical Systems in: *Electrocatalysis*, Wiley-VCH, **2013**, Chapter 1, pp. 1–74.

[78] A. C. T. van Duin, S. Dasgupta, F. Lorant, W. A. Goddard: ReaxFF: A Reactive Force Field for Hydrocarbons, *J. Phys. Chem. A* **2001**, *105*, 9396–9409.

[79] K. Chenoweth, A. C. T. van Duin, W. A. Goddard: ReaxFF Reactive Force Field for Molecular Dynamics Simulations of Hydrocarbon Oxidation, *J. Phys. Chem. A* **2008**, *112*, 1040–1053.

[80] G. Henkelman, H. Jónsson: Improved tangent estimate in the nudged elastic band method for finding minimum energy paths and saddle points, *J. Chem. Phys.* **2000**, *113*, 9978–9985.

[81] G. Henkelman, B. P. Uberuaga, H. Jónsson: A climbing image nudged elastic band method for finding saddle points and minimum energy paths, *J. Chem. Phys.* **2000**, *113*, 9901–9904.

[82] W. Koch, M. C. Holthausen: A Chemist's Guide to Density Functional Theory, 2nd Edition, Wiley-VCH, Weinheim, **2001**.

[83] P. Hohenberg, W. Kohn: Inhomogeneous Electron Gas, *Phys. Rev.* **1964**, *136*, B864–B871.

[84] W. Kohn, L. J. Sham: Self-Consistent Equations Including Exchange and Correlation Effects, *Phys. Rev.* **1965**, *140*, A1133–A1138.

[85] D. M. Ceperley, B. J. Alder: Ground State of the Electron Gas by a Stochastic Method, *Phys. Rev. Lett.* **1980**, *45*, 566–569.

[86] J. P. Perdew, A. Zunger: Self-interaction correction to density-functional approximations for many-electron systems, *Phys. Rev. B* **1981**, *23*, 5048–5079.

[87] F. Giustino: Materials Modelling Using Density Functional Theory: Properties and Predictions, 1st Edition, Oxford University Press, Oxford, **2014**.

[88] R. Car, M. Parrinello: Unified Approach for Molecular Dynamics and Density-Functional Theory, *Phys. Rev. Lett.* **1985**, *55*, 2471–2474.

[89] J. P. Perdew: Generalized gradient approximation for the fermion kinetic energy as a functional of the density, *Phys. Lett. A* **1992**, *165*, 79–82.

[90] J. P. Perdew, K. Burke, M. Ernzerhof: Generalized Gradient Approximation Made Simple, *Phys. Rev. Lett.* **1996**, *77*, 3865–3868.

[91] J. Lee: Computational Materials Science: An Introduction, 2nd Edition, CRC Press, Boca Raton, **2017**.

[92] F. Jensen: Introduction to Computational Chemistry, 3rd Edition, Wiley, Hoboken, **2017**.

[93] L. Liu, Y. Liu, S. V. Zybin, H. Sun, W. A. Goddard: ReaxFF-/g: Correction of the ReaxFF Reactive Force Field for London Dispersion, with Applications to the Equations of State for Energetic Materials, *J. Phys. Chem. A* **2011**, *115*, 11016–11022.

[94] C. Zou, A. Van Duin: Investigation of Complex Iron Surface Catalytic Chemistry Using the ReaxFF Reactive Force Field Method, *JOM* **2012**, *64*, 1426–1437.

[95] A. van Duin: ReaxFF User Manual, Materials and Process Simulation Center, Beckman Institute (139-74), California Institute of Technology, **2002**, `https://www.scm.com/wp-content/uploads/ReaxFF-users-manual-2002.pdf` (accessed: 05/2023).

[96] T. P. Senftle, S. Hong, M. M. Islam, S. B. Kylasa, Y. Zheng, Y. K. Shin, C. Junkermeier, R. Engel-Herbert, M. J. Janik, H. M. Aktulga, T. Verstraelen, A. Grama, A. C. Van Duin: The ReaxFF reactive force-field: Development, applications and future directions, *npj Comput. Mater.* **2016**, *2*, 15011.

[97] A. van Duin, W. Goddard, M. Islam, H. van Schoot, T. Trnka, A. Yakovlev: ReaxFF 2021, SCM, Theoretical Chemistry, Vrije Universiteit, Amsterdam, The Netherlands, **2021**, `https://www.scm.com` (accessed: 05/2023).

[98] R. Rüger, M. Franchini, T. Trnka, A. Yakovlev, E. van Lenthe, P. Philipsen, T. van Vuren, B. Klumpers, T. Soini: AMS 2021, SCM, Theoretical Chemistry, Vrije Universiteit, Amsterdam, The Netherlands, **2021**, `https://www.scm.com` (accessed: 05/2023).

[99] W. J. Mortier, S. K. Ghosh, S. Shankar: Electronegativity-equalization method for the calculation of atomic charges in molecules, *J. Am. Chem. Soc.* **1986**, *108*, 4315–4320.

[100] T. Verstraelen, P. W. Ayers, V. Van Speybroeck, M. Waroquier: ACKS2: Atom-condensed Kohn-Sham DFT approximated to second order, *J. Chem. Phys.* **2013**, *138*, 074108.

[101] A. C. T. van Duin, J. M. A. Baas, B. van de Graaf: Delft molecular mechanics: a new approach to hydrocarbon force fields. Inclusion of a geometry-dependent charge calculation, *J. Chem. Soc. Faraday Trans.* **1994**, *90*, 2881.

[102] E. Iype, M. Hütter, A. P. J. Jansen, S. V. Nedea, C. C. M. Rindt: Parameterization of a reactive force field using a Monte Carlo algorithm, *J. Comput. Chem.* **2013**, *34*, 1143–1154.

[103] A. Jaramillo-Botero, S. Naserifar, W. A. Goddard: General Multiobjective Force Field Optimization Framework, with Application to Reactive Force Fields for Silicon Carbide, *J. Chem. Theory Comput.* **2014**, *10*, 1426–1439.

[104] H. Larsson, B. Hartke: Fitting reactive force fields using genetic algorithms, *Comput. Methods Mater. Sci.* **2013**, *13*, 120–126.

[105] M. Dittner, J. Müller, H. M. Aktulga, B. Hartke: Efficient global optimization of reactive force-field parameters, *J. Comput. Chem.* **2015**, *36*, 1550–1561.

[106] B. M. Rice, J. P. Larentzos, E. F. C. Byrd, N. S. Weingarten: Parameterizing Complex Reactive Force Fields Using Multiple Objective Evolutionary Strategies (MOES): Part 2: Transferability of ReaxFF Models to C–H–N–O Energetic Materials, *J. Chem. Theory Comput.* **2015**, *11*, 392–405.

[107] D. Gaissmaier, M. van den Borg, D. Fantauzzi, T. Jacob: KVIK Optimiser - An Enhanced ReaxFF Force Field Training Approach, *ChemRxiv* **2022**, DOI `10.26434/chemrxiv-2022-lrsjd-v2`.

[108] R. Stumpf, M. Scheffler: Ab initio calculations of energies and self-diffusion on flat and stepped surfaces of Al and their implications on crystal growth, *Phys. Rev. B* **1996**, *53*, 4958–4973.

List of Abbreviations

ACKS2	atom-condensed Kohn-Sham DFT approximated to second order
ACN	acetonitrile
$AlCl_3$	aluminum trichloride
AMS	Amsterdam Modeling Suite
APC	all-phenyl complex
a.u.	atomic units
B3LYP	Becke, 3-parameter, Lee–Yang–Parr
bcc	body-centered cubic
$[B(HFP)_3]$	tris(hexafluoroisopropyl)borate
BR_3	triarylborates
Bu_2Mg	dibutylmagnesium
DCC	dichloro-complex
DFT	density functional theory
diglyme	1-methoxy-2-(2-methoxyethoxy)ethane
DME	1,2-dimethoxyethane
EC	ethylene carbonate
EEM	electron equilibration method
$EtAlCl_2$	ethylaluminum dichloride
EV	electric vehicles

fcc	face-centered cubic
GCMC	grand-canonical Monte Carlo
GGA	generalized gradient approximation
GHG	greenhouse gas
H	hydrogen
hcp	hexagonal close-packed
HMDS	hexamethyldisilazane
IEA	International Energy Agency
***i*GMM**	*in-situ* Grignard metallation method
LDA	local density approximation
Li	lithium
LIB	lithium-ion battery
MACC	magnesium aluminum chloride complex
MC	Monte Carlo
MD	molecular dynamics
Mg	magnesium
$Mg(BH_4)_2$	magnesium borohydride
$MgCl_2$	magnesium chloride
MIB	magnesium-ion battery
NEB	nudged elastic band
PBE	Perdew, Burke, and Ernzerhof
PhMgCl	phenylmagnesium chloride
PZC	potential of zero charge
QC	quantum mechanical

SEI	solid-electrolyte interface
SHE	standard hydrogen electrode
SOPPI	successive one-parameter parabolic interpolation
THF	tetrahydrofuran
TSK	terrace-step-kink

List of Figures

1.1 Schematic overview and working principle of a rechargeable battery with the main components anode, cathode, separator, and electrolyte. Based on Guo *et al.* and Bella *et al.*[10,11] 2

2.1 Schematic presentation of a polyhetero microphase SEI on lithium or carbon electrode. Taken from Peled *et al.*[37] 6
2.2 Schematic open-circuit energy diagram of an aqueous electrolyte. ϕ_A and ϕ_C are the anode and cathode work functions. E_g is the window of the electrolyte for thermodynamic stability. A $\mu_A >$ LUMO and/or a $\mu_C <$ HOMO requires a kinetic stability by the formation of an SEI layer. Taken from Goodenough and Kim.[38] 7
2.3 Schematic pictures of SEI film formation processes based on (a) surface growth mechanism, and (b) near-shore aggregation mechanism. Taken from Ushirogata *et al.*[42] 8
2.4 Minimum energy pathways for the most favorable DME decomposition reactions on (a) Mg(0001), (b) MgO(100), and (c) $MgCl_2$(0001) obtained using the nudged elastic band method. Energies are with respect to the intact, adsorbed configuration on each surface, corresponding to the point at which the reaction coordinate is equal to zero. Taken from Lowe and Siegel.[44] 10
2.5 Digital photograph of fractal Mg structure. Taken from Davidson *et al.*[53] 11

3.1 Outline of the multi-scale approach. The circular boxes contain the methods (DFT, ReaxFF) operating on different time and length scales. The square box contains tasks that can be performed using either method but in ReaxFF with bigger systems for longer time but at the cost of accuracy. ReaxFF force fields are obtained by successive training and testing cycles against DFT reference data. Based on Mueller *et al.*[77] 16

3.2 Overview of the working principle of ReaxFF. Based on van Duin.[95] . 22

Achnowledgement

First and foremost, I would like to thank Prof. Dr. Timo Jacob for providing me the opportunity to do my doctorate. Thank you very much for the excellent supervision during my time at the Institute of Electrochemistry.

Furthermore, I would like to thank Prof. Dr. Axel Groß, who kindly accepted the second grading of this thesis.

A special thanks goes to Prof. Dr. Adri van Duin, with whom I was allowed to do a research stay in his institute at Penn State University to learn the ReaxFF method, and for the many discussions, even during the time when I was already back in Germany.

Moreover, I would like to say a special thank you to all my friends and colleagues at the Institute of Electrochemistry. Especially to Dr. Daniel Gaissmaier and Matthias van den Borg, who made my start in theoretical chemistry so easy and taught me all the basics of DFT and ReaxFF. I would also like to thank Dr. Björn Kirchhoff and Dr. Christoph Jung for their scientific support and advice. Additionally, I would like to thank my master's student Julian Beßner for his work, whose results contributed to this dissertation.

Next, I would like to thank my cooperation partners, in particular, Dr. Steve Zaubitzer, who was the initiator for the collaboration between his institute, the Center for Solar Energy and Hydrogen Research (ZSW), the Institute of Inorganic and Analytical Chemistry at the University of Jena and my institute. In addition, I would like to thank Philipp Schüler, Simon Sengupta, Dr. Helmar Görls, Dr. Sven Krieck, and Prof. Dr. Matthias Westerhausen from the University of Jena as well as Dr. Saustin Dongmo, Dr. Magret Wohlfahrt-Mehrens and Dr. Mario Marinaro from the ZSW.

I would also like to thank the German Research Foundation (DFG) for the financial support within the Cluster of Excellence Post Lithium Storage (POLiS), especially for funding my research position and the research stay abroad.

And finally, I would like to thank my beloved ones for their magnificent support throughout my doctorate.

Publications

Paper

(1) **F. Fiesinger**, D. Gaissmaier, M. van den Borg, T. Jacob: First-Principles Studies on the Atomistic Properties of Metallic Magnesium as Anode Material in Magnesium-Ion Batteries, *ChemSusChem* **2022**, *15*, e202200414.

(2) **F. Fiesinger**, D. Gaissmaier, M. van den Borg, J. Beßner, A. C. T. van Duin, T. Jacob: Development of an Mg/O ReaxFF Potential and Passivation of the Magnesium Anode by Oxygen Impurities in Magnesium-Ion Batteries, *ChemSusChem* **2023**, *16*, e202201821.

(3) P. Schüler, S. Sengupta, S. Zaubitzer, **F. Fiesinger**, S. Dongmo, H. Görls, M. Wohlfahrt-Mehrens, M. van den Borg, D. Gaissmaier, S. Krieck, M. Marinaro, T. Jacob, M. Westerhausen: Suitability of Carbazolyl Hauser and Turbo-Hauser Bases as Magnesium-Based Electrolytes, *Eur. J. Inorg. Chem.* **2022**, e202200149.

(4) S. Zaubitzer, S. Dongmo, P. Schüler, S. Krieck, **F. Fiesinger**, D. Gaissmaier, M. van den Borg, T. Jacob, M. Westerhausen, M. Wohlfahrt-Mehrens, M. Marinaro: A Novel and Highly Efficient Indolyl-Based Electrolyte for Mg Batteries, *Energy Technol.* **2022**, *10*, 2200440.

Poster

(1) **F. Fiesinger**, O. El-Khafif, M. van den Borg, D. Gaissmaier, T. Jacob: Atomistic Multiscale Modelling Of Magnesium Based Batteries, POLiS Conclave meeting **2019**.

(2) **F. Fiesinger**, D. Gaissmaier, M. van den Borg, T. Jacob: Theoretical studies of surface and diffusion properties of metallic Mg, POLiS Summer school **2021**.

(3) **F. Fiesinger**, D. Gaissmaier, M. van den Borg, A. C. T. van Duin, T. Jacob: Development of an Mg-O ReaxFF potential, POLiS Conclave meeting **2022**.

(4) **F. Fiesinger**, D. Gaissmaier, M. van den Borg, J. Beßner, A. C. T. van Duin, T. Jacob: Passivation process in Magnesium-Ion Batteries – A ReaxFF Study, Workshop: Computational modelling of batteries: First-principles quantum chemistry meets continuum approaches, Castle Reisensburg **2022**.

Curriculum Vitae

Personal details	
Name	Florian Nikolaus Fiesinger
Nationality	German

Education	
09/2019 – 12/2022	**Ph.D. (Dr. rer. nat.)** *Institute of Electrochemistry, Ulm University, Ulm, Germany*
09/2021 – 12/2021	**Visiting scholar** *Department of Mechanical and Nuclear Engineering, Pennsylvania State University, State College, USA*
08/2015 – 10/2017	**Master of Science, Chemistry and Management** *Ulm University, Ulm, Germany* *Master thesis at Institute of Inorganic Chemistry II*: Influence of a PEG functionalization on silica nanoparticles on the transport properties with the help of nanofibrils
08/2015 – 12/2012	**Erasmus+ exchange semester** *Åbo Akademi, Turku, Finland*
10/2012 – 08/2015	**Bachelor of Science, Chemistry and Management** *Ulm University, Ulm, Germany* *Bachelor thesis at Institute of Organic Chemistry II and Advanced Materials*: Synthese und Charakterisierung von sternförmigen Lochtransport-Materialien
09/2004 – 06/2012	**Allgemeine Hochschulreife** *Maria-Theresia-Gymansium, Augsburg, Germany*

Work experience

03/2023 – today	**Junior Consultant** *Roland Berger GmbH, Munich, Germany*
07/2018 – 08/2019	**Research scientist** *Research Center Energy Storage Technologies, TU Clausthal, Goslar, Germany*
11/2017 – 03/2018	**Intern** *Accenture GmbH, Technology Consulting, Frankfurt, Germany*
10/2016 – 01/2017	**Intern** *Deloitte GmbH Wirtschaftsprüfungsgesellschaft, Munich, Germany*

Declaration

Name: Florian Nikolaus Fiesinger

Declaration of Authorship

I hereby declare that I have written the present dissertation independently and that I have not used any sources or resources other than those indicated. I also declare that any phrases taken from published or unpublished texts have been identified as such and that I have complied with the Ulm University Statutes for Safeguarding Good Scientific Practice.

Ulm, ...

Florian Nikolaus Fiesinger